Bergische Universität Wuppertal
Fakultät für Architektur
und Bauingenieurwesen

Berichte des Lehr- und Forschungsgebietes Geotechnik

Nr. 39 Dezember 2021

Rowena Verst

Stabilisation mechanisms of polymer solutions in the context of temporary earth-wall support

Stabilisierungswirkung von Polymerlösungen bei der Stützung von Erdwänden

Herausgegeben von Prof. Dr.-Ing. M. Pulsfort

Stabilisation mechanisms of polymer solutions in the context of temporary earth-wall support

Stabilisierungswirkung von Polymerlösungen bei der Stützung von Erdwänden

by
Rowena Verst, M. Sc.

Dissertation

accepted by
the School of Architecture and Civil Engineering
at the University of Wuppertal

in partial fulfillment of the requirements
for the degree of Dr.-Ing.

1. Gutachter (primary examiner)	Univ.-Prof. Dr.-Ing. Matthias Pulsfort University of Wuppertal
2. Gutachter (secondary examiner)	Univ.-Prof. Dr.-Ing. habil. Achim Hettler (formerly) TU Dortmund University

Tag der Einreichung (date of submission)	2 Sep 2020
Tag der mündlichen Prüfung (date of oral examination)	19 Feb 2021

The PhD thesis can be quoted as follows:

urn:nbn:de:hbz:468-urn:nbn:de:hbz:468-20211220-111418-7
[http://nbn-resolving.de/urn/resolver.pl?urn=urn%3Anbn%3Ade%3Ahbz%3A468-20211220-111418-7]

DOI: 10.25926/z3fw-4x10
[https://doi.org/10.25926/z3fw-4x10]

Bergische Universität Wuppertal
Fakultät für Architektur und Bauingenieurwesen

Berichte des Lehr- und Forschungsgebietes Geotechnik

Nr. 39 **Dezember 2021**

Rowena Verst

Stabilisation mechanisms of polymer solutions in the context of temporary earth-wall support

Stabilisierungswirkung von Polymerlösungen bei
der Stützung von Erdwänden

Herausgegeben von Prof. Dr.-Ing. M. Pulsfort

Veröffentlicht als Heft Nr. 39
des Lehr- und Forschungsgebietes Geotechnik

Herausgeber (im Eigenverlag):
Prof. Dr.-Ing. M. Pulsfort
Bergische Universität Wuppertal
Lehr- und Forschungsgebiet Geotechnik

Print: ISBN 978-3-00-071148-0
eBook: ISBN 978-3-00-071149-7

Zugl.: Wuppertal, Univ., Diss., 2021

Vorwort des Herausgebers

Zur Frage der Flüssigkeitsstützung von Erdwänden sind am Lehr- und Forschungsgebiet Geotechnik bereits unter der Leitung von Herrn Prof. Dr.-Ing. Bernhard Walz in den 1980er Jahren mehrere Veröffentlichungen entstanden. In dieser Tradition ist die vorliegende Arbeit von Frau Dr.-Ing. Rowena Verst zu sehen, die sich mit der Flüssigkeitsstützung von Erdwänden mit Hilfe von Polymerlösungen aus wasserlöslichen Polymeren befasst hat. Die Verwendung dieser sowohl aus natürlichen, modifizierten Zellulosepolymeren als auch aus synthetischem Polyacrylamid-Polymeren herzustellenden Stützflüssigkeiten ist in Deutschland im Gegensatz zu Bentonitsuspensionen noch nicht sehr weit verbreitet, wird jedoch im englisch- und französischsprachigen Ausland bereits häufiger sowohl in der Schlitzwandtechnik als auch beim Tunnelbau im Schildvortrieb praktiziert. Allerdings fehlt es bisher noch an einem wissenschaftlich begründeten Nachweisformat zur Prognose der Stützwirkung, die sich bei Polymerlösungen grundsätzlich von der Stützwirkung von Bentonitsuspensionen unterscheidet, da sie im Gegensatz zu den Letztgenannten keine ausgeprägte Fließgrenze aufweisen.

Frau Verst hat es sich daher zur Aufgabe gemacht, die Eindringung von Polymerlösungen in unterschiedliche Bodenarten in Abhängigkeit von der Art des Polymers und seiner Konzentration in der Lösung in Laborversuchen systematisch zu untersuchen. Sie konnte dabei zeigen, dass das Eindringverhalten der reinen Polymerlösung in den Boden als Vorgang eines viskosen Fließens mathematisch beschrieben werden kann, indem das sog. Kapillarbündelmodell mit geeigneten Anpassungsfaktoren modifiziert wird. Damit kann das etablierte Nachweiskonzept für die Flüssigkeitsstützung mit Bentonitsuspension zeitabhängig formuliert werden, so dass sich eine maximal zulässige Standzeit der flüssigkeitsgestützten Erdwand ermitteln lässt. Bei Berücksichtigung einer Aufladung der Stützflüssigkeit mit Schwebstoffen wie Quarzmehl bzw. bei gezielter Beladung der Stützflüssigkeit mit Bentonitflocken bzw. Grobgranulat aus quellfähigen Polymeren konnte in den Laborversuchen eine Kolmation der Porenkanäle auch in groben Böden nachgewiesen werden, so dass die Übertragung des Flüssigkeitsdrucks auf das Korngerüst über eine Art inneren Filterkuchen im Boden gewährleistet werden kann. Dabei ist zu berücksichtigen, dass die Feststoffe bzw. gequollenen Granulatkörner ausreichend lang in Schwebe gehalten werden und ein ausreichender Materialvorrat zur effektiven Kolmation der Porenkanäle zur Verfügung steht. Im Ergebnis ist für beladene Polymerlösungen ein Standsicherheitsnachweis für flüssigkeitsgestützte Erdwände nach dem Ansatz der DIN 4126:2013 auch unabhängig von der Standzeit der Erdwand möglich, obwohl die Stützflüssigkeit keine regelgerechte Fließgrenze aufweist.

Mit den Erkenntnissen aus der Arbeit von Frau Verst ist ein großer Schritt in Richtung auf die realistische Prognose der Stützwirkung von Polymerflüssigkeiten auch für praktische Anwendungen in der Schlitzwandtechnik und im Tunnelbau mit flüssigkeitsgestützter Ortsbrust gelungen. Es ist zu hoffen, dass sich die Anwendung von Polymerlösungen anstelle von Bentonitsuspensionen auch in Deutschland in Zukunft mehr verbreitet, da die natürlichen Ressourcen an Bentonitvorkommen endlich sind und im Sinne der Nachhaltigkeit Alternativen zu deren Verwendung angebracht erscheinen.

Matthias Pulsfort Wuppertal, im Dezember 2021

Abstract

Water-soluble polymers, mostly of modified natural cellulosic polymers or synthetic polyacrylamide, are being used more and more frequently around the world as fluid support for pile drilling and diaphragm walling as well as for tunnel construction including pipe jacking. Adequate parameters for quality control on site and reliable precalculations, for safety, environmental and economic reasons, are still the subject of research. With respect to analytical design methods, the stability concept underlying DIN 4126:2013 can be utilized to assess micro and macro stability. However, knowledge on pressure-penetration relationships was found to be lacking for polymer support fluids as a basis for the definition of worst-case scenarios for each failure mechanism and to quantify pressure mobilization within the critical failure body (Δp_{mob}) and locally ($f_{s0,wall}$) at the earth wall. In this regard, a broad theoretical and experimental investigation was conducted within the scope of this work in order to improve the understanding of the polymer category with respect to its impact on penetration behaviour and support mobilization during temporary earth-wall stabilization.

Primarily, it was demonstrated that categorization into viscous flow behaviour vs. colmation provides a reasonable basis for the analysis of pressure-penetration relationships, related interaction mechanisms and subsequent classification by means of laboratory experiments. A laboratory concept was developed based on four soil penetration testing devices and prior material classification with focus on bulk rheology and fluid stability of the viscous base products and granular additive characterization for pore blocking.

The laboratory investigations further established that the flow behaviour of viscous polymer solutions in non-cohesive soil, the so-called in-situ viscosity, is governed by interactions between the specific structure of each polymer type and the porous matrix. These can be associated with characteristic moderately non-linear pressure drop curvatures along progressing penetration depths, which can be considered regardless of the pressure level. It was further found that bulk rheological characterisation at high shear rates (around 100-500 1/s) can provide a useful basis for the assessment of in-situ rheology for numerical analysis – e.g. based on capillary bundle models – in combination with characteristic correction factors to account for the specific soil-polymer interaction. This mainly comprises a vertical shift, i.e. dilution, and more pronounced Newtonian plateaus than are found with bulk rheology. These could be implemented within stability formulations as a basis to calculate temporary stability based on maximum stand-up times.

With respect to colmation behaviour, it was shown that the polymers of natural origin CMC and xanthan gum function considerably well with quartz mineral grain addition if amount and grain size distribution of the granular additives are adequately chosen with respect to the characteristic grain diameter d_{30} of the ground to be stabilized. Thin stable filter cakes with full pressure transfer at the earth wall were observed in soils ranging from medium sand to gravel. However, filter cake evaluation indicates that this favourable colmation process should be taken into account for stability mainly with sand, as only the filter cakes in sand seem internally stable against easy removal (sticky, dense, cohesive), while the thin filter cakes formed in gravel may be more easily removed by agitation.

With high-molecular weight synthetic polymers, the laboratory results revealed bentonite

flocks created by adding bentonite suspensions at low concentration to the prepared polymer solutions to be the optimal colmation material. The formation of these flocks was found to be highly dependent on the molecular weight of the polymer. Filter cake evaluation based on horizontal penetration tests before and after concreting revealed that these filter cakes based on bentonite flocks create a gum-like, but thin filter cake similar to that for polymer-modified bentonite, which is not entirely removed by rising fresh concrete. Aqueous polymeric grains (hydrogels) as a possible choice for all types of viscous base polymers for coarser subsoils were found to work moderately well in comparison, but also raised questions concerning the resulting quality of the contact zone.

With respect to the classification of colmation mechanisms for stability regardless of the type of granular additive, it was observed that the colmation process can be described by two characteristic penetration depths. At these levels, the penetration velocity deviates clearly, which coincides with changes in pressure transfer from viscous penetration to full membrane formation, visible within velocity plots as a significant decrease in penetration velocity of several decimal powers. In this regard, small-scale soil penetration tests were found to be suitable for the determination of these characteristic values with reference soil material chosen related to the effective diameters d_{30} (natural polymers) or d_{50} (synthetic polymers) of the targeted ground conditions.

A compact stability approach was derived based on these findings which can be formulated independently of time based on critical states derived from these characteristic values. Furthermore, suitability matrices were derived as a basis for recommendations on the choice of granular additive types depending on the type of polymer and the related effective grain diameter of the soil.

Moreover, a range of simple testing devices were found suitable to assure the functionality of polymer support fluids to provide their stabilizing qualities. These comprise Marsh funnel in combination with filter testing for the control of viscous flow behaviour and a combination of sieving, areometer testing and/or mud balance testing for quartz mineral material and aqueous polymeric grains. Additionally, small-scale soil penetration tests, e.g. by means of a filter press, are proposed for the assessment of bentonite flocks.

The findings from these experimental investigations can be considered to have identified the main components of polymer-based support fluids and subsoil which control their contact behaviour and explain the interaction mechanisms with regard to temporary stability. The derived calculative stability concepts can therefore be assumed to reflect the polymer-soil behaviour more realistically and are recommended as a useful tool for pre-calculations for a more realistic assessment of safety levels.

Zusammenfassung

Wasserlösliche Polymere, im Besonderen natürlich modifizierte Zellulosepolymere oder synthetisches Polyacrylamid, werden weltweit immer häufiger zur Flüssigkeitsstützung bei der Pfahl- oder Schlitzwandherstellung und auch im Tunnelbau angewendet. In Bezug auf sinnvolle Parameter zur Qualitätskontrolle auf der Baustelle sowie verlässlichen Vorkalkulationen besteht noch Forschungsbedarf. Auf Basis von DIN 4126:2013 ist es theoretisch möglich, die innere und äußere Standsicherheit zu quantifizieren. Jedoch mangelt es hinsichtlich polymerer Stützflüssigkeiten an gesicherten Informationen bezüglich Überdruck-Eindring-Beziehungen, auf Basis derer worst-case-Szenarios für jeden Versagensfall formuliert werden und eine Stützkraftmobilisierung quantifiziert werden kann. Vor diesem Hintergrund wurde innerhalb dieser Arbeit eine breite theoretische und experimentelle Untersuchung durchgeführt, um das Verständnis im Hinblick auf die Polymerkategorie und das zugehörige Eindringverhalten zu verbessern.

Es konnte dargestellt werden, dass das Verhalten der polymeren Stützflüssigkeiten in zwei Kategorien eingeteilt werden kann: viskoses Fließen und Kolmation. Ein laborgestütztes Untersuchungskonzept wurde entwickelt, das vier Versuchsstände sowie eine vorherige Klassifizierung der verwendeten Materialien mit Fokus auf das rheologische Verhalten und die Stabilität der Stützflüssigkeit und eine Charakterisierung der granularen Zuschläge zum Verstopfen der Bodenporen umfasst.

Aus den Versuchsergebnissen lässt sich schlussfolgern, dass das Fließverhalten von viskosen Polymerlösungen in kohäsionslosen Böden von Interaktionsmechanismen zwischen der spezifischen Polymerstruktur eines Polymertyps und der porösen Bodenmatrix gesteuert wird. Dies kann in Verbindung zu einem leicht nichtlinearen Spannungsabfall entlang der Eindringzone gebracht werden, der unabhängig vom Überdruckniveau berücksichtigt werden kann. Darüber hinaus zeigte sich, dass das Fließverhalten bei hohen Scherraten (gemessen im Rheometer) mithilfe von analytisch-numerisch-kombinierten Konzepten auf das Fließverhalten im Boden übertragen werden kann, wenn charakteristische Korrekturfaktoren berücksichtigt werden, die diese spezifische Interaktion reflektieren (Kapillarbündelmodelle). Dies betrifft vor allem eine Vertikalverschiebung (Verdünnungseffect) sowie ausgeprägte Newton-Plateaus in der rheologischen Darstellung. Diese Erkenntnisse wurden in ein bestehendes Stabilitätskonzept implementiert, als Basis für eine Quantifizierung der temporären Standsicherheit mit Fokus auf maximale Standzeiten einer ’offenen’ Erdwand.

Im Hinblick auf Kolmationseffekte konnte aufgezeigt werden, dass Polymere natürlicher Herkunft (CMC, Xanthangummi) besonders gut mit Addition von Quarzkörnern funktionieren, wenn Menge und Korngrößenverteilung auf den zu stützenden Boden angepasst werden. Dünne, stabile Filterkuchen mit voller Druckübertragung unmittelbar an der Erdwand wurden in Böden von Mittelsand bis zu Kies festgestellt. Allerdings wurde durch visuelle Auswertung der Filterkuchenbeschaffenheit der Schluss gezogen, dass auf der sicheren Seite liegend eine solche Filterkuchenbildung nur im Sand anzusetzen ist. Im Sand scheint der Filterkuchen intern stabil (dicht, klebrig, kohäsiv) zu sein, d.h. nicht leicht von Aushubwerkzeugen entfernt werden zu können; Filterkuchen in Kies dagegen sind leichter durch Bewegung zu lösen.

Hochmolekulare synthetische Polymere dagegen zeigten optimale Kolmationseffekte in Kombination mit Bentonitflocken, die erzeugt werden, indem Bentonitsuspensionen in geringer Konzen-

tration einer fertigen Polymerlösung zugeschüttet werden. Ob sich Bentonitflocken formieren oder sich die Bentonitkörner – ohne sichtbaren Flockungseffekt – perfekt in der Polymerlösung verteilen ist eng verknüpft mit dem Molekulargewicht des Polymers (Kettenlänge). Eine Auswertung von Filterkuchen vor und nach dem Einbringen des Betons (erzeugt durch horizontale Eindringversuche) konnte zeigen, dass die Bentonitflocken einen gummiartigen dünnen Filterfilm erzeugen, der einem Filterkuchen einer polymermodifizierten Bentonitsuspension ähnelt. Dieser Filterkuchen ist durch den aufsteigenden Beton bei der Betonage nicht leicht zu entfernen. Wässrige Polymerkörner (Hydrogele) als eine Alternative für gröbere Boden erzielten ebenfalls gute Ergebnisse, jedoch konnte auch hier eine klare Ablagerung als verbleibender Filterkuchen ermittelt werden, welche die Qualität der Kontaktzone beeinflussen könnte.

Insgesamt haben die Eindringversuche mit Kolmationseffekten ergeben, dass sich die zugrundeliegenden Prozesse unabhängig vom Zuschlagstyp für Stabilitätsbetrachtungen über zwei charakteristische Eindringtiefen klassifizieren lassen. Auf Basis dieser charakteristischen Größen konnte ein kompaktes Standsicherheitskonzept hergeleitet werden, das zeitunabhängig, d.h. anhand eines maßgebenden Falls, formuliert werden kann. Die notwendigen charakteristischen Parameter können über kleinmaßstäbliche Eindringversuche ermittelt werden, da aufgezeigt werden konnte, dass Veränderungen im Eindringverhalten mit Veränderungen in der Stützdruckübertragung korrelieren. Außerdem konnte das Kolmationsverhalten im Hinblick auf einen kritischen Korndurchmesser d_{30} oder d_{50} (je nach Polymertyp) klassifiziert werden, auf Basis dessen geeignete Additive ermittelt werden können.

Schließlich wurden Baustellenversuche im Hinblick auf Ihre Aussagekraft bezüglich der Stützfähigkeit von Polymerlösungen analysiert. Es konnten geeignete Versuchsgeräte gefunden werden, mithilfe derer Qualitätskontrollen auf der Baustelle im Hinblick auf Standsicherheitsanforderung durchführbar sind. Die Ergebnisse der experimentellen Untersuchungen konnten die Hauptkomponenten der Interaktion zwischen Stützmedium und zu stützendem Boden ermitteln und im Hinblick auf ihre Relevanz für die Standsicherheit klassifizieren. Es kann daher davon ausgegangen werden, dass daraus abgeleitete Standsicherheitsberechnungsmethoden aussagekräftige Ergebnisse liefern und daher als ein sinnvolles Medium für Vorkalkulationen und für eine realistischere Einschätzung von Sicherheitsniveaus bezüglich Stabilität angesehen werden können.

Contents

List of Tables

List of Figures

List of Abbreviations and Symbols

Latin symbols

a_W	Water activity [-]
b	Depth of differential soil element at the earth wall [m]
c	Cohesion [kPa]
c_{poly}	Polymer concentration in solution [g/l]
D	Average grain diameter [m]
$d_{10}, d_{15}, ...$	Effective grain diameters at 10/15/...% sieve passage [mm]
d_{ref}	Filter cake reference depth [m]
E_{ah}	Lateral earth pressure force [kN]
f_{corr}	Correction factor [-]
f_{s0}	Pressure gradient [kN/m^3]
$f_{s0,wall}$	Pressure gradient at the earth wall [kN/m^3]
g	Gravitational acceleration [m/s^2]
ΔH	Pressure difference [m]
i	Gradient $\frac{\Delta p/\gamma_F}{s(t)}$ [-]
K	Intrinsic permeability [m^2] / [m^3/m]
k_f, k_w	Permeability coefficient (water: $k_w = \frac{K \cdot \gamma_w}{\eta_w}$) [m/s]
L	Permeated length [m]
M_W	Weight-average molecular weight [Da]
M_N	Number-average molecular weight [Da]
m	Power-law parameter [-]
n	Porosity [-] (related to void ratio e by $n = \frac{e}{1+e}$)
Δp	Pressure difference [bar] or normalised pressure difference [-] (along penetration depth)
p	Pressure [bar] / [Pa]
p_w	Compressed air pressure [bar]
p_F	Hydrostatic pressure of the support fluid [bar]
$\Delta p_{mob,wall}$	Support pressure mobilized immediately at the earth wall (within depth b) [bar]
p_w	Hydrostatic groundwater pressure [bar]
R_{e_p}	Particle Reynolds number
R_{eq}	Equivalent hydraulic radius (Eq. 2.16) [m]
R_H	Hydraulic radius (V_{flow}/S) [m]
S	Specific surface (= wetted pore surface) [m^2] (for spheres: $S = \frac{1-n}{d_{sphere}}$)
S_k	Pressure force from support fluid [kN]
s	Penetration depth based on volumetric calculation [m]

Δs	Penetration depth correction factor [m]
$s_{crit,2}$	Characteristic penetration depth for full membrane behaviour [m]
s_{max}	Stagnation or maximum penetration depth [m]
s_{eq}	Equivalent penetration depth calculated from V-S testing [m]
s_p	Penetration depth based on start of pressure transfer [m]
t / T	Time / time step [hr] OR tortuosity [-]
Δt	Time difference [bar]
$\vec{u}$	Vectorial representation of movement
V	Volume (of differential soil element) [m^3]
v	Flow velocity / sinking velocity [m/s]
$v_{capillary}$	Capillary velocity [m/s]
v_{Darcy}	Filter velocity ($= n \cdot v_{capillary}$) [m/s]
V_{flow}	Volume available for flow [m^3]
x	Position along penetration depth [m]
z	Depth below ground level [m]
$\tilde{z}$	Depth below top of penetrated zone [m]

Greek symbols

α^*	Correction (shift) factor for fluid-soil interaction [-]
γ	Specific weight [kN/m^3]
$\gamma_G, \gamma_{G,stb}, \cdots$	Partial safety factors [-]
γ'	Buoyant specific weight (under water) [kN/m^3]
γ''	Buoyant specific weight (under support fluid) [kN/m^3]
$\dot{\gamma}$	Shear rate [1/s]
$\dot{\gamma}_{crit}$	Newton plateau limit [1/s] ($\dot{\gamma}_{crit,max}$ at η_{min}, $\dot{\gamma}_{crit,min}$ at η_{max})
Δ	Difference
η	(Dynamic) viscosity [Pa·s]
η'	Kinematic viscosity [m^2/s]
η_F	Correction factor DIN 4126:2013 [-]
η_{max}, η_{min}	Newtonian plateaus [Pa·s]
η_i	Inherent viscosity ($= \ln \eta_r / c_{poly}$) [l/g]
$[\eta]$	Intrinsic viscosity ($= \lim\limits_{c_{poly} \to 0} \frac{\eta_{sp}}{c_{poly}}$) [l/g]
η_r	Relative viscosity [-]
η_{red}	Reduced viscosity ($= \eta_{sp}/c_{poly}$) [l/g]
η_{sp}	Specific viscosity ($= \eta_r - 1$) [-]
η_w	(Dynamic) viscosity of water [Pa·s]
θ	Slip surface angle [°]
κ	Power-law parameter [Pa·s]
μ	Viscosity constant [Pa·s]
μ'	Kinematic viscosity constant [m^2/s]
ρ	Specific density [g/cm^3]
τ	Shear stress [Pa]

τ_F	Shear strength according to DIN 4126:2013 [Pa] (best approximated by a ball harp test or a pendulum test according to DIN 4127:2014 (after 1 min rest). It is most closely related to the gel strength G_{10m} according to API RP 13D:2017 measured with a viscometer/rheometer after 10 min rest. In contrast, the API RP 13D:2017 yield point equals the Bingham intersect extrapolated from dynamic shear measurements (appendix C.5))
φ'	Friction angle [°]

Abbreviations

AN	Synthetic anionic copolymer of acrylamide and acrylate with varying molecular weight and charge density
B	Bentonite suspension / bentonite flocks
CMC	Carboxymethylcellulose
COD	Chemical oxygen demand
DDL	Diffuse double layer (theory)
DFI	Deep Foundations Institute
DLVO	Derjaguin, Landau, Verwey, Overbeek (theory)
DS	Degree of substitution (number of substituted hydroxyl groups per repeat unit, e.g., for CMC)
dw	Deionised water
EFFC	European Federation of Foundation Contractors
EIA	Environmental impact assessment
FSR	Free swell ratio according to Prakash and Sridharan (2004)
GSD	Grain size distribution
H-P, H-R	Plane (P) and radial (R) penetration tests with horizontal (H) penetration
IUPAC	International Union of Pure and Applied Chemistry
P_{XS}, P_{S}, ...	Polymeric granular additive (hydrogel) (grain diameters 0.25 – 21.5 mm)
PAM	Polyacrylamide
PAC	Polyanionic cellulose (high-viscosity CMC)
PE	Polyethylene
PHPA	Partially hydrolysed polyacrylamide (also used for high-viscosity AN regardless of the way of production)
PVC	Poly(vinyl chloride)
RH	Relative humidity [%]
SAP	Superabsorbing polymer
SFG	Support Fluid Guide
S_{XS}, S_{S}, ...	Mineral granular additive (grain diameters [mm]: XS 0/0.125,S 0.125/0.25,M 0.4/0.5, G 0.71/1)
TOC	Total organic carbon
tw	Tap water
V-S, V-L	Vertical small-scale (S) and large-scale (L) penetration tests
WGK	German Water Hazard Class
XAN	Xanthan (gum)

1. Introduction

Water-soluble polymers, mostly of modified natural cellulosic polymers or synthetic polyacrylamide, are being used more and more frequently around the world as a support fluid for pile drilling, diaphragm walling and for tunnel construction, including pipe jacking. Adequate parameters for quality control on site and reliable precalculations, for safety, environmental and economic reasons, are still the subject of research. The application of polymer support fluids therefore currently faces the challenges of weighing possible advantages over uncertainties. In this regard, the presented study aims at improving the understanding of support mechanisms of polymer solutions with a focus on requirements for temporary polymer fluid support.

1.1. Research demand and objectives

Outside of Germany, polymers in aqueous solutions are increasing in popularity on projects with temporary fluid-supported earth walls, replacing the commonly used clay suspensions (SFG:2019; Borghi, 2006; Lam and Jefferis, 2018). Within Germany, polymers are mostly established as an additive for clay-based support and lubrication fluids only (Heinz, 2006; Praetorius and Schößer, 2017).

Until now[1] only one project with pure polymer-fluid support (Lesemann, 2010) has been realised in Germany. This is explained by uncertainties concerning possible environmental impacts and adequate control parameters. Internationally, however, a considerable number of projects are reported where polymer solutions are favoured over bentonite suspensions for environmental concerns towards bentonite, among other reasons (Lam and Jefferis, 2018). However, generally, the reasons to choose polymer solutions over bentonite suspensions are diverse; they vary depending on the specific boundary conditions of each project; and polymer solutions are not always applied with success (Berkovitz and Long, 1995; Wheeler, 2003; Lesemann, 2010; Jefferis and Lam, 2013; Lam and Jefferis, 2014; Lam and Jefferis, 2015b).

The implementation of polymers in geotechnical engineering is linked to developments within the oil and gas industry. Aqueous polymer solutions have been used in this field as drilling fluids for oil and gas exploration or for polymer flooding in enhanced oil recovery (EOR) at least since the 1960s, i.a. for favourable flowing patterns[2], for environmental and economic reasons, for salt stability of the fluid, improved lubrication and for clay swelling inhibition towards the surrounding ground (Sorbie, 1991; Patel et al., 2007; Anderson et al., 2010; Wilson and Wilson, 2014; Xiong et al., 2018; Murtaza et al., 2020).

Similar reasons can be found regarding the application of polymer solutions for temporary fluid support in geotechnical engineering and tunnelling, where the implementation process is advancing more rapidly (Lam and Jefferis, 2018; Borghi, 2006; FHWA-NHI-10-016:2010; Zumsteg, Puzrin, and Anagnostou, 2016; Mielenz and Mielenz, 2016).

In Thailand, (synthetic) acrylate-acrylamide-based polymer solutions were applied with success as a lubricating fluid for pipe-jacking in swelling/clogging ground where a bentonite suspension

---

[1] to the knowledge of the author

[2] good sweep efficiency

had failed (Alexanderson, 2001). Operational and economic advantages, e.g. concerning space requirement, mixing time, fluid treatment and disposal costs, were observed with a more recent example in London, where a similar polymer solution was applied for the construction of bored piles, which could be compared directly to piles drilled under bentonite-slurry support on the same construction site (Ouyang, Jefferis, and Wiltcher, 2018). As for (modified) natural polymers, cellulosic ethers have been used successfully in aqueous solutions for temporary fluid support at another construction site in London for diaphragm walling due to their considerably lower sensitivity towards salt in ground conditions critical for bentonite suspensions. Moreover, laboratory and on-site tests suggest that piles constructed under polymer-fluid-support give better fresh concrete displacement (Mobley, Costello, and Mullins, 2018) and higher shaft friction (Lam, Jefferis, and Martin, 2014a; Lam et al., 2015; Yoo and Han, 2019).

Fluid-supported geotechnical excavation techniques comprise tunnel excavation from micro-tunnelling to large diameters, both vertical and horizontal (VSM[3]), as well as diaphragm walling and pile drilling. Even though the specific circumstances such as pressure levels and geometries may differ with the type of technique, they generally share the concept of relatively large temporarily open soil or rock segments, which need to be supported by a fluid until the support fluid is replaced by concrete or mortar. Additionally, in each case, the support fluid may have other functions, such as debris transport or lubrication, which will not be the focus of this study.

In terms of standardised stability assessment, requirements cannot easily be transferred from oil and gas exploration to classical geotechnical excavation techniques as boundary conditions and therefore research focus and appropriate design differ distinctly in some aspects. Over 75% of drilled formations encountered in the context of oil and gas exploration can be assigned to low-permeability clay-bearing rock: shale. The percentage of shale in wellbore-stability-related problems is estimated at 90 % (Steiger and Leung, 1992), often related to swelling or clogging (Sorbie, 1991; Anderson et al., 2010; Wilson and Wilson, 2014; Farrokhrouz and Asef, 2013; Caenn, Darley, and Gray, 2017; Gholami et al., 2018). Fluid-supported geotechnical excavation techniques concern soil and especially non-cohesive material with higher permeability to a much larger fraction. Besides subsoil properties, oil and gas wells are typically drilled at relatively small diameters compared to e.g. drilled piles of 0.3 m $\leq d \leq$ 3.2 m (Pulsfort, Walz, and Faes, 1988, EA-P:2013), i.e. with more favourable cross section in terms of arching around the excavated hole. With considerably smaller exposed cross sections in relation to the drilling depth, local instabilities in terms of serviceability will most likely be more significant than macro stability. Moreover, diaphragm walling, deep foundations and tunnelling works are often carried out closer to built-up areas at comparably low pressure with direct impact on the nearby ground surface. This implies soil-fluid interaction at preferably low to zero flow velocity of the support fluid. In oil and gas exploration, the majority of published research focusses not on well drilling fluids, but on fluids for enhanced oil recovery, i.e. polymer flooding, with oil displacement at high injection rate and subsequently differing required fluid properties (Sorbie, 1991).

For fluid-supported geotechnical excavation techniques, internationally, DIN 4126:2013 (German standard for the calculative stability assessment of diaphragm walls) represents the only standardised concept for a calculative stability assessment of fluid-supported earth walls. However, it was specifically designed for clay suspensions, which are chemically and mechanically different to polymer solutions. Moreover, the great variability of the polymer category, comprising all macromolecules consisting of several molecular repeat units, complicates a direct comparison. Calculative concepts for fluid-supported tunnel faces, e.g. from Anagnostou and Kovarí (1994), generally adapt the concept from DIN 4126:2013 and Horn (1961).

---

[3] vertical shaft sinking machines as, e.g., developed by Herrenknecht (Frey and Schmaeh, 2019)

Based on the failure mechanisms of the stability concept for clay suspensions, Steinhoff (1993) developed an analytical approach for viscous polymer solutions with focus on diaphragm walls and bored piles, which was further evaluated by Lesemann (2010). However, besides being mathematically complex, the concept proved to be too conservative as it assumes an infinite penetration of polymer solutions into the ground over time without ever stagnating which is not found in practice, possibly due to the evolution of new base polymers and additives. E.g., Ouyang, Jefferis, and Wiltcher (2018) do not report any measurable fluid losses into the ground with application of a synthetic polymer mix for the construction of bored piles.

Internationally, field trials and on-site fluid testing prevail as the common methods to avoid instabilities, in addition to minimum requirements for the excess head of the support fluid towards the piezometric groundwater level varying between the standards: FHWA-NHI-10-016:2010 (USA, bored piles) 3 m (10 ft), ICE-SPEARWall:2016 (UK, bored piles and retaining walls) 2 m, EN 1538:2015 (EU, diaphragm walls) 1 m, EN 1536:2015 (EU, bored piles) 2.5 m, all without specification concerning the origin of these values. Yet, according to European guidelines EN 1536:2015 and EN 1538:2015, full-scale tests are only named third as suitable procedures to ensure stability after comparable experience and a calculative assessment and need to be executed with guarantee of a certain safety level.

Unsuccessful projects, with application of polymer solutions among others, have lead to the formation of an international working group[4] within the European Federation of Foundation Contractors (EFFC) and the American Deep Foundations Institute (DFI) aiming at developing recommendations/specifications for operations with support fluids. A first edition has been published in 2019 under the name ‘Guide to Support Fluids for Deep Foundations’, hereafter referred to as SFG:2019 (2019), with acceptance values from American and European execution guidelines for polymer solutions adapted from clay suspensions; they are based on practical experience mostly with test equipment designed for clay suspensions. A systematic field research study has been initiated by this Support Fluid Task Group underlining that the information available until now is not sufficient in quantity and quality to provide a solid basis for either of the three allowed safety assessments according to EN 1536:2015 and EN 1538:2015. Even trials cannot guarantee sufficient safety levels as long as the parameters which govern the failure mechanisms are not sufficiently understood to be implemented in related pre-calculations. A refined basis both for design (safety level) and execution (quality control) is needed which considers the functionality of polymer fluid support more realistically.

So far, some polymer producers, contractors and guidelines explain the good stabilizing performance of specific polymer mixtures with an uptake of fines from finer layers of the subsoil with continuous excavation methods as in-situ filtrate reducing material (a), especially with cellulose-based polymer solutions (e.g. diaphragm wall Earl Pumping Station, London), through formation of a polymer membrane at the earth wall (b) with synthetic polymer mixtures similar to an external or thin internal filter cake build-up or by colmation of synthetic polymeric additives as filtrate reducers (c) in high permeable ground (Goodhue and Holmes, 1997; FHWA-NHI-10-016:2010; DIN 4126:2013; Lesemann and Schwab, 2015; ICE-SPEARWall:2016; Lam and Jefferis, 2018).

Colmation effects from mineral fines (a) and other types of filler have been studied for bentonite suspensions by Heinz (2006) and Thienert (2011). It may be presumed that the mode of action will be similar for polymer solutions. (b)-(c) have not been metrologically proven until now. Moreover, it is not evident how the three aspects may affect stability considerations and how their effect can be guaranteed. The testing methods transferred from clay suspensions may not

---

[4] ‘Support Fluid Task Group’

be able to capture all of these specific functionalities.

This discrepancy between the performance of existing research approaches and practical experience shows that interaction mechanisms between the components of polymer-based support fluids and the subsoil need to be studied in more detail. The objectives of this study can therefore be summarised as follows:

(1) identify the relevant components of polymer-based support fluids and subsoil which control their contact behaviour and explain the interaction mechanisms,
(2) derive a compact calculative stability approach for fluid-supported earth walls similar to DIN 4126:2013, preferably formulated independently of time to be safely representative for the construction stage, which enables a more realistic assessment of the supporting effect of polymer solutions with regard to the design of diaphragm walls, piles, tunnel faces or lubrication in pipe jacking,
(3) develop a matrix or matrices as a basis to assess/evaluate the applicability of different polymer types and additives depending on respective soil characteristics of the subsoil, e.g. grain size distribution and
(4) discuss current testing methods and possible alternatives or supplements for quality control of polymer support fluids on site with focus on stability issues.

1.2. Methodology

Empirical laboratory studies are considered best suited to analyse the aforementioned aspects. A numerical model is not regarded to prove successful at this point. The physical and mechanical processes which determine the penetration behaviour of polymer solutions are not sufficiently understood to provide a model law with the accuracy needed to significantly improve the current approaches.

In order for suitable variation parameters to be chosen for the laboratory study, a theoretical basis will be laid out in chapter 2 by constituting a framework concerning required fluid functions in the context of fluid-supported geotechnical excavation techniques. On this basis, polymers and polymer solutions are analysed and classified. In the first instance, they are addressed separately with focus on the properties of the products themselves including rheology. Subsequently, analysis and classification of the individual products are complemented with a discussion on approaches for physical interaction mechanisms, in particular with regard to the transfer of support pressure, with penetration of polymer solutions into the ground.

In the context of an empirical study presented in chapter 3, four specially designed devices for the analysis of the penetration behaviour of the support fluid into the soil and a related pore pressure distribution are subsequently applied to address the open questions raised before and to identify options for improvement. These fluid penetration tests are complemented by standardized and adapted support fluid testing equipment for classification. This combination aims at enabling substantiated conclusions for a more compact stability assessment and for the choice of suitable methods for quality control summarized in chapter 4.

2. Theoretical background

The subject of polymer fluid support combines several fields of expertise: soil mechanics and modelling, polymer physics and chemistry, environmental processes and operational and economical aspects related to the construction site. This chapter provides insights into these viewpoints with differing degree of in-depth analysis as required both for an understanding of support mechanisms and related open questions and as a theoretical basis for the laboratory experiments.

The vocabulary used to describe interactions of these fields may differ from the wording used in literature of the respective field as the focus is set on the geotechnical viewpoint.

2.1. Requirements for support fluids in deep foundations and tunnelling

2.1.1. General requirements

Requirements for support fluids in deep foundations and tunnelling concern a variety of aspects, which can differ with the type of application, environmental conditions, excavation techniques, construction stages and global economical and operational restrictions. The objective of the following paragraphs is to give a general overview.

Clearly, the main requirement is the guarantee of a stable open trench, borehole, tunnel face or annular gap during the excavation process in terms of temporary stability. The required time to guarantee the stability of the respective earth wall support varies with the type application.

For tunnel face support, temporary stability needs to be guaranteed for each revelation of the cutting wheel, i.e. stability may have to be reformed with every revelation. The annular gap area immediately behind the tunnel shield should be held stable until placement and hardening of the final grout mortar. In pipe jacking, the pipe segments are continuously added from the starting pit and the previously placed segments are pressed further into the ground from there. The annular gap needs to be lubricated and stabilized continuously along the whole pipe length to ensure stability and limited jacking forces. The annular gap section closest to the starting pit can be considered critical in terms of the longest open standing time, which may often mean several weeks.

For panel trenches or boreholes, earth wall support is necessary until full excavation to the total depth, which will probably range within a number of days at maximum. For diaphragm walling, this can comprise several excavation segments before concrete placement. In this context, stability is influenced by the excavation method and related excavation stages (continuous or stepwise with temporary stand-still times). Furthermore, the movement of the excavation tools and subsequent placement of reinforcement cages within the excavated panels or holes can affect the stabilizing behaviour and generate additional requirements for stability in these conditions. Calculative concepts to assess temporary earth wall stability and related requirements for support fluids will be addressed in section 2.1.2.

The second main requirement concerns the effect of the support fluid on the final stability of the construction, which is related to successful concrete (or grout) placement after excavation without debris inclusions and good bond properties between the filling and the ground and possibly reinforcement. For bored piles and diaphragm walls, the related standards and guidelines (EN 1536:2015; EN 1538:2015; ICE-SPEARWall:2016; FHWA-NHI-10-016:2010; SFG:2019) therefore demand particular measures for base cleaning and formulate control parameters for support fluid quality before concreting. The respective values are summarized in SFG:2019 as ‘acceptance values’. On this matter, the solids content is considered a decisive parameter to be reduced in order to guarantee successful concrete placement. Internationally, limiting parameters differ between 1 % and 4 % for different types of polymer solutions (SFG:2019).

In addition to stability requirements, environmental and economical factors generally limit the range of applicable material properties and operational methods. This can be quantified in terms of environmental impacts and material, operational and disposal costs. In this respect, the operational footprint comprises the required material transport and necessary site equipment and space for fluid preparation, transport, recycling, reuse, treatment and disposal. Long fluid preparation times combined with a low recycling ratio require more space and material consumption. If necessary, settling plants or complex fluid treatment plants to separate fluid and fines during recycling before the concreting stage or for disposal create additional space requirements. Disposal requirements may comprise additional chemical treatment before discharge.

Aside from general requirements and stability functionality, support fluids may also be required to fulfil other fluid functions depending on the excavation method as discussed in Praetorius and Schößer (2017), Lam and Jefferis (2018) and SFG:2019. These can comprise

- good pumpability (sufficiently low shear resistance at higher shear rates), especially for tunnelling which requires pumping along large differences,
- a sufficient carrying capacity during flow for debris transport (tunnelling, reverse circulation drilling, e.g. hydromill),
- lubrication and cooling of the drilling tools (anti-clogging),
- lubrication of the annular gap (pipe jacking) and
- easy fluid/solids separation, e.g. a good encapsulation of soil colloids for quick settlement (bucket/grab).

These fluid functionalities need to be provided throughout the excavation process, which additionally requires a sufficient degree of mechanical stability depending on the type of application and chemical stability against environmental influences (e.g. salts). In this context, especially circulation drilling requires a high resistance against shear, which cannot be provided by all types of polymers. Pumping can also affect these properties and has to be chosen adequately (Lam and Jefferis, 2018; SFG:2019). Polymer physicochemical and mechanical stability is addressed in section 2.2.4.

It is evident that the requirements from different viewpoints need to be evaluated with focus on specific applications and excavation stages to find the best-fit option, e.g. between easy handling, environmental impact, low cost and sufficient temporary and final stability. The following chapters will focus on requirements for stability during fluid support and bear in mind their effects on other demands.

2.1.2. Stability conditions of fluid-supported earth walls

Temporary stability by fluid support is associated with the ultimate limit states (ULS) HYD/UPL and GEO-3 according to EN 1997-1:2014 (DIN 4126:2013), with fluid pressure (stabilizing) balancing hydrostatic groundwater pressure and earth pressure (destabilizing). In this regard, the considered geotechnical excavation techniques can be primarily differentiated with respect to the geometry of the supported earth walls, i.e. the cut face (Fig. 2.1). While the concept of mobilisation of fluid support is similar in all cases due to similar interaction mechanisms between support fluid and the ground matrix (Fig. 2.2), the actual amount of mobilised support can be a function of time and thus differ in each case. Furthermore, the relevant earth pressure varies significantly due to the influence of arching for each single excavation depth and differing geometries.

Generally, analytical stability assessment for diaphragm walls and bored piles (DIN 4126:2013; Stocker and Walz, 2003; Haugwitz and Pulsfort, 2018) as well as tunnel faces (Kirsch, 2010; Broere, 2015; Sterling, 2020) with fluid support essentially considers the same critical stability fields described by mechanical failure mechanisms:

(1) Inflow of groundwater
(2) Internal/micro/local stability
(3) External/macro/overall stability

This section will focus on these fields mainly by means of analytical calculative concepts for differentiation of the underlying mechanisms. Physico-chemical stability between soil and support fluid (section 2.1.3) is considered ensured in this context. The applicability of numerical modelling for the analysis of these states, e.g. with the possibility to study more complex geometries, is considered a subsequent step and will therefore be discussed separately in section 2.3.2.

The German standard DIN 4126:2013, designed for diaphragm walls with 'clean'[1] clay suspensions for fluid support, currently represents the only established standardised concept with a discrete calculative formulation for the three failure mechanisms for fluid-supported earth walls in non-cohesive soil yet. Since its first version in 1986, it includes the interaction mechanisms between support fluid and ground from the basic concepts developed by Weiß (1967) and Müller-Kirchenbauer (1977), on which many of the above mentioned stability considerations for the different fields of application are based, in some cases without specifying fixed formulas, e.g. by the practical guideline SFG:2019.

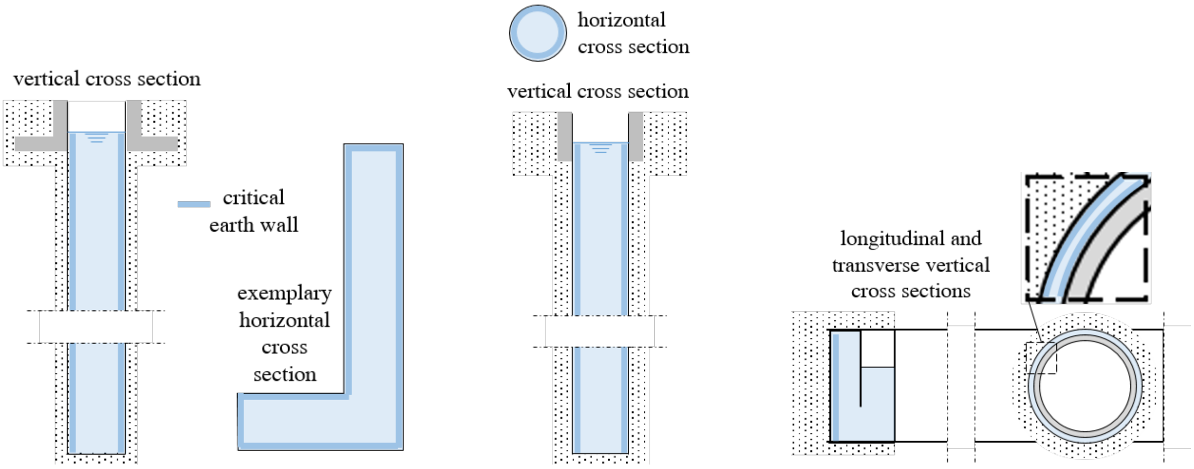

(a) Panel trench (b) Borehole (c) Tunnel face and annular gap

Figure 2.1.: Earth wall geometries

---

[1] 'clean', as named by the author, is referring to a suspension for which favourable effects of fines or other additives on the penetration behaviour can be neglected

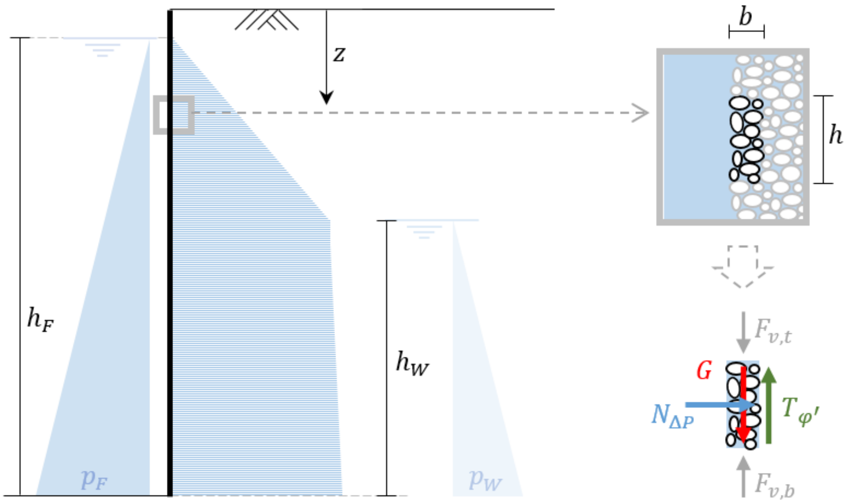

Figure 2.2.: Geometry and variables

On the basis of generalized fluid-independent formulations of the failure mechanisms given by DIN 4126:1986, Steinhoff (1993) developed an analytical approach for viscous polymer solutions with focus on diaphragm walls and bored piles, which was outlined in more detail by Lesemann (2010) and Lesemann, Vogt, and Pulsfort (2016).

In this respect, the following paragraphs will summarize the failure mechanisms (1)-(3) firstly based on the generalized DIN formulas with complementation for bored piles and tunnels, but without relation to fluid specifications. Soil swelling will be addressed separately for the specific case of cohesive ground. Subsequently, the existing specifications for 'clean' bentonite support fluids are presented and compared to the state-of-the-art approaches for polymer solutions to reveal differences and possible connecting points for experimental investigations on polymer solutions.

The generalized formulations based on DIN 4126:2013 for each failure mechanism in non-cohesive ground expressed independently of the type of fluid and of the failure geometries are given by Eq. 2.1-2.3. The index 'd' always refers to the design value according to the partial safety factor concept[2].

$$p_{w,dst,d}\left(z\right) \leq p_{F,stb,d}\left(z\right) \tag{2.1}$$

$$f_{s0,wall,d} \geq \frac{\gamma''_d}{\tan \varphi'_d} = f_{s0,wall,req,d} \tag{2.2}$$

$$max\left(\frac{E_{ah,dst,d}(h)}{S_{stb,d}}\right) \leq 1 \tag{2.3}$$

The first critical stability state refers to failure induced by inflow of groundwater (Eq. 2.1). It is considered averted if the stabilizing fluid pressure $p_{F,stb}$ equals or surpasses the destabilizing hydrostatic groundwater pressure $p_{w,dst}$ along the full height of the earth wall to be stabilized. For diaphragm walls and bored piles, $p_{F,stb}$ is given by the hydrostatic pressure of the support

---

[2] Classification according to DIN 4126:2013 and EN 1997-1:2014: groundwater inflow (HYD/UPL): accidental situation ('BS-A'): $\gamma_{G,dst} = 1.00$, $\gamma_{G,stb} = 0.95$; internal stability (GEO-3): transient situation ('BS-T'): $\gamma_G = 1.00$, $\gamma_\varphi = 1.15$; external stability (HYD/UPL) transient=permanent situation ('BS-P=T'): $\gamma_{G,dst} = 1.05$, $\gamma_{G,stb} = 0.95$

fluid $p_{F,stb}$ at depth z_i. For tunnelling, $p_{F,stb}$ may be supplemented by an additive pressure component from compressed air $p_{air,stb}$. In all cases, this term can be formulated independently of time as the hydrostatic terms defined by the specific weight of the respective fluid can be determined accordingly.

Internal failure as the second failure mechanism describes the successive falling of single grains or small groups of grains initiated at the earth wall as a local form of failure. Immediately at the earth wall, for cohesionless soil, it can be assumed that cutting forces (from gravitation and friction) between the vertically adjacent elements cannot yet be taken into account with a sufficient degree of security and, if so, would cancel each other out anyway ($F_{v,b} \approx F_{v,t} \approx 0$). An individual (plane) differential soil element of volume V (represented at cross section by b and h) can then be stabilized by friction mobilized by the normal pressure $\Delta p_{mob,wall}$. This pressure represents the amount transferred to the soil matrix within the described soil volume (Fig. 2.2 & Fig. 2.3). It can be summarized by the normal force $N_{\Delta P}$ (Eq. 2.4):

$$T_{\varphi'} = N_{\Delta P} \cdot \tan\left(\varphi'\right) = \left(\Delta p_{mob,wall} \cdot dh\right) \cdot \tan\left(\varphi'\right) \tag{2.4}$$

with φ' being the soil friction angle and assuming that the pressure level Δp is approximately constant over the differential height h of the soil element at depth z_i and cohesion $c = 0$. The destabilizing force can then be described by the gravitational force $G = \gamma'' \cdot b \cdot h$ with buoyant specific weight γ''. Force balance at element level gives:

$$T_{\varphi'} \geq G \leftrightarrow \frac{\Delta p_{mob,wall}}{b} \geq \frac{\gamma''}{\tan\left(\varphi'\right)} = f_{s0,wall,req} \tag{2.5}$$

The amount of pressure mobilized within V ($\Delta p_{mob,wall}$) depends on the course of pressure transfer to the soil matrix. As illustrated in Fig. 2.3, it can be significantly higher in the case of a non-linear pressure drop as compared to the linear case. The curvature of the pressure drop is described by the pressure gradient f_{s0} at any distance x from the earth wall for a given point in time, i.e. (Eq. 2.6)

$$f_{s0}(x) = \frac{\partial p}{\partial x} \tag{2.6}$$

As visualized in Fig. 2.4, f_{s0} is constant in the case of a linear pressure drop as assumed in DIN 4126:2013 (Fig. 2.3a & Fig. 2.4a) or dependent upon x otherwise (Fig. 2.3b & Fig. 2.4b). Fig. 2.4c represents a limiting case. $\frac{\Delta p_{mob,wall}}{b}$ (secant modulus) (Eq. 2.5) for the differential soil

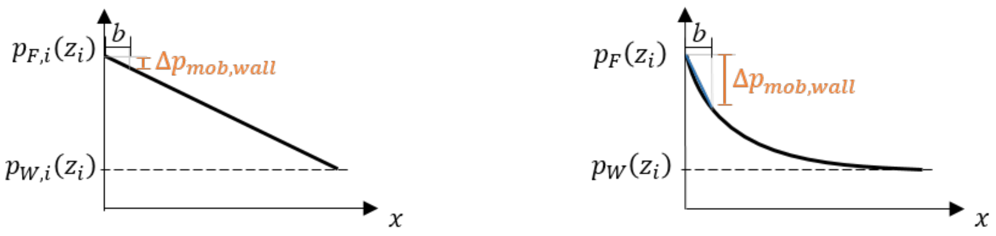

(a) Linear pressure drop

(b) Non-linear pressure drop

Figure 2.3.: Influence of the pressure drop curvature at time step t_j at a given depth z_i on the pressure transfer at the earth wall

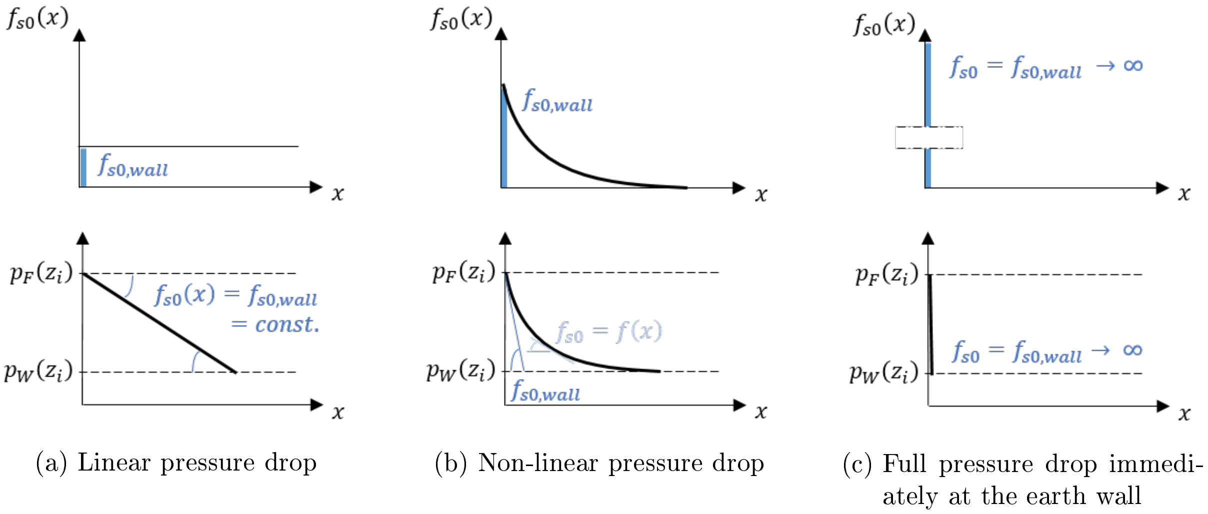

(a) Linear pressure drop (b) Non-linear pressure drop (c) Full pressure drop immediately at the earth wall

Figure 2.4.: Pressure gradient f_{s0} – influence of curvature at time step t_j and depth z_i

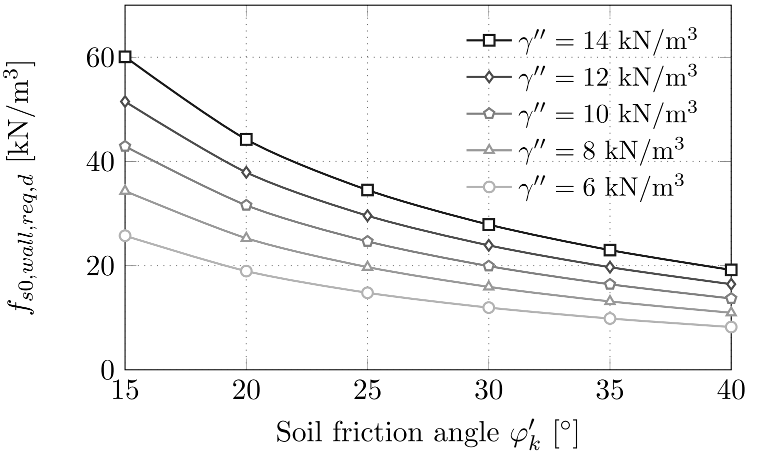

Figure 2.5.: Quantification of the required earth wall pressure gradient $f_{s0,wall,req,d}$

element reflects the pressure gradient at the earth wall

$$\frac{\Delta p_{mob,wall}}{b} = f_{s0,wall} = f_{s0}(x \to 0) \tag{2.7}$$

Therefore, Eq. 2.5 leads to the formulation from Eq. 2.2. The ratio $\gamma''/\tan\varphi'_d$ can be named the required pressure gradient $f_{s0,req}$. Fig. 2.5 visualizes the magnitude range of the design value of the required pressure gradient for a range of γ'' and φ'^3.

Fig. 2.6 compares the development of the pressure drop over time for three different fluid penetration cases according to Haugwitz and Pulsfort (2018) (Fig. 2.7):

- viscous penetration with pressure transferred to the ground through flow resistance, i.e. mobilization of shear stresses during inflow along the pore walls,
- (internal) colmation, i.e. the successive filtration of finer particles within the pores and
- an external filter cake formation with negligible penetration.

In the case of no or negligible penetration, full overpressure is transferred immediately at the fluid-soil interface. This case will be referred to as ideal ‘membrane’ behaviour, i.e. full pressure transfer with $f_{s0,wall} \rightarrow \infty$ and guaranteed internal stability (Fig. 2.4c & 2.7c). In the case of ideally viscous penetration (Fig. 2.7a), the pressure curvature is governed by the fluid flow behaviour[4]. Thereby, overpressure $\Delta p = p_F - p_w$ will drop linearly along the penetration depth under 1D flow conditions if the dependency between shear rate and mobilised friction (shear stress between fluid and soil) is approximately linear (constant viscosity approaches, e.g. Newton, Bingham), resulting in a constant pressure gradient $f_{s0,wall,lin}(t) = f_{s0,lin}(t)$ along the penetration depth for a given time step (Eq. 2.8) (Fig. 2.4a). A non-linear pressure drop (Fig. 2.4b) can be the result of a geometric increase of circumference (e.g. pile: radial flow) or non-linear shear-rate/shear-stress relationships (e.g. power law).

With purely viscous penetration, $f_{s0,wall}$ decreases over time as long as the penetration depth advances, though to a lesser degree for a non-linear pressure drop than for the linear case (Fig. 2.6a & 2.6b). The penetration can stagnate if the viscous support fluid possesses the ability to mobilise sufficient shear strength at rest (‘yield strength’ τ_F) along the penetration depth to balance the hydraulic pressure difference (cf. p. 15 on bentonite suspensions). With a linear pressure drop along the penetration depth, the pressure gradient can be simplified as follows (Eq. 2.8):

$$f_{s0,wall,lin}(t) = f_{s0,lin}(t) = \frac{\Delta p}{s(t)} \tag{2.8}$$

In contrast, colmation or other soil pore blocking effects induced by filtration or adsorption processes (Fig. 2.7b) ideally reduce the permeability by successively reducing the pore diameter, which increases the flow resistance and yields a full penetration stop. Consequently, f_{s0} must yield Fig. 2.4c. This effect is illustrated in Fig. 2.6c. The related degree of pressure drop depends upon the effectiveness of the colmation or absorption material.

Even an external filter cake can grow as long as material is available and filtration progresses. The earth wall pressure gradient can then be derived from the amount of pressure absorbed at the earth wall $\Delta p_{mob,wall}(t)$ over time (Eq. 2.9) and is likely to increase with progressing colmation/absorption.

$$f_{s0,wall}(t) = \frac{\Delta p_{mob,wall}(t)}{d_{ref}(t)} \tag{2.9}$$

The reference depth $d_{ref}(t)$ for $\Delta p_{mob,wall}(t)$ is likely to decrease with progressing permeability

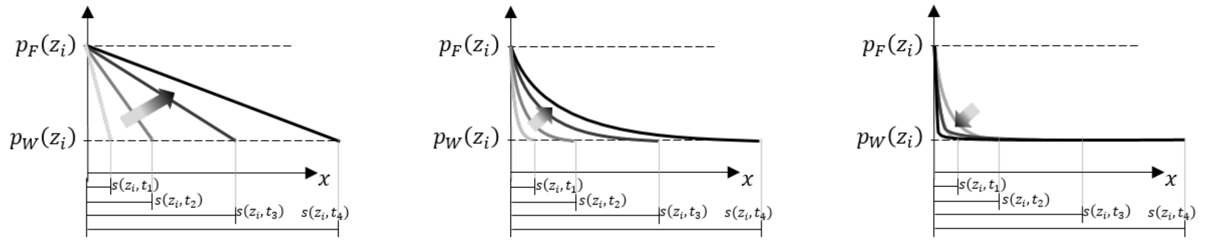

(a) Viscous flow:
linear pressure drop

(b) Viscous flow:
non-linear pressure drop

(c) Membrane formation

Figure 2.6.: Penetration and support pressure mobilization – influence of time

---

[3] determination of design parameters $\gamma''_d = \gamma''_k \cdot 1.00$ and $\tan\varphi'_d = \tan\varphi'_k/1.15$ according to DIN 4126:2013

[4] The bulk flow behaviour of polymer solutions will be addressed in more detail in section 2.2.2.

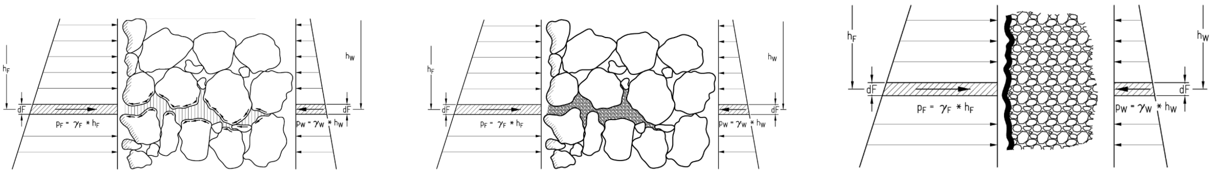

(a) Viscous penetration (b) Colmation (c) External filter cake

Figure 2.7.: Visualization of the penetration behaviour from Haugwitz and Pulsfort (2018)

reduction growing towards the earth wall (internal colmation); an external filter cake build-up could lead to a slight decrease of $f_{s0,wall}(t)$ if $\Delta p_{mob,wall}(t) = const.$ combined with a slight increase in $d_{ref}(t)$. In this case, $f_{s0,wall}$ is linked to, but not directly controlled by the penetration depth but rather governed by the colmating or adsorbing material and its concentration and effectiveness. With respect to internal stability considerations, two decisive (critical) points in time, i.e. with the lowest possible $f_{s0,wall}$ values, can be distinguished:

(1) Penetration dependency (Fig. 2.4a→2.6a or Fig. 2.4b →2.6b): stagnation or maximum penetration time (Fig. 2.7a)
(2) Advancing filter cake formation towards membrane functionality (Fig. 2.4a –2.4b → 2.6c): first cake-initiating step (Fig. 2.7b)

The third failure mechanism (Eq. 2.3) describes the shear failure of a more or less monolithic soil body (Fig. 2.8), where the destabilizing lateral earth pressure force E_{ah} opposes the stabilizing pressure force S_k. For the formulation of the destabilizing earth pressure (E_{ah}), a variety of analytical approaches for spatial lateral earth pressure for fluid supported excavation can be found in literature. For diaphragm walls, detailed discussions on differences between earth pressure approaches in terms of suitability for the respective geometry are given by e.g. Walz and Hock (1987), Stocker and Walz (2003), Klein and Moormann (2015), Haugwitz and Pulsfort (2018), and Lei et al. (2019). Stocker and Walz (2003), EAB:2013 and EA-P:2013 summarize earth

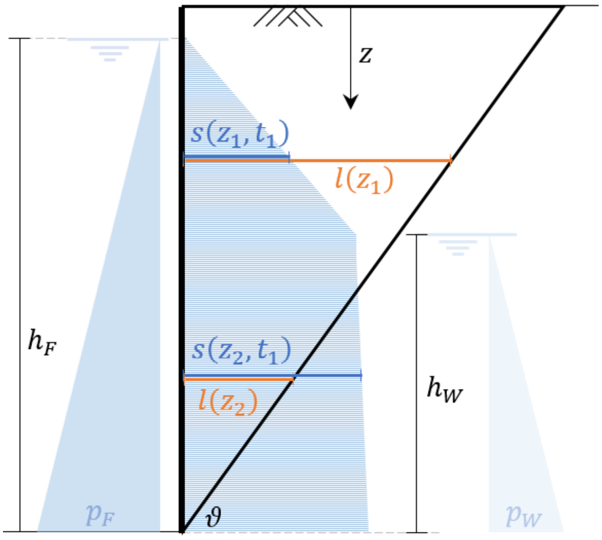

Figure 2.8.: Geometry and variables – macro stability

pressure approaches for bored piles or shafts (e.g. VSM). Kirsch (2010), Broere (2015), and Sterling (2020) review earth pressure models for tunnels.

The approaches can be mostly divided into kinematic and static methods. The kinematic models are based on force balance at the level of a monolithic failure body following Coulomb (1773). They consider spatiality either through geometric limitations or in terms of additional friction and/or cohesion forces at the edges with pseudo-spatial models. These forces are mainly based on von Terzaghi's (1943) trapdoor (or otherwise named arching or silo) theory following the silo theory by Janssen (1895). Static methods start from stress balance at soil element level following Rankine (1857), von Terzaghi (1936a), and von Terzaghi (1936b) (named 'element slice theory' by Walz and Hock, 1987).

Fig. 2.9-2.10 show typical analytical earth pressure models for all considered fields as a basis for visualisation of the influence of the earth pressure model on the determination of the necessary support force. Fig. 2.9a shows the pseudo-spatial kinematic wedge approach as proposed by DIN 4126:2013 for diaphragm wall elements, which involves a triangular prism as a monolithic soil body with shear forces T integrated over the triangular edges to account for the influence of friction and cohesion based on Terzaghi's trapdoor theory. The combination of a truncated cone (Walz, 1978) and a cylinder shown in Fig. 2.9b represents a static earth pressure model for axisymmetric problems such as bored piles or VSM developed by Walz and Hock (1987) (element slice theory). Fig. 2.9c shows the model employed by Anagnostou and Kovarí (1994) for tunnel faces adapted from Horn (1961), which essentially adds an overburden pressure p (trapdoor theory) to the monolithic wedge with a rectangular face area A equal to the square of the outside tunnel diameter D with $D = H_{wedge}$.

In pipe jacking with lubrication, macro stability needs to be considered for the annular gap in addition to face stability, i.e. $p_{F,stb} + p_{air,stb} \geq \sigma_r$. Fig. 2.10 shows an exemplary approach for earth pressure according to DWA-A 161:2014 (trapdoor theory).

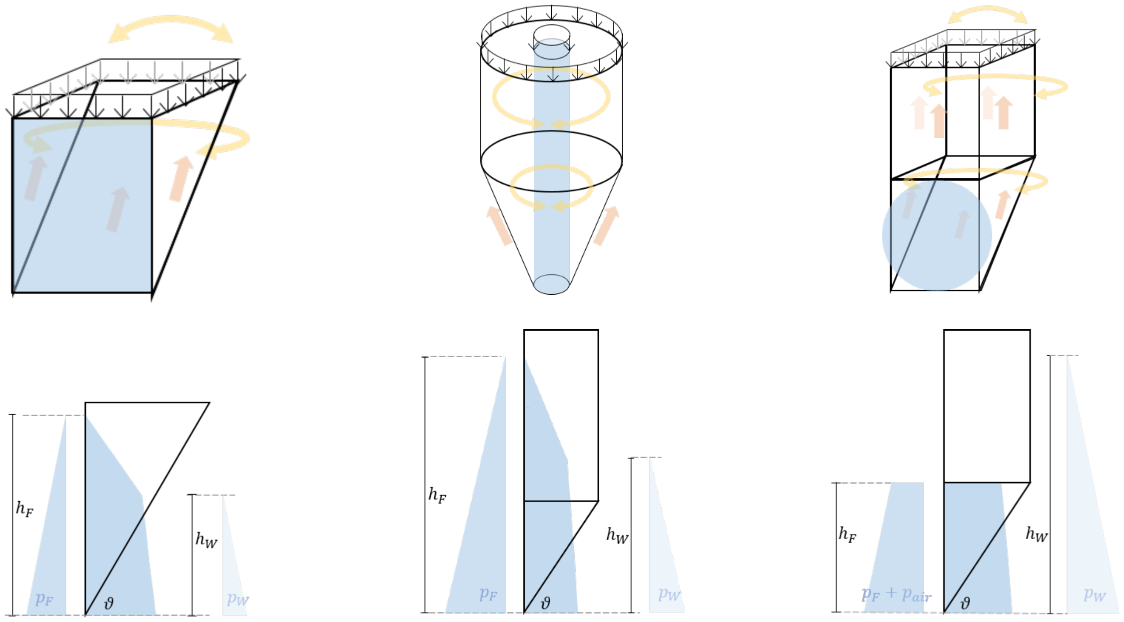

(a) D-wall
(DIN 4126:2013)

(b) Bored pile
(Walz and Hock, 1987)

(c) Tunnel face
(Horn, 1961)

Figure 2.9.: Analytical approaches for spatial earth pressure and penetration

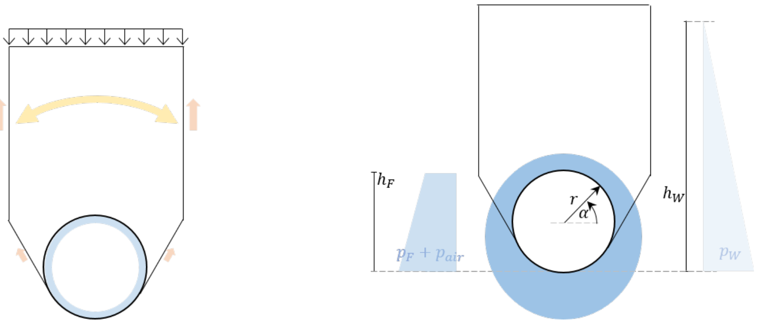

Figure 2.10.: Plane earth pressure model for pipes (DWA-A 161:2014) and penetration

The stabilizing force S_k represents the flow force transmitted to the granular structure of the soil body to be supported. In the case of a filter cake formation, e.g. via internal colmation or external filter cake formation, a certain amount of the overpressure can be transferred directly to the soil skeleton by normal stresses acting on the cake, which can then be considered as a pressure transferring membrane.

If the support fluid penetrates into the ground to a significant depth, a stabilizing force can be integrated from the shear resistance of the fluid mobilised along the penetration depth within the failure body as illustrated in Fig. 2.11. As long as the respective length of the failure body equals or surpasses the penetration depth, i.e. $l \geq s$ (at level z_1 in Fig. 2.8), full pressure $\Delta p = p_F - p_W$ is mobilizable for support regardless of the pressure drop curvature (Fig. 2.11a-2.11b). However, when $s > l$ (level z_2 in Fig. 2.8), only the pressure transferred within the failure body takes effect for support of the failure body (Fig. 2.11c). Despite showing the same penetration depth, $\Delta p_{mobilizable}$ can then significantly differ due to differences in pressure drop curvature (f_{s0}). DIN 4126:2013 considers only the two extremes of full filter cake formation with

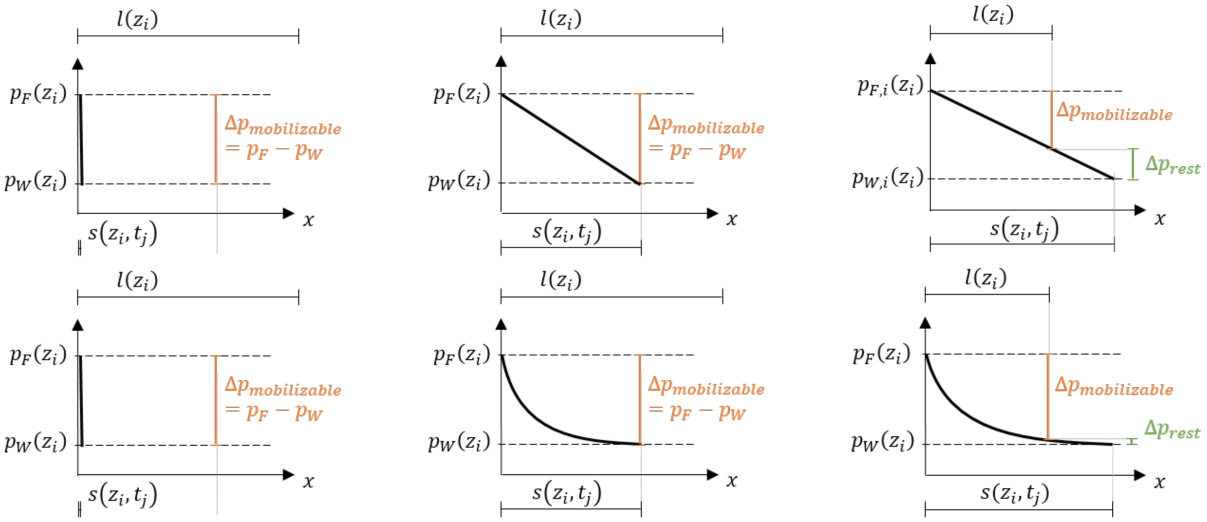

(a) $s \approx 0$

(b) $l \geq s$ (z_1)

(c) $l < s$ (z_2)

Figure 2.11.: Penetration and support pressure mobilization – influence of curvature at time step t_j: linear pressure drop (top) vs. non-linear pressure drop (bottom)

full pressure adsorption immediately at the earth wall (Fig. 2.11a) or full penetration to a limited depth without cake (Fig. 2.11b-2.11c). However, hybrid cases are possible.

In all cases, the critical stability state for macrostability needs to be determined by maximizing the ratio between $E_{ah,d}$ and S_d. Both variables can be calculated independently of each other only in the case of no or negligible penetration and the critical earth pressure will then equal the maximum earth pressure found by variation of the slip surface angle ϑ. However, in the case of fluid penetration, the support fluid slightly changes the buoyant specific weight of the soil body and, additionally, ϑ influences the magnitude of the mobilizable flow force for support of the failure body (Fig. 2.8 & 2.11).

In general, the time-dependency of penetration and pressure mobilisation needs to be considered, e.g. at the tunnel face, where the revolution rate of the cutting wheel dictates the time span for possible filter-cake build-up.

Bentonite suspensions

For 'clean' clay suspensions, empirical investigations have resulted in classification of the slurry-soil interaction into either full membrane formation by external filter cake build-up, full penetration or colmation.

In the case of penetration, the shear stresses mobilised along the penetrated pore channel necessary to balance the hydraulic pressure difference can be adequately represented by the yield strength τ_F, defined as the value needed to initiate flow[5], with bentonite suspensions following the Bingham rheological model with a comparably low viscosity contribution[6]. In a plane model with primarily one-dimensional flow, the overpressure Δp will therefore drop linearly along the penetration depth $s(t)$ with the pressure gradient decreasing with increasing $s(t)$ (Fig. 2.6a); and the point of stagnation (s_{max}), when force balance is reached, can be considered as the decisive point in time for both internal and external stability verifications for these clay suspensions with $f_{s0,min} = f_{s0,wall} = f_{s0}$ (Stocker and Walz, 2003; Haugwitz and Pulsfort, 2018).

Experimental measurements of fluid penetration into non-cohesive soil based on variations of τ_F as the adequate rheological representative and the effective grain diameter d_{10} (diameter at 10 % sieve passage) as a significant measure for the pore size found a proportional factor of $a = 2 - 3.5$ (variation depending on the type of bentonite; Ruppert, 1980) between the pressure gradient $\Delta p/s_{max}$ (Eq. 2.8) and the ratio of τ_F/d_{10} at stagnation. DIN 4126:1986 and DIN 4126:2013 have implemented these results with a safe-side choice of $a = 2$ for a calculative determination of f_{s0} for internal failure and subsequently for the determination of the maximum penetration depth s_{max} (Eq. 2.10). As a result, all three failure mechanisms can be formulated independently of time. For internal stability checks according to DIN 4126:2013, a correction factor $\eta_F = 0.6$ is applied on $f_{s0,min}$ to cover thixotropic variations as well as fluctuations of τ_F due to simplified measurements on site (Stocker and Walz, 2003; Haugwitz and Pulsfort, 2018).

$$f_{s0,min} = \frac{\Delta p}{s_{max}} = \eta_F \cdot \frac{a \cdot \tau_F}{d_{10}} \tag{2.10}$$

In relatively fine soils, an external filter cake will form through filtration of hydrated clay particles at the soil surface creating a nearly impermeable membrane with full pressure adsorption

---

[5] τ_F is best approximated by a ball harp test or a pendulum test according to DIN 4127:2014 (after 1 min rest). It is most closely related to the gel strength G_{10m} according to API RP 13D:2017 measured with a viscometer/rheometer after 10 min rest. In contrast, the API RP 13D:2017 yield point equals the Bingham intersect extrapolated from dynamic shear measurements (appendix C.5).

[6] Rheometer measurements for a range of bentonite concentrations are shown in Fig. C.10 (appendix)

and low permeability for water filtrating from the suspension. This case is assumed according to DIN 4126:2013, when $f_{s0,min} \geq 200$ kN/m^3 is reached along the earth wall over the whole excavation depth. Following Eq. 2.10 with $\tau_F = 20$ kPa and $\eta_F = 1$, this value is reached for soils described by $d_{10} \leq 0.2$ mm.

Currently no established standard considers the contribution of pore blockers such as mineral grains or other material on a possible internal filter cake formation for coarser soils, even though especially mineral grains are often found in samples of filter cakes from construction sites (Arwanitaki, 2009) and laboratory studies on penetration depths have shown a significant colmation effect leading to a hybrid penetration behaviour (Thienert, 2011). Haugwitz and Pulsfort (2018) suggest not to consider favourable colmation effects from filtration of finer material from previous excavated soil strata resulting in hybrid pressure transfer for stability calculations due to sensitive and not easily predictable influencing parameters.

Polymer solutions

Pure polymer solutions for the targeted fields of application differ distinctly chemically and, in some aspects, mechanically from bentonite suspensions. In particular, they generally do not show a considerable yield strength and the contained polymer chains are significantly smaller than clay particles (Jasmund and Lagaly, 1993; Brazel and Rosen, 2012; Lam and Jefferis, 2018). The design approaches established for clay suspensions, based on a significant shear strength τ_F at rest or a relation between swollen bentonite particle size and the effective grain diameter of the soil, cannot, therefore, directly capture the soil-fluid interaction with polymer-fluid support, especially concerning realistic penetration depths and related pressure gradients.

Under the assumptions of an equally linear pressure drop along the penetration depth and no filter cake formation in any case due to the small size of the polymer chains, Steinhoff (1993) formulated a first concept to implement a time-dependent penetration depth into the above failure calculations (Eq. 2.1-2.3, but with reference to DIN 4126:1986) for diaphragm walls and bored piles. His method represents polymer solutions as ideal power-law fluids based on the material law of Ostwald and de Waele (Ostwald, 1929), i.e. fluids described by a shear-rate dependent viscosity increasing with decreasing shear rate, but adds a viscosity plateau (‘Newton plateau’) for shear rates $\dot{\gamma} < 1.5$ 1/s as an upper viscosity boundary. A simple bundle model of parallel capillaries is chosen which represents the soil by porosity n and permeability coefficient k_W. Fluid flow and capillary bundle models will be discussed in more detail in sections 2.2.2 & 2.3.2.

Without any yield strength at rest, polymer solutions, according to this model, cannot stagnate; the penetration velocity can only significantly decrease with increasing penetration depth and a subsequent decrease in the pressure gradient $\Delta p/s$ inducing the flow, though velocity drops faster than with a Newtonian fluid as the viscosity increases with decreasing flow velocity. Consequently, stability based on Eq. 2.2-2.3 can only be guaranteed for a limited time interval T_{crit}. Concerning external stability verifications in particular, this method needs extensive effort, as it requires an iterative calculation of both the critical penetration depth and the critical angle of the slip surface for every relevant excavation level and time step. Experience from construction sites suggests that pressure gradient and penetration behaviour are not approximated with sufficient accuracy with this approach for ‘clean’ polymer solutions, in particular, as regularly applied fluid additives such as filtrate reducers or other pore blockers (Goodhue and Holmes, 1997, FHWA-NHI-10-016:2010, ICE-SPEARWall:2016, Lam and Jefferis, 2018), are not considered. Moreover, the great variability of the polymer category concerning viscosity modification, adsorption properties, swelling ability etc. (section 2.2) suggests that the polymer-water-soil interaction mechanisms at the earth wall are governed by more parameters than are taken into account in this model.

Similarly to the experimental programme for bentonite suspensions, which resulted in empirical correlations between fluid (τ_F) and soil (d_{10}) for the determination of s and f_{s0}, soil penetration tests with different polymer solutions should enable a detailed analysis on further significant parameters affecting stability. These could help improve the concept by Steinhoff (1993) to be applicable as a solid basis for quality control or parameter sensitivity analysis. Of special interest in this context are the following questions:

(1) Does the pressure difference Δp indeed drop linearly along the penetration depth?
(2) Can bulk rheological parameters for polymer solutions measured with standard rheological testing equipment adequately reflect their flow behaviour in soil?
(3) Which parameters control the pressure gradient at the earth wall?
(4) In which circumstances does this gradient depend upon the penetration depth and/or in which cases is this dependence relevant, e.g. concerning colmation effects?
(5) Can a residual filter velocity be defined as a reference value to declare stagnation or a certain amount of pressure drop at the earth wall?
(6) Can the effective grain diameter d_{10} also be used as a reference value of the soil pore sizes for polymer solutions?

2.1.3. Swelling-related stability

Stability issues concerning swelling ground, even though also critical e.g. in diaphragm walling or piling, have been mostly reported from tunnelling. They can be associated with a considerable uptake of water in soil or rock combined with a reduction of mobilizable shear strength and stiffness, a loss of integrity, a change in consistency and extensive convergence, or, when the uptake is impeded, swelling pressure build-up, and can be related to clogging and accretion problems. A significant reduction in the mechanical properties of the ground can thereby impact temporary stability under fluid support, but also the bearing capacity of the finished structure. In pipe jacking, swelling of the supported ground can cause economical or serviceability problems (stuck pipe, high jacking forces) or even problems of structural safety (cracking of the pipe). In shield tunnelling, costly constructional measures are often undertaken to prevent extensive swelling pressures or floor heave on the final lining (DAUB-SSWG, 2005; Borghi, 2006; Wittke, 2006; Anagnostou, 2007; Burbaum, Böhme, and Sass, 2011; Mielenz and Mielenz, 2016; Lam and Jefferis, 2018).

Two fundamental and commonly acknowledged prerequisites for swelling are the availability of water, e.g. provided by the support fluid (filtrate water), and a predisposition or affinity of the ground for volumetric water uptake. Water molecules can thereby either be physically integrated between crystalline structures (e.g. clay minerals) or chemically incorporated during recrystallization (e.g. sulphatic rocks with gypsum or ettringite precipitation) (Jasmund and Lagaly, 1993; Pimentel, 2003; Sievert, Wolter, and Singh, 2005).

This section will focus on clay swelling. The underlying mechanisms of clay swelling and related inhibiting mechanisms are more broadly studied and are more likely to be positively or negatively affected by a support fluid. Polymeric interaction with calcium sulphate precipitation is scarcely discussed, e.g. by Lioliou et al. (2006). Moreover, even in sulphatic rocks with comparably high swelling pressures or large deformations, it is considered as likely that clay contained in the rock is a major initiating factor with clay swelling occurring more quickly, thereby facilitating water distribution in the otherwise highly impermeable anhydrous rock (Butscher, Mutschler, and Blum, 2015).

Swelling problems in clay-bearing soil or rock comprise various mechanisms at different scales. A clay matrix at soil or rock level, at which level total and effective stresses are evaluated, consists of (compacted) assemblies of aggregated particles with inter-aggregate pores, the particles consist of stacks of layers with inter-particle and interlayer pores (fabric) creating a specific structure influenced by mineralogy with the possibility of capillary effects at unsaturated level. Each layer represents an anionic crystalline structure of two or three aluminosilicate sheets compensated for by cations permanently embedded within the sheets (central ions) and interlayer cations with differing exchange capacity depending on how strongly they are bound at or between layers. The permanent negative charge of the basal surface, for which outside cation compensation is needed, originates from isomorphic substitution (similar size, lower valence) of central cations. The electric charge of the layer edges depends upon pH. Attractive and repulsive forces act between surfaces at all levels, e.g. described by the DLVO theory (Derjaguin, B. V. and Landau, L. D., 1941; Verwey and Overbeek, 1948). Moreover, each type of cation possesses a specific affinity to hydrate (in other words dissolve) through ion-dipole bonds with water molecules and possibly form hydration shells (Jasmund and Lagaly, 1993; Yong, 1999; Baille, 2014). This multi-scale interaction complicates the differentiation towards main driving mechanisms and is still under discussion.

From a geotechnical or ‘mechanistic’ point of view, Lam and Jefferis (2018), Bol et al. (1994) and Farrokhrouz and Asef (2013) associate swelling with softening, i.e. a decrease in stiffness, generated by negative pore pressure from stress relief and low-permeability ground balancing with hydrostatic overpressure generating pressure penetration. Swelling or swelling pressure in soil or rock resulting from unloading as differentiation to effects from a physicochemical affinity is considered by Mesri, Pakbaz, and Cepeda-Diaz (1994) and Kolymbas (2008) as ‘mechanical swelling’ and to be subordinate.

At mineralogy level, swelling can be differentiated into crystalline swelling and osmotic swelling (Jasmund and Lagaly, 1993; Baille, 2014). The former essentially describes the hydration of cations which balance the permanently negative charge of the clay surface. Potential hydration pressures for crystalline swelling of Na-montmorillonite can reach several hundred Megapascals (Jasmund and Lagaly, 1993). An osmotic swelling potential, which is considered the main reason for swelling from mineralogical point of view, is driven by a concentration gradient. The mechanism is often explained with reference to the diffuse double layer (DDL) theory. Following DDL theory, the cations at the clay surface are chemically bound or viscously impeded by the diffuse electric field created between anionic surface layer and the cation compensation layer forming a semipermeable membrane. The concentration difference can therefore only be balanced if water molecules diffuse towards these cations. However, diffusion only occurs if the repulsive forces generated by the concentration difference exceed the attractive forces of two clay layers around these cations. This is only thought to hold true for smectic clay minerals with monovalent highly hydratable cations for pressure balance, usually Na^+, and a low net negative charge at interlayer level (Jasmund and Lagaly, 1993; Theng, 2012; Baille, 2014).

A discussion on different approaches for the implementation of electrochemical forces as well as suction stresses during semi-saturation for different types of clay minerals within the effective stress concept by von Terzaghi (1936c) is given by Baille (2014).

It is assumed from minimum water content levels in natural ground that crystalline swelling in the interlayer is usually fully terminated (Jasmund and Lagaly, 1993). However, hydration at the larger pore surfaces of particles or aggregates may still be possible. Osmotic swelling of smectic clays is thought to be a major reason for swelling problems in the oil and gas industry (Hawkes et al., 2000; Anderson et al., 2010; Farrokhrouz and Asef, 2013; Gholami et al., 2018).

Wilson and Wilson (2014) suggest that a swelling potential not only for smectites, but also for kaolinites and illites, can be explained by evaluating the effect of overlapping diffuse double layers (DDL) of the outer surfaces of two opposing particles in micro- and mesopores (≤ 50 nm) according to DLVO theory instead of osmotic swelling. They further argue that the resulting compression of the DDL causes electrostatic repulsion forces which generate hydration pressures, with the effect increasing with increasing overburden stress and also differentiating in magnitude for each mineral type.

Thermodynamically formulated, imbalances are differences in the total energy level. They can be expressed by potentials or gradients, e.g. a hydraulic gradient (overpressure) or a chemical gradient (diffusion, osmosis, hydration). However, balance may be reinstated by compensation of a different element of the equation (Yong, 1999; Farrokhrouz and Asef, 2013; Baille, 2014). Equally, the effect of a hydro-mechanically imposed gradient or a gradient, evoked e.g. by an affinity towards hydration, by a concentration imbalance or other attractive and repulsive forces within the soil structure, may be reduced regardless of the cause.

With regard to influencing parameters during fluid support, the following factors have been found to be modifiable by the support fluid (Jasmund and Lagaly, 1993; Hawkes et al., 2000; Anderson et al., 2010; Theng, 2012; Farrokhrouz and Asef, 2013; Caenn, Darley, and Gray, 2017; Lam and Jefferis, 2018; Gholami et al., 2018; Quainoo et al., 2020):

(1) decrease the chemical potential for water adsorption within the soil (reduce net repulsion) by
    (a) increase of the tensile strength between particles by bridging adsorption (encapsulation)
    (b) reduction of the thickness of the DDL by increasing the concentration of dissolved ions in the pore fluid (salts, density, polymer concentration)
    (c) exchange of highly hydratable cations by thermodynamically favoured cations or larger cationic molecules (polymers) with less hydration potential (may have adverse effect on mechanical strength)
    (d) hydrophobic shielding of the clay surface by large molecules
(2) mechanically minimise penetration and filtration
(3) equalize the chemical potential for water uptake of soil and fluid by choosing a fluid with similar water activity (or lower to create a reverse potential)

Water activity a_W, i.e. the availability of water for reaction with reference to 'free' water, is related to the water potential, which is proportional to the relative humidity RH. It can therefore be measured e.g. by adjusting RH until dew point by means of a chilled mirror hygrometer (Yong, 1999; Baille, 2014). It can also be calculated based on a modified Flory-Huggins equation if the average molar mass of the polymer, the concentration of the solution and an interaction coefficient are known (Lieske et al., 2020).

Water activity and the ability for encapsulation for polymer solutions depend upon the chemistry and structure of the polymer, cf. section 2.2.4, and can therefore be chosen appropriately (Farrokhrouz and Asef, 2013; Lam and Jefferis, 2018). Clay suspensions cannot form particle bridges, their water activity value will exceed that of the native ground, their filtrate is 'free' water, consequently, they aggravate the swelling potential.

The effectiveness of polymeric swelling inhibitors or stabilizers in terms of volumetric swelling reduction is usually tested by means of linear uni-axial swelling tests (swellmeters), e.g. with pre-compressed clay samples without surcharge. Additionally, the effect of polymers mixed with clay on the chemical potential of the clay can be assessed e.g. by means of interlayer space measurements or by evaluating the residual swelling potential of the mix by means of index swelling tests such as the hot rolling test or an evaluation of the free swell ratio (FSR) (Prakash and Sridharan, 2004; Anagnostou, 2007; Xie et al., 2017; Gholami et al., 2018; Theng, 2012; Sridharan and Prakash, 2016). Buja (2009) and Mielenz and Mielenz (2016) describe water release testing with suction induced by filter paper as the method to assess the ability of a polymer fluid for clay swelling reduction. This method is likely to correlate with the water activity of the polymer solution, i.e. with its water retention capacity.

The influence of support fluids on swelling ground and physico-related stability in general is described here for the sake of completeness. An evaluation of the influence of polymer characteristics on the swelling inhibition mechanisms described above will be given in section 2.2.1 as a brief overview. The laboratory investigations will focus on the influence of (possibly significant) support fluid penetration on the mechanical failure mechanisms as described in the previous section 2.1.2 primarily for non-cohesive soils, thereby assuming physico-chemical stability.

2.2. Polymer solutions

2.2.1. Polymer products and classification

The polymer[7] category comprises all macromolecules consisting of a large number of repeating base elements connected by covalent bonds (shared electrons).

The repeating units consist of basic structural elements provided by single chemical compounds, so-called monomers, with a characteristic skeletal base (backbone) and functional side (or pendant) groups of different sizes, charges and polarity. Fig. 2.12 shows exemplary monomers and Fig. 2.13 shows their related repeat units. The units are connected to form linear or branched chains (e.g. with single side chains or star-shaped) or networked (cross-linked) structures (Fig. 2.14). A summary of common structural and functional elements is given in Tab. 2.1.

The skeletons of the structures most commonly recognized as polymers in geotechnical engineering are carbon-based, i.e. with a C-H-backbone, and consequently categorized as 'organic'. Exemplary organic polymers of synthetic origin, mostly made from petroleum oil, are polyacrylamide, polyethylene (PE) or poly(vinyl cloride) (PVC), prominent natural organic polymers, mostly from plants or animals, are cellulose, xanthan gum and starch. However, minerals are essentially composed of natural inorganic polymeric networks, some forming three-dimensional structures (quartz), some sheets (clay minerals). Portland cement is a synthetic inorganic polymer.

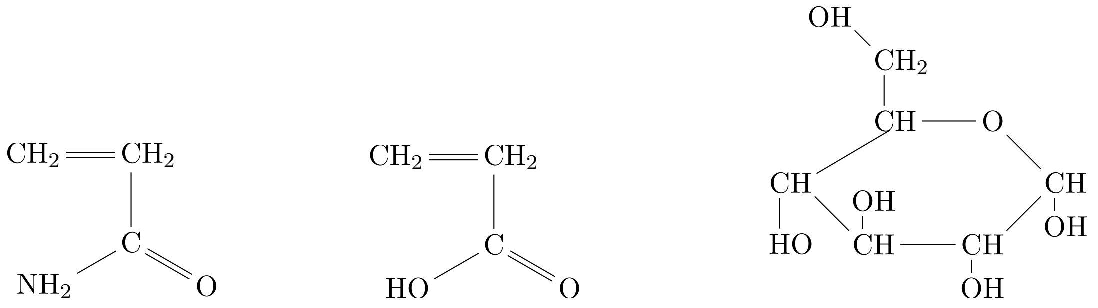
(a) Acrylamide (b) Acrylic acid (c) Glucose

Figure 2.12.: Monomer examples

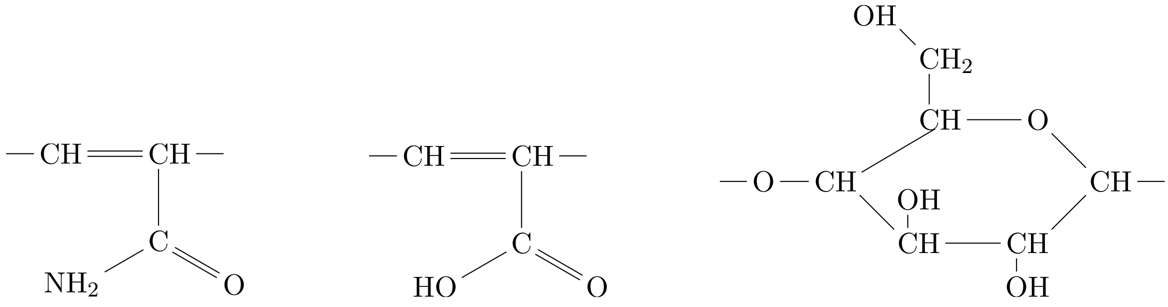
(a) Acrylamide unit (b) Acrylate unit (c) Anhydroglucose unit

Figure 2.13.: Repeat unit examples

---

[7] Greek 'poly meros' translates as 'many parts'; oligomers containing only 2-10 base elements can be considered a subgroup of polymers (Carraher Jr., 2018).

(a) Linear (b) Branched (c) Crosslinked/networked

Figure 2.14.: Polymer molecular structure

The functional groups as well as the number, size and arrangement of the repeating units, are the key factors which dictate the polymer behaviour in different chemical or mechanical boundary conditions, that is, solubility in different solvents, swelling capacity, elasticity (conformation change), biodegradability, stability against deformation or degradation, etc. Each functional group can be associated with a characteristic reactivity (e.g. hydrophobicity, polarity, ionic function), while the size and number of the repeating units reflect the magnitude and complexity of the accumulated electrochemical forces and other interacting mechanisms (Brazel and Rosen, 2012; Lechner, Gehrke, and Nordmeier, 2014; Carraher Jr., 2018; Lam and Jefferis, 2018).

Given the vast variety of these macromolecules, a comprehensive review of all polymers suitable for use with support fluids would be beyond the scope of this work. The following paragraphs and chapters will use the term ‘polymer’ primarily in the sense of the polymeric base product and thus as a separate category to e.g. mineral grains, of which some can be used in colloidal suspensions, e.g. bentonite. With focus on support fluids, these polymers will be grouped according to their supportive use as viscosifiers, pore blockers and clay swelling inhibitors. They will be described by their most prominent representatives used in geotechnical engineering practice, which are all organic polymers of natural or synthetic origin. Viscosifiers and pore blockers are usually provided in powder/granulate form, in some cases in the form of inverse (oil) emulsions[8]. In the experimental studies presented hereinafter, only polymer powder/granulate is used (appendix Fig. B.1). Clay swelling inhibitors are usually available as liquids of higher concentration.

Organic polymers are advised to be named based on their structural elements or monomers according to IUPAC[9] preceded by the term ‘poly’. This nomenclature is mainly applied for

Table 2.1.: Polymer structural and functional elements

C-H compunds	-methyl	1 C (e.g. -CH_3)
	-ethyl/-vinyl	2 C (e.g. -CH_2-CH_3)
	-propyl/-acryl	3 C (e.g. -C-CH_2 =CH_2)
Functional elements	Hydroxy	-OH
	Carbonyl	-C=O
	Carboxy (carbonyl & hydroxy)	-COOH
	Carboxymethyl	-CH_2-COOH
	(primary) Amine	-NH_2
	Amide (amine + carboxy)	-$CONH_2$
	Pyruvic (carbonyl & carboxy)	-COCOOH

---

[8] In differentiation to oil-in-water emulsions (o/w), water dispersed in oil (w/o) is named ’inversed’. Jouenne, Klimenko, and Levitt (2016) discuss differences in application between polymer powders and emulsions.

[9] The International Union of Pure and Applied Chemistry regularly publishes recommendations for chemical

synthetic polymers. Some synthetic polymers are preferentially described by their composition, e.g. ‘copolymer’ as formed by more than one repeat unit, their forming process, e.g. ‘partially hydrolysed’ as a reaction product from hydrolysis or their use and appearance, e.g. ’elastomer’ or ’fiber’. Names for polymers of natural origin, such as polysaccharides and proteins, often contain the name of the source monomers and important functional groups (Lechner, Gehrke, and Nordmeier, 2014; Carraher Jr., 2018).

Viscosifiers

Viscosity η is defined as the resistance of a fluid mobilised during flow. Clearly, suitable polymers with viscosifying properties towards pure water need to be water-soluble and influence the fluid viscosity towards $\eta_{fluid} > \eta_{water}$, as visualized examplarily in Fig. 2.15.

The solubility of molecules (solute) in water depends on the extent to which they are able to form polar bonds (hydrogen bonds) and disperse in the solvent (solvent quality). Essentially hydrophobic (non-polar) molecules do not dissolve in water. Thermodynamically, entropy (affinity towards disorder / maximum dispersion) is the governing mechanism for solubility. Therefore, solubility decreases with increasing molecule size and concentration. This can be explained with the Flory-Huggins lattice model, according to which the polymer components are fixed to certain positions relative to each other in contrast to the free water molecules with a multitude of configurational possibilities. This is associated with high entropy. In addition, polymer dissolution at higher molecular weights is slower, because water diffusion within the polymer matrix takes more time (Carraher Jr., 2018). Following the lattice model, crosslinking impedes solubility (Brazel and Rosen, 2012). It can be concluded that only linear or slightly branched macromolecules with polar groups are water-soluble.

In contrast to clay suspensions, aqueous polymer fluids are generally considered as ‘solutions’ in polymer chemistry and macromolecular physics. ‘Suspensions’ are defined as mixtures of essentially insoluble components created by introduction of mixing energy (Brazel and Rosen, 2012). In this context, the crystalline structure of clay mineral layers is essentially hydrophobic, hydrogen bonds can only strongly form at the edges and through hydrophilic cations (hydrophobic bonds are weaker), clay can therefore be considered essentially water-insoluble, but can form the solid part of a suspension.

Figure 2.15.: Viscosifying effect: short-chain (left) vs. long-chain (right) AN polymer

---

nomenclature and terminology in its own IUPAC journal.

Dissolved polymer chains mobilize resistance against flow through size, chain entanglement and rigidity. For chain entanglement to occur, a certain minimum polymer concentration level c_e needs to be surpassed. Chain entanglement increases with increasing chain length ($\propto$ average molecular weight) and concentration. Rigidity and size are described by cross-links and/or high inter-molecular forces. Polymers with electrolyte groups (polyelectrolytes) of the same charge are forced to take more stretched conformations compared to non-ionic polymers of the same length due to repulsion between these groups (electroviscous effect), which is linked to a larger effective hydrodynamic volume. The charge distribution along the chain length can thereby significantly influence the flexibility of the chain (Larson, 1999; Lam and Jefferis, 2018; Carraher Jr., 2018). The functionality of the ionic groups can depend upon solution pH and hardness (electrolyte concentration) of the solvent (section 2.2.4). Further information on viscosity-related rheology is given in section 2.2.2.

The following Tab. 2.2 and Fig. 2.16 give an overview of the characteristics of the most common polymer types used as viscosifiers and their usual product variety. A comprehensive overview of polymers used as support fluids in geotechnical engineering can be found with Lam and Jefferis (2018).

Water-soluble sodium carboxymethylcellulose (Na-CMC or just CMC) is derived from cellulose (insoluble) e.g. by reaction with sodium hydroxide (reaction product alkali cellulose) and subsequently sodium monochloroacetate, which essentially results in a replacement of some hydroxyl

Table 2.2.: Characteristic property variety of selected polymer types used as viscosifiers

Polymer	Na-Carboxy-methylcellulose	Xanthan	Acrylamide-acrylate copolymer
Abbreviation	Na-CMC	XAN	AN
Origin	Natural, modified	Natural	Synthetic
Charge	Anionic, $DS = 0.7 - 1.2$ [a)]	Anionic	Anionic, Anionicty= $5 - 70$ % [c)]
M_W	$0.9 - 7 \cdot 10^5$ [a)]	$1 - 50 \cdot 10^6$ [b)]	$3 - 30 \cdot 10^6$ [c)]
Repeat units	Anhydroglucose	Pentasaccharide	Acrylamide, acrylate
Electrolyte groups	Carboxy groups	Carboxy groups in pyruvate & glucuronic groups	Carboxy groups
Structure	Moderately rigid & complex	Rigid, complex	Flexible, thin
Stability[d)]	Sensitive to pH & polyvalent dissolved cations, slowly biodegradable	Sensitive to bacterial degradation, readily biodegradable, sensitive to mechanical degradation	Sensitive to pH & polyvalent dissolved cations, non-biodegradable, sensitive to mechanical degradation at high M_W

[a)] from SigmaAldrich.com, Lam and Jefferis (2018)

[b)] from Sorbie (1991)

[c)] from SNF.com & Xiong et al. (2018)

[d)] rheometer results on shear-rate-induced mechanical degradation see section 3.2.2

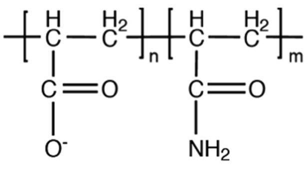

(a) Acrylamide-acrylate copolymer

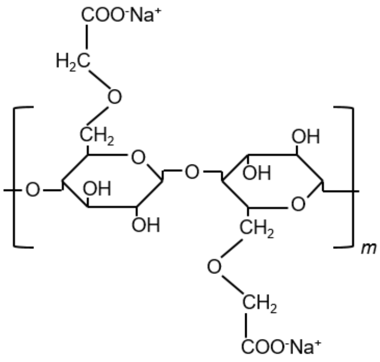

(b) Na-Carboxymethylcellulose

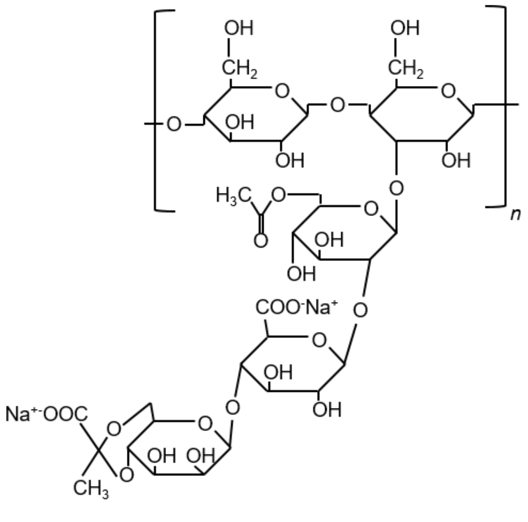

(c) Xanthan gum

Figure 2.16.: Characteristic structure of selected polymeric viscosifiers

(-OH) by sodium carboxymethyl groups ($-CH_2-COO^-Na^+$). The average number of substituted hydroxyl groups per repeat unit (anhydroglucose, Fig. 2.13c) is named 'degree of substitution' (DS) and reflects the degree of anionicty of the polymer chain, which influences viscosity, salt stability and biodegradability (sections 2.2.2 & 2.1.3). In this context, 'polyanionic cellulose' (PAC) refers to the marketed form of Na-CMC with the best viscosifying properties, that is, a high viscosity related to a sufficiently high DS, high M_W and small residues of NaCl as compared to 'technical' CMC, the 'raw' product with considerable NaCl from the reaction process (Klemm et al., 2005; Caenn, Darley, and Gray, 2017; Lam and Jefferis, 2018). Cellulose is one of the most abundant renewable resources on earth with comprising more than one-third of all plant matter. As it is a polydisperse polymer, i.e. it contains a distribution of different chain lengths, usually following a Gaussian distribution (Carraher Jr., 2018), it is likely that Na-CMC, too, is polydisperse. The polydispersity index is defined as the ratio of the weight-average molecular weight[10] (M_W) and the number-average molecular weight (M_N) of the polymer product. Metodiev (2013) names a polydispersity index range of 1.6-2.7 for low M_W CMC. The underyling values of individual molecular weights are subject to considerable measurement inaccuracies due to the large number of repeat units and are therefore less precise than for small molecules. Average values are often indirectly obtained, e.g. from viscosity measurements in salt solutions (to eliminate the electroviscous effect) (Ward, 1981; Carraher Jr., 2018; Lam and Jefferis, 2018). However, there is a variety of other methods for the determination if molecular weights (Ward, 1981). In the context of food production, CMC is sometimes mixed with the natural polysaccharide guar gum for improved viscosity (BeMiller, 2019).

Xanthan (or xanthan gum) (XAN) belongs to the natural polysaccharides and is mostly pro-

---

[10] Molecular mass and molecular weight are usually given in Dalton [Da], which is defined as the unified atomic mass unit, or in relation to the unified atomic mass and then unitless (IUPAC definition) [-]. The molar mass [g/mol] in mass per amount of substance is nearly equivalent. Consequently, all of the above units are often used interchangeably.

duced by aerobic fermentation of e.g. glucose or sucrose with micro-organism ‘xanthomonas campestris’, but can also be found naturally on leaves of the cabbage family. It is formed by a cellulosic backbone with a trisaccharide branch (three saccharide rings: mannose – glucuronic acid – mannose) on every second glucose unit, which shields the chain, thereby creating rigidity and insensitivity towards temperature, pH, electrolytes and physical damage. Anionicity and solubility are mainly related to glucuronic and pyruvic functional group (2nd and 3rd saccharide ring) of the side chain, which contain a carboxy group. Variations in structural and physicochemical properties are associated with the use of different strains of micro-organisms for fermentation, which result in variations of the functional elements within the mannose units (Sorbie, 1991; Caenn, Darley, and Gray, 2017; Lam and Jefferis, 2018; Dai and Zhao, 2018). According to Sorbie (1991), the polydispersity index for xanthan is estimated at around 1.4-2.8, with average molecular weights (probably M_W, but not specified) more frequent in the lower range around $1 - 3 \cdot 10^6$ [g/mol]. In the context of food production, Xanthan can be equally mixed with guar gum for synergistic viscosity effects (Lam and Jefferis, 2018; BeMiller, 2019).

Compared to these naturally derived products, the synthetic polymer production, that is, the construction of polymers from small molecules (polymerization), offers the advantage of considerable property variations, e.g. of chain length, branching and cross-linking, sequence and types of functional groups and related charge density, and the consequences thereof for rheology and stability. However, synthetic products generally originate from oil and gas production. The monomers acrylamide (Fig. 2.12a) and acrylic acid (Fig. 2.12b) are produced from propylene, which is synthetized in industrial reactors from crude oil (naphta) or gas (propane).

The anionic acrylamide-acrylate copolymer (AN) can then be produced e.g. by direct copolymerization or crosslinking of the two monomers or by partial hydrolysis of polyacrylamide (PAM) with PAM being formed as a non-ionic homopolymer from acrylamide beforehand (Sorbie, 1991; Caenn, Darley, and Gray, 2017; Carraher Jr., 2018; Xiong et al., 2018). Production methods allow the control of polydispersity. Copolymers of extremely high molecular weight ($M_W > 17 \cdot 10^6$ Da) in powder form can only be produced by hydrolysis in order to guarantee sufficient product quality due to monomer mobility limitations during copolymerization (reactor size). [11]. Regardless of the way of production, this acrylamide-acrylate copolymer is often referred to as PHPA (partially hydrolysed polyacrylamide) even if it is not produced by hydrolysis.

Due to the small size of the monomers and no side chain elements, AN has a relatively slim polymer chain with solubility and ionic charge resulting from the polar amide groups (-C(=O)NH_2) and the carboxy groups (polar, usually anionic) of the respective monomers. The percentage of acrylate units relative to the total number of acrylate and acrylamide units, alternatively named degree of hydrolysis (even though technically only true for PHPA), therefore reflects the anionicity of the polymer chain. According to Lam and Jefferis (2018), optimal viscosity and stability are reported for anionicity levels around 30-40 %. Common average molecular weights for viscosifiers range around $(10 - 16) \cdot 10^6$ Da (high) and $(25 - 30) \cdot 10^6$ Da (extremely high) according to Levy and Warrington (2015) and Xiong et al. (2018) and the SNF product range.

It is evident that the three types of polymers presented here are similar concerning their electrolyte group. The carboxy group (-COOH) contains a highly electronegative (polar) carbonyl part (-C=O) and a hydroxyl group (-OH). The latter is polarised by the carbonyl group and consequently easily dissociated in the presence of water (dissociated form -COO^-), similar to carboxylic acids, e.g. acetic acid. However, differences primarily related to their charge position and distribution along the chains and their geometric complexity result in differing rheological

---

[11] Ref.: Laurent Giuranna (SNF), personal communication, July 9, 2020

behaviour in solution as well as mechanical and chemical stability. The repeat units of AN polymers are only loosely interconnected with a significant degree of flexibility remaining compared to the more complex connections formed by CMC-H or especially XAN. Therefore, conclusions e.g. drawn from average molecular weight values towards viscosity should only be drawn on the basis of similarity concerning structural complexity and intermolecular forces.

Pore blockers

Pore blockers are aqueous polymeric grains (Fig. 2.17), which are used as additives to viscous support fluids similarly to a load of mineral grains in the context of geometric blocking of soil pores to reduce penetration. However, they distinctly differ in density, as the density of aqueous grains nearly equals that of water or a clean polymer support fluid, and stiffness. As will be further elaborated in section 2.3.3, the correct range of grain size is essential for the functionality. Therefore, for aqueous grains to be suitable, they need to be available in distinct size fractions and be able to reach their swollen state quickly enough and maintain it to a sufficient degree under mechanical exposure and fluid overpressure.

Aqueous polymeric grains are superabsorbing polymers (SAP), otherwise named hydrogels or highly hydrophilic gels, so essentially swellable, but not water-soluble, physically or chemically crosslinked network polymers with extensive capacity for the absorption of water or aqueous solutions (Peppas, Slaughter, and Kanzelberger, 2012; Brax, Buchmann, and Schaumann, 2017). Similar to clays with considerable osmotic swelling potential, these 3D structures need to be loosely interconnected and contain sufficient hydrophilic (polar) functional groups (e.g. -OH, -COOH) and cations for water attraction, absorption and subsequent accumulation (Jagur-Grodzinski, 2009; Gulrez, Al-Assaf, and Phillips, 2011). Most hydrogels found in application are synthetic products, e.g. polymerized from acrylic acid (acrylate) and/or acrylamide, but hydrogels based on natural polymers, e.g. CMC, xanthan, starch, or hybrid products are also used (Gulrez, Al-Assaf, and Phillips, 2011; Brax, Buchmann, and Schaumann, 2017). They are most commonly applied for concrete construction for fluid absorption and control of water availability (retention and release) and porosity, for biomedical or pharmaceutical applications, for baby diapers and in agriculture and forestry (Jagur-Grodzinski, 2009; Yu et al., 2012; Peppas, Slaughter, and Kanzelberger, 2012; Oyen, 2013; Schroefl and Mechtcherine, 2014).

Hydrogels in the form of aqueous grains for civil engineering applications with a sufficiently high strength, size and adsorption velocity and capacity are so far mainly based on acrylamide and acrylic acid monomers forming acrylamide-sodium-acrylate copolymers (Schroefl and Mechtcherine, 2014). Aqueous grains from e.g. SNF are available in specific size fractions between around 0.5 mm and 25 mm in diameter in their swollen state (dry state 0.1 – 4 mm) and can absorb up to 500 % in deionized water of their initial weight. Besides, viscosifiers such as xanthan can contain certain amounts of microgels from their production process (Chauveteau and Kohler, 1984; Sor-

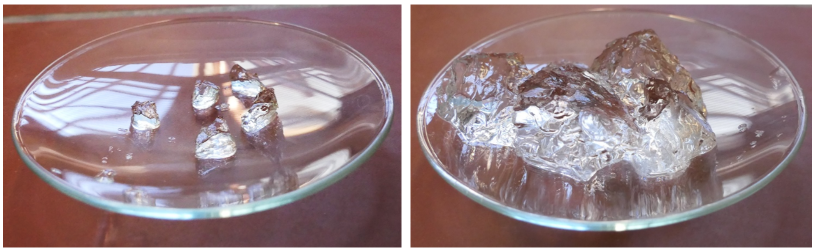

Figure 2.17.: Polymeric grains $d \approx 0.5 - 2$ cm

bie, 1991). Otherwise, certain support fluid products may comprise cross-linking agents sensitive to a specific environment or SAPs may be installed specifically to penetrate into the ground before reaching full volume expansion. Both ways may postpone the swelling process to within the penetrated soil matrix (Feng et al., 2003; Peppas, Slaughter, and Kanzelberger, 2012). However, the functionality of these mechanisms may not be as easily ensured if quantities and sizes cannot safely be predicted.

Swelling inhibitors / clay stabilizers

With reference to section 2.1.3, clay swelling inhibition or stabilization can be realized in different ways. With respect to classification into polymer characteristics, the related acting mechanisms can be grouped as follows:

(1) Water activity control
(2) Penetration and filtrate control
(3) Encapsulation
(4) DDL compression
(5) Cation exchange and hydrophobic shielding

Mechanisms (1)–(3) are essentially achieved with hydrophilic (water-soluble) polyelectrolytes (usually anionic) of high molecular weight and chain length, which are also used in their viscosifying functionality (see above). Their behaviour towards clay is sometimes referred to as clay 'stabilization' (Borghi, 2006; Mielenz and Mielenz, 2016; Praetorius and Schößer, 2017).

Their stability against separation from water, which is linked to a low water activity value (1), is related to its structure, which fixes the positions of the hydrophilic functional groups and thus hinders the diffusion of water molecules. This geometric stabilizing effect on water (osmotic pressure), therefore, does not occur for the separate monomers and has been found to increase with crosslinking. Thus it is referred to as the 'polymer effect' in analogy to the capillary wall effect (Trombetta, Di Bona, and Grazi, 2005; Ferapontov, Tokmachev, and Gagarin, 2009). Penetration (or infiltration) reduction (2) controlled by the rheology of the solution (here: essentially viscosity) additionally limits the amount of water available for adsorption at the earth wall.

Encapsulation (3) is created by bridging adsorption, i.e. by connection of two clay surfaces by one polymer chain, with the electrolyte functional groups stretching the chain. Adsorption can occur e.g. at the clay edge surface and the polar an non-polar bonds between polymer and clay can form (Fig. 2.18). In this context, CMC and AN will be more effective than XAN at the same level of molecular weight, as the polymer chains of XAN are considerably thicker. The bridging adsorption mechanism is widely applied for flocculation, i.e. for solid-fluid separation, mostly in the context of drinkwater and wastewater treatment. Synthetic polymers with this functionality are therefore also referred to as 'flocculants' (Jasmund and Lagaly, 1993; Fawell, 2017; Xiong et al., 2018). However, in the environment of a soil matrix, the encapsulating mechanism will not separate the components, but stabilize or freeze the current amount of absorbed water within the soil (Fig. 2.19a).

Polymers with a charge distribution matching the clay surface 'too well' (e.g. certain cationic polymers vs. an anionic basal surface of a specific clay mineral) could be preferentially adsorbed in the form of so-called 'trains' (flat), that is, with too many functional groups along the polymer chain bound to one clay surface (Fig. 2.18), so that the remaining part of the chain ('tail' or 'loop') cannot bridge to the adjacent surface (Jasmund and Lagaly, 1993; Alagha et al., 2013). This train-like adsorption is considered nearly irreversible due to the so-called 'octopus effect',

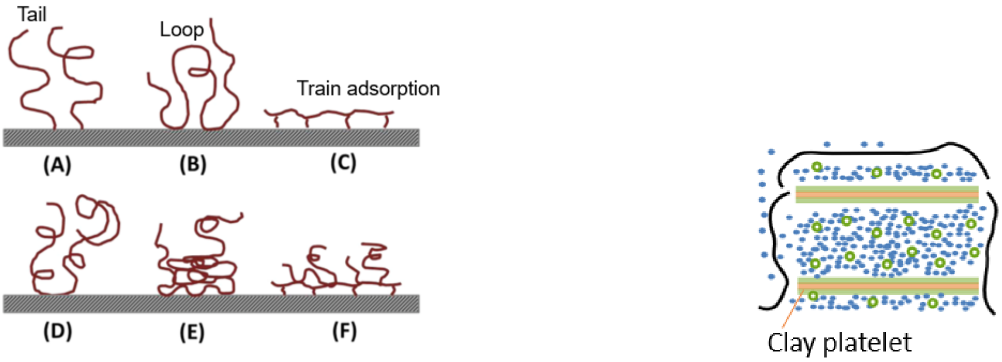

(a) Configurations according to Alagha et al. (2013) (modified)

(b) Bridging adsorption and encapsulation

Figure 2.18.: Polymer surface adsorption

meaning that the probability for all attachments to loosen at the same time is very low (as long as no unusual amount of energy is applied) (Theng, 2012). Aside from purely anionic polymers with viscosifying function, derivatives of polysaccharides, namely cellulose and starch, with amphoteric (both anionic and cationic) functional groups have been established. Their often pH-independent cationic groups increase their potential adsorption points towards conventional anionic viscosifiers by additionally being able to form ionic bonds with the negatively charged clay surface. This increases the octopus effect, strengthens the bond while equally preventing train-like adsorption (Zhang, 1999; Anderson et al., 2010; Theng, 2012; Lei et al., 2020).

DDL compression (4) is provided by an increase in ionic concentration. Cation exchange and hydrophobic shielding (5) can be performed by polymers, which are able to penetrate and reach the surfaces, from which swelling is initiated. These polymers are usually referred to as 'clay swelling inhibitors'. Certain cationic polymers of relatively low molecular weight have been developed for oil and gas drilling operations, often in combination with PHPA of high molecular weight. They are designed to be thermodynamically favoured to penetrate the basal surfaces of Na-montmorillonite clay minerals, replace or shield the hydrophilic counter-ions and shield against further water accumulation and even bind to adjacent clay layers together. Preferential characteristics are relatively long, thin chains without significant branching, cationic groups which are geometrically favoured over the existing counter-ion for charge compensation (usually amines) or hydrophilic groups which encapsulate the counter-ion (chelate), while a hydrophobic backbone decreases the affinity for further water uptake, e.g. polyether diamines. These polymers can even cause the release of water molecules from the interlayer. The efficiency of such inhibitors depends on how well their distribution of functional groups matches the charge distribution of the clay (Anderson et al., 2010; Suter et al., 2011; Theng, 2012; Xie et al., 2017; Gholami et al., 2018). A modification of the clay characteristics in this way from within the interlayer is likely to reduce the soil plasticity (Verst and Pulsfort, 2017) resulting in an increased sensitivity to disintegration. However, in combination with PHPA, the encapsulating function of the large molecular weight component PHPA may provide compensation. Lei et al. (2020) present a study on amphoteric carboxymethyl chitosan, a polysaccharide derivative, which concludes that this polymer can both encapsulate clay and partly penetrate into clay interlayers, i.e. combine both functionalities.

Attempts for an evaluation of these swelling inhibition mechanisms with respect to fluid support boundary conditions have been addressed in Verst and Pulsfort (2017) and Verst and Puls-

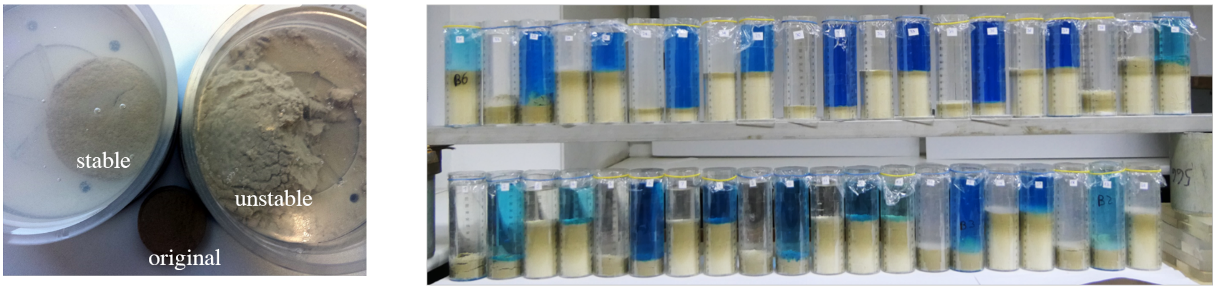

(a) Volumetric (b) Linear

Figure 2.19.: Exemplary free swelling tests

(a) Free swell ratio (FSR) according to Prakash and Sridharan (2004)

(b) Ring apparatus test according to DVGW W 116:2019

Figure 2.20.: Swelling-related testing methods

fort (2018). These studies focussed on volumetric swelling quantification based on free swelling heave testing of pre-compressed clay samples of different thickness in contact with polymeric support fluids (Fig. 2.19b). The influence of the contact behaviour was further evaluated with respect to the effect on residual soil plasticity and free swell ratio (FSR) (Fig. 2.20a). Support fluid water separation (or retention) as e.g. indicated by means of the mud testing ring according to DVGW W 116:2019 as described by Buja (2009) and Mielenz and Mielenz (2016) (Fig. 2.20b) could be correlated for further differentiation into respective polymer functionalities. Pressure-swelling related testing, e.g. according to Huder and Amberg (1970) is a useful tool to assess the general swelling capacity of soil in contact with water. However, in order to study the effect of polymer solutions as saturation fluids, devices would have to be constructed specifically for these viscous fluid to ensure free contact between polymer fluid and soil, but equally fixate the soil. Otherwise, the results may not be representative. Particularly with highly viscous fluids containing long polymer chains, this is relatively difficult to achieve.

2.2.2. Rheology of viscous polymer solutions

Rheology[12] is the science of deformation and flow of matter, as defined by Bingham and officially introduced in 1929 with the foundation of the American Society of Rheology. This definition divides into reversible elasticity, as dominant in solids, and irreversible viscosity, as dominant in liquids. Polymers are classified as visco-elastic materials, i.e. they combine both properties (Barnes, Hutton, and Walters, 1989; Carraher Jr., 2018).

The shear resistance of viscous polymer fluids[13] against deformation is commonly addressed by

---

[12] from Greek "rheo" meaning flow or current and "logus" science

[13] here specifically referring to aqueous solutions of water and dissolved polymeric viscosifiers

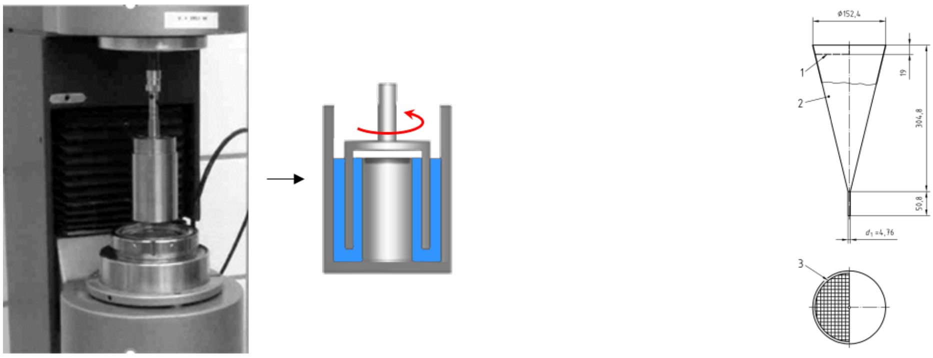

(a) Exemplary rotational rheometer system

(b) Marsh funnel(DIN 4127:2014)

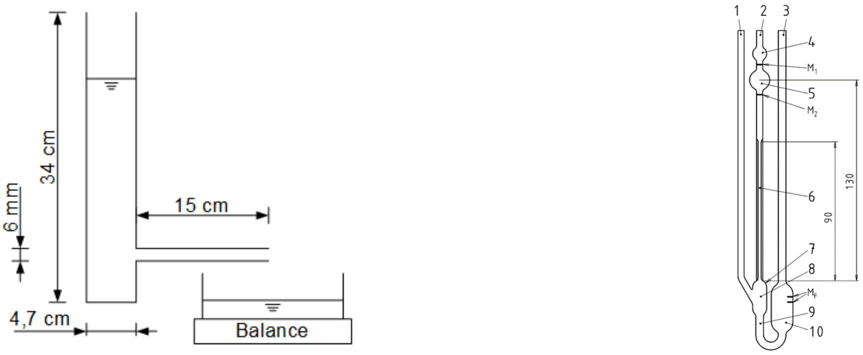

(c) Capillary viscometer (‘casumeter’)

(d) Ubbelohde capillary viscometer (DIN 51562-1:1999)

Figure 2.21.: Exemplary bulk flow behaviour testing devices

means of stress-strain relationships obtained from rotational rheometer or viscometer tests. These comprise measurements of shear stresses τ $[\mathrm{kN/m^2}]$ at specified shear rates $\dot{\gamma}$ $[1/\mathrm{s}]^{14}$, usually at stepwise steady-state conditions (laminar flow). A different approach to rheological behaviour of polymer solutions is given by efflux measurements, i.e. recordings of outflow volume/mass over time performed at specific overpressure levels or with falling head relative to a certain pipe geometry with fixed length and diameter (Marsh funnel, capillary models, etc.) (Fig. 2.21). These flow tests are generally referred to as ‘bulk’ rheological measurements, for which the tested fluid can be idealised as a homogeneous fluid. They are used with respect to the rheological classification of polymers or as a basis for determining a viscosity-related average molecular weight (Sorbie, 1991; Steinhoff, 1993; Lam and Jefferis, 2018).

Theoretically, efflux measurements can be related to stress-strain formulations by introducing a relationship between average flow velocity and shear rate at the pipe wall, then forming equilibrium between normal stresses from the pressure level and shear stresses mobilized at the pipe surface (Sorbie, 1991; Steinhoff, 1993; Bird, Stewart, and Lightfoot, 2007). U-tube viscometers, such as the Ubbelohde viscometer (Fig. 2.21d), base on the definition of viscosity without referring to a specific shear rate. Thereby viscosity values η_{poly} (polymer solution) and η_{sol} (its solvent) are assumed to be proportional to their efflux times t_{poly} and t_{sol}. Related viscosity terms for polymer solutions at polymer concentration in solution $_{poly}$ are defined based on a relative ($\eta_r = \frac{\eta_{poly}}{\eta_{sol}} \approx \frac{t_{poly}}{t_{sol}}$) and a specific viscosity formulation ($\eta_{sp} = \frac{\eta_{poly}-\eta_{sol}}{\eta_{sol}} = \eta_r - 1$). This gives

---

[14] 1/s =‘revolutions per second’ = Hz, otherwise rpm (‘revolutions per minute’)

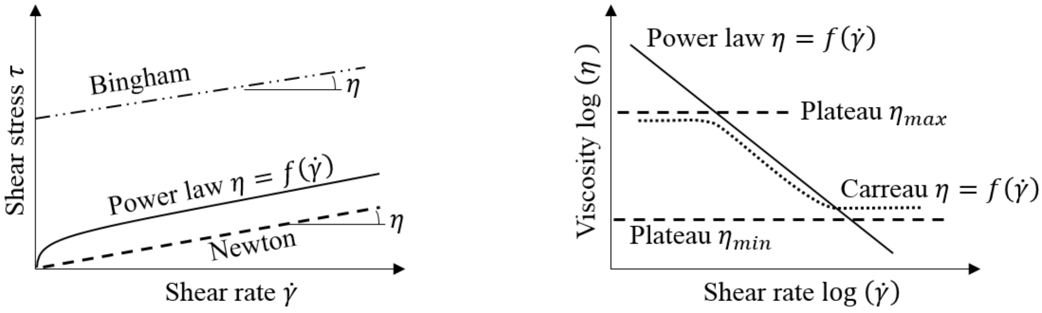

(a) Shear stress

(b) Viscosity

Figure 2.22.: Typical $\tau - \dot{\gamma}$ bulk rheological models for polymer solutions

a reduced ($\eta_{red} = \frac{\eta_{sp}}{c}$), inherent ($\eta_i = \frac{\ln \eta_r}{c}$) or intrinsic viscosity ($[\eta] = \lim\limits_{c_{poly} \to 0} \frac{\eta_{sp}}{c_{poly}}$). Kinematic viscosity ($\eta'$) formulations are obtained by relating the viscosity values to their respective fluid density ρ_{fluid}: $\eta' = \eta/\rho_{fluid}$ (Carraher Jr., 2018; Lam and Jefferis, 2018).

Only in the case of Newtonian flow behaviour with constant viscosity are the viscosity values obtained from U-tube viscometers immediately comparable to shear-rate-controlled measurements from rotational rheometry. However, polymer solutions exhibit shear thinning behaviour. Polymers derive their viscosifying properties in solution from their ability to stretch or entangle when sheared. Depending upon entropic and drag forces governed e.g. by molecule composition, chain length, complexity, ionicity and concentration in solution, their shear resistance against flow increases significantly with decreasing shear rate $\dot{\gamma}$ (and corresponding flow velocity), when the flexible polymer chains get more entangled (Brazel and Rosen, 2012; Lam and Jefferis, 2018; Skauge et al., 2018).

For medium shear rates, the bulk rheology of polymer solutions can be represented adequately by the power-law model ($\eta = \tau/\dot{\gamma} = \kappa \cdot \dot{\gamma}^{(m-1)}$) developed by Ostwald and de Waele (Ostwald, 1929), which describes an exponential increase of the viscosity η with decreasing shear rate $\dot{\gamma}$ (Fig. 2.22b). Some bulk rheological models add an upper (Steinhoff, 1993) or upper and lower viscosity plateau (Carreau, 1968) at very low and very high shear rates respectively to take into account the viscosity-limiting effects of a fully coiled or fully stretched conformation of the polymer chains. 'Upper' and 'lower' with respect to a Newtonian plateau here are labelled based on the viscosity value, i.e. η_{max} 'upper' plateau vs. η_{min} 'lower' plateau. Instead, some formulations use a shear-rate-based labelling, that is, the η_{max} plateau is referred to as the 'lower' plateau due to it being a limitation at lower shear rates $\dot{\gamma}$ as compared to the η_{min} plateau for higher ('upper') shear rates. A time-dependency of the flow behaviour in the sense of a thixotropic hardening effect (increase of shear rate level at rest over time, as defined by DIN 4127:2014, Fig. 2.23) is usually not noticed for AN solutions (Lam and Jefferis, 2015a). XAN may show a small thixotropic effect (Ghannam et al., 2019).

It is not evident that the bulk flow behaviour of polymer solutions as described above can be immediately transferred to the flow through real narrow pores of soil matrices, i.e. 'in-situ' rheology. Numerical and analytical models often rely on this assumption (section 2.3.2). However, e.g. Skauge et al. (2018) observed an increase in viscosity with increasing shear rates, i.e. shear-thickening behaviour, during soil permeation tests with shear rates above $\dot{\gamma} = 10$ 1/s. Lesemann (2010), too, found considerable deviations. It can therefore be assumed that the interaction between polymer, solvent and soil skeleton can become more complex. This will be

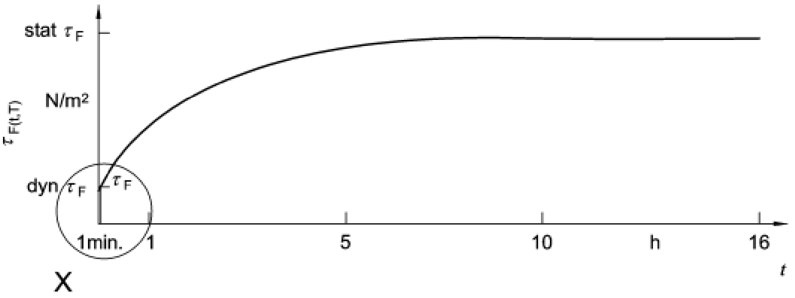

Figure 2.23.: Thixotropic hardening at rest according to DIN 4127:2014

further addressed in sections 2.3.1 and 2.3.2.

2.2.3. Transport behaviour and sedimentation of suspended material

A reliability on available suspended material of specific geometries is essential for related effects to be taken into account for stability assessment.

Material in form of particles, mineral, aqueous or other, can be directly introduced manually; soil grains (mineral particles) are are often taken up by the support fluid from the native soil through movement of the excavation tool (grab, hydromill, cutting wheel, etc.), both provided the support fluid facilitates dispersion over agglomeration and soil-colloid formation. If particles can indeed easily be dispersed, then material can be considered available if the support fluid can reliably carry the desired geometries for a sufficient amount of time.

Especially the thin and flexible chains of high-molecular-weight synthetic acrylamide-acrylate copolymers (flocculants) are more likely to bridge mineral particles and encapsulate soil colloids, which makes dispersion more difficult and increases the sedimentation velocity. This effect is considered positive for hole cleaning, internal stability or soil stabilization against swelling (sections 2.1.1 & 2.1.3), but has the adverse effect for the possible use of suspended grains for fluid support. Therefore, mineral particles can more easily be dispersed in solutions of CMC, XAN and low-molecular-weight AN. Bentonite can be considered a special form of mineral particle as it is not easily dispersed as a dry product. However, in contrast to e.g. quartz grains, hydrated bentonite forms a stable suspension, which can be easily mixed with polymer solutions. Dispersibility within the polymer solution as described above will then apply to the swollen bentonite aggregates. In a less dispersed state, e.g. in a high-molecular-weight AN solution, these swollen bentonite aggregates can have a significantly lower bulk density compared to single quartz grains as they contain a significant percentage of water, similar to polymeric hydrogels.

The carrying capacity of a fluid is governed by gravity and buoyancy, that is, volume forces within the gravity field which essentially act even if the fluid is at rest, by the fluid's shear resistance against flow (viscosity, yield strength) and by related transport forces as induced by flow (Stieß, 2009). Consequently, the direction of movement of a single particle can be described by the vectorial sum of these movement directions (Fig. 2.24) (Eq. 2.11):

$$\vec{u}_{tot} = \vec{u}_{shear} + \vec{u}_{fluid} \tag{2.11}$$

with $\vec{u}_{shear}$ limited by frictional forces created from relative movement between fluid and particle as induced by gravity surpassing buoyancy effects and $\vec{u}_{fluid}$ referring to the velocity term from fluid movement.

In the case of practically equal specific weight γ of fluid and particle (e.g. in the case of aqueous grains), a single particle has no tendency to settle. Consequently, there is no relative movement between fluid and particle ($\vec{u}_{shear} = 0$) and the direction and speed of movement of the particle are uniquely governed by fluid flow ($\vec{u}_{tot} = \vec{u}_{fluid}$). Otherwise, $\vec{u}_{shear}$ needs to be calculated based on the friction mobilization between particle and support fluid, i.e. either based on yield strength τ_F or on viscosity $\eta = f(\dot{\gamma})$ (or both).

If the respective fluid provides a significant resistance against relative movement, which has to be overcome for relative movement to occur (yield strength τ_F), then a spherical particle with diameter D and $\gamma_{sphere} > \gamma_{fluid}$ is considered perfectly suspended (no settlement) with a sufficient yield strength τ_F according to Eq. 2.12. This equation (without f_{corr}) was derived by Weiß (1967) for the movement of a pendulum-guided ball in fluid and introduced into DIN 4126:1986 as a calculative basis for the ball harp test with a formulation matching Eq. 2.12 with $f_{corr} = 0.7$.

$$\tau_F \geq f_{corr} \cdot \frac{2}{3\pi} \cdot D \cdot (\gamma_{sphere} - \gamma_{fluid}) \tag{2.12}$$

However, as most polymer solutions are considered to exhibit no or only a relatively small yield strength, this approach can only rarely be applied and only with respect to very small particles. This approach is more likely to be of significance for polymer-enhanced bentonite suspensions. As polymer solutions are primarily described by their viscosity in terms of rheological behaviour, the approach by Stokes (1850) on the sinking velocity of spherical particles in a resting Newtonian fluid can be used as an approximation at low shear rates or with reference to a lower viscosity plateau. Under the assumption of a considerably slow movement of the particle in the solution, i.e. laminar flow around the particle, a constant viscosity value $\mu = \eta(\dot{\gamma}_i)$ at a sufficiently low shear rate of $\dot{\gamma}_i = 10^{-3}$ 1/s is chosen for a conservative estimate of the actual friction mobilized by viscous flow, even though the polymer actually shows an increase in viscosity with decreasing flow velocity (shear rate).

Stokes (1850) obtained the terminal falling velocity v of a single spherical grain in an unmoving Newtonian fluid under laminar flow conditions around the grain, i.e. particle Reynold numbers $Re_p = (\rho_{fluid} \cdot v_{sphere} \cdot D_{sphere})/\mu \leq 0.25$ (Stieß, 2009), by determining a frictional resistance force

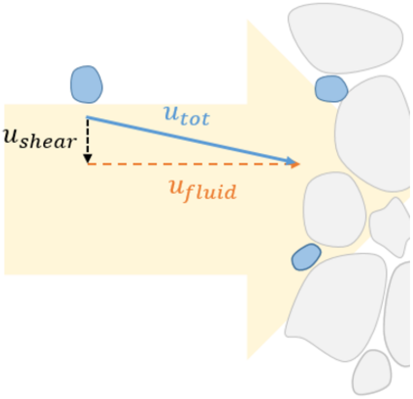

Figure 2.24.: Direction of movement of a particle at the earth wall

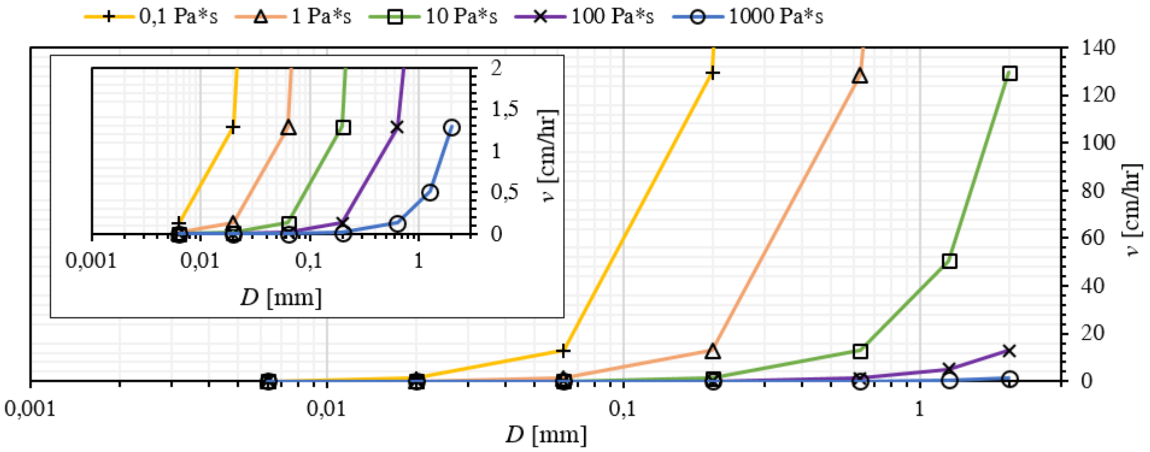

Figure 2.25.: Sinking velocity of spheres in viscous fluids according to Stokes (1850) for $Re_{ep} \leq 0.25$

or drag force F_r as given in Eq. 2.13:

$$F_r = 6\pi \cdot (\mu' \cdot \rho_{fluid}) \cdot R \cdot v = 6\pi \cdot \mu \cdot R \cdot v \tag{2.13}$$

The Newtonian fluid is represented by density ρ_{fluid} and kinematic viscosity μ', or equally dynamic viscosity $\mu = \mu' \cdot \rho_{fluid}$; and the contact area is referenced by the sphere radius R. This friction force is mobilised from viscosity by upwards movement of the fluid relative to the sphere and balances the difference of gravitational weight force $F_g = V \cdot (\rho_{sphere} \cdot g) = V \cdot \gamma_{sphere}$ and buoyancy force $F_b = V \cdot \gamma_{fluid}$, with the sphere volume $V = \frac{4}{3}\pi \cdot R^3$ acting within the earth gravity field ($g \approx 9.81$ m/s^2). Force balance $F_g - F_b - F_r = 0$ results in (Eq. 2.14):

$$v = \frac{2}{9} \cdot \frac{g}{\mu'} \cdot \left(\frac{\rho_{sphere}}{\rho_{fluid}} - 1\right) \cdot R^2 = \frac{D^2}{18 \cdot \mu} \cdot (\gamma_{sphere} - \gamma_{fluid}) \tag{2.14}$$

Tab. 2.3 shows the resulting values for the settling velocity v over a diameter range of $D = 0.00063 - 2$ mm and a range of viscosity of $\mu = 0.1 - 1000$ Pa·s (realistic range for polymer

Table 2.3.: Terminal sinking velocity of spheres in viscous fluids in [cm/h] based on Stokes (1850)

Diameter [mm]	Viscosity [Pa·s]				
	0.1	1	10	100	1000
2	$(1.3 \cdot 10^4)^{(a)}$	$1.3 \cdot 10^3$	$1.3 \cdot 10^2$	$1.3 \cdot 10^1$	$1.3 \cdot 10^0$
1.25	$5.1 \cdot 10^3$	$5.1 \cdot 10^2$	$5.1 \cdot 10^1$	$5.1 \cdot 10^0$	$5.1 \cdot 10^{-1}$
0.63	$1.3 \cdot 10^3$	$1.3 \cdot 10^2$	$1.3 \cdot 10^1$	$1.3 \cdot 10^0$	$1.3 \cdot 10^{-1}$
0.2	$1.3 \cdot 10^2$	$1.3 \cdot 10^1$	$1.3 \cdot 10^0$	$1.3 \cdot 10^{-1}$	$1.3 \cdot 10^{-2}$
0.063	$1.3 \cdot 10^1$	$1.3 \cdot 10^0$	$1.3 \cdot 10^{-1}$	$1.3 \cdot 10^{-2}$	$1.3 \cdot 10^{-3}$
0.02	$1.3 \cdot 10^0$	$1.3 \cdot 10^{-1}$	$1.3 \cdot 10^{-2}$	$1.3 \cdot 10^{-3}$	$1.3 \cdot 10^{-4}$
0.0063	$1.3 \cdot 10^{-1}$	$1.3 \cdot 10^{-2}$	$1.3 \cdot 10^{-3}$	$1.3 \cdot 10^{-4}$	$1.3 \cdot 10^{-5}$

(a) $Re_p > 0.25$

support fluids, cf. section 3.2.2) based on a safe-side definition for the polymer solution density ($\rho_{fluid} = 1$ g/cm^3) and an average sphere density $\rho_{sphere} = 2.65$ g/cm^3 for typical mineral grains. Fig. 2.25 visualizes the dependency of sinking velocity with grain diameter D for different viscosity values under laminar flow conditions defined by $Re_p > 0.25$.

It is evident that differences between sinking velocities given in [cm/hr] with variation of viscosity and grain diameter are significant (range: 5 decimal powers). Sand grains will settle relatively fast in polymer solutions with relevant viscosities around $\eta = 0.1 - 10$ Pa·s. Smaller grain sizes (< 0.06 mm) can reach settling velocities below 1 cm/hr even with lower viscosity values, which can be considered negligible.

It can be concluded that polymer solutions have the tendency to load especially with small particle sizes (silt, etc.), if aggregation and colloid formation of the grains do not prevent dispersion. Moreover, in the case of grain stabilizing effects governed by the fluid viscosity, it can be concluded that grains can be considered available for e.g. filtration and colmation if either the settling velocity calculated according to Stokes (1850) is negligible or if $\vec{u}_{fluid}$ surpasses the tendency for settling. This effect is favoured by movement of the excavation tools. Sand particles and larger soil colloids, however, will settle more quickly, which is relevant with respect to operational considerations (solid-fluid separation equipment, in-hole settling, base cleaning, etc.), as is described in more detail by Ouyang, Jefferis, and Wiltcher (2018) and Lam and Jefferis (2018).

2.2.4. Physicochemical and mechanical stability

During the excavation process, the support fluid can be exposed to different chemical, biological and mechanical boundary conditions, which can affect the fluid properties depending on the sensitivity of the polymer. All these processes can be related to a viscosity reduction, which can be significant and therefore affect the overall functionality of the polymer.

Mechanical degradation describes the process of chain scission, i.e. a shortening of polymer chains, by mechanical influence (Xiong et al., 2018; Lam and Jefferis, 2018). Understandably, the effect is more pronounced for long-chain polymers at high shear rates when they reach their maximum stretched form. Especially the long, thin and flexible AN polymers of high molecular weight are highly sensitive to shear. A significant impact can be observed when these polymers are dissolved and dispersed at high shear rates (Nagashiro and Tsunoda, 1977; Lam and Jefferis, 2018). Lam, Jefferis, and Goodhue Jr. (2010) reported a significant influence of centrifugal pumps and recirculation on the viscosity values of PHPA polymers. Therefore, bentonite mixing devices and pumping systems cannot be applied for these fluids. Instead, hydration and dispersion of the polymer grains need to be performed at low shear rates (SFG:2019). XAN, too, is sensitive to mechanical degradation to a certain extent, though not as pronounced owing to its complex structure (section 2.2.1). CMC-H is comparably smaller and more resistant to mechanical degradation, similarly to low-molecular weight AN. Consequently, of the group AN/XAN/CMC-H, only CMC-H polymers are recommended for excavation techniques which require circulation drilling (e.g. hydromills) and high viscosity values (SFG:2019). Aside from operational reasons for mechanical degradation, it can also be assumed that the polymers degrade to a certain degree when they penetrate the earth wall at high pressure gradients. Mechanical degradation will be addressed experimentally in section 3.2.2.

Chemical stability of polymer support fluids can be mainly associated with their reaction towards changes in pH, electrical conductivity or salt concentration (Lam and Jefferis, 2018; SFG:2019). Salts can be present in the groundwater, result from the manufacturing process of the polymers (denominated as ‘technical’ products instead of ‘pure’ clean products) or e.g. from contact with fresh concrete. The electrical conductivity (EC) is a measure of the total amount of dissolved ions (cations) in a fluid and is estimated at ranging between 50 and 500 μS/cm for potable water (Lam and Jefferis, 2018).

Depending on whether polyelectrolytes (polymers with ionic charge) contain ‘weak’ or ‘strong’ electrolyte (ionic) groups, they only partly or fully dissociate in solution (depending on pH). Dissociation results in the creation of ionic charge by release of counter-ions (commonly cations). Acrylic acid groups, which are found in most polymers used as support fluids, are weak groups. (Lam and Jefferis, 2018; Carraher Jr., 2018). Therefore, especially for AN polymers, a certain minimum pH is essential for the development of viscosifying properties as their effectivity is related to a certain stretched conformation created by adjacent ionic charges along the chain repelling each other (section 2.2.1. They reach their maximum effectivity around pH 7-10 (Lam and Jefferis, 2018; SFG:2019). With the presence of salts in solution, mainly polyvalent cations (e.g. Ca^{2+}), the flexible chains previously stabilized by their anionic charge distribution collapse, which reduces their mobilizable resistance during flow. Additives for pH adjustment can counter this effect to a certain degree, e.g. with the application of Na_2CO_3. In contrast, the addition of NaOH for pH adjustment has been found to decrease viscosity (Lam and Jefferis, 2018).

CMC-H is considered less sensitive to salt due to its different structure, with higher insensitivity with increased anionicity, even though it contains ‘weak’ groups. XAN with its even more complex and rigid structure contains partly shielded ionic groups, which makes it more resistant to pH and salt. However, while XAN can be considered stable towards salt and pH, it can be easily broken down biologically by microbes, in contrast to CMC-H and especially AN polymers (Lam and Jefferis, 2018).

Polymer reaction to temperature can equally be a factor in the classification of polymer flow behaviour. However, temperature changes, which would significantly alter the polymer flow behaviour, are usually not reached with support fluids in the addressed fields of application (rather for oilfield application) and will therefore not be addressed further.

2.2.5. Environmental relevance

Evidently, environmental relevance is a broad field, which can be addressed from various angles, even regardless of the materials used, e.g. by re-evaluation of the need for a specific construction at a specific place, by discussing alternative techniques and by economization of resources, e.g. in the context of an environmental impact assessment (EIA). Environmental considerations specifically for polymer fluid usage as compared to the application of bentonite suspensions comprise natural resources, production, application and long-term effects, namely the manufacturing footprint, people’s health in contact with the material during application and the environmental long-term effects on soil and groundwater and related consequences for humans, animals and plants. These aspects are influenced by production procedures, the choice of polymers, related equipment and quantities needed, handling (reuse, recycling, solid-fluid separation) as well as disposal measures.

This section will outline selected aspects, mainly on used concentrations, operational footprint, degradability and mobility in soils and groundwater and discharge considerations. More detailed evaluations on the environmental impact of different support fluids for diaphragm walling and pile drilling can be found with Lam and Jefferis (2018) and the practical guideline SFG:2019.

Bentonite (B)

In terms of production, bentonite is a mining product with limited global reserves. As an alternative for natural high-quality sodium bentonite with declining production rates, sodium-activated calcium bentonites are used. Many products sold as bentonites are actually polymer-modified bentonites treated with anionic low-molecular-weight Na-CMC or synthetic polymeric additives, e.g. sodium polyacrylate (Na-PA). They are used in suspension at concentrations between 20 g/l and 60 g/l; contained polymer dosages are often unknown (Praetorius and Schößer, 2017; Haugwitz and Pulsfort, 2018). They can be estimated at 2-4 kg for Na-CMC and 0.5-1.5 kg for Na-PA per ton of clay[15]. Suspensions can mostly be re-used during excavation. However, with respect to an operational site footprint, bentonite hydration tanks are needed as well as complex separation and treatment plants for reuse and disposal, e.g. desander, desilter, decanting centrifuge, filter press or a flocculation unit with application of polymeric flocculants or other chemical additives, as clay slurries can take up considerable amounts of soil particles difficult to remove due to their yield strength (Praetorius and Schößer, 2017; Lam and Jefferis, 2018; SFG:2019). Natural bentonite is considered non-hazardous waste in the UK and non-hazardous ("nwg"[16]) to water according to the German Water Hazard Class ("WGK"[17]), but environmental concerns have been raised for the mixed waste material in several countries. Moreover, bentonite usage has been forbidden in certain sensitive areas for possible pollution of groundwater or rivers (Lam and Jefferis, 2018).

Acrylamide-acrylate copolymers (AN)

Acrylamide-acrylate copolymers are petrochemicals, i.e. produced from oil or gas (section 2.2.1). They are usually provided in the form of dry powder or sometimes as inverted oil emulsions[18]. Synthetic viscosifiers and hydrogels are applied at concentrations between 0.5 g/l and 2 g/l for the addressed fields of applications ($\approx$ 30-40x reduction compared to pure bentonite). As separation plants are usually not used, settlement tanks may be necessary for fluid recycling, if soil settling is not fully performed in-hole. Chemicals for coagulation and aggregation are sometimes added into the hole before concreting to accelerate particle settlement, e.g. polyamines or polyDADMAC, i.e. cationic polymers of low molecular weight in liquid form. Particle-freed fluid is then chemically treated to be dischargeable as regular sewage. Chemical treatment can involve calcium or sodium hypochlorite solution (bleach), sodium or calcium chloride (salts) or hydrogen peroxide to break viscosity and in some cases acid to adjust pH. The amount of oxygen needed to break down the polymer can be determined based on the biological oxygen demand (BOD) (for biodegradable polymers) or the chemical oxygen demand (COD) (otherwise) (Lam and Jefferis, 2018; SFG:2019).

While the monomer acrylamide is classified as extremely toxic (carcinogen, neurotoxin) (Caulfield, Qiao, and Solomon, 2002; Xiong et al., 2018) and a severe hazard to water (WGK 3), polyelectrolyte acrylamide-acrylate copolymers are classed as relatively non-toxic [19], though hazardous to waters (WGK 2), and are considered not to be degradable to their monomers, especially heavy cross-linking is considered irreversible (Barvenik, 1994; Xiong et al., 2018). Moreover, mobility in soils is restricted for high molecular weights and soil adsorption in the case of viscosifiers or the inert state of hydrogels. Mobility in soil and water can increase with partial degradation (Araújo et al., 2002; Caulfield, Qiao, and Solomon, 2002; Peppas, Slaughter, and Kanzelberger, 2012; Oyen, 2013; Xiong et al., 2018).

---

[15] Ref.: Laurent Giuranna (SNF), personal communication, July 9, 2020

[16] "Nwg" nicht wassergefährdend

[17] "WGK" Wassergefährdungsklasse

[18] Inverted emulsions meaning water in oil as opposed to regular emulsions of oil in water

[19] E.g., info from safety data sheets for 'Mud P' (Clariant) and 'Floset CE 131' & 'Floset CE 130 XF35' (SNF): LD50 oral, rat: > 5000 mg/kg

However, products usually contain a certain residue of unpolymerized acrylamide monomer from the production process, the amount varying with the process used, but usually residing < 0.05 % for anionic polymers (Araújo et al., 2002; Caulfield, Qiao, and Solomon, 2002; Peppas, Slaughter, and Kanzelberger, 2012; Oyen, 2013; Xiong et al., 2018). Environmental regulations therefore formulate maximum amounts of residual acrylamide monomer, e.g. < 0.1 ppb (w/v) by the European Commission (EC) or polymer concentrations at < 1 mg/l for drinking water treatment to ensure < 0.5 ppb (w/v) (Xiong et al., 2018).

They are generally considered non-biodegradable (Lam and Jefferis, 2018) although Zohourian and Kabiri (2008) and Xiong et al. (2018) list several studies, which found that they are biodegradable in certain environments such as soils, where natural microbes can degrade acrylamide within days or months to acrylic acid and ammonia (NH_3), which are considered non-toxic, and then convert to water, carbon dioxide and organic matter.

Na-Carboxymethylcellulose (CMC)

As a derivative of cellulose, which is contained in many plants, Na-CMC is a renewable resource (section 2.2.1). It is applied at concentrations between 1.5 g/l and 5 g/l (≈10-15x reduction compared to pure bentonite) (SFG:2019). Fluid recycling and disposal treatment are essentially comparable to AN. However, as CMC is less sensitive to mechanical shear, it is also applied with reverse-circulation excavation (e.g. hydrofraise), which promotes soil particle dispersion (as is often intended). Consequently, separation plants are sometimes used on site (Lam and Jefferis, 2018).

Na-CMC is considered slowly biodegradable (>28 days) and is classified as a low hazard to waters in Germany (WGK 1) and non-toxic [20]. According to VanGinkel and Gayton (1996) and Karimi and Naimi-Jamal (2019), CMC is considered non-toxic and biocompatible, even after partial degradation, and is degraded entirely in rivers and soils.

Xanthan (XAN)

Xanthan gum is a renewable resource as it is produced by aerobic fermentation (section 2.2.1). According to Sorbie (1991), xanthan production requires a significant energy input. It is applied at concentrations between 1.0 g/l and 2.5 g/l (10-25x reduction compared to bentonite). Fluid recycling and disposal treatment are essentially comparable to AN and CMC. As compared to CMC, xanthan is readily biodegradable (safety data sheet for 'SC XGUM' (Clariant)) and considered a low hazard to waters in Germany (WGK 1). However, it is easily degraded by bacteria, in which case fungicides would need to be applied (Lam and Jefferis, 2018; Dai and Zhao, 2018).

Regulations in Germany

Fluid treatment and disposal as regular waste water, as described above, has been internationally established as common practice and often listed as a main advantage over the application of bentonite suspensions. Concerns on environmental impacts on ground seem to be rarely raised (Lam and Jefferis, 2018; Ouyang, Jefferis, and Wiltcher, 2018). In Germany, Lesemann (2010) has performed a broad ecotoxicological investigation and groundwater impact analysis in accordance with guidelines developed with the local water authority within the context of the

---

[20] E.g., info from safety data sheet for 'SC VIS HVP' (Clariant): LC50 > 2000 mg/kg (rabbit, dermal), LC50 > 5800 mg/l (rat, inhalation), LC50> 100 mg/l (fish)

construction of three test piles produced in Germany. The test piles were produced at significantly higher maximum polymer dosages (e.g. 8 g/l) than proposed here. Initial evaluation based on eluate classification (daphnia testing) according to DIBt:2009 found a threshold concentration 2 g/l for a positive evaluation of the tolerance for soil and groundwater for the tested polymer products (AN, CMC, XAN). However, owing to the high maximum reference concentration, detailed groundwater testing was performed in accordance with the guidelines from the local water authority based on groundwater samples from selected places around the excavation. Despite high polymer dosage, deviations were mainly found with respect to a small temporary change in TOC (total organic carbon) values, which suggested the existence of significantly smaller polymer dosages (<1 g/l), and a temporary decrease in oxygen levels. The remaining polymer solutions were accepted at the local sewage works and there diluted and introduced into the regular sewage circulation, which can be considered in accordance with the procedures followed internationally.

This investigation programme could serve as a basis for a general type approval, which was not intended within the scope of this investigation. Furthermore, it can be assumed that limit values can be met more easily with improved knowledge on the penetration behaviour of polymer solutions into the ground and related methods for material optimization.

Generally, chemico-physical investigations on eluate with realistic product dosages according to DIN 38414-S4:1984 (or EN 12457-4:2003) are currently considered sufficient for evaluation of a potential groundwater impact for bentonite suspensions in Germany without specifying types of (possibly polymeric) additives for standard application conditions (outside of water protection areas, etc.), thereby taking into account the limited area of impact of the support fluid on ground and surface water due to limited penetration into the ground. With sufficient knowledge on the penetration behaviour (especially predicted maximum penetration depths) of polymer solutions, the same concept should be applicable for these types of support fluid.

2.3. Penetration behaviour of polymer solutions into soil

2.3.1. Interaction parameters

With respect to stability, fluid penetration into soil and related pressure transfer have been differentiated into two different mechanisms, namely

- purely viscous penetration and
- membrane formation (e.g. by colmation),

as elaborated in section 2.1.2. Given a sufficient chemical stability (section 2.2.4), bulk properties of support fluids with regard to penetration are influenced by their composition (section 2.2.1), their ability to suspended and transport grains (in the case of colmation) (section 2.2.3) and their bulk rheological behaviour (section 2.2.2).

The interaction with the confined space of the soil matrix and different types of pore blockers further complicates the determination of relevant interaction mechanisms explaining the above differentiation necessary for stability assessment, as illustrated in Fig. 2.26. The interacting mechanisms have been phenomenologically and empirically described in literature and to a certain extend integrated in analytical or semi-analytical models.

Analytical and semi-analytical capillary bundle models currently applied for a calculative stability assessment of polymer fluid support (Steinhoff, 1993; Lesemann, Vogt, and Pulsfort, 2016) base on the assumption of a linear pressure drop along the penetration depth and purely viscous flow behaviour of ‘clean’ polymer solutions in the soil pores relatable to their bulk rheology. This assumption is in line with common soil-mechanical approaches for fluid permeation through soil derived in the last century, so-called engineering or generalized Newtonian approaches (Bird, Stewart, and Lightfoot, 2007). Well-known examples are Darcy’s law (Darcy, 1856), the Blake-Kozeny equation (Blake, 1922; Kozeny, 1927) or the Kozeny-Carman equation (Carman, 1937), which describe an average flow velocity of water or salt solutions idealized as incompressible ideal Newtonian fluids ($\tau = \dot{\gamma} \cdot \eta$) under laminar flow conditions through a soil matrix (or e.g. glass beads as idealized soil).

While irrelevant for Newtonian fluids with $\eta = const.$, for fluids with shear-rate-dependent viscosity, the actual shearing conditions are decisive input parameters for the correct amount shear stresses calculated from bulk rheological models. Capillary bundle models, however, do

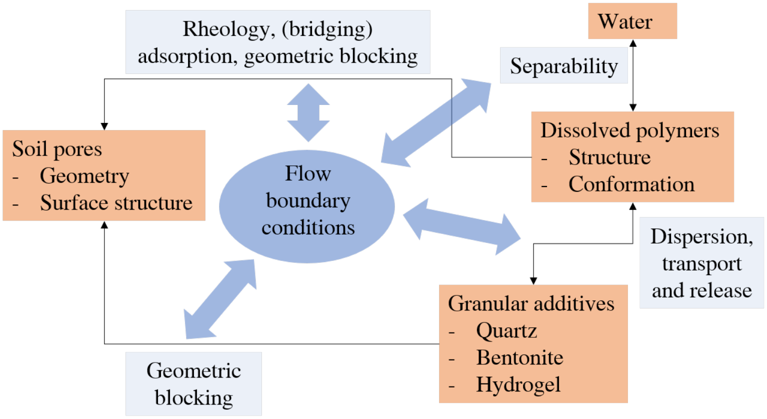

Figure 2.26.: Interaction mechanisms in the context of support fluid penetration into soil

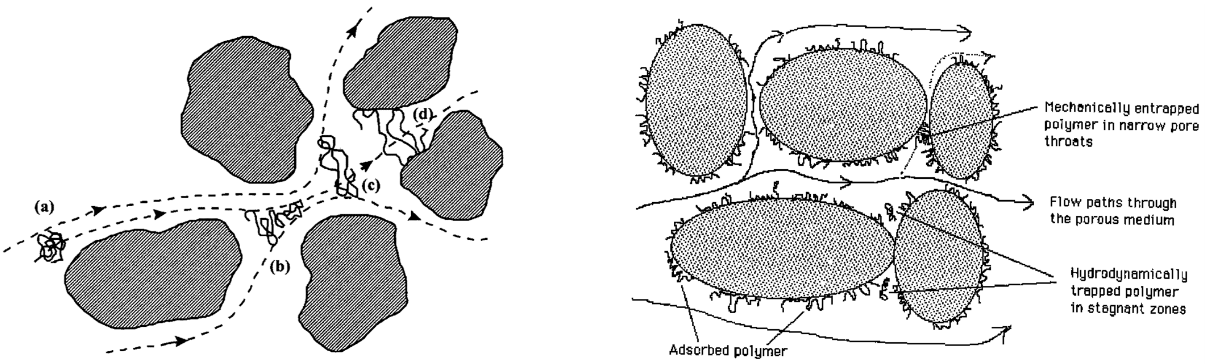

Figure 2.27.: Visualization of penetration and adsorption mechanisms of dissolved polymer chains in porous media according to Zitha, Chauveteau, and Léger (2001) (left) and Sorbie (1991) (right)

not reflect the exact shearing geometry of the soil pores for the determination of the corresponding shear rate. As they describe macroscopic average flow rates, the shearing impact of the polymer conformation in distinct pore environments cannot be immediately taken into account. Furthermore, polymers have been found to react towards rough, charged as well as uncharged surfaces, which can create local depletion zones on the one hand (local polymer-water separation) physical flow hindrance and pore blocking through adsorption on the other (Liao and Siems, 1990; Sorbie, 1991; Zitha, Chauveteau, and Léger, 2001) (Fig. 2.27). Possibilities for considering these effects in capillary bundle models as a semi-analytical calculative basis for the prediction of the time-dependent penetration behaviour of 'clean' viscous polymer support fluids are further discussed in the following section 2.3.2.

In the context of bonding mechanisms even between non-cohesive soil and polymer, the FHWA-NHI-10-016:2010 guideline describes the possibility of a web-like membrane formation by bonding to the earth wall for permeability reduction and related pressure transfer directly at the interface ranging "from a small strength increase to something approaching a true chemical grout effect". This can relate to bridging adsorption of long-chain polymeric viscosifiers (section 2.2.1), which form the base of polymer support fluids. This mechanism may be enhanced by bridging or crosslinking agents (Goodhue and Holmes, 1997). However, control parameters ensuring this mechanism and linking it to reliable degrees of permeability reduction or pressure adsorption for support mobilization are not yet available.

Membrane formation by means of physical pore blocking (colmation) is equally sparsely described in literature in the context of polymer solutions and related permeability reduction and pressure transfer mechanisms to the soil skeleton. They concern the interaction between soil, fluid phase (dissolved viscous polymers) and granular additives with differing geometric and surface characteristics. Thereby the additives are considered to alter the pore geometry, that is, reduce permeability, influencing the flow behaviour of the fluid phase.

Quartz grains as solid particles have distinct and thus easily relatable characteristics. Hydrogels are not marketed with reference of specific achievable diameters due to water uptake, rather concerning absorption capacity, which may be associated with a certain swollen size average (section 2.2.1). Aside from their differing bulk specific weight, the different surface condition of quartz grains (rough) and hydrogels (smooth) may influence their dispersion, release and filtration in the granular environment. Bentonite lamellae can be considered an intermediate in this regard. When predispersed as an aqueous suspension before mixing with the viscous phase for maximum dispersion, the dispersibility of the suspension within the viscous phase largely governs the extend to which the water contained within the suspension dilutes the support fluid or otherwise remains in electric interaction with the clay aggregates forming partly aqueous globules within the viscous fluid phase. Possible relevant parameters are the quality of bentonite hydration associated with the stirring speed and time of the suspension and the polymer structure and chain length associated with polymer entanglement. It can be concluded that the relevant size for colmation in this case is yet unclear.

Given an average grain size of a granular additive, geometric considerations relevant for a colmation effect can be formulated based on filter criteria, as will be further evaluated in section 2.3.3.

The following two sections will discuss concepts for the prediction of viscous penetration behaviour (section 2.3.2) and colmation effects (section 2.3.3) in more detail.

2.3.2. Analytical-empirical approaches for viscous fluids

Kozeny (1927) (and consequently both the Blake-Kozeny and the Kozeny-Carman equation) essentially idealized the porous media by a bundle of straight parallel capillaries with constant cross-section (Carman, 1937). Equally, analytical engineering models for polymer flow through porous media, as reviewed e.g. by Sorbie (1991) and Skauge et al. (2018), have been derived by modification of these Newton-based formulations by using different bulk rheological models and correction factors, as will be elaborated hereafter. The main parameters used in these models are given in Tab. 2.4.

The average flow velocity of a Newtonian fluid through a single straight capillary of radius R and length L (and cross section A_{tube} and number of tubes N) under constant pressure Δp and laminar flow conditions is described by the Hagen-Poiseuille equation (Eq. 2.15). Its derivation from equilibrium at capillary level is described in appendix A.

$$\bar{v}_{capillary,HP} = \frac{R^2 \cdot \Delta p}{8 \cdot L \cdot \eta} \tag{2.15}$$

Predominantly one-dimensional (laminar) flow through a soil matrix is then represented by a bundle of these uniform cylindrical capillaries by choosing their total volume $N \cdot A_{tube}$ to be of the same size as the total soil pore volume A_0 (Fig. 2.28). The same average flow velocity can then be achieved by defining an equivalent hydraulic radius R_{eq} as given in Eq. 2.16, where K represents the intrinsic permeability.

$$R = R_{eq} = \sqrt{\frac{8 \cdot K \cdot T}{n}} \tag{2.16}$$

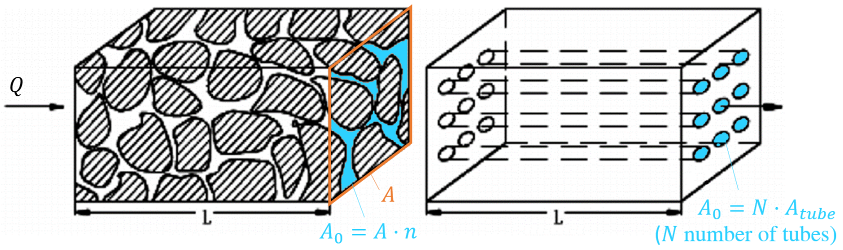

Figure 2.28.: Capillary bundle idealization, adapted from Al-Doury (2010)

Table 2.4.: Parameter sets for capillary bundle models

Soil	D	Average grain diameter [m]
	n	Porosity [-] (related to void ratio e by: $n = \frac{e}{1+e}$)
	K	Intrinsic permeability [m^2 or m^3/m] or
	k_w	permeability coefficient (water) [m/s] (related to K by $k_w = \frac{K \cdot \gamma_w}{\eta_w}$ 1))
	T	Tortuosity [-]
	V_{flow}	Volume available for flow [m^3]
	S	Specific surface (= wetted pore surface) [m^2] for spheres: $S = \frac{1-n}{d_{sphere}}$ 2)
Polymer solution	κ	Power-law parameter [Pa·s]
	m	Power-law parameter [m]
	$\dot{\gamma}_{crit}$	Newton plateau limit [1/s]
Test conditions	$\Delta H, \Delta p$	Pressure difference [m, Pa]
	L	Permeated length [m]
Capillary bundle	R_{eq}	Equivalent hydraulic radius (Eq. 2.16) [m]
	R_H	Hydraulic radius $R_H = \frac{V_{flow}}{S} = \frac{D \cdot n}{3 \cdot (1-n)}$ 2) [m]
Fluid-soil interaction	α^*	Shift/ Correction factor for capillary vs. in-situ shear rate [-]

1) viscosity η_w and specific weight γ_w from flow tests with water

2) geometric parameters S and R_H as introduced by Carman (1937)

K is related to permeability coefficient k_w for water flow by $k_w = K \cdot \gamma_w / \eta_w$ with γ_w being the specific weight of water. A pore tortuosity T, defined as the ratio between the actually more tortuous permeated length L_e within the soil and the idealized straight capillary length L by $T = L_e/L$, is implemented additionally in certain models. Some models, e.g. the above mentioned equations related to Kozeny (1927), apply T not only within the formulation of the equivalent hydraulic radius, but equally for the capillary length L ($L^* = L \cdot T = L_e$).

The Darcy filter velocity $\bar{v}_{Darcy}$ can be obtained from the average pore velocity $\bar{v}_{capillary}$ according to Dupuit, whose equation is given in Eq. 2.17, i.e., $\bar{v}_{Darcy} = Q/A$, $\bar{v}_{capillary} = Q/A_0$ (Fig. 2.28).

$$\bar{v}_{Darcy} = n \cdot \bar{v}_{capillary} \tag{2.17}$$

Combining Eq. 2.15-2.17 with $T = 1$ results in Darcy's law. Instead of a direct implementation of K (or k_w), the Blake-Kozeny equation and the Kozeny-Carman equation contain an analytically derived term for K, which differs slightly due to different choices of tortuosity values and different implementations thereof to correctly capture the equivalence of pore surface and cappillary surface in their respective derivation.

The Blake-Kozeny equation (Eq. 2.18) for relatively uniform and ideally spherical particles with diameter D can be obtained from Eq. 2.15-2.17 with $T = 25/12$ and $K = \frac{D^2 \cdot n^3}{150 \cdot (1-n)^2}$ and additionally applying T within the permeated length $L^* = L \cdot T$. This results in $R_{eq} = R_H$. The respective form of the Kozeny-Carman equation (Eq. 2.19) uses $T = \sqrt{2}$ resulting in $K =$

$\frac{D^2 \cdot n^3}{180 \cdot (1-n)^2}$, because T is also applied to the Dupuit formulation[21].

$$\bar{v}_{Darcy,BK} == \frac{D^2 \cdot n^3}{150 \cdot (1-n)^2} \frac{\Delta p}{L \cdot \eta} \tag{2.18}$$

$$\bar{v}_{Darcy,KC} == \frac{D^2 \cdot n^3}{180 \cdot (1-n)^2} \frac{\Delta p}{L \cdot \eta} \tag{2.19}$$

Eq. 2.20 shows the power-law equivalent to the Hagen-Poiseuille equation (Eq. 2.15), i.e. a 'reference' model for approaches for polymer solutions, with m and κ as the required bulk rheological power-law variables. The Hagen-Poiseuille term (Eq. 2.15) can be derived from Eq. 2.20 with $m = 1$ and $\kappa = \eta$.

$$\bar{v}_{capillary,OdW} = \left(\frac{m}{3 \cdot m + 1}\right) \cdot R^{\frac{m+1}{m}} \cdot \left(\frac{\Delta p}{2 \cdot L \cdot \kappa}\right)^{\frac{1}{m}} \tag{2.20}$$

Christopher and Middleman (1965) and Hirasaki and Pope (1974), e.g., used the Blake-Kozeny approach, mainly regarding the implementation of T, in combination with power-law behaviour in order to describe the flow of polymer solutions in porous media. K can then be either calculated according to original Blake-Kozeny (from D and n) or gained from permeability testing (Darcy) according to the approach by Christopher and Middleman (1965).

Steinhoff (1993) used $T = 1$ and K as obtained from permeability tests with water (k_w from Darcy), but complemented the power-law behaviour with an upper Newtonian plateau at $\dot{\gamma}_{crit} = 1.5$ 1/s to more accurately capture the behaviour observed with polymer solutions (section 2.2.2). Below $\dot{\gamma}_{crit}$, Newtonian behaviour is assumed with $\eta_{Newton} = \eta_{OdW}(\dot{\gamma}_{crit}) = \kappa \cdot \dot{\gamma}_{crit}^{m-1} = const.$. The effect of an introduction of $\dot{\gamma}_{crit}$ is illustrated in Fig. 2.29. No reason is stated for the determination of $\dot{\gamma}_{crit}$ at 1.5 1/s. Ejezie et al. (2020) found an upper Newtonian plateau with one test sample at $\dot{\gamma}_{crit} \approx 0.01$ 1/s.

Lesemann (2010) (engl.: Lesemann, Vogt, and Pulsfort, 2016) used pure power-law behaviour following Eq. 2.20, but added a factor 3 to the equivalent hydraulic radius term from Eq. 2.16

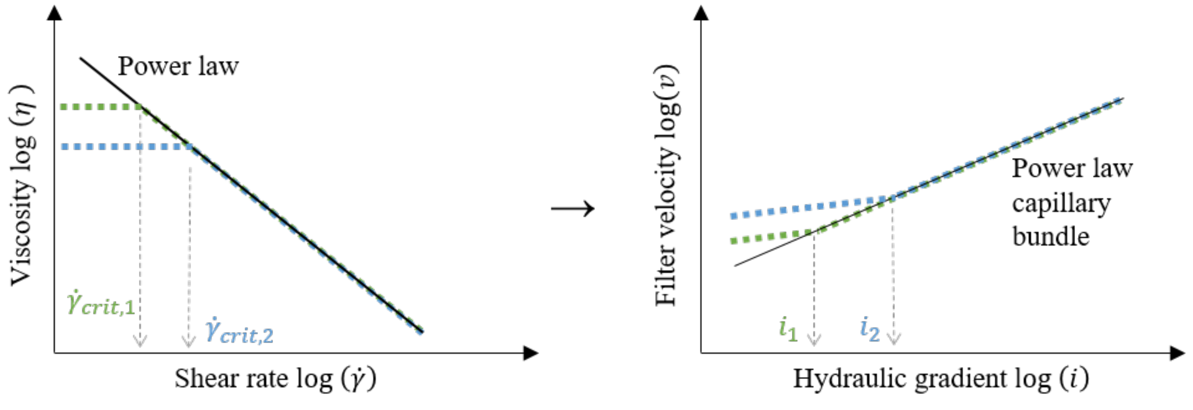

Figure 2.29.: Effect of $\dot{\gamma}_{crit}$ on rheology and capillary bundle velocity

---

[21] $\bar{v}_{Darcy} \cdot T = n \cdot \bar{v}_{capillary}$ as a modification of Eq. 2.17

$\left(R = R_{eq,3D} = \sqrt{\frac{(3 \cdot 8) \cdot K \cdot T}{n}}\right)$ to consider three-dimensional flow conditions, i.e. three equal directions of flow, as described by Sorbie (1991).

Further variations of model parameters related to the above equations are found in literature. Some studies for polymer flooding application used more complex formulations, e.g. to implement a pore size distribution (Hirasaki and Pope, 1974) or to account for Carreau bulk rheological behaviour (Cannella, Huh, and Seright, 1988). However, Chauveteau (1986), Sorbie (1991), Navarrete, Himes, and Seheult (2000), Balhoff and Thompson (2006), and Skauge et al. (2018) summarized several studies for oil and gas industry applications, which indicate that bulk rheological parameters obtained from rotational rheometer or viscometer measurements in combination with uniform capillary bundles cannot fully capture the flow behaviour of polymer solutions in soil. The general curvature seemed correct. Numerical network modelling, which allows a more realistic depiction of the hydraulic conductivity by means of more complex pore structure implementations, showed a linear correlation between the average shear rate and the flow rate (Sorbie, 1991) or a proportionality between the capillary velocity and $(\Delta p)^{\frac{1}{n}}$ and between R_{eq} and R_H (Balhoff and Thompson, 2006). It is therefore generally concluded that capillary bundles can be used to predict the flow of polymer solutions in porous media, if a constant 'shift' factor is introduced as an empirical correction term to more accurately account for the respective shearing environment.

In this context, Cannella, Huh, and Seright (1988) and Balhoff and Thompson (2006) found a relation between a correction factor and pore connectivity, pore size distribution, permeability and porosity based on numerical network modelling. Chauveteau (1986), among others, explained deviations e.g. by wall effects creating local depletion zones, that is, zones of lower polymer concentration and thus reduced viscosity near the grain surface, especially pronounced with flexible macromolecules such as acrylamide-acrylate copolymers. Sorbie (1991) and Skauge et al. (2018), however, pointed out that investigations give very different results, so that no generalization can be made on any general quantification of the shift.

Here, an experimental investigation on correction factors usually implies a macroscopic approach based on the determination of an 'apparent' or 'in-situ' viscosity η_{app} from soil permeability testing ($\bar{v}_{Darcy,test}$) by means of Darcy's law. The empirical correction is then introduced within the double-logarithmic rheology plot ($\dot{\gamma}$ vs. η), i.e. as a correction factor for $\dot{\gamma}$. This macroscopic approach combined with some basic representations of the interacting factors and experimental calibrations can be associated with the "effective medium theory" (Choy, 2016; Skauge et al., 2018).

Taking into account uncertainties about the specific value of a shift factor, especially with focus on implementation within the $\bar{v} - i$ plots (instead of $\dot{\gamma}$ vs. η), a macroscopic correction parameter α^* is proposed for the combination of Eq. 2.16 & 2.20 resulting in $\frac{\Delta p}{2 \cdot L \cdot \kappa} \rightarrow \frac{\Delta p}{2 \cdot L \cdot \kappa \cdot \alpha^*}$ and an omission of an explicit parameter T within the equivalent hydraulic radius term (i.e. $T = 1$) as shown in Eq. 2.21.

$$\bar{v}_{capillary,OdW\alpha^*} = \left(\frac{m}{3 \cdot m + 1}\right) \cdot \left(\frac{8 \cdot K}{n}\right)^{\frac{m+1}{2m}} \cdot \left(\frac{\Delta p}{2 \cdot L \cdot \kappa \cdot \alpha^*}\right)^{\frac{1}{m}} \tag{2.21}$$

This factor can be interpreted as an effective parameter comprising several potential functions, such as

(1) viscosity modification ($\alpha^* \cdot \kappa$) indicating depletion by a vertical shift within the double-logarithmic $\dot{\gamma} - \eta$ plot for $\alpha^* < 1$ (Fig. 2.30),

(2) shift between an applied and an 'in-pore' gradient ($\frac{1}{\alpha^*} \cdot \frac{\Delta p}{L}$) or

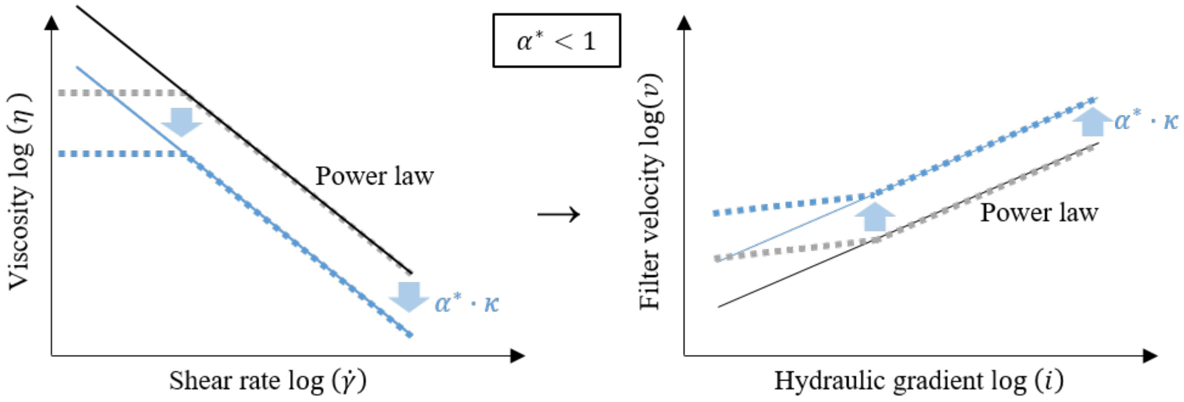

Figure 2.30.: Effect of $\kappa \cdot \alpha^*$ on rheology and capillary bundle velocity with $\alpha^* < 1$

(3) tortuosity or otherwise pore shape influence ($\alpha^* \cdot L$), though not within R_{eq}.

Steinhoff (1993) derived a time-dependent penetration depth for one-dimensional flow by defining L as the penetration depth at time step t, i.e. $L = s(t)$, with an average pressure gradient $\Delta p/s(t)$ decreasing with increasing penetration depth at constant Δp. Rearranging $v_{capillary} = ds(t)/dt$ (based on Eq. 2.21) then leads to the following differential equation, where $\kappa \cdot \alpha^*$ is included

$$s^{\frac{1}{m}}\ ds = dt \cdot \left[\left(\frac{m}{3 \cdot m + 1}\right) \cdot \left(\frac{8 \cdot K}{n}\right)^{\frac{m+1}{2m}} \cdot \left(\frac{\Delta p}{2 \cdot \kappa \cdot \alpha^*}\right)^{\frac{1}{m}}\right]$$

and which can be solved by integration

$$\int s^{\frac{1}{m}}\ ds = \int dt \cdot \left[\left(\frac{m}{3 \cdot m + 1}\right) \cdot \left(\frac{8 \cdot K}{n}\right)^{\frac{m+1}{2m}} \cdot \left(\frac{\Delta p}{2 \cdot \kappa \cdot \alpha^*}\right)^{\frac{1}{m}}\right]$$

With integration constant $C = 0$ as $s(t = 0) = 0$, this results in the formulation of the time-dependant penetration depth $s(t)$ as given in Eq. 2.22:

$$s(t) = \left[\left(\frac{m+1}{3 \cdot m + 1}\right)^{\frac{m}{m+1}} \cdot \sqrt{\frac{8 \cdot K}{n}} \cdot \left(\frac{\Delta p}{2 \cdot \kappa \cdot \alpha^*}\right)^{\frac{1}{m+1}}\right] \cdot t^{\frac{m}{m+1}} \tag{2.22}$$

The original[22] equation by Steinhoff (1993) can be obtained with $\alpha^* = 1$ within the proportionality term relating the two variables $s(t)$ and $t^{\frac{m}{m+1}}$.

A possible Newtonian plateau can be complemented within this otherwise power-law based approach by introducing a limit criterion with η_{max} (or likewise η_{min}), e.g. according to the concept by Steinhoff (1993), but with consideration of $\kappa^* = \kappa \cdot \alpha^*$. A time-dependent formulation for the penetration depth purely based on plateau behaviour can be obtained from Eq. 2.21 with $m = 1$ and $\eta_{crit} = \kappa^* \cdot \dot{\gamma}_{crit}^{m-1} \rightarrow \kappa^* = \eta_{crit}$:

---

[22] The equations used by Steinhoff (1993) are written in a different form, so equality is not immediately notable. They have been rearranged to the form presented here to be relatable more easily to the components of the capillary velocity basis from Eq. 2.21.

$$s_N(t) = \sqrt{\frac{2 \cdot K \cdot \Delta p \cdot t}{n \cdot \eta_{crit}}} \tag{2.23}$$

K can be implemented based on flow test evaluation or predicted, e.g. according to Blake-Kozeny or Kozeny-Carman.

Overall, it can be concluded that there are significant interactions between a polymeric viscous fluid and the soil medium, which have not yet been taken into account for the calculation of support forces. Especially small flow velocities as encountered in geotechnical applications are scarcely addressed in the studies for oil and gas application. Generally, differing soil conditions are likely to have a significant effect, so that empirical data from oil and gas research is not likely to be immediately relatable. It is possible that a broad experimental programme can reveal adequate correction factors for the targeted context to more accurately describe the interaction. If found, an implementation within the current concept developed by Steinhoff (1993) for the calculation of support forces would be trivial.

Eq. 2.22-2.23 will be used as a basis for parameter calibration within the scope of the experimental investigation (section 3.3.3) and thus a basis for discussion on the applicability of these capillary bundle models and possible transferability of found calibration parameters.

2.3.3. Influence of suspended material

Under the premise that the polymer solution easily releases particles and does not hinder them from being caught at or within the earth wall, the effect of fines colmation, mineral or aqueous or other, around the earth wall interface is a subject of geometric blocking of soil pores (Fig. 2.31).

It can be addressed starting from the Terzaghi filter criterion in terms of a mechanical filter stability as given by Eq. 2.24 (Fannin, 2008; Semar, Witt, and Fannin, 2010; MMB:2013).

$$\frac{d_{15,F}}{d_{85,s}} \leq 4 \tag{2.24}$$

Thereby, the diameter of the filter (native ground to be supported) at 15 % sieve passage $d_{15,F}$ is defined as the representative filter value, the respective value of the soil (suspended material) is represented by $d_{85,s}$, i.e. the grain diameter at 85 % sieve passage (evaluated by weight). MMB:2013 allows a widening of the application range to ≤ 5. The second Terzaghi criterion (Eq. 2.25) refers to the hydraulic ability for drainage, with $d_{15,s}$ representing the effective soil grain diameter at 15 % sieve passage. According to Witt (2018), who judges these filter criteria to be the most reliable base for filter stability assessment for practical application, this second criterion ensures free hydrostatic pressure transfer.

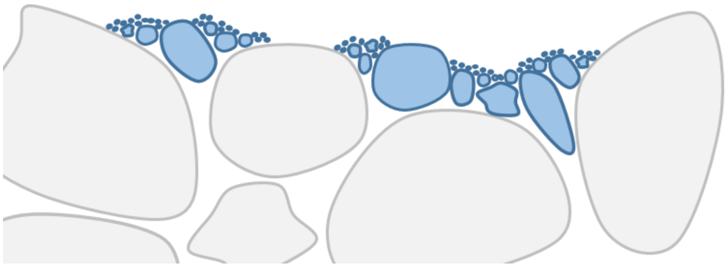

Figure 2.31.: Visualization of the colmation process

$$\frac{d_{15,F}}{d_{15,s}} \geq 4 \tag{2.25}$$

Following this geometric approach and based on the assumption that the fluid can indeed provide the relevant sizes of grains, as explained in section 2.2.3, a permeability reduction can be expected from the native soil towards a permeability governed by the colmated material.

A grain size distribution of the suspended material ranging from this filter criterion ($d_{85,s}$) as the largest required grain size fraction and step-wise down to a fine-grained material with a permeability value sufficiently low for a polymer fluid to significantly slow down could consequently result in a full pressure transfer at the earth wall. The upper boundary of the filtrate can be taken from the mechanical criterion ($d_{max} = d_{15,F}/4$ or $d_{max} = d_{15,F}/5$). Following an inversion of the drainage criterion, fine material with $d_{15,s} < d_{15,F}/4$ could affect the pressure transfer at this interface.

It is possible, however, that the effective diameter of the suspended material actually surpasses the dry grain diameter due to polymer encapsulation, the geometrical effect depending on the polymer structure. Therefore, if the ratio $d_{15,F}/d_{85,s}$ is maintained as a reference for mechanical colmation, it may be possible to formulate higher safety levels for specific polymer types based on filtration tests. The grain size of the lower boundary (d_{min}) for specific filtrate-polymer relationships can be determined similarly.

2.4. Conclusions and open questions

As an important tool for safety evaluation, stability checks for polymer support fluids need reliable pressure-penetration relationships. Following sections 2.1.2 and 2.1.3, the main target values for a calculative quantification in this context are

- the penetration depth as a function of time ($s(t)$),
- the curvature of the pressure transfer to the ground ($\Delta p_{mob}(x,t)$), in particular the earth wall pressure gradient ($f_{s0,wall}(t)$) and
- the physicochemical potential of fluid and soil (for swelling-related problems),

preferably formulated for the worst case scenario as a then time-independent safe-side representative. However, it has been shown that it is not yet fully understood how these parameters are linked to relevant bulk properties of the interacting materials, which are primarily

- the viscosifying base polymer,
- the penetrated soil and
- suspended granular material for colmation.

The main open question is whether, and if so, how, pressure-penetration relationships can be linked to easily measurable parameters, e.g. in the sense of d_{10}-τ_F representatives, to improve current design methods and standard material testing equipment. This will be addressed by means of laboratory investigations in the following sections, thereby taking into consideration different material interaction.

Polymer fluid penetration tests into soil combined with pore pressure measurements along the penetration depth have been chosen here as a direct means to evaluate the functionality of different combinations of polymers and additives in different granular environments.

For a realistic assessment, fluid penetration testing devices at laboratory scale should refer to the boundary conditions encountered during the excavation process for diaphragm walls, bored piles and tunnels under fluid support wherever possible. These comprise

- soil type, density and saturation,
- direction of flow and penetration (horizontal/vertical/radial),
- contact between earth wall and support fluid,
- limiting pressure levels,
- penetration depths,
- geometry and arching effects with respect to macro stability and
- step-wise excavation of earth wall with pre-penetration zones.

Furthermore, sections 2.2.1-2.2.3 and 2.3.3 have highlighted three functionality-related groups, on which material variation and classification can be based:

- viscous flow characterization (bulk rheology),
- pore blocking characterization (geometries, sedimentation, transport properties and colmation behaviour) and
- clay swelling reduction potential.

3. Laboratory experiments

3.1. Experimental methods for preparation and testing

3.1.1. Setup for fluid penetration

The conceptual structure of the experimental investigation at laboratory scale on pressure-penetration relationships is set up around four fluid-soil penetration testing devices contrasted in Tab. 3.1 and abbreviated as follows:

(1) **v**ertical soil penetration – **l**arge scale model (V-L)
(2) **v**ertical soil penetration – **s**mall scale model (V-S)
(3) **h**orizontal soil penetration – **p**lane model (H-P)
(4) **h**orizontal soil penetration with concreting – **r**adial model (H-R)

V-L is the main large uniaxial testing device. The three additional devices are chosen to compensate for certain disadvantages of the main testing device. (1) and (2) are adapted for shear-thinning fluids from soil penetration testing standardized in EN ISO 17892-11:2019 and DIN 4127:2014 with focus on Newtonian (water) or Bingham (clay suspension) fluids. (3) describes a testing device similar to the one employed by Steinhoff (1993) explicitly for polymer solutions. The following list gives an overview on the target values from each device:

- V-L: analyse pressure-transfer behaviour as a basis for fundamental differentiation into Fig. 2.3-2.6, mainly
  - ◇ $s(t)$ (and possibly stagnation),
  - ◇ $\Delta p_{mob}(s)$ (and $\Delta p_{mob}(t)$), especially $\Delta p_{mob,wall}$ and related levels of $f_{s0,wall(s)}$ and $f_{s0,wall(t)}$,
  - ◇ $v_{Darcy}(s)$ (or equally $v_{Darcy}(i)$),
  - ◇ filter cake evaluation (between soil filter and test material)
- V-S: small-size version of V-L without pressure sensors for simplified property variation with the aim of creating a suitability matrix for soil-polymer-additive combinations regarding
  - ◇ $s(t)$ (and possibly stagnation),
  - ◇ $v_{Darcy}(s)$ (and $v_{Darcy}(t)$),
  - ◇ filter cake evaluation (between soil filter and test material)
- H-P: vertical earth wall with horizontal penetration and direct contact between supported soil and fluid to verify whether the processes found in V-L and V-S can really be transferred to this case regarding
  - ◇ cumulated outflow $\sum m(t)$ (and possibly stagnation),
  - ◇ direct filter cake evaluation
- H-R: radial penetration with susbequent concreting to compare the filter cakes before (V-L, V-S, H-P) with the case after concreting

Table 3.1.: Comparison of testing devices for fluid penetration

	V-L	V-S	H-P	H-R
Direction of flow	Vertical (1D)	Vertical (1D)	Horizontal (1D/2D) [b]	Horizontal (2D: radial) [b]
Soil-fluid contact [a]	Indirect (↑),	Direct (↓), indirect (↑)	Direct	Direct
Pressure difference [bar]	0.15-0.7 (with air cushion)	0.15-0.7 (with air cushion)	0.025 (purely hydrostatic)	0.125 (purely hydrostatic)
Soil collapse possible	No	No	Yes [c]	Yes [c]
Inflow cross-section [cm^2]	315 (circular)	12 (circular)	380 (rectangular)	4200 (cylindrical)
Soil mass [kg]	12-50	0.1	75	2000
Fluid volume [L]	8-16	1-2	12-20	100-200
Max. penetration depth [cm]	90	5	50	35-80
Measured parameters	Outflow/time, interface at filter, P drop curvature	Outflow/time, interface at filter	Outflow/time, interface before concreting	Outflow/time, interface after concreting

[a] Direct fluid-soil contact or indirect via filter (sieve or grains)

[b] Secondary vertical penetration is possible

[c] With stabilizing arching effects from geometry and boundary conditions

V-L

The setup of the main testing device (V-L) (Fig. 3.1) is designed at allowing the analysis of the time-dependency of penetration and related pressure distribution for one-dimensional flow into the void fixed soil matrix (i.e. unable to collapse) of defined compactness for a soil element with a maximum penetration depth of ca. 90 cm which has been regarded as a sufficiently large depth with respect to an economical fluid consumption. In this respect, it is similar to the device presented in Lesemann, Vogt, and Pulsfort (2016) with the primary difference that V-L is designed to enable upwards flow needed to avoid favourable effects from sedimentation of not perfectly suspended fines within the support fluid on pressure and penetration development, which could not take effect at a vertical earth wall (horizontal flow) or at the top of the annular gap (upwards flow).

In this respect, the experimental testing regime focusses only on homogeneous soils with evenly distributed density, as inhomogeneity is considered subordinate for an investigation aiming at an overall better understanding of polymer-soil interaction. Consequently, the penetration of the support fluid into the soil will primarily follow the direction of an applied overpressure, i.e. perpendicular to the earth wall. If it is further assumed that fluid penetration depths have to remain low for successful fluid support to be realized at an economical scale, a plane experimental

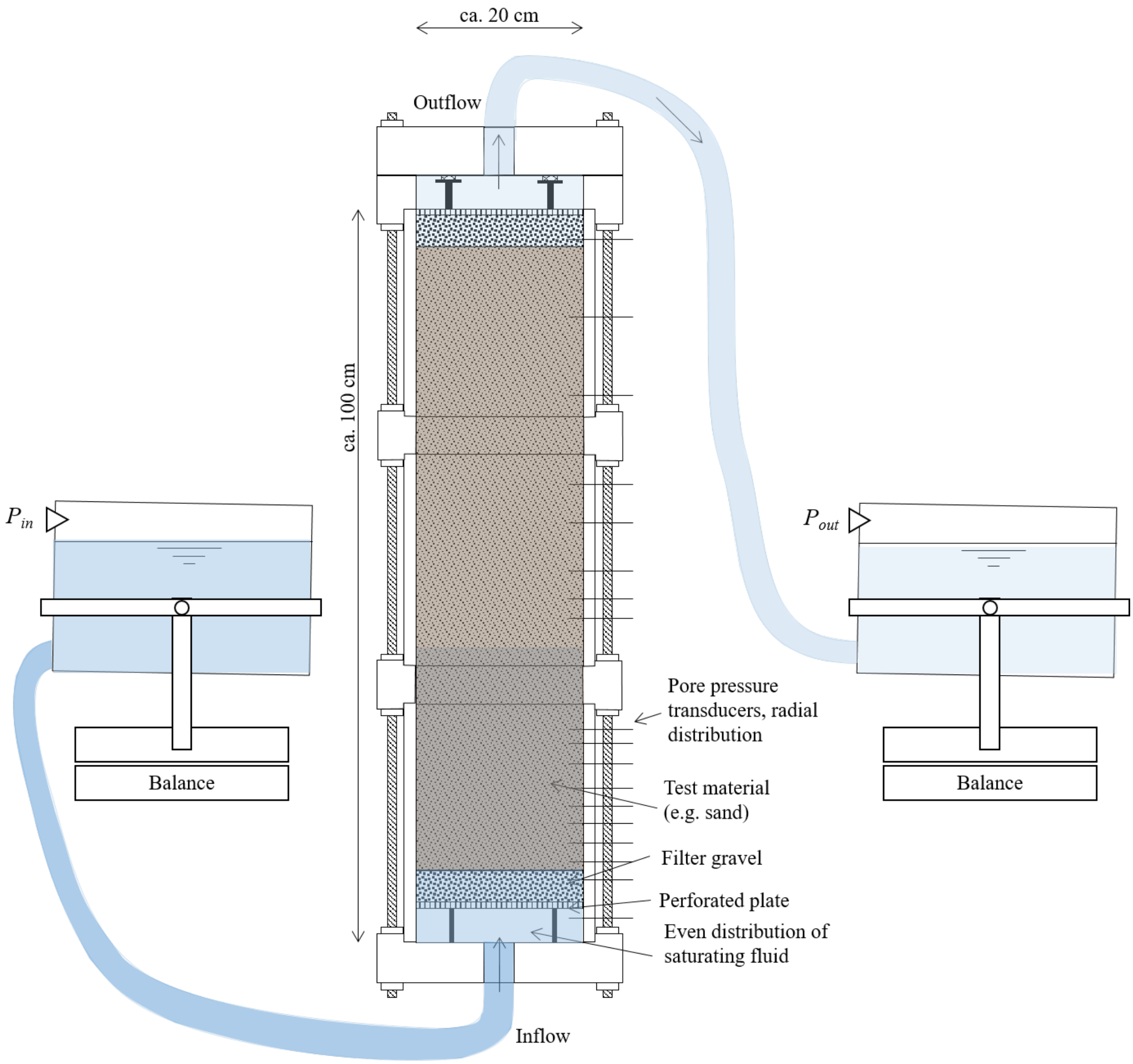

Figure 3.1.: Vertical fluid penetration test with pore pressure measurement (V-L)

model with one-dimensional flow can be considered sufficiently accurate even for the reflection of radial (pile, pipe) or spatial penetration (excavation corners) and related pressure drop as long as the penetrated depth into the soil is small relative to the circumference of the supported geometry.

The primary testing device (V-L) consists of a cylindrical container of transparent acrylic glass ($d = 20$ cm) with 1-3 elements in height ($h \approx 40/70/100$ cm) filled with soil material air pluviated at high compaction. In the case of sand, the soil material is placed by means of a travelling air pluviator, here more precisely consisting of a hopper with a tilted and constricted opening of grain-size-specific diameter ($d \leq 1$ cm) connected to a rigid tube ($d/h = 3/50$ cm) with smooth surface to spread the sand particles without significantly reducing the fall velocity. A perforated plate with a clear space towards inflow/outflow pipes, combined with filter gravel or a sieve for finer soil material, is used as an upper and lower fixation and to ensure vertically uniform flow conditions. Soil filters are designed according to the Terzaghi filter criteria to ensure mechanical stability (Eq. 2.24) and drainage without creating a pressure boundary (Eq. 2.25). Pressure transducers are distributed along the height to measure the pore pressure over time and to verify that the boundary conditions (filter material, constrictions) do not affect the pressure development. Permanent weighing of inflow and outflow allows a calculation of penetration rates based on the known soil porosity and the assumption of an even penetration distribution over the soil cylinder cross-section. Prior to testing, the soil material is fully saturated with water, with valves positioned above every sensor and at the top of the cylinder enabling the release of air which could impede pore pressure and penetration measurements.

Water penetration tests are then performed at two pressure levels for pore pressure sensor calibration and for soil permeability determination. Penetration is performed upwards for all tests and is regulated by constant air pressure[1] for each penetration test from the inflow container (p_{in}) with reference to a fixed outflow pressure ($p_{out} = 0.4$ bar).

The resulting air pressure differences $\Delta p_{air} = p_{in} - p_{out}$ for water penetration testing are $\Delta p_{air,1} = 0.10$ bar and $\Delta p_{air,2} = 0.15$ bar for standard soil material (medium grained sand) and $\Delta p_{air,1} = 0.05$ bar and $\Delta p_{air,2} = 0.10$ bar for soil of higher permeability. The influence of a change in hydrostatic pressure within the fluid containers is minimised to a maximum of 15 cm between p_{in} and p_{out} with a maximum flow volume of 16 l by horizontal positioning of the cylindrical fluid containers.

Subsequently to water penetration, the fluid in inflow container and pipe is replaced by polymer solution. Polymer fluid penetration is performed at $p_{air,1} = 0.15$ bar for a duration of approx. 24 hrs or until nearly full consumption of the inflow volume (16 l) and is supplemented by a stepwise increase in air pressure difference $p_{air,2-5} = 0.30/0.50/0.70$ bar for an evaluation of the influence of higher pressure levels[2].

With respect to the interpretation of the hereby acquired test results, the following factors are considered:

- frictional head losses along the inflow and outflow pipes and at connection points (constrictions, e.g. from filter),
- the accuracy of the weight and pressure measurements and
- soil and support fluid variability during placement and mixing.

Fluid bulk rheology (Marsh funnel & rheometer), soil porosity n and soil water permeability coefficient k_W of the soil are determined for every individual test to take into account material variation. The inflow and outflow containers are placed centrally and in a level position on large platform balances which register changes with an accuracy of ±20 g (technical data sheet) equal to ±1.7 mm of even penetration depth within the test material for an exemplary porosity of $n = 0.38$. Air pressure regulation in the fluid containers is controlled by manometers with a maximum error of ±0.004 bar (technical data sheet).

Screw sensors with an external ceramic membrane (contact surface 8 mm) suitable for viscous liquids are chosen as pressure transducers with an accuracy < 0.5 % relative to the maximum pressure. Seven sensors with a maximum pressure of 1 bar (maximum error ±0.005 bar) are distributed along the soil cylinder with one transducer placed at each end of the soil column within the filter material or immediately outside the perforated plate and one < 3 cm into the test material, i.e. immediately behind the interface, to control the pressure boundary conditions. Up to five sensors of lower accuracy, i.e. 3x 2.5 bar (maximum error ±0.0125 bar), 1x 4 bar (maximum error ±0.02 bar), 1x 10 bar (maximum error ±0.05 bar), are added depending on

---

[1] Pressure values are always given as relative to the atmospheric pressure.

[2] The last pressure step is applied by adjusting the lower air pressure boundary.

the number of additionally available slots/cylinder elements used. The sensors are connected to the soil-containing cylinder by pipes separated by sieves with passage diameters exchangeable with respect to the individual tested soil to fixate the grains, but to equally allow relatively undisturbed pressure transmission between soil pore fluid and water within the pipes towards the sensor membranes.

The analogue signals from pressure sensors and balances are recorded with a sample rate of 0.5 Hz by means of two A-D converters. Frictional head losses were tested with the small test unit ($h \approx 40$ cm) and new 1 bar sensors before the first soil test with purely water-filled cylinders and were found to be negligible for the targeted pressure difference range. A subsequent water penetration test with soil confirmed a linear pressure drop along the saturated soil test material with reference to the pressure levels applied from the fluid containers. Consequently, a linear pore pressure drop based on the manometer values in combination with water head levels from the first water penetration step (1) of every test was chosen as a target distribution for pore pressure sensor data calibration for each following individual test to ensure a continuing accuracy of the sensor output.

V-S

The second testing device (V-S) (Fig. 3.2) for parameter variation is designed as a small simplified representative of the V-L test. A small cylinder ($d = 4$ cm) containing soil of $h_{soil} = 5$ cm is connected to a fluid container (2 L), both made of transparent acrylic glass. Penetration can be performed with upwards (support fluid with load) or downwards (pure polymer solutions) flow depending on the point of connection of the the fluid supply with the soil cylinder. Soil placement by air pluviation and soil fixation by means of perforated plates, sieves or soil filter material are applied the same ways as for V-L.

The pressure difference is generated from a hydrostatic head difference between inflow fluid level and outflow position in addition to air pressure regulation within the fluid container con-

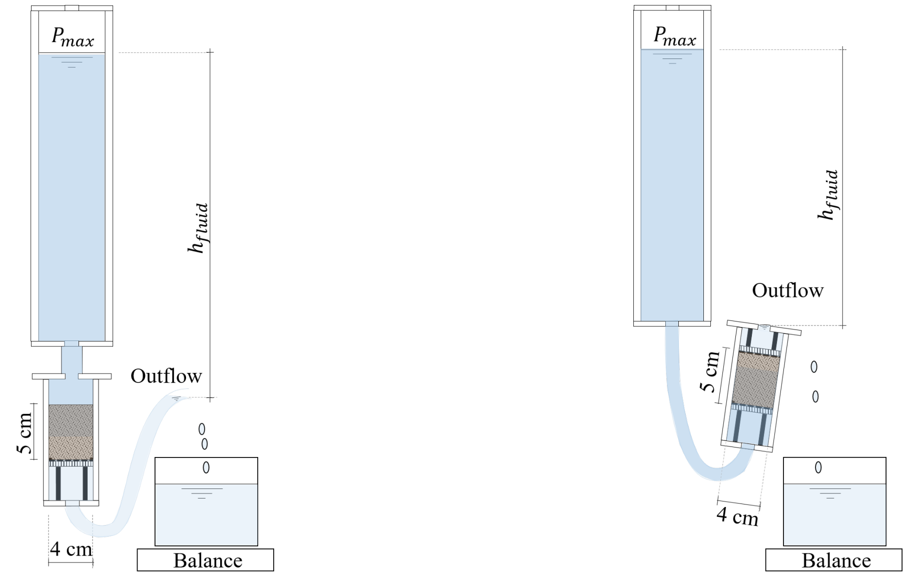

(a) Downwards flow

(b) Upwards flow

Figure 3.2.: Small-scale vertical fluid penetration test (V-S)

trolled by a manometer with a maximum error of ±0.0125 bar (technical data sheet). Air pressure is continuously regulated during the test to balance hydrostatic head losses within the fluid container targeting $\Delta p = const.$ throughout the measurement resulting in an additional error from manual readjustment estimated at ±0.003 bar. Support fluid bulk density as a basis for the determination of the hydrostatic fluid head is conservatively considered as $\rho_F = \rho_W = 1$ g/cm^3 (at ca. 20 °C room temperature), i.e. the not easily quantifiable effect of loaded fines due to sedimentation effects is ignored. Fluid bulk rheology (Marsh funnel & rheometer) is determined for every test.

Following V-L, support fluid penetration tests are performed after saturation with water at $\Delta p = 0.15$ bar and in selected cases for different pressure levels. For upwards flow, the support fluid is filled into fluid container and supply pipe. For downwards flow, the support fluid is carefully filled onto the saturated soil and subsequently connected to the fluid supply. Water penetration tests at lower pressure level are not performed prior to every polymer penetration test as with V-L due to higher repeatability of similar soil samples, but soil permeability is controlled with respect to reproducible porosity values. Penetration is conducted until emptying of the fluid supply or with a minimum duration of 30 min until visual stagnation or relatively stationary flow conditions are reached. The outflow rate is recorded at sample rates starting at 0.1-0.5 Hz by means of table balances with a maximum error of ±0.1 g with an open collecting vessel. Evaporation from the collecting vessel needs to be taken into account for low outflow rates.

Time-dependent fluid penetration depths calculated based on penetration rates measured over time with this device overestimate V-L penetration due to a possibly higher applied earth wall gradient $f_{s0,wall,VS} \geq f_{s0,wall,VL}$ for a given pressure difference $\Delta p = const.$ once the outflow volume $\sum V_{out,VS}$ exceeds the total sample pore volume $V_{0,VS}$ as no further friction mobilization for > 5 cm can be taken into account. The obtained values are consequently categorized as a comparably safe-side result. The deviation is smaller in soils where the pressure drops 'under-linearly' along the penetration depth, which is the assumed curvature for polymer solutions. Besides, with respect to adsorption or filtration mechanisms and given a soil of evenly distributed density, the first few cm from the earth wall represent the pressure-penetration-governing soil fraction, i.e. area of lowest permeability.

H-P

The third testing device (H-P) (Fig. 3.3) is designed as a plane horizontal penetration model with direct fluid/soil contact. It consists of a box of transparent acrylic glass (width $d = 20$ cm) with three rigid separating plates as soil boundaries, one of which perforated and covered with a wire mesh, and the third as a support fluid boundary. The soil material is air-pluviated up to a height of ca. $h_{soil} = 40$ cm. Ballast (approx. 1.4 kPa) is added to prevent the soil from uplifting during subsequent soil saturation and support fluid penetration. The initially dry soil material is fully saturated at first, then the water level is lowered to its final level of $h_W = 27$ cm. This minimum moisture content above the water level is chosen to reduce capillary effects promoting secondary (vertical) penetration. Support fluid is then filled between the two impermeable separating plates up to $h_F = 52$ cm creating a pressure difference of approx. $\Delta p = 0.025$ bar.

Penetration starts with lifting of the central vertical plate. The final position is reached within ca. 10 sec creating an inflow cross-section of 19 cm x 20 cm. A water-filled chamber with water head h_W adjacent to the soil, separated by the perforated plate, ensures primarily one-dimensional horizontal outflow conditions for the tested soil and enables a visual control of this head. Outflow is allowed by means of tubes discharging into a collecting vessel (possible

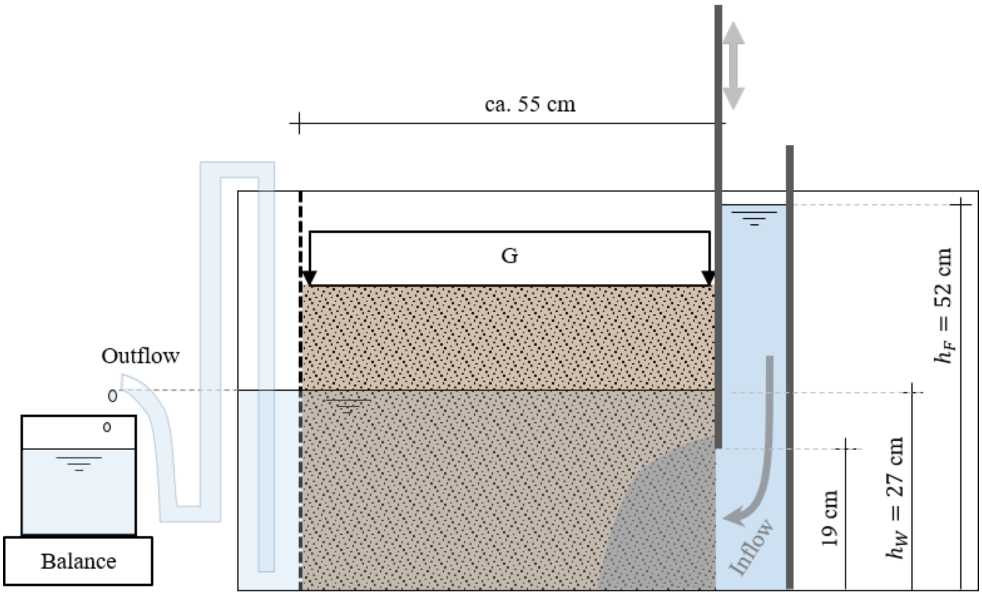

Figure 3.3.: Horizontal plane fluid penetration test (H-P)

evaporation) placed on a table balance. Outflow masses are recorded for a duration of max. 24 hrs with sample rates starting at 0.1-0.5 Hz with a maximum balance error of ±0.1 g. The support fluid head is kept constant by careful refill towards the back plate (to reduce the impact of related turbulences on the earth wall stabilized at this low pressure level) with a maximum deviation from the targeted fluid head h_F of 2 cm.

If the soil has not collapsed during penetration, the soil is drained afterwards and a possible filter cake formation at the earth wall can be visually evaluated after slow lowering of the upper fluid pressure by lifting of the second separating plate. A visual penetration development can be monitored at the acrylic glass walls over time in certain cases (e.g. with a significant amount of loaded fines clouding the otherwise relatively transparent polymer solution). This visually measured penetration distribution may surpass the average penetration within the soil due to the smooth and even surface of the acrylic glass, especially for coarser soil grain fractions.

H-R

Fig. 3.4 shows the fourth testing device (H-R) with the largest open earth wall segment targeted at creating a model concrete pile. It is designed similarly to H-P, but with a cylindrical earth wall, i.e. radial penetration, with two-directional permeation and outflow and higher Δp. Moreover, unlike H-P, the significantly larger soil volume necessary for H-R is placed in layers (ca. $d =$ 20 cm) around a previously installed central metallic pipe ($h = 120$ cm) and compacted after each layer placement by means of external vibrators. The pipe is filled up to $h_{F,start} = 115$ cm ($\Delta p_{start} = 0.065$ bar) with support fluid when it is pulled upwards and gradually filled with more fluid until the final position ($\Delta p = 0.125$ bar) is reached (total duration ca. 30 sec). A constant fluid head is controlled by continuous refill (max. 200 l).

If the earth wall does not collapse, the penetration continues for approx. 24 hrs and is followed by concrete placement by means of the tremie method. A container connected to flexible tubes is fixated at the top of the metallic fluid-containing pipe to lead away the support fluid displaced from insertion of tremie pipe and fresh concrete filling. A balloon is used to separate support

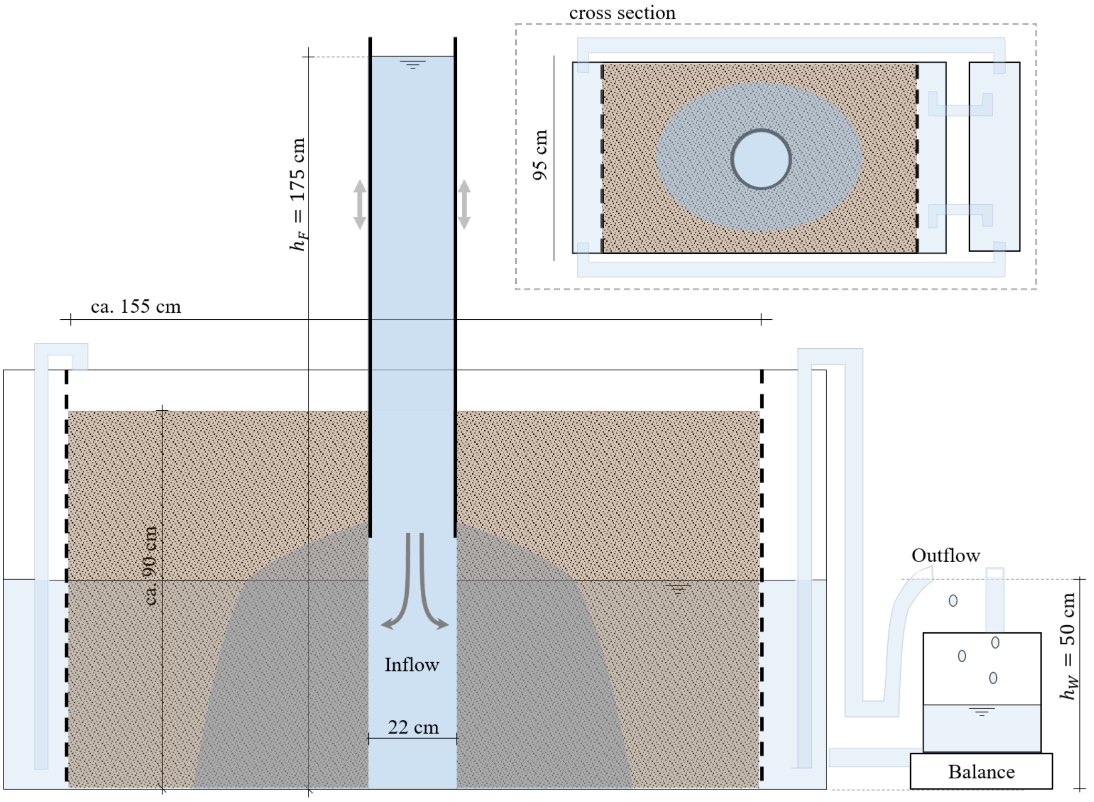

Figure 3.4.: Horizontal radial fluid penetration test (H-R)

fluid and fresh concrete in the tremie pipe ($h = 200$ cm, $d = 10$ cm, polypropylene). The balloon is deflated and pulled once the concrete has reached the container bottom. Concrete is placed at a concrete head of $h_c = 195-225$ cm during pull and refill cycles lowering down to $h_{c,end} = 98$ cm for the last interval.

An ordinary self-compacting, flowable tremie concrete (0/16 mm) for bored piles is chosen with a mix design in accordance with EN 206:2017 with consistency control based on slump flow spread testing (appendix B.3).

After a minimum of 24 hrs of concrete hardening, the surrounding soil is carefully removed to reveal the concrete-soil interface for visual study.

3.1.2. Setup for fluid preparation

Viscous base fluid

With respect to preparation of the viscous base fluid, three mixing techniques have been tested by means of rheometer and Marsh funnel tests and revealed to produce repeatable results. They are therefore used interchangeably for all performed tests.

(1) 60 min mechanical stirrer at max. 500 rpm with straight paddle (powder sprinkled within the first 10 min)

(2) 10 min magnetic stirrer (powder sprinkling & hydration) plus 50 min mechanical stirrer at max. 500 rpm with straight paddle (dispersion)

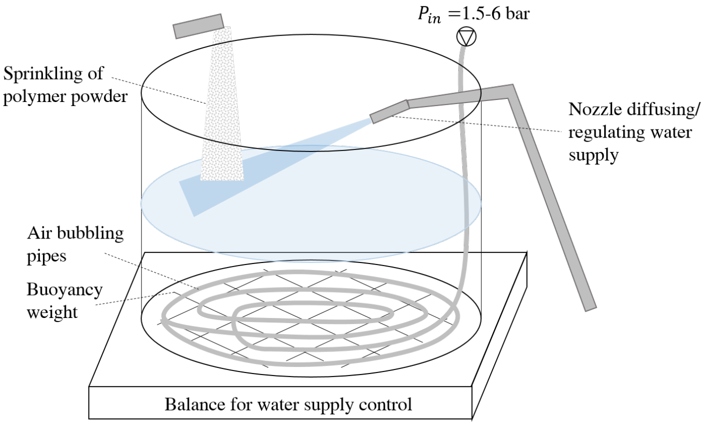

Figure 3.5.: Fluid mixing device for larger volumes

(3) Powder sprinkling on jet of water plus 60 min air bubbling for dispersion (two container sizes: <20 l or <200 l) (Fig. 3.5)

The more viscous solutions are mixed at least a few hours before usage to provide additional time for dispersion, especially for larger fluid volumes, as longer and more complex polymer chains take more time to dissolve in solution. The air bubbling pipes used for technique (3) are removed from the fluid container for this period to allow the air bubbles to dissipate and to disperse partly hydrated polymer from the container bottom. The usability time span for different types of polymers in solution is analysed in more detail in section 3.2.

As the synthetic polymer products have revealed a dependency of resulting maximum viscosity levels on the powder granule size distribution during testing at low fluid volumes ($\leq$ 2 l), these products are mixed according to a fixed granule size distribution for fluid volumes up to 20 l.

Addition of pore blockers

Larger mineral grains ($d \geq 0.125$ mm) are carefully sprinkled dry into the ready-made viscous fluid and mixed by means of a whisk or a straight paddle (mechanical stirrer) until maximum dispersion is reached. The influence of mixing on the settling behaviour of the grains especially for the flexible and large chains of dissolved AN-H is displayed in Fig. 3.6. The smallest quartz grains ($d < 0.125$ mm) are mixed into the support fluid after prior dispersion in a small portion of water (50 % w/w) for improved and simplified dispersion especially with long-chain viscosifiers. The effect of dry mixing compared to solution mixing for AN-H and CMC-H is shown in Fig. B.2 (appendix).

Bentonite is introduced into the fluid in the form of a suspension in equal parts. That is, bentonite powder (IBECO B1) is dispersed separately at double concentration (10 g/l [3]) at 10'000 rpm (UltraTurrax) for 5 min, led to hydrate for a minimum of 12 hr and subsequently mixed into polymer solution at a ratio of 1:1, e.g. AN-H at 0.75 g/l plus B at 10 g/l at 1:1 result in 'AN-H 0.375 + B 5'. This leads to a slightly lower proportion of water within the mix as compared to a pure AN-H 0.375 g/l mix, firstly owing to the bentonite volume fraction, secondly due to the lower degree of free water available for polymer hydration as a result of the electric layers created around the clay particles.

---

[3] Mass of bentonite with respect to suspension volume

(a) No mixing – $\Delta t = 40$ sec (b) Dry mixing – $\Delta t = 10$ min

Figure 3.6.: Influence of mixing of quartz grains (0.125/0.25 mm) with AN-H at 0.75 g/l

The superabsorbing polymer granules are dispersed dry into the viscous solution. The mix is used after a minimum hydration time of 15-60 min sufficient for SAP to fully swell. This is considered a safe-side choice with regard to pore blocking as further swelling within the soil can be considered an even more favourable pore blocking effect as compared to filtration.

3.1.3. Setup for fluid classification

Following sections 2.2.1-2.2.3 and 2.3.3, support fluid characterization and classification is chosen to comprise the following regime:

(1) bulk rheology
  - $\eta - \dot{\gamma}$ relationship (rotational rheometer)
  - outflow rate (Marsh funnel)

(2) colmation and sedimentation
  - density (areometer)
  - visual grain settling speed (cylinder)

(3) stability and clay swelling: water retention (filter paper test)

Rheometer

The testing device chosen for the evaluation of the dependency of shear stress and viscosity on the shear rate is a Haake Rheostress RS600. It is equipped with a double-gap cylinder geometry, i.e., a cylindrical rotor (DG43Ti) and an inner and outer fixed cylinder (DG41). This geometry combines the Searle- and Couette-type measuring systems. The rotor forms the outer boundary for the inner gap (Couette) and the inner boundary for the outer gap (Searle). Further device properties are given in appendix C.1.

The $\tau - \dot{\gamma}$ relationships represent the experimental results obtained from torque measurements (spring) at the rotor head referenced to the sheared surface of the double gap. The viscosity curves for polymer solutions are derived as (Eq. 3.1)

$$\eta_{calc} = \tau_{exp} / \dot{\gamma}_{exp} \tag{3.1}$$

following the power-law model. The tests are performed at controlled shear rate (CR) with τ determined for each shear rate step with gradient control as displayed in Fig. 3.7 until a tolerance of $\frac{\Delta \tau_i}{\tau_i} / \Delta t \leq 0.001$ is reached. Consequently, each step has an individual duration, which can reach around 20 min for high viscosity values at low shear rates.

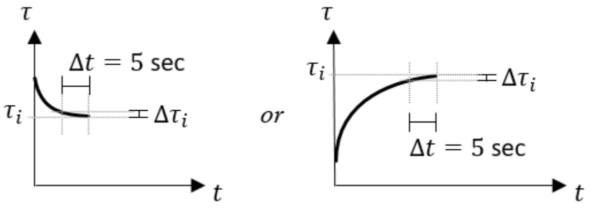

Figure 3.7.: Rheometer equilibrium criterion with CR measurement

The measurements are generally recorded in three stages (if not otherwise specified):

(1) ascending $\dot{\gamma}$ ($10^{-1} \rightarrow 10^3$ 1/s) for even fluid distribution within the testing geometry, important for higher viscosity solutions (e.g. AN-H),
(2) descending $\dot{\gamma}$ ($10^3 \rightarrow 10^{-6}$ 1/s) considered to be related to soil-penetration as encountered at the earth wall with decreasing penetration velocity and
(3) ascending $\dot{\gamma}$ ($10^{-6} \rightarrow 10^3$ 1/s) for possible deviations at low shear after rheometer acceleration.

The measurement output directly obtained from the rheometer ('raw output') is cleared before usage with reference to a $\eta - \tau$ measurement range specified by the manufacturer for the used shearing geometry, as displayed in appendix C.1. Subsequently, the measurements of solutions at lower viscosities are further cleared from deviations at η_{max} plateau level. This measurement point clearing is graphically explained in appendix C.2.

Marsh funnel

The Marsh funnel test (Fig. 2.21b) is performed according to DIN 4127:2014. The outflow time is recorded at 1000 ml and 1500 ml ($t_{M,1000}$ and $t_{M,1500}$) at room temperature (ca. 20 °C). The Marsh values given in the following experimental investigation always refer to $t_{M,1000}$ as this value was found to be the representative parameter. The outflow time in seconds is named 'funnel viscosity' according to API RP 13D:2017.

Areometer

Grain suspendability or sedimentation speed is assessed by means of a Bouyoucos-Casagrande areometer in accordance with EN ISO 17892-4:2017 for fluid densities in the range of $\rho_F = 0.995$–1.03 g/cm^3. The areometer (or hydrometer) interpretation gives a density-time relationship based on buoyancy, which can be associated with a settling velocity following Stokes' law. In contrast to the EN ISO 17892-4:2017 method, in this case, the settling grain sizes are known, the target values are the density development over time and an associated average settling velocity of the grains. 40 g/l of grains are thereby mixed into 1.50 l of polymer solution ($\rho_{mix,start} = 1.025$ g/cm^3) until the grains have reached maximum dispersion. Subsequently, 1 l of this mix is inserted into a cylindrical container as shown in Fig. 3.8, the areometer is quickly placed into the mix and the relative density drop is recorded over time.

Filter paper test

The filter paper test applied here is adapted from the mud testing ring according to the technical guideline DVGW W 116:2019 for drilling fluids (Fig. 2.20b). The filter test consists of a cylindrical

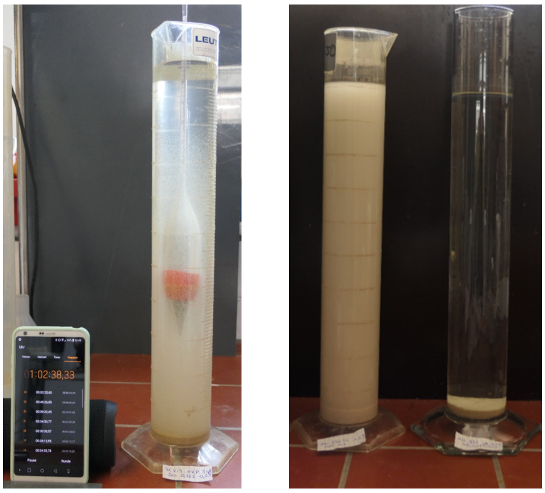

Figure 3.8.: Areometer test

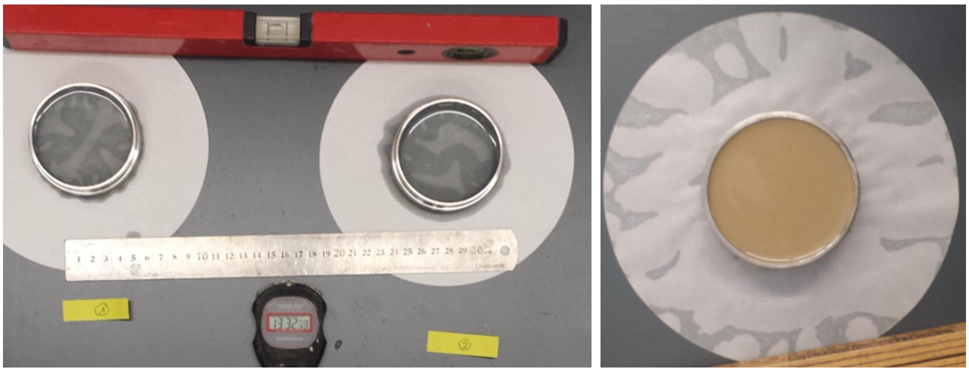

Figure 3.9.: Adapted filter test

ring (h = 2 cm, d = 7 cm) placed on regular filter paper (d = 18 cm) also used for Proctor compaction testing and filled with the test solution. The saturation propagation of the filter paper outside the ring is measured over time. In contrast to the test as described by DVGW W 116:2019 and Buja (2009) and Mielenz and Mielenz (2016), the filter paper has a larger diameter allowing a broader range of time-dependency evaluation of the filter saturation propagation which is not intended in the original test. The weight of the metallic ring is considered high enough to ensure that the fluid cannot leave the cylinder boundaries without separating. It is manually ensured during the test that the filter paper is firmly placed on a smooth base plate, so that fluid cannot accumulate between filter paper and plate without visible saturation.

DVGW W 116:2019 defines a limit criterion of >1000 s for the full hydration of the filter paper with their test, which can be reformulated to a propagation of 7.5 cm within ca. 17 min. Fluids matching this criterion are considered applicable for swelling inhibition and for sealing the ground by means of a thin polymeric filter cake according to this guideline. No properties are given for the suction capacity of the used filter paper.

3.2. Material characterization

3.2.1. Soil characteristics

The soil material classified in Fig. 3.10 and Tab. 3.3 is chosen to provide a range from low to high permeability non-reactive soil material. A more detailed evaluation of narrow soil fractions in the context of V-S soil penetration testing comprises soil fractions sieved from the same soil material as listed in Tab. 3.2. The same material is used as soil filter base for testing devices V-L and V-S according to the Terzaghi filter criteria (Eq. 2.24 & 2.25).

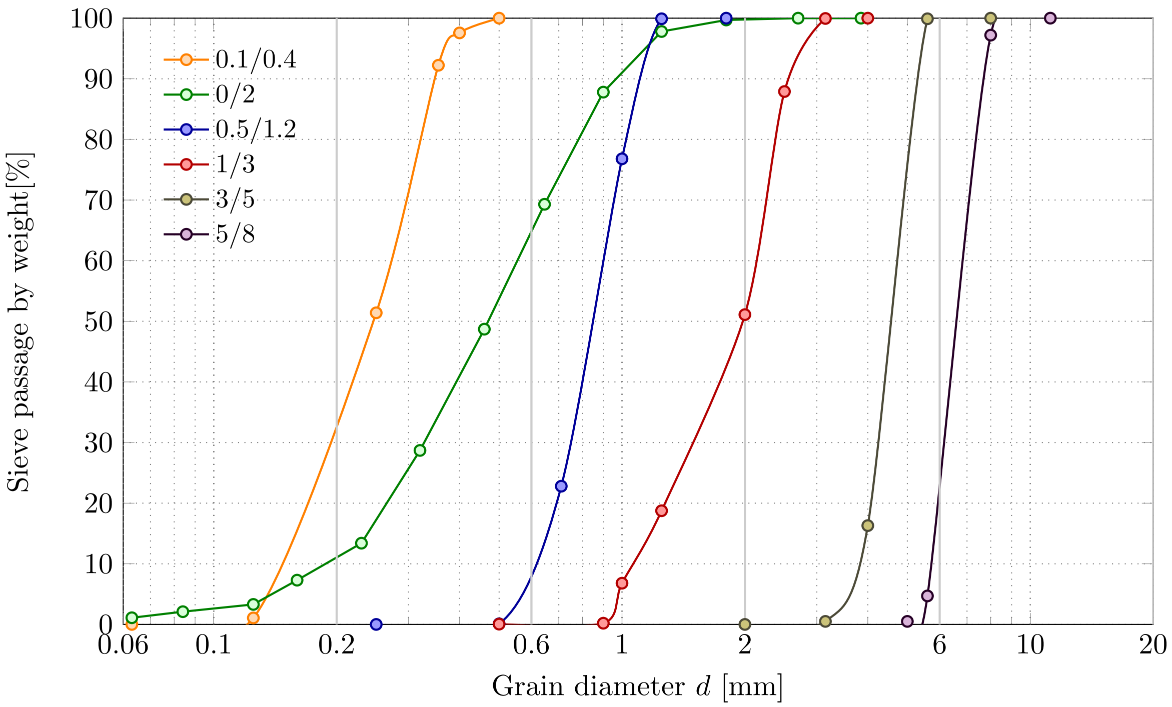

Figure 3.10.: Grain size distribution of soil test material

Table 3.2.: Soil fraction properties

Fraction [mm]	Name as additive	Type	Sieved from
0/0.125	S_{XS}	Quartz	-
0.125/0.25	S_S	Quartz	0.1/0.4
0.4/0.5	S_M	Rhine sand	0/2
0.71/1	S_G	Quartz	0.5/1.2
1.6/2	S_L	Quartz	1/3
2.8/4	-	Quartz	3/5.6
5.6/6.3	-	Quartz	5.6/8

Table 3.3.: Soil test material properties

		0.1/0.4	0/2	0.5/1.2	1/3	3/5.6	5.6/8
Type		Quartz	Rhine sand	Quartz	Quartz	Quartz	Quartz
d_{10} a)	[mm]	0.15	0.20	0.59	1.07	3.66	5.74
d_{50} a)	[mm]	0.25	0.45	0.86	1.97	4.64	6.78
C_U a)	[-]	1.8	2.7	1.5	2.0	1.3	1.2
$k_{w,Hazen}$	[m/s]	$2.3 \cdot 10^{-4}$	$4.9 \cdot 10^{-4}$	$3.8 \cdot 10^{-3}$	$1.2 \cdot 10^{-2}$	$1.5 \cdot 10^{-1}$	$3.7 \cdot 10^{-1}$
$k_{w,exp}$ b)	[m/s]	$1.7 - 1.8 \cdot 10^{-4}$	$4.3 - 8.5 \cdot 10^{-4}$	$1.8 - 2.1 \cdot 10^{-3}$	-	$1.2\text{-}4.1 \cdot 10^{-1}$	-
ρ_k c)	[g/cm^3]	2.65	2.65	2.65	2.65	2.65	2.65
$\rho_{d,exp}$ b)	[g/cm^3]	1.67-1.68	1.66-1.68	1.65-1.66	1.63	1.59-1.61	1.56-1.60
n d)	[-]	0.37	0.37	0.38	0.38	0.39-0.40	0.4-0.41

a) $d_{10}/d_{50}/d_{60}$ grain diameters at 10/50/60 % sieve passage, $C_U = d_{60}/d_{10}$

b) experimental values from V-L tests: hydraulic conductivity $k_{w,exp}$ and dry density $\rho_{d,exp}$

c) Grain density

d) Porosity $n = 1 - \frac{\rho_{d,exp}}{\rho_k}$

3.2.2. Viscosifier properties and bulk rheology

Tab. 3.4 summarises the chosen range of polymer products and related concentrations. They are named according to Tab. 2.2. The concentration ranges were selected as upper and lower boundaries on the basis of manufacturer recommendations. Specific boundary conditions on construction sites, e.g. regarding mixing water and ground water chemistry, may, of course, require higher or allow lower concentrations in practice.

The bulk rheology values (Marsh outflow time and rheometer viscosity) from Tab. 3.4 give an overview on the whole range of tested material as influenced mainly by environmental conditions (e.g. solvent type, different supply charges, storage conditions etc.) encountered during the time span of usage, not by variability due to preparation. This will be further evaluated below.

CMC-H and XAN are Clariant products (SC VIS HVP; SC XGUM). The AN- range of pure copolymers of acrylamide and acrylate covers a variation in molecular weight (AN-H – AN-M – AN-S) at medium anionicity and a variation in anionicity at medium molecular weight (AN-MH – AN-M – AN-ML) and is provided by SNF (e.g. Floset CE 130 XF 35). ANmix is a synthetic product mix available under the name SlurrySMART by KB International combining a viscosifier and a defined combination of additives from the SlurryPro CDP product range. According to its material data sheet, it contains a sodium acrylamide-acrylate copolymer (AN) (referred to

Table 3.4.: Characteristic properties of the used viscosifiers

	Polymer		... in solution	
	Molecular weight [Da] a)	Anionicity [%] b)	Concentration [g/l]	Marsh time at 1 l [sec]
CMC-H	unknown	unknown	5.00	84-93
			2.50	49-52
XAN	unknown	unknown	2.50	49-52
			1.50	41-43
AN-H	$22 - 27 \cdot 10^6$	30	1.50	140-290
			0.75	105-115
AN-MH	$7 - 12.5 \cdot 10^6$	70	1.50	80-84
			0.75	60-62
AN-M	$14 - 16 \cdot 10^6$	30	1.50	85-95
			0.75	65-68
AN-ML	$10 - 14 \cdot 10^6$	5	1.50	50-52
			0.75	44-46
AN-S	$5 - 7.5 \cdot 10^6$	30	1.50	48-56
			0.75	44-50
ANmix	unknown	unknown	1.50	135-295
			0.75	105-115

a) manufacturer info

b) $\eta_{0.001}$ and η_{10} represent the viscosity values at $\dot{\gamma} = 0.001$ 1/s and $\dot{\gamma} = 10$ 1/s, respectively as 'polyacrylamide') and a hydrophobically modified polymer and other products not further classified. The description of the predecessing product Slurryshield PBS also listed carboxylated vinyl polymers and a blend of alkaline salts as additives. Lam and Jefferis (2018) state that the product contains hydrophobically modified cellulose ether and CMC.

Hereinafter, bulk shear stress and viscosity characterization is differentiated into boundary effects (mixing variability, environmental conditions, measuring technique) and polymer property variation (concentration, molecular weight, etc.).

Boundary effects

The following aspects are taken into consideration as boundary conditions with respect to their influence on bulk rheology for each polymer type:

- variability of individual mixes (Fig. 3.11)
- environmental conditions (Fig. C.4)
  - type of solvent (effect of dissolved ions)
  - solvent pH
  - viscosifier supply charge
  - viscosifier storage conditions
  - (viscosifier grain size distribution of the dry granules, addressed in appendix C.4)
  - viscosifier degradation in solution
- measuring technique (Fig. C.7-C.8)
  - shear history and direction of shear rate steps (increasing vs. decreasing)
  - thixotropy and yield strength
- testing device precision (Fig. C.7-C.8 and section C.2)

The influence of these boundary conditions on bulk rheology is further elaborated in appendix section C.3. Some main aspects are briefly addressed here.

Most fluid classification as well as fluid penetration tests described in the following paragraphs and sections (with the exception of some early tests) have been performed with base polymer granules (viscosifiers) dissolved in Wuppertal tap water (tw) because dissolved ions are present in most mixing waters at construction sites and because of easier handling with large fluid consumptions. Important properties of Wuppertal tap water have been determined as follows:

- electric conductivity: 160-220 μS/cm at 22 °C,
- pH: 7-7.5,
- viscosity at 20 °C: 0.001 Pa·s (20 °C).

As not only the type of solvent, but also storage conditions, age and supply charge were found to have a pronounced (though not totally behaviour-changing) impact on the bulk rheological results, tests with specific property variations were performed preferably with the same solvent and within a narrow time span of $<$3 days.

The following figures primarily show rheometer results in the form of $\tau - \dot{\gamma}$ or $\eta - \dot{\gamma}$ relationships from a stepwise descent in shear rate as described in section 3.1.3. The descending stage is chosen as it is most closely related to the soil penetration with decreasing flow velocities.

In some cases, the bulk rheology curves of the tested polymer solutions are compared to exemplary curves of bentonite suspensions at 40 g/l or 60 g/l for reference. In contrast to polymer viscosity obtained from $\eta = \tau / \dot{\gamma}$ (power law), the viscosity values of the bentonite suspensions are calculated from experimental results based on a Bingham approximation ($\eta = (\tau - \tau_0)/\dot{\gamma}$) as further explained in appendix C.5.

Fig. 3.11 shows a first comparison of four distinct polymers for the upper polymer concentration in solution for each polymer type, i.e. as an upper viscosity boundary, compared to bentonite curves. The respective Marsh outflow times at 1 l are given in brackets (in sec). The curves represent individual mixtures prepared at different dates over a time span of max. two months and are chosen to reflect representative deviations between individual mixes. The displayed range

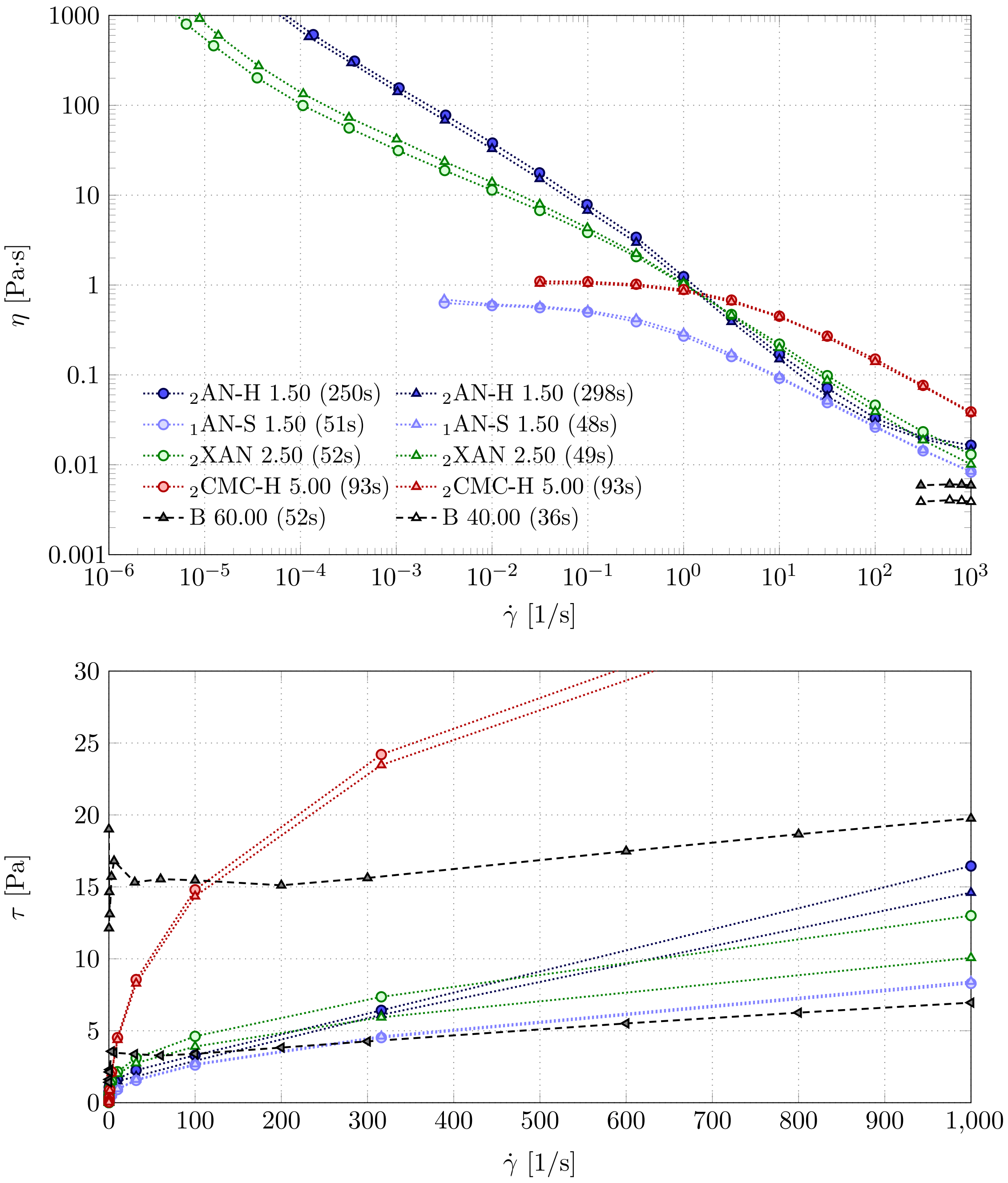

Figure 3.11.: Mixing influence – rheometer vs. Marsh funnel (solvent: tw)

of deviations is considered insignificant. Aside from the mixing techniques, deviations displayed here can also be a result of small inhomogeneities within a fluid as the rheometer measurements require only a small fluid volume for testing (11.5 ml).

As a first display of bulk rheology results, these curves will also be used both as a basis for comparison of the general flow behaviour of different polymer types with reference to bentonite suspensions and as comparability basis between rheometer and Marsh bulk rheology characterization.

Fig. 3.11 (top) already reflects the distinct shear-thinning characteristic of polymer solutions developing through reaction of the polymer chains towards movement ('Strukturviskosität'): the viscosity curves (Fig. 3.11 top) follow a nearly straight line in the double-logarithmic plot within a range of $\eta = 0.01$ Pa·s at high shear rates up to $\eta > 1000$ Pa·s at low shear rates in comparison to comparably negligible viscosity values of the bentonite examples ranging around $\eta = 0.001 - 0.01$ Pa·s. While XAN and AN-H span the whole viscosity range, CMC-H and the short-chain synthetic representative AN-S reveal a lower Newton plateau formation around $\eta \approx 1$ Pa·s at shear rates below $\dot{\gamma} \approx 1$ 1/s and $\dot{\gamma} \approx 10^{-1}$ 1/s, respectively.

The shear stress plot (Fig. 3.11 bottom), however, ranges most of the polymer curves in the lower shear stress range with values around $\tau < 10$ Pa at $\dot{\gamma} < 500$ 1/s, except for CMC-H, which can be explained by the different concentrations in solution. In comparison to the exemplary bentonite suspensions, it is clearly visible that shear resistance mobilization with polymer solutions highly depends upon movement, while the bentonite suspensions show a shear stress plateau at low shear rate visibly independent of shear rate (yield strength) and only slightly increased by a viscosity component.

With respect to a comparison of rheometer to Marsh funnel results, it can be noted that the short-chain synthetic representative AN-S show similar viscosity ranges at higher shear rates as well as similar Marsh values. However, this relation cannot be transferred to CMC-H, the bentonite representative B 60 and especially not for AN-H, neither in the viscosity nor in the shear stress plot, as CMC-H shows the highest values in all plots and AN-H vs. AN-S and especially AN-H vs. XAN show comparable rheometer viscosity values at high shear rates, but distinctly different Marsh values.

It is plausible that both testing devices cannot immediately reflect the shearing behaviour of the polymer fluids in a soil matrix, with the rheometer results possibly being closer related due to the more narrow shearing gap.

Property variation

Polymer property variation in the context of bulk rheology classification is evaluated hereinafter with respect to:

- concentration (Fig. 3.12-3.15)
- molecular weight at medium anionicity (Fig. 3.14a & Fig. 3.15a)
- anionicity at medium molecular weight (Fig. 3.14b & Fig. 3.15b)
- additive type (Fig. 3.16-3.17)

The effect of a variation in concentration on both the polymers of natural origin (Fig. 3.14b & Fig. 3.15b) and the synthetic mixes (ANmix and the AN product range) (Fig. 3.14 & Fig. 3.15) in deionized water (dw) can be primarily described by a vertical shift in the double-logarithmic viscosity plot, which in terms of power-law behaviour results in a change of κ while m stays the same. This shift leads to a significant increase in mobilized shear stress levels. A small to moderate deviation in viscosity curvature at lower shear rates can also be detected. With the influence of dissolved ions, this vertical shift is complemented by a change of slope with decreasing shear rate, i.e. a change in power law parameter m, as visualized for a selection of polymers in Fig. C.4.

A molecular weight variation as illustrated in Fig. 3.14a and Fig. 3.15a takes increasing effect with decreasing shear rate. At high shear rates, the polymer chains are arranged in parallel, which results in the same cumulated sheared surface regardless of molecular weight. Consequently, the mobilized shear stress levels at $\dot{\gamma} > 10$ 1/s almost uniquely depend upon polymer concentration, not on molecular weight (Fig. 3.15a). Lower M_W values (AN-S), i.e. shorter chains, visibly form a Newtonian plateau – associated with the maximum coiled state of polymer chains – at higher shear rates than the higher M_W counterparts with longer polymer chains (AN-M towards AN-H). This can be explained by higher M_W needing a broader shear rate spectrum to fully coil due to the longer chains and therefore probably form a plateau at a significantly lower shear rate not measurable with the rheometer range; an increase in curve inclination is clearly developing from AN-H over AN-M towards AN-S, especially at shear rates $\dot{\gamma} < 10$ 1/s. In this regard, the difference between AN-M and AN-S is significantly greater than between AN-M and AN-H (Tab. 3.4). It can therefore be concluded that there is no linear correlation between the viscosity logarithms and M_W.

The effect of anionicity shown in Fig. 3.14b & Fig. 3.15b is visible over the whole range of shear rates (both in η and in τ), which can be explained by means of the influence on anionicity on the polymer structure, e.g. on the degree of flexibility of the acrylamide-acrylate copolymer chain. The polymers with higher anionicity create more rigidity due to anionic charges distributed along the chains repelling each other. This behaviour can be related to an increased resistance against deformation, i.e. an increase in viscosity and shear stress at a given shear rate. The coil formation of the nearly uncharged polymers in solution (AN-ML) is consequently significantly facilitated due to a significantly higher degree of flexibility. This behaviour does not seem beneficial for a support fluid. The difference between AN-M and AN-MH is less pronounced. It could be the result of small deviations between the M_W values (Tab. 3.4).

The composition of ANmix, especially concerning molecular weights and anionicities of the components, is unknown. According to Fig. 3.14c and Tab. 3.4, it can be classified concerning its bulk rheology in the range of AN-H and AN-M. Its curvature and also Marsh time is more similar to AN-H. This may suggest that the copolymer of acrylamide and acrylate contained in the mix dominates its bulk rheology.

Conclusions with regard to the influence of variations in molecular weight and anionicity on XAN and CMC-H, e.g. resulting from differences in production, may be drawn with care. It is plausible that an M_W variation will have a comparable effect, though maybe not to the same degree. However, the polymer complexity and intrinsic rigidity owing to its basic structure will certainly influence this effect. The complexity is of particular relevance with respect to variations in anionicity as the chain flexibility, which is a significant factor for AN polymers, is already restricted, especially with XAN.

Generally, in comparison to the exemplary bentonite suspension curves, most polymer solutions tested can be ranged within into the shear stress range of the bentonite suspension of lower concentration (B 40), except for CMC-H, which still ranges below B 60 at lower concentration (2.5 g/l), but which significantly surpasses these ranges at 5 g/l. This could make the solution difficult to pump at high velocity rates or an excavation tool difficult to move fast in solution.

With respect to mineral load, Fig. 3.16-3.17 illustrate that the effect on bulk rheology differs with the type of additive. Each figure shows a comparison between solutions containing additives and pure reference solutions without additives.

Fig. 3.16 shows representative rheometer results of the mixes used for settlement analysis in section 3.2.4. Thereby the quartz grains are mixed into the polymer solutions at a concentration of 40 g/l (resulting suspension density $\rho_F \approx 1.024$ g/cm^3) in addition to a small amount of water for improved mixing (section 3.1.2). The rheometer measurements are performed with samples from the upper part of the settling cylinder after several hours of settlement to verify whether grain settlements create a measurable diluting effect. The results show no marked diluting effect at this density level.

The addition of bentonite in suspension at 10 g/l mixed at a ratio of 1:1 into polymer solutions is tested with the AN range including ANmix. Synthetic solutions at higher M_W have been used in combination with bentonite suspensions on construction sites. Mixes with CMC-H and AN-S are analysed as well for classification.

The respective results displayed in Fig. 3.17 show an increase in bulk viscosity of all mixes increasing with decreasing shear rate as compared to the curves of the reference concentration. This deviation can be attributed to concentration differences of tap water to a certain extent. Firstly, due to the presence of bentonite, slightly less water is used for mixing. Secondly, it is likely that the bentonite binds a certain amount of water and therefore contained dissolved ions as well, which would otherwise impair viscosity performance at lower shear rates to a larger extent (Fig. C.4). The same effect can be seen for the addition of superabsorbing polymers (Fig. 3.17, top left) at 1 g/l (P$_S$) creates a similar effect. The mix with the lowest anionicity value 'ML 0.75 + B 5' was found to be completely unstable creating large polymer-bentonite flocks. The rheometer result is therefore not shown.

It can be concluded that quartz grains with settling tendency may have a diluting influence on the solution mix, but this effect is not yet significant at the tested ranges. The use of bentonite suspensions or hydrogels reduces the amount of water available for polymer hydration resulting in an increase in bulk viscosity.

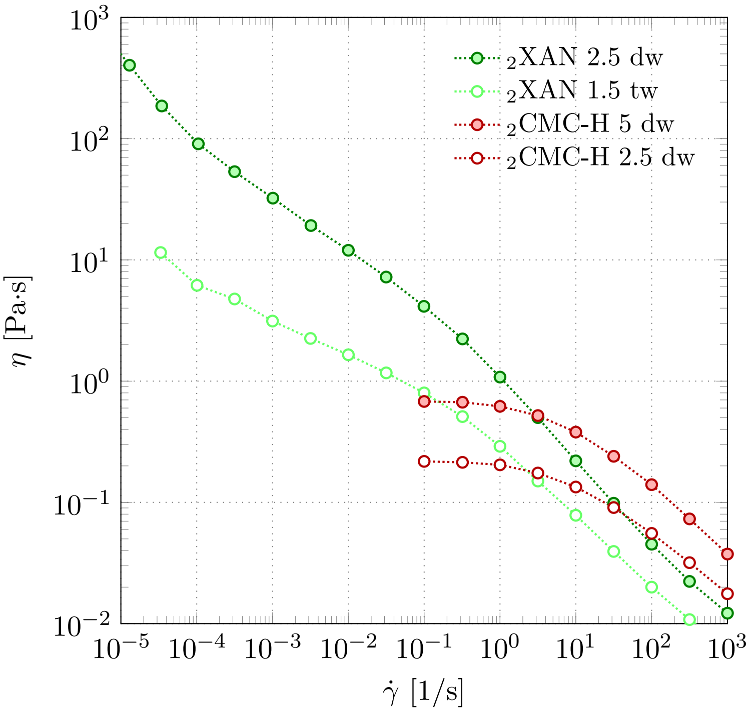

Figure 3.12.: Rheometer viscosity results – CMC-H and XAN influence of concentration

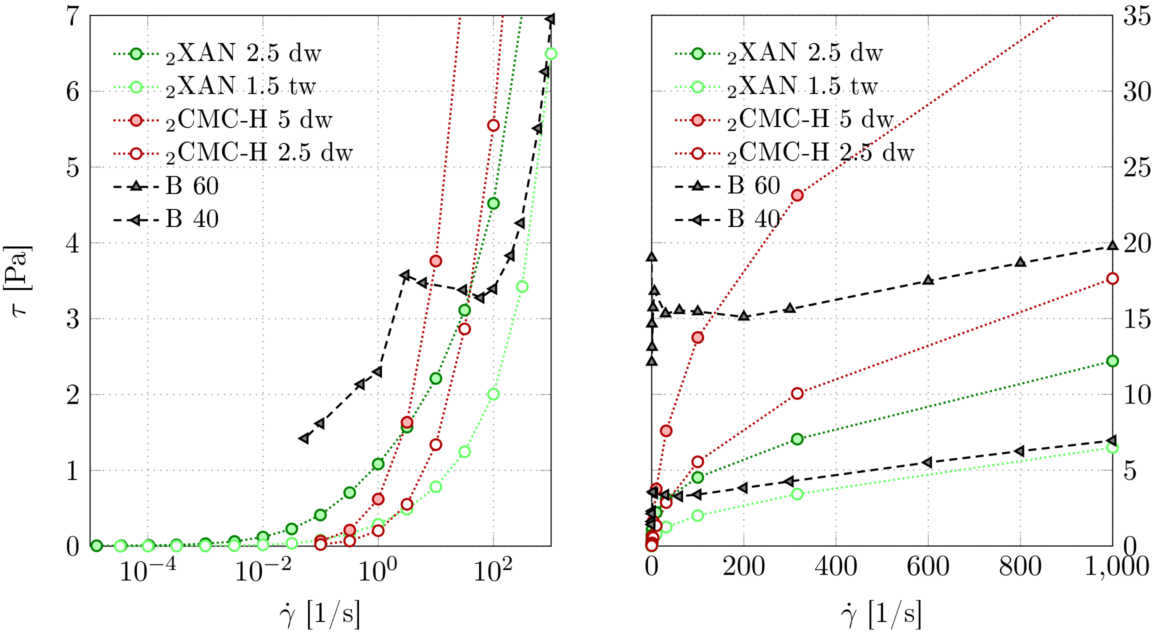

Figure 3.13.: Rheometer shear stress development – CMC-H and XAN influence of concentration (from Fig. 3.12)

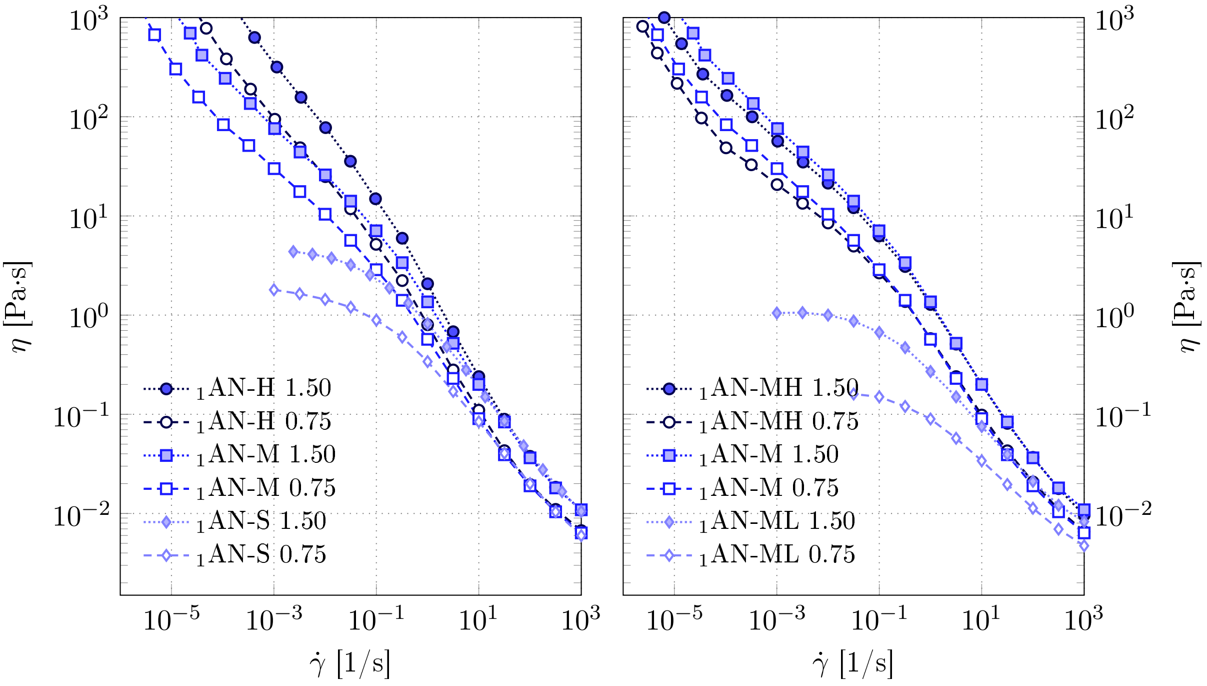

(a) M_W variation

(b) Anionicity variation

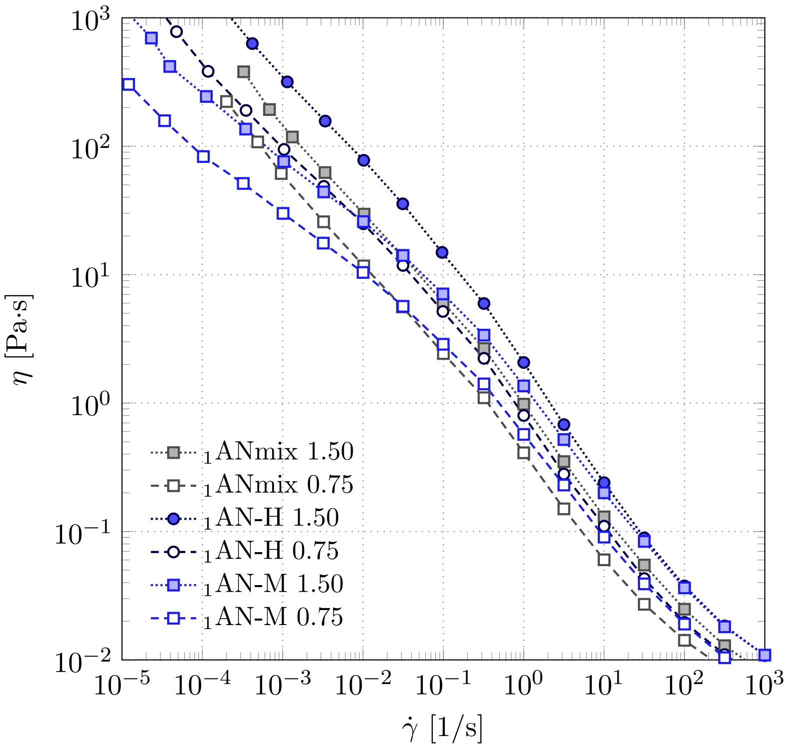

(c) Classification of ANmix within the AN range

Figure 3.14.: Rheometer viscosity results – AN range property variation (solvent: dw)

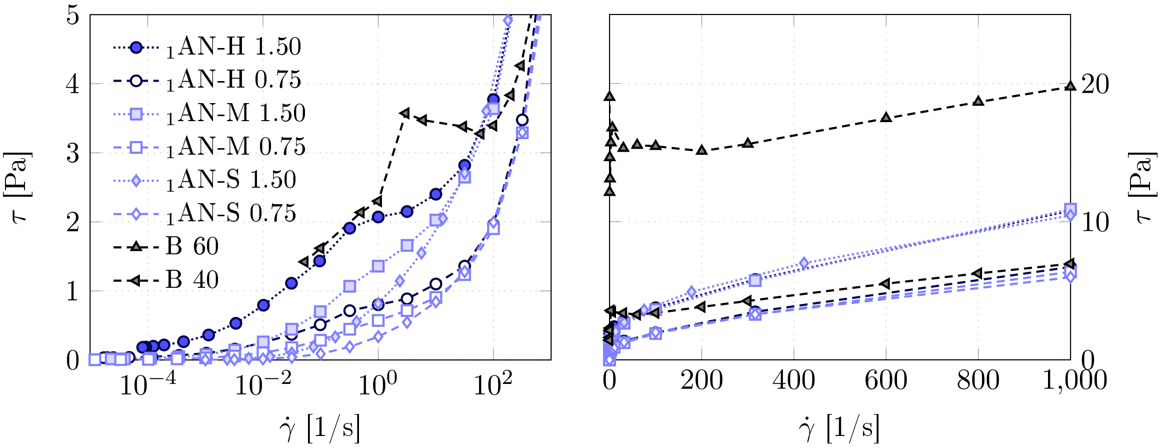

(a) M_W variation

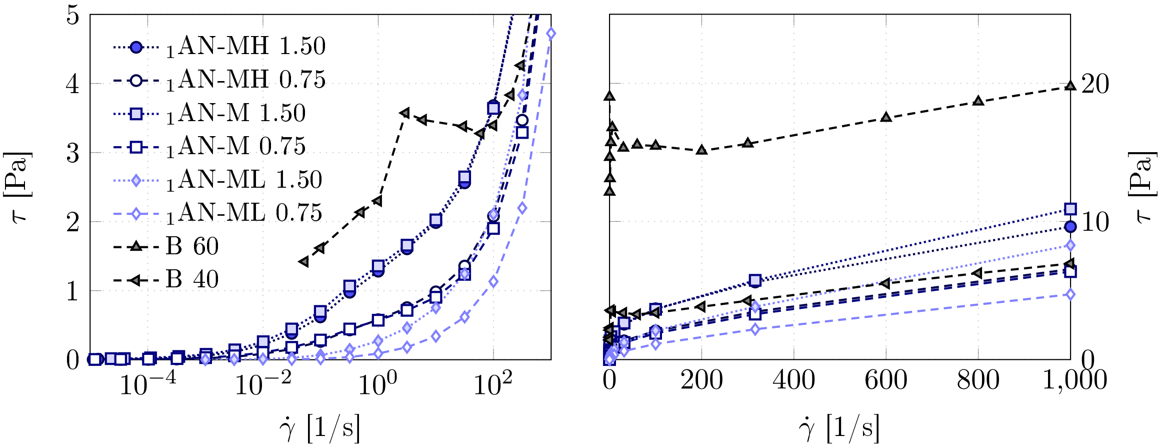

(b) Anionicity variation

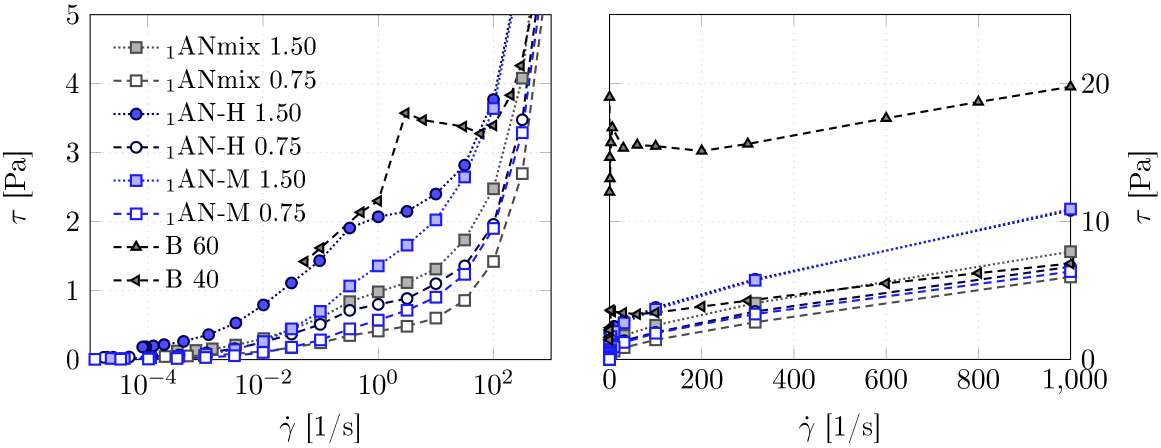

(c) Classification of ANmix within AN range

Figure 3.15.: Overview rheometer shear stress development – AN range property variation (solvent: dw) (from Fig. 3.14)

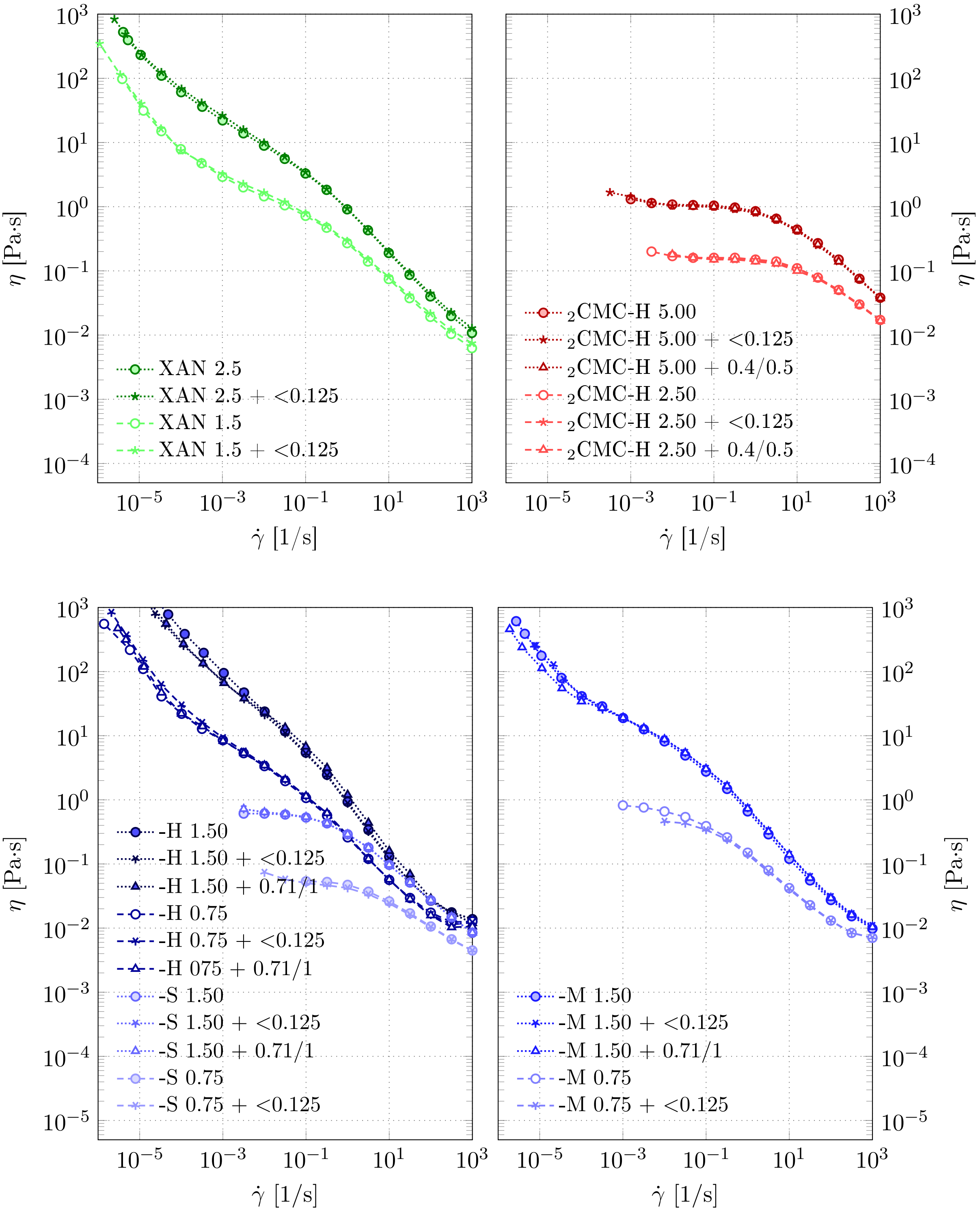

Figure 3.16.: Rheometer results – influence of granular additives: quartz grains at 40 g/l (solvent: tw)

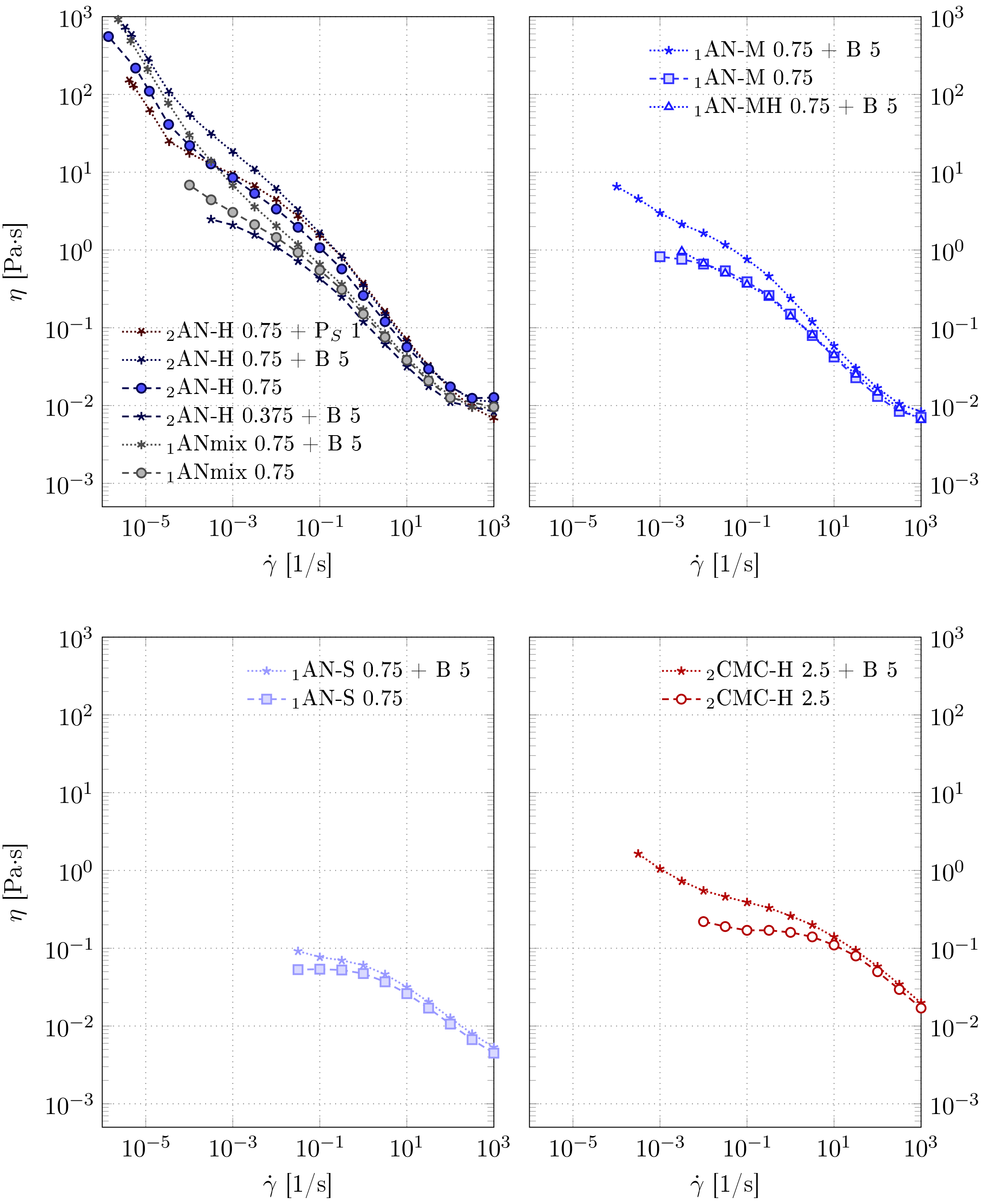

Figure 3.17.: Rheometer results – influence of granular additives: bentonite suspension and polymeric grains (solvent: tw)

3.2.3. Base fluid stability

The following Fig 3.18-3.19 show the results of 21 modified filter tests as a means to assess water retention and separability of the viscous base fluid. It displays the propagation of the filter paper saturation outside the metal ring over time differentiated by polymer type (all) and solvent (only AN). Black and red lines are added for water and bentonite suspension (at 60 g/l) in order to give a reference. 55 mm mark the depth of full saturation of the filter paper.

The results show the expected dependency of the propagation rate on polymer concentration, degree of anionicity and chain length for all polymers. With XAN, only moderate deviations could be observed with a change in concentration, but otherwise differences are relatively clear. This underlines the relation between viscosity and the water retention capacity of the polymer solution.

Moreover, it can be derived from Fig 3.18 that even a small amount of change in solvent quality (presence of salts, etc.), here shown as a comparison between tw and dw, can significantly increase the tendency to release water from the solution, i.e. decrease the stability of the mix. This is particularly pronounced for medium to lower chain lengths (AN-M, AN-S). In deionised water (dw), only the product of low anionicity releases water as quickly as the bentonite suspension, which underlines the importance of a sufficient level of ionic charge along the polymer chain to bind the water within the mix. The high-molecular-weight solutions can still be considered relatively stable with the highest concentration showing no marked difference in different solvents.

The CMC-H curves at 2.5 g/l and 5 g/l (Fig. 3.19) range in the same propagation rate level as the high-molecular weight AN representatives at 0.75 g/l and 1.5 g/l, respectively (in the same solvent: tw). The behaviour of XAN is comparable to the medium-molecular weight AN representative at higher concentration (1.5 g/l).

With reference to the limit criterion set by the technical guideline DVGW W 116:2019 for

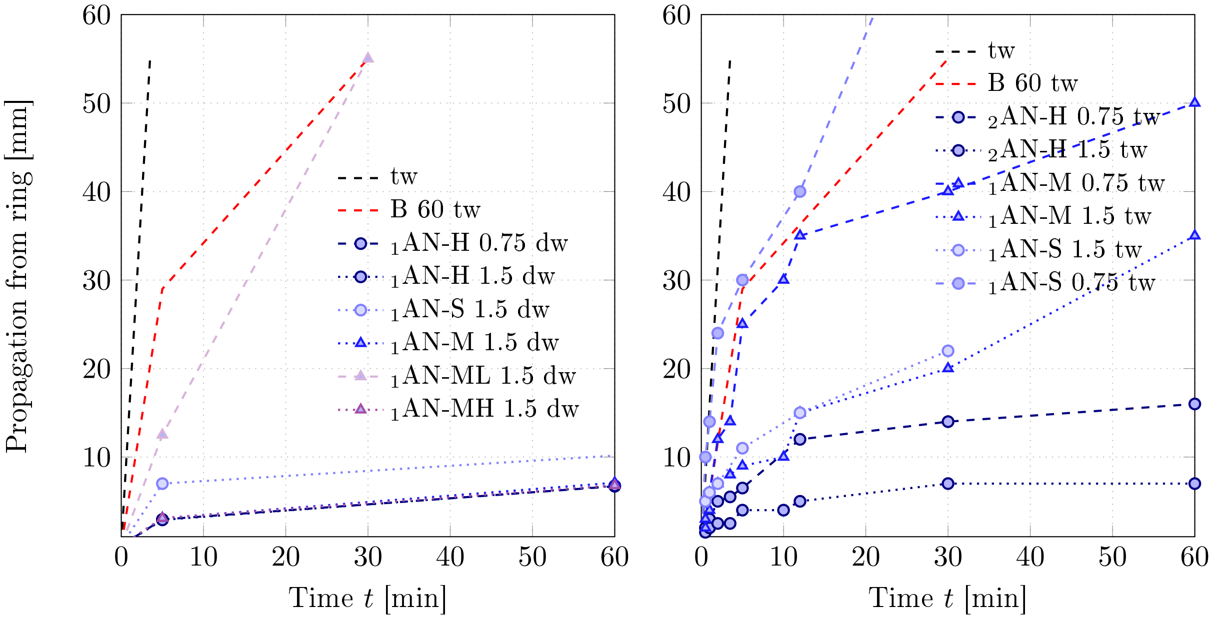

(a) dw

(b) tw

Figure 3.18.: Evaluation of filter saturation propagation over time: AN range

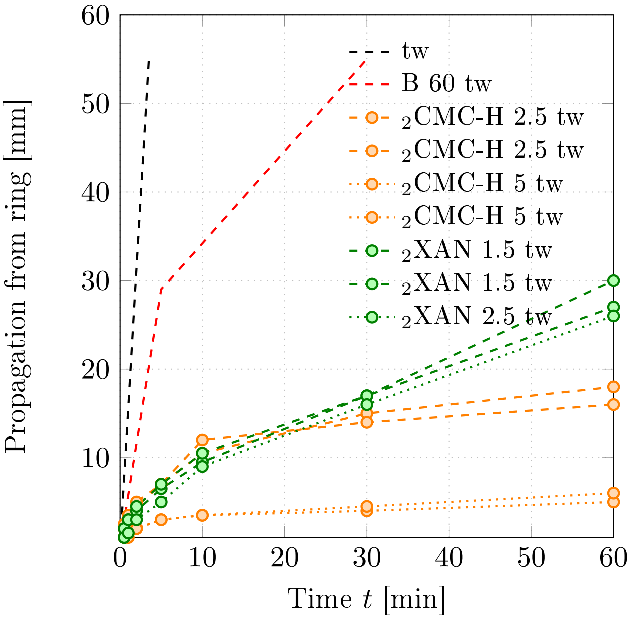

Figure 3.19.: Evaluation of filter saturation propagation over time: CMC-H/XAN (tw)

drilling fluids (<7.5 mm within the first 17 min), in tap water, only the higher concentration levels of CMC-H and AN-H match the criterion and can be considered applicable for ground with clay swelling (or clogging) potential. The AN solutions of at least medium molecular weight and XAN can still be considered considerably more effective in retaining water within the support fluid than a typical bentonite suspension at high concentration (60 g/l). AN-S at higher concentration is still moderately effective, but it could penetrate further into the ground due to its low viscosity, so it might need a certain amount of suspended fines to additionally seal the earth wall.

These results can be considered as a first reference by means of a relatively simple test for the classification of support fluids with respect to their ability to retain water. As different results can be achieved for different molecular weights and concentrations, this procedure could also be considered useful as an index test for construction sites to control that a sufficient amount of polymer of sufficient chain length is still present in the mix (at least for CMC-H and AN polymers).

3.2.4. Granular additive characteristics

Mixing and geometry

Fig. 3.20 shows the different types of pore blockers used:

- quartz mineral grains: $d_{grain} = 0 - 1$ mm (sieved)
- bentonite suspension flocks (relevant size and stability unclear)
- polymeric grains (SAP): $d_{grain} = 0.25 - 21.5$ mm (Fig. 3.21)

The quartz grain range represents the full range of grains at the density that the tested polymer solutions can carry. As visible in Fig. 3.20e-3.20i, the form of the bentonite flocks seems to depend upon the dispersion behaviour of bentonite suspension in polymer solution and is distinct to the respective viscosifier. CMC-H, XAN as well as the low-molecular weight AN create a rather homogeneous dispersion with bentonite suspension, only small bentonite grains may be distinguished. Progressing in chain length from AN-S towards AN-H at medium anionicity, however, aqueous flocks with increasing size develop. The flocks in ANmix are comparable to those for AN-H. The stability with respect to a certain bore blocking geometry is yet unclear.

The diameter distribution of the hydrogel range shown in Fig. 3.21 reflects the median values reached after full hydration in tap water and measured from a minimum of six representative grains per fraction. The maximum sizes were reached after approx. 5-10 min for XS/S, 10-30 min

(a) 0/0.1 mm (b) 0.125/0.25 mm (c) 0.4/0.5 mm (d) 0.71/1 mm

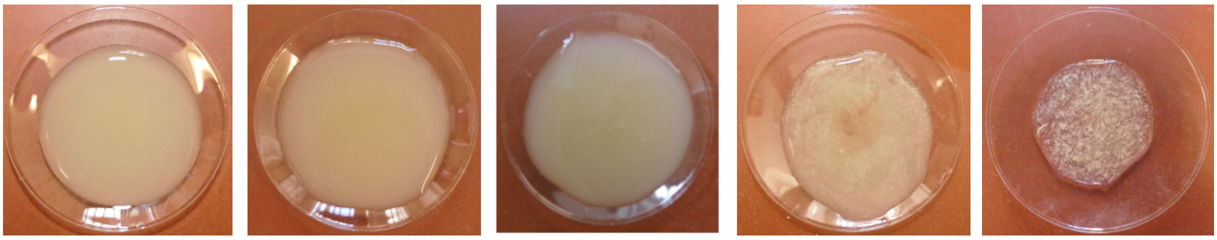

(e) CMC-H + B 5 (f) XAN + B 5 (g) AN-S + B 5 (h) AN-M + B 5 (i) AN-H + B 5

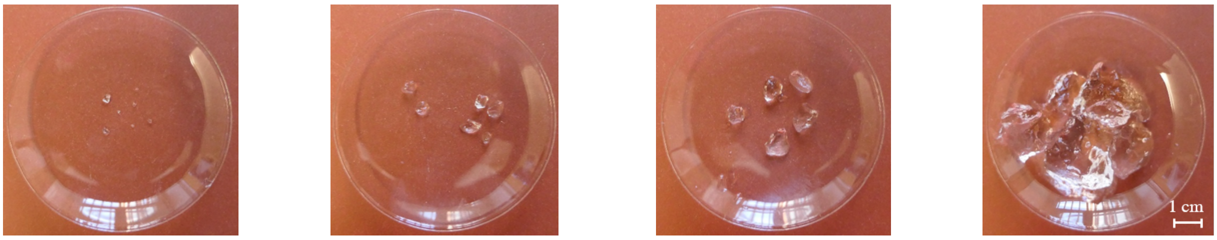

(j) SAP S (k) SAP M (l) SAP G (m) SAP L

Figure 3.20.: Quartz (top), bentonite suspension (center) and polymeric (bottom) grains

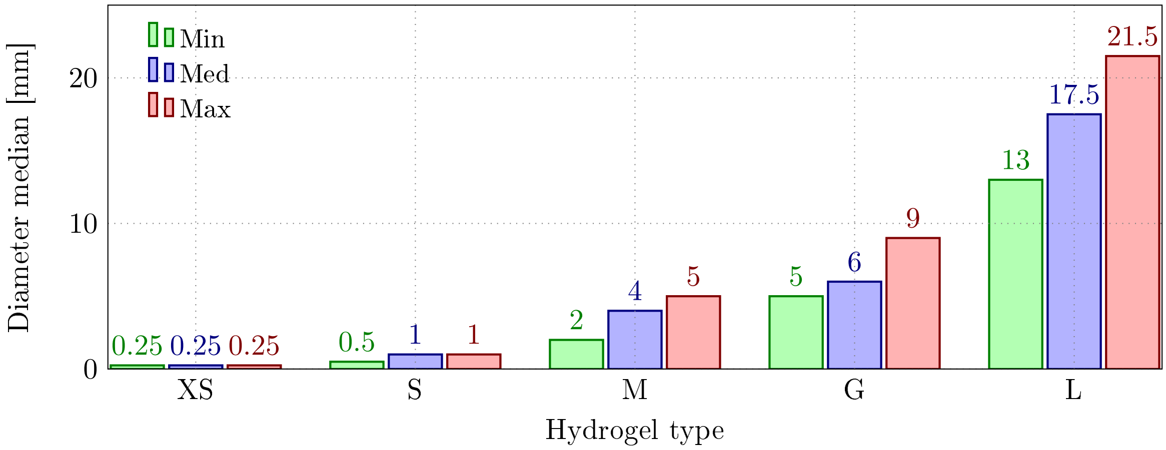

Figure 3.21.: Hydrogels: diameter median reached after swelling in tap water

for M/G and 1-2 hrs for L. Hydration in polymer solutions did not show significant deviations in size compared to the values displayed here. In relation to their dry granule weight, these results amount to an absorption capacity of 100-200 g/g (gram of water per gram of dry granulate, rough estimation).

Given a maximum density of a support fluid loaded with fines of $\rho_{F,mix} = 1.2$ g/cm^3 and a density of the 'pure' fluid without fines of $\rho_F = 1$ g/cm^3. Then this mix would contain around 320 g/l of quartz fines with an assumed grain density $\rho_k = 2.65$ g/cm^3. For the same concentration of fines and the same diameter (volume), an equivalent amount of hydrogels would mean approximately 120 g/l (320/2.65) of swollen grains. With an absorption capacity of 100-200 g/g, this would result in 0.6-1.2 g/l of dry granulate of superabsorber (Fig. B.1) being equivalent to 320 g/l of quartz fines.

Quartz grains: sedimentation

The results of the sedimentation tests with the quartz grain fractions from Fig. 3.20 dispersed in polymer solutions are shown in Fig. 3.22-3.23 for the first 30 min of testing. Each curve represents one individual test. The mixing time ranged from around 30-60 sec (XAN, CMC-H, AN-S) to several minutes (AN-M, AN-H) targeted at creating the best possible dispersion.

It can be observed that the measured density levels are relatively stable with the finest material (quartz powder) for all tested solutions. The distribution then further varies with increasing grain size. Especially the larger grain sizes settle relatively fast in the solutions of lower concentration. With higher bulk velocity values at low shear rates, AN-H vs. XAN behave as expected. The fines in AN-H solution generally settle slightly faster than in XAN solution at maximum dispersion of the particles. CMC-H can be classified in the range of AN-M and AN-H, but closer to AN-M. This is in accordance with the CMC-H viscosity plateau values (low-shear-rate behaviour) ranging more closely to the AN-M values.

However, if the take-up of finer soil fractions from the native ground is to be considered the main method of loading of the polymer solution with fines (as compared to manual addition with controlled dosage and mixing time), the duration of mixing is a critical parameter. As assumed (section 2.2.3), AN of larger molecular weight does not mix easily. This effect is illustrated in Fig. 3.25 by means of a comparison between AN-S (shortest average chain length) and AN-H (longest average chain length). Dispersion of fines in CMC-H and XAN was found to be relatively

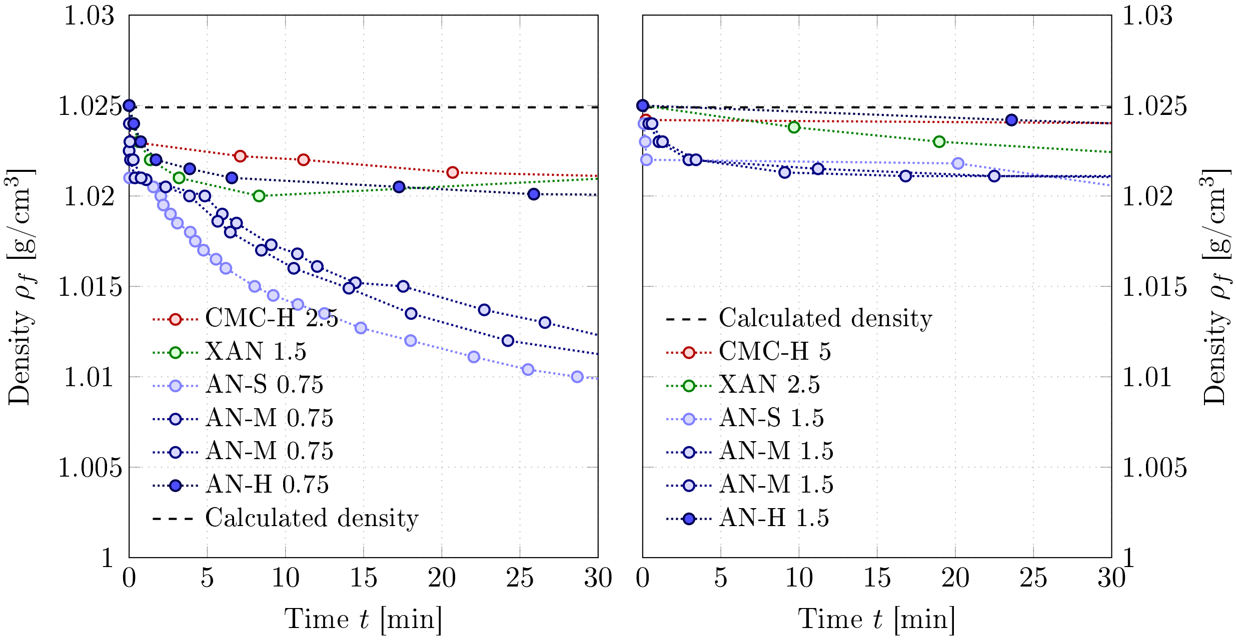

(a) $S_{XS} = 0/0.125$ mm

;

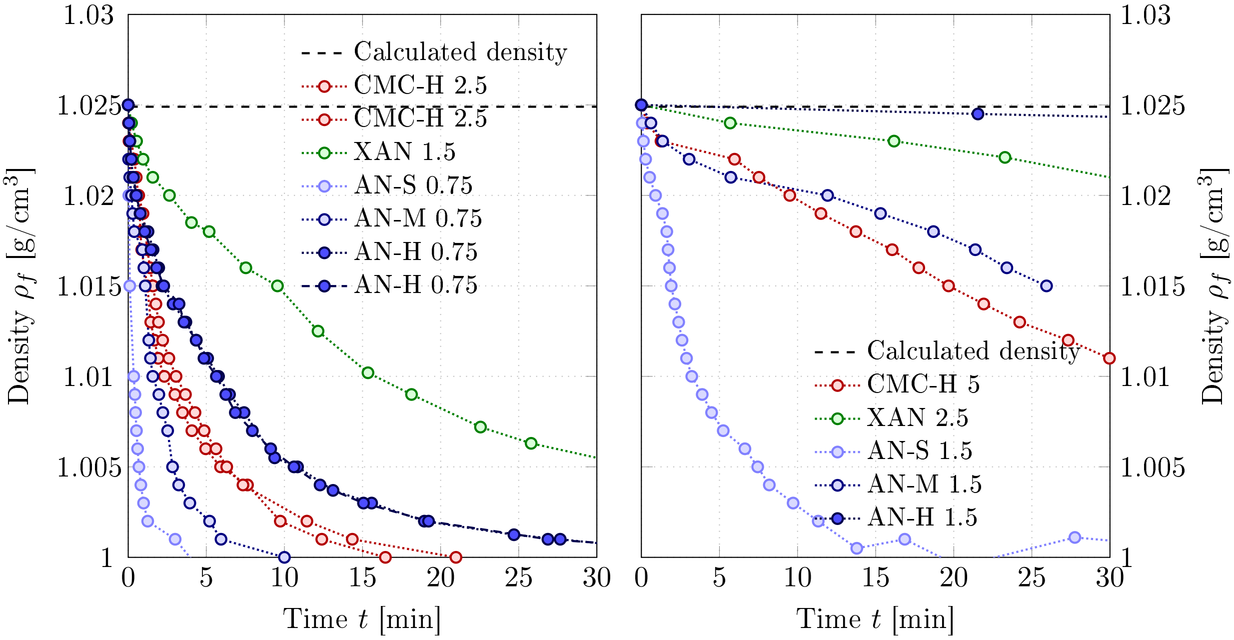

(b) $S_S = 0.125/0.25$ mm

; ;

Figure 3.22.: Areometer tests: polymer solution (low concentration) + 40 g/l mineral (quartz) fines – fine

easy and similar to the behaviour of the short-chain representative of the AN range.

The influence of the mixing time on the areometer results was studied exemplarily for fines of

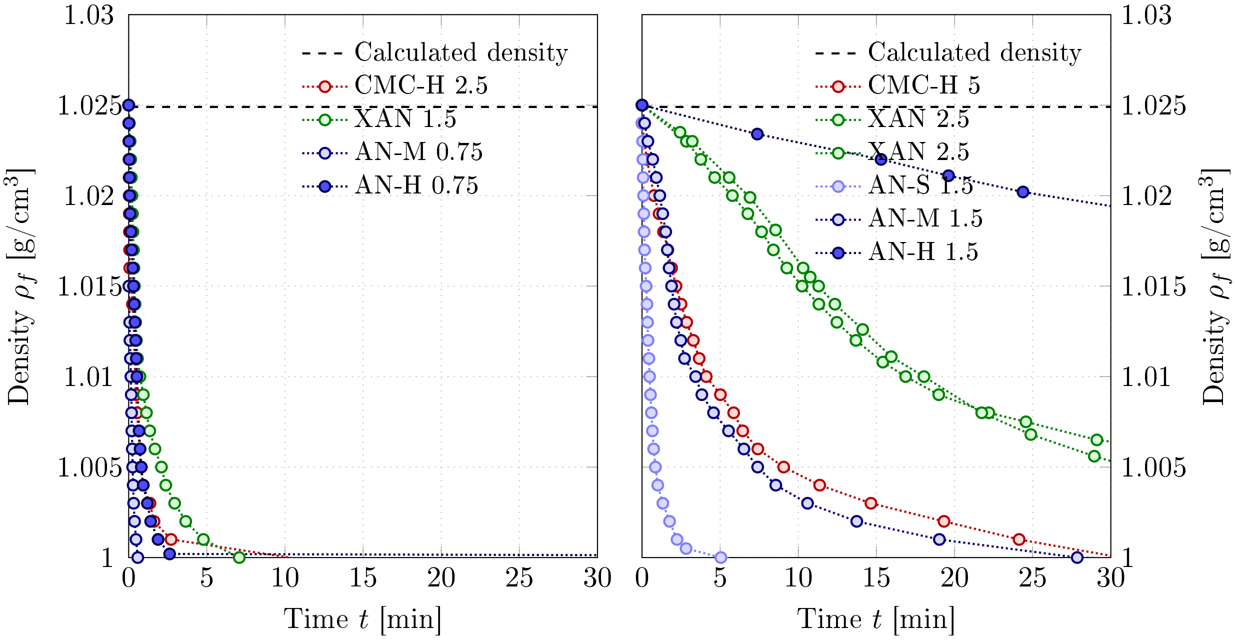

(a) $S_M = 0.4/0.5$ mm

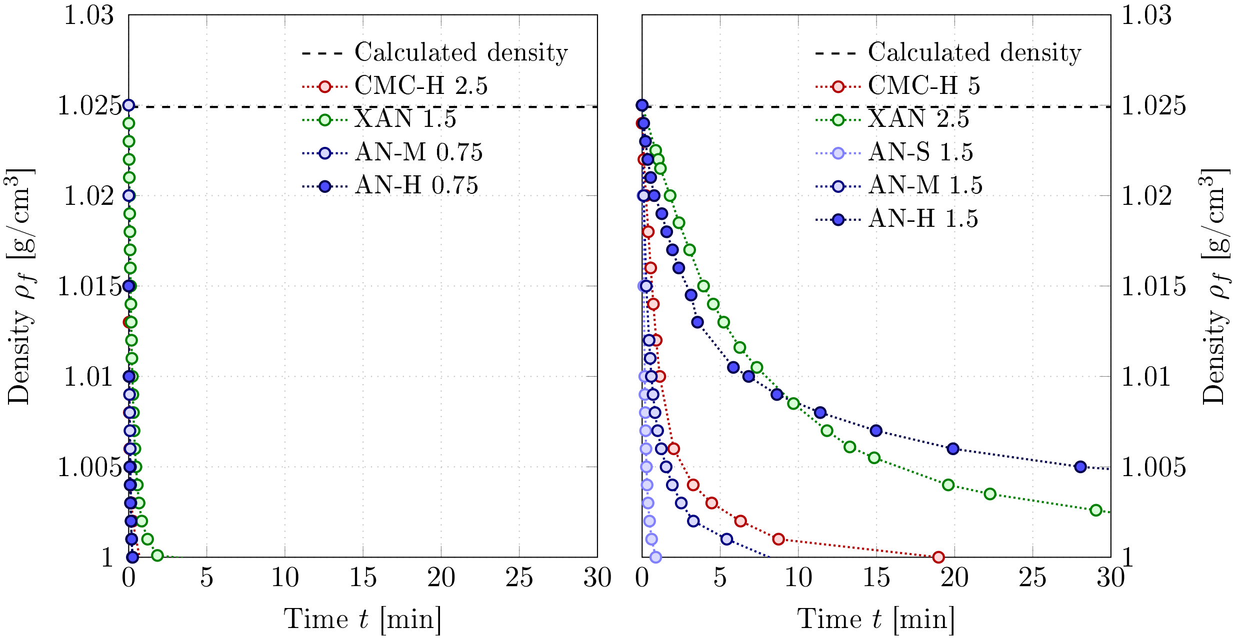

(b) $S_G = 0.71/1$ mm

Figure 3.23.: Areometer tests: polymer solution + 40 g/l mineral (quartz) fines – coarse

the 0.125/0.255 mm fraction with AN-S 1.5 vs. AN-H 0.75 and CMC-H 2.5 (Fig. 3.24). It can be seen that both the AN-S and the CMC-H mixes were already perfectly dispersed after mixing for 30 sec. The AN-H mix, however, was still relatively poorly dispersed, i.e. still containing

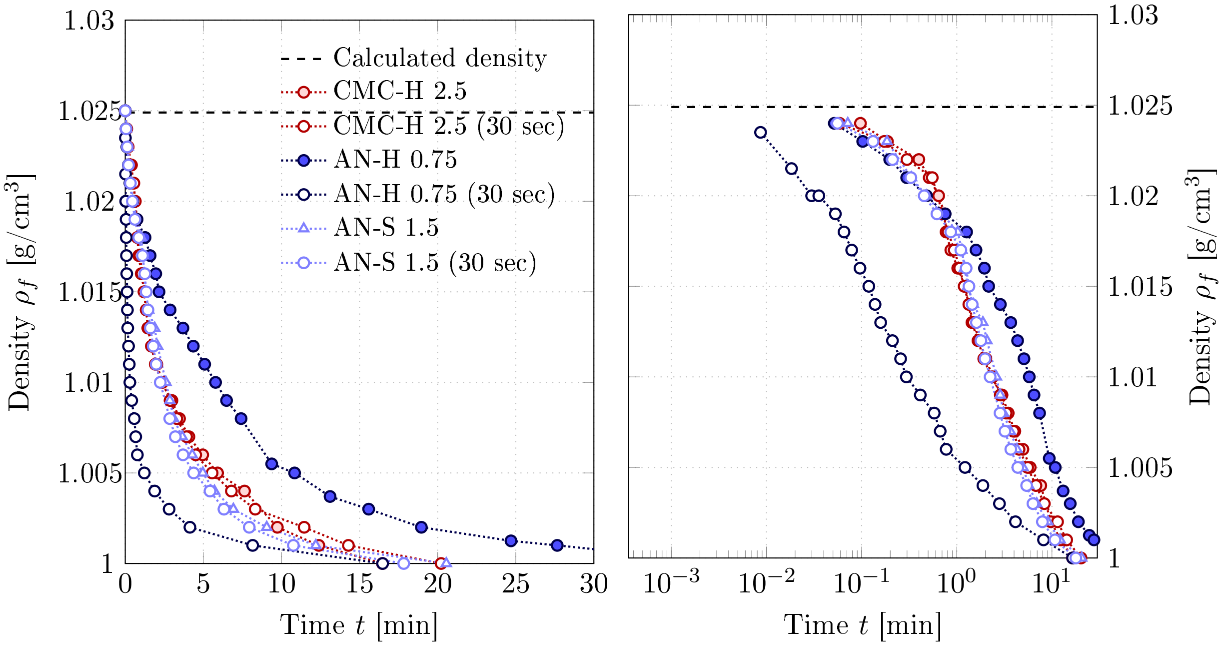

Figure 3.24.: Areometer tests: polymer solution + 40 g/l mineral (quartz) fines 0.125/0.25– effect of mixing time

a considerable amount of agglomerated fines, which sink significantly faster than the individual grains (Fig. 3.25b). It can therefore be concluded that AN-H (and to a certain extent also AN-M) are not likely to take up fines from the ground but rather encapsulate groups of grains to increase grain settlement. They are therefore less likely to be available for colmation with a significant amount if not manually added and dispersed.

Fig. 3.26 therefore shows the development of calculated velocity values for these two types of polymer solutions for an estimate on related settling velocities based on the measured density decrease over time. For this purpose, ideal spherical particles based on a the mean grain diameter were assumed to adequately represent the grains within Stokes' equation (Eq. 2.14). Viscosity values were chosen conservatively based on bulk rheology (Fig. 3.16) for a reference shear rate $\dot{\gamma} = 0.1$ 1/s.

It can be seen that the calculated settling velocities are relatively constant over time. This shows that the areometer values measured within the first few minutes can be considered representative already. Moreover, it can be clearly noted that the derived settling velocities are relatively low for most mixes. Low in this context is considered to be $v < 3$ m/hr, i.e. $v < 8 \cdot 10^{-4}$ m/s which is below the initial flow velocity of the support fluid at least for medium to coarse sand, for which larger fines fractions are necessary (section 3.4.2). Only with the lower concentration of CMC-H it cannot be assured that the settling velocity of the larger fractions ($d > 0.4$ mm) is sufficiently low for them to be available for colmation.

A general conclusion for the applicability of certain ranges of fines solely based on these velocity values should, however, not be drawn. Such a conclusion would suggest that the effectiveness of XAN for colmation is superior to CMC-H. CMC-H solutions exhibit a higher initial penetration velocity during the first few minutes of penetration when the main filtration of the larger fractions should take place because of their viscosity plateau. The viscosity curves of XAN solutions, on the other hand, possess a larger power-law fraction, which should lead to a faster decrease in

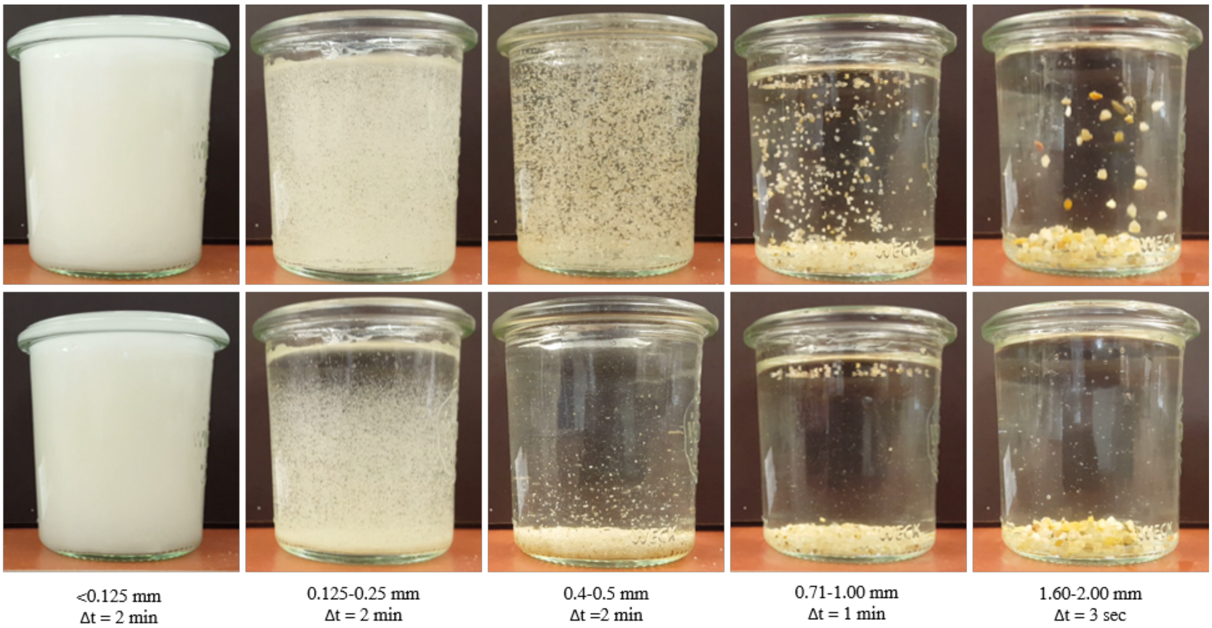

(a) $_1$AN-S 1.50 tw

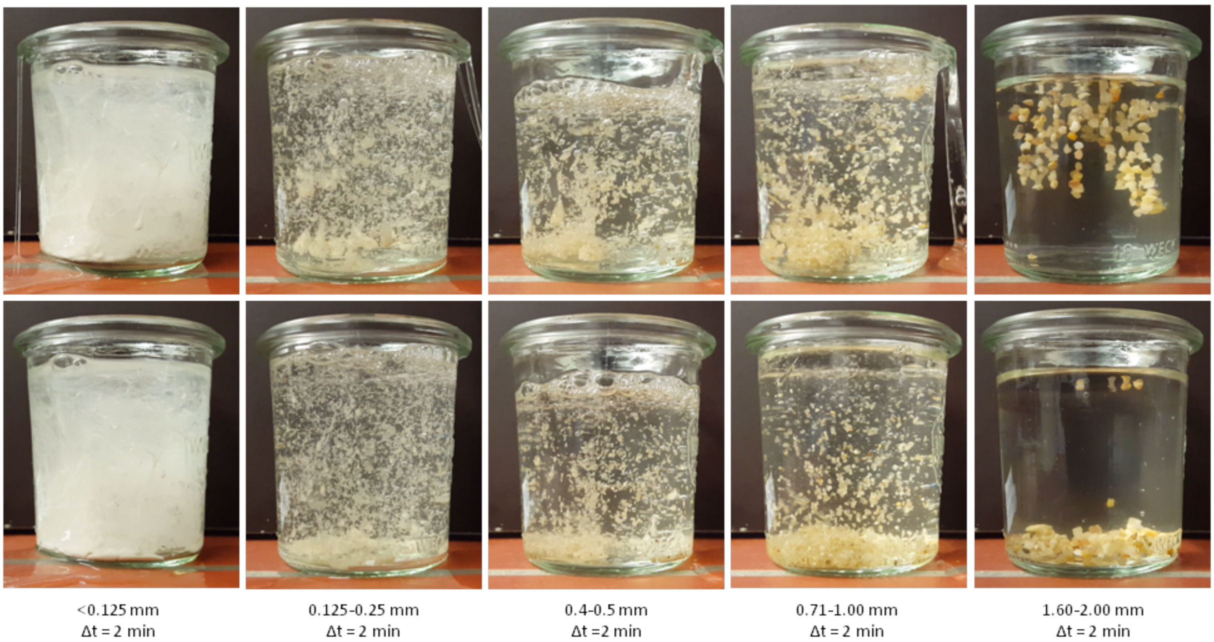

(b) $_2$AN-H 1.50 tw

Figure 3.25.: Suspendability after short mixing time (30 sec) AN-S vs. AN-H

penetration velocity. Therefore, it is possible that they are actually comparable with respect to their carrying capacity and availability of fines for colmation.

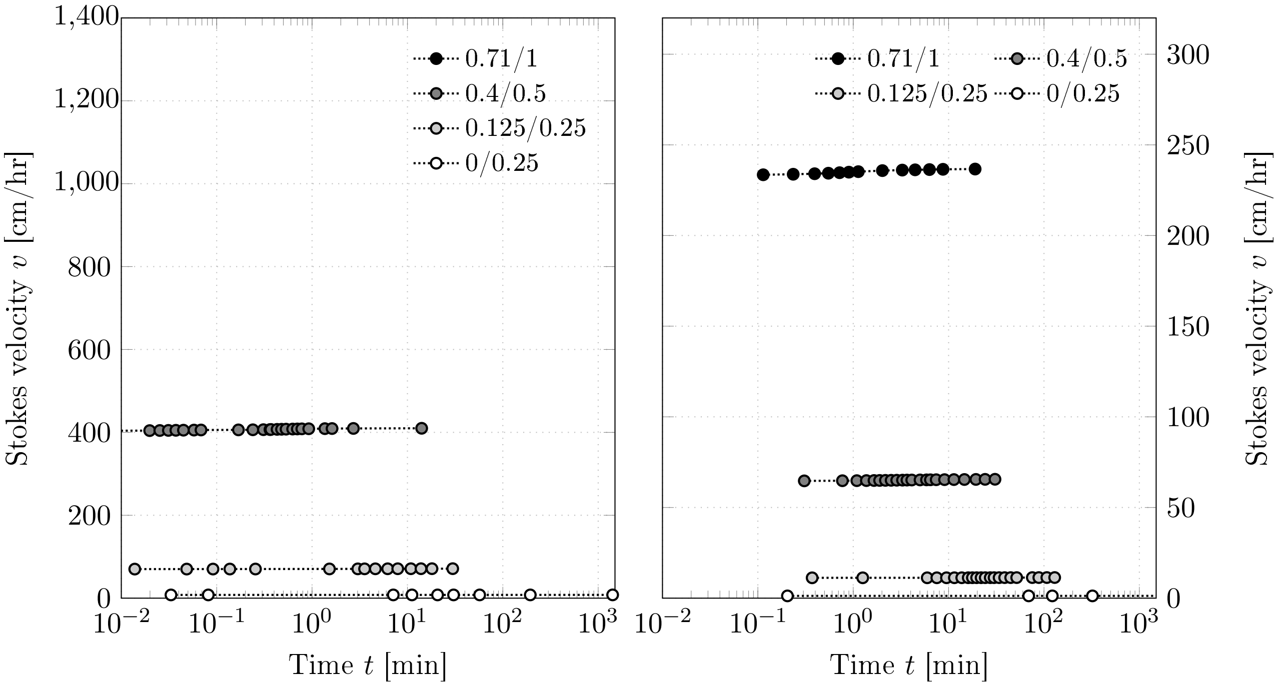

(a) ${}_2$CMC-H 2.5 tw ($\eta_{0.1} = 0.16$ Pa·s)

(b) ${}_2$CMC-H 5 tw ($\eta_{0.1} = 1.0$ Pa·s)

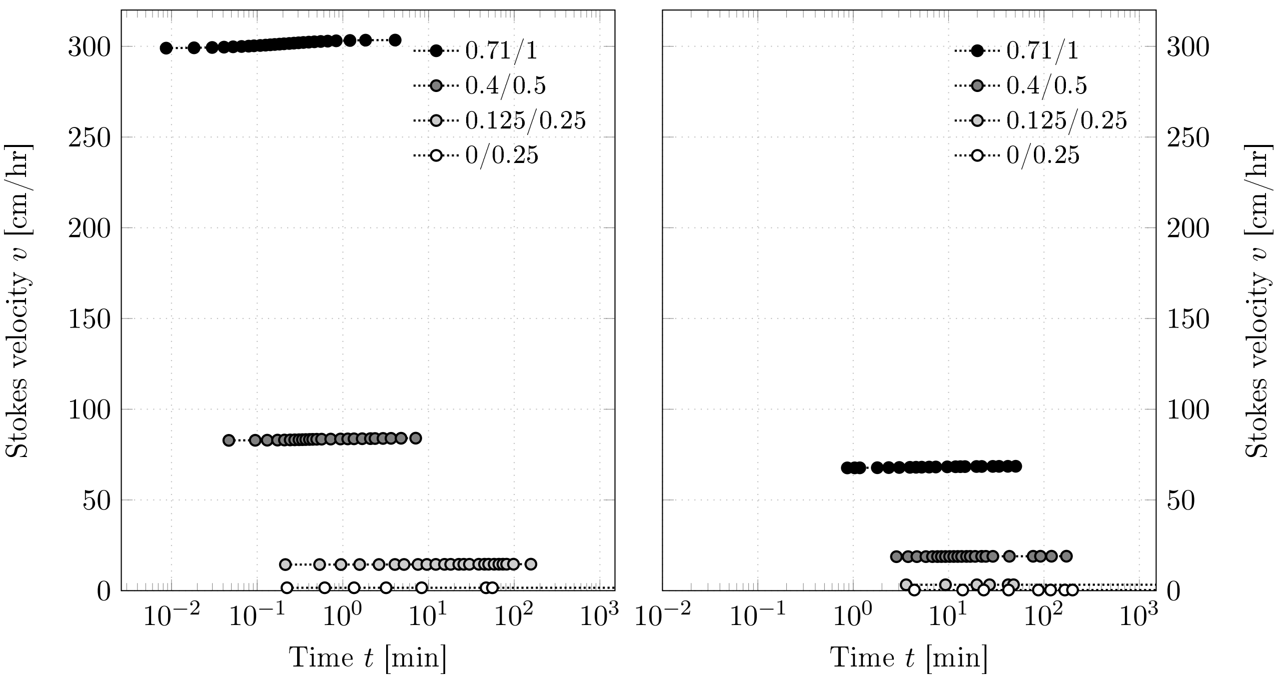

(c) ${}_2$XAN 1.5 tw ($\eta_{0.1} = 3.18$ Pa·s)

(d) ${}_2$XAN 2.5 tw ($\eta_{0.1} = 26.2$ Pa·s)

Figure 3.26.: Estimated settling velocity of quartz fines (40 g/l) with CMC-H/XAN

3.3. Results: vertical penetration – large scale (V-L)

3.3.1. General

Following section 2.4, the time-dependent development of

- penetration depth s
- and related relationships of penetration velocity v and gradient i,
- the curvature of the pressure transferred to the soil ($\Delta p_{mob}(t)$ or $\Delta p_{mob}(s)$) and
- in particular the earth wall pressure gradient ($f_{s0,wall}(t)$ or $f_{s0,wall}(s)$)

will be investigated by means of the V-L testing device.

In a first instance, fine (0.125/0.355) and medium (0/2) sand will be used as a base material to study the effect of different viscosifying base polymers (section 3.3.2). The evaluation is followed by a discussion on the applicability of the capillary bundle approach to predict the experimental penetration results (section 3.3.3). Subsequently, the effect of granular additives (quartz grains, bentonite grains in suspension and aqueous polymeric grains) is analysed with coarser soil material (0.5/1.2, 3/5, 6/8) (sections 3.3.4-3.3.6).

The investigation encompasses a total of 28 individual tests chosen to differentiate characteristics related to different forms of pressure transfer. This differentiation forms the basis for a detailed variation of granular additive combinations and polymer concentrations in different soil fractions performed with the V-S testing device (section 3.4), for which a pressure-penetration relationship cannot be measured directly.

With respect to the interpretation of the experimental output variables, Fig. 3.27 illustrates the pore pressure output evaluation. The pressure boundaries are measured by pore pressure sensors positioned immediately outside the test material ($h_{rel,W}$ and $h_{rel,F}$). The positions h_{rel} of the pressure transducers along the height of the test cylinder are given relative to the lowest sensor.

Due to upwards flow, a hydrostatic pressure component p_{HW} (Fig. 3.27a blue triangles) needs to be taken into account in between the pressure boundary conditions [4]. All pressure variables used hereafter will give the flow-controlling pressure, referred to as p, i.e. excluding p_{HW}. Consequently, the upper pressure boundary (cylinder bottom) is defined by p_F resulting in a flow-generating overpressure Δp relative to the lower pressure boundary p_W (top), as visualised in Fig. 3.27b. Fig. 3.27c shows a horizontal representation of Fig. 3.27b in the form of a normalised pressure drop along h_{soil} relative to the first sensor S_F at $h_{rel,F}$. This depiction will be used as the primary form of representation of pressure drop curves.

The start of polymer penetration into the soil is determined based on three options:

(1) based on the water volume to be replaced until the lower soil interface is reached (approx. 2.7 l)
(2) drop in penetration rate
(3) start of pressure transfer (deviation of p_{S1} relative to p_F)

(2) and (3) were found to be closely related and always below the value of (1), i.e., pressure transfer started a few seconds and cm before the soil interface is reached. A discussion on the definition of the start of polymer penetration is given in appendix D.2. If not otherwise specified, the start of the polymer penetration into the test material will be based on the volumetric calculation method (1). A penetration level based on method (1) will be indicated by s_p.

---

[4] Fluid density is assumed at $\rho_{fluid} = 1$ g/cm^3, which is sufficiently accurate for both water and polymer solutions without additives of higher density. Granular additives cannot be assumed to penetrate far enough into the soil structure (earth wall colmation!) to have a significant and calculable effect on p_{HW}.

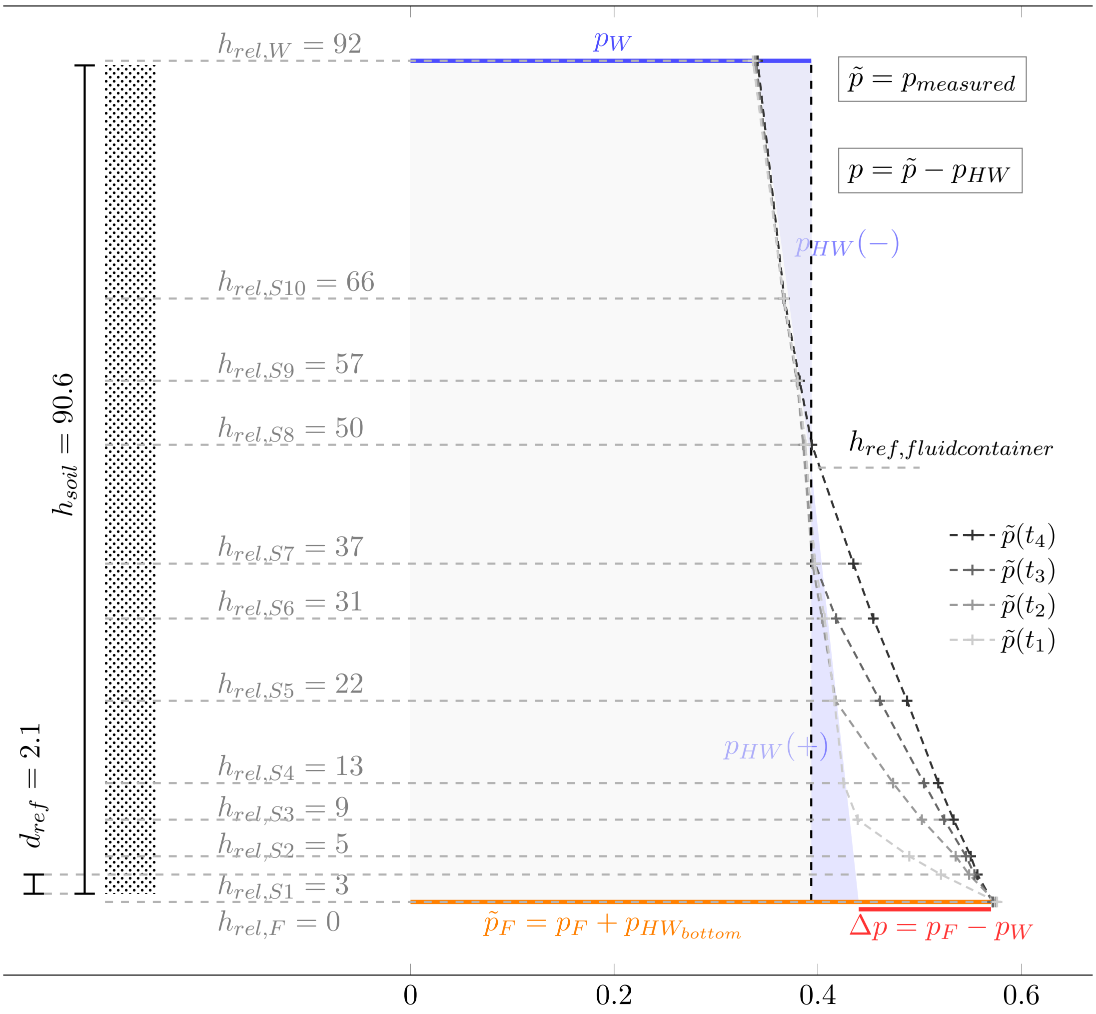

(a) Pressure including p_{HW} [bar]

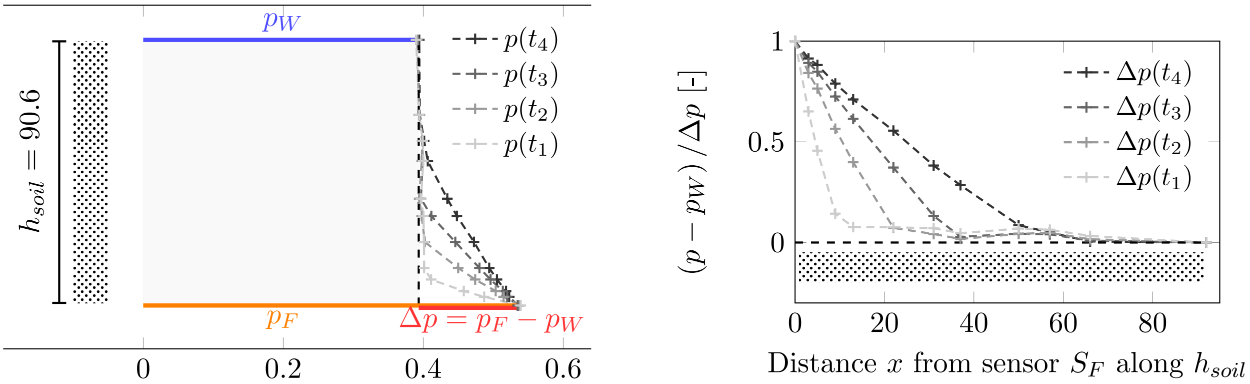

(b) Pressure excluding p_{HW} [bar]

(c) Normalised pressure drop excluding p_{HW}

Figure 3.27.: Variables and sensor heights for testing device with 3 elements (measures in cm)

3.3.2. Viscous base polymer solutions – no additives

The pressure-penetration behaviour of the base solutions is studied with 0/2 as a reference soil material with focus on

(1) type of polymer and molecular weight
  - CMC-H
  - XAN
  - AN range with molecular weight variation (AN-S vs. AN-H)
  - synthetic mix polymer (ANmix)

(2) polymer concentration
  - AN-H (closest ANmix representative)
  - synthetic mix polymer (ANmix)

(3) degree of anionicity
  - AN-S/-H
  - AN-MH

(4) finer sand (0.1/0.4)
  - AN-H ('slim' and 'flexible' representative)
  - CMC-H ('complex' representative)

The following paragraphs will analyse the effect of this polymer (1)-(3) and soil (4) variation with differentiation into penetration and pressure relationship at an overpressure of $\Delta p = 0.15$ bar as a lower boundary. Subsequently, higher levels of Δp will be addressed.

0/2 mm: penetration relationships

Fig. 3.28 shows the development of the penetration depth s, calculated based on volumetric determination of the penetration start, over a maximum time span of 24 hrs for the basic polymer types tested with the 0/2 mm soil fraction. Fig. 3.29 gives a comparison of the synthetic mix polymer ANmix with its closest bulk-rheological representative from the polymer type range AN-H.

For the basic polymer types, initial penetration within the first 30 min (Fig. 3.28a) seems to follow two paths, one for AN-S 1.50 / AN-H 0.75 and one for the remaining curves. This development then further shifts over the following hours (Fig. 3.28b) with especially AN-H 1.50 and even earlier XAN 2.50 deviating within the first 40 cm of penetration towards a significantly flatter subsequent course. The variation of penetration depths after 5 hrs covers a relatively wide range between around 25 cm (XAN) and 90 cm (AN-H 0.75) with the maximum deviation increasing with time. A doubling of the concentration of AN-H amounts to a halving of the penetration level at 5 hrs. Though at double concentration, CMC-H shows twice the penetration depth compared to XAN at 5 hrs.

This behaviour cannot be explained entirely by bulk rheological effects (Fig. 3.12 & Fig. 3.14), which is particularly visible when comparing the bulk viscosity values for CMC-H or XAN vs. AN-H to their penetration rates. A combination of concentration, rigidity and complexity of the polymers seems to trump bulk rheological expectations in the narrow porous environment of this medium-grained sand. This effect becomes especially apparent when ranking the polymers of natural origin within the AN range. However, even within the AN range, a deviation from bulk rheology can be discovered, especially when comparing AN-H 0.75 and AN-MH 1.50, where

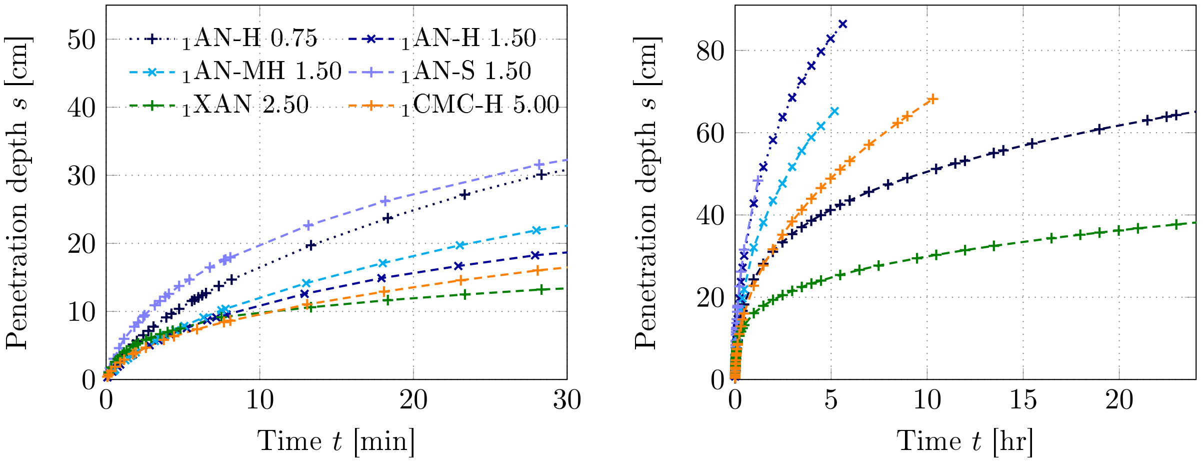

(a) Start

(b) Continuation

Figure 3.28.: 0/2 mm – no additives: penetration behaviour at $\Delta p \approx 0.15$ bar – polymer type (dw)

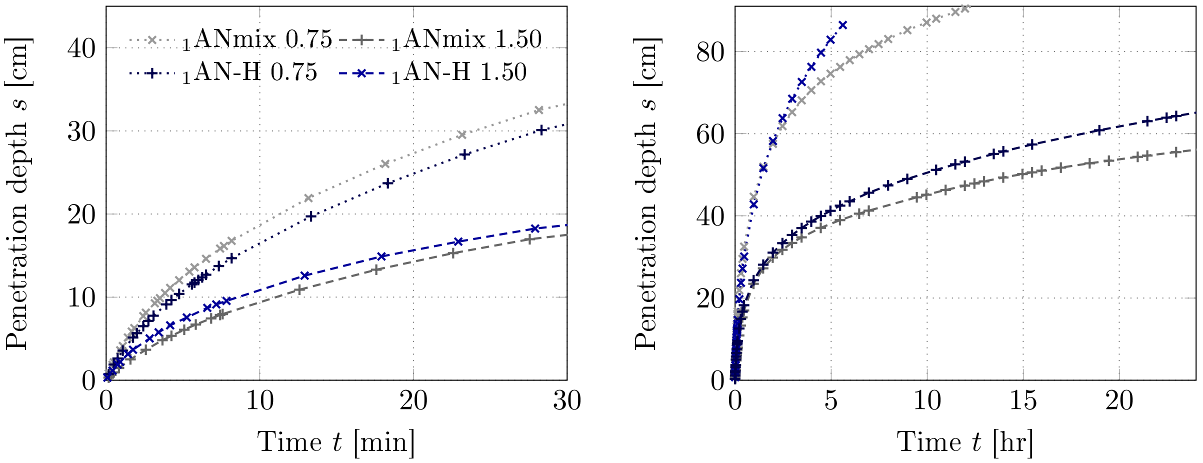

(a) Start

(b) Continuation

Figure 3.29.: 0/2 mm – no additives: penetration behaviour at $\Delta p \approx 0.15$ bar – polymer mix (dw)

AN-MH has a lower molecular weight, but is less flexible towards conformational changes due to its higher degree of anionicity. ANmix of both concentrations start off similarly to AN-H (Fig. 3.29), but decreases in penetration rate slightly more rapidly than AN-H despite similar bulk rheology. This behaviour is visible more clearly in the $v - i$ representation of the same data as illustrated in Fig. 3.30.

Fig. 3.30 shows the development of the filter velocity according to Darcy $v_{Darcy}(t)$ in relation to a falling gradient $i = \Delta H/\Delta L$ (determined as backward differences). The gradient is calculated as a macroscopic representative of the full penetration depth $s(t)$ with the assumption of a full pressure drop $\Delta p(t)$ along $s(t)$, i.e. $\Delta H = \Delta p/\gamma_F$ and $\Delta L = s$, with ρ_F being the fluid density (polymer solution $\approx$ water) and g the gravity. The data displayed here show the full range of the testing time, so in certain cases up to three days. As further illustrated in appendix D.2 and D.3, pressure transfer starts before the calculated zero-penetration depth. Consequently, ΔH may be slightly overestimated; Moreover, the data points are obtained from falling gradient measurements (though falling slowly) and full pressure transfer to the ground is reached only around 25 cm of calculated penetration depth. The values at the higher gradient range, especially $i > 30$, i.e. $s < 5$ cm, may not be representative.

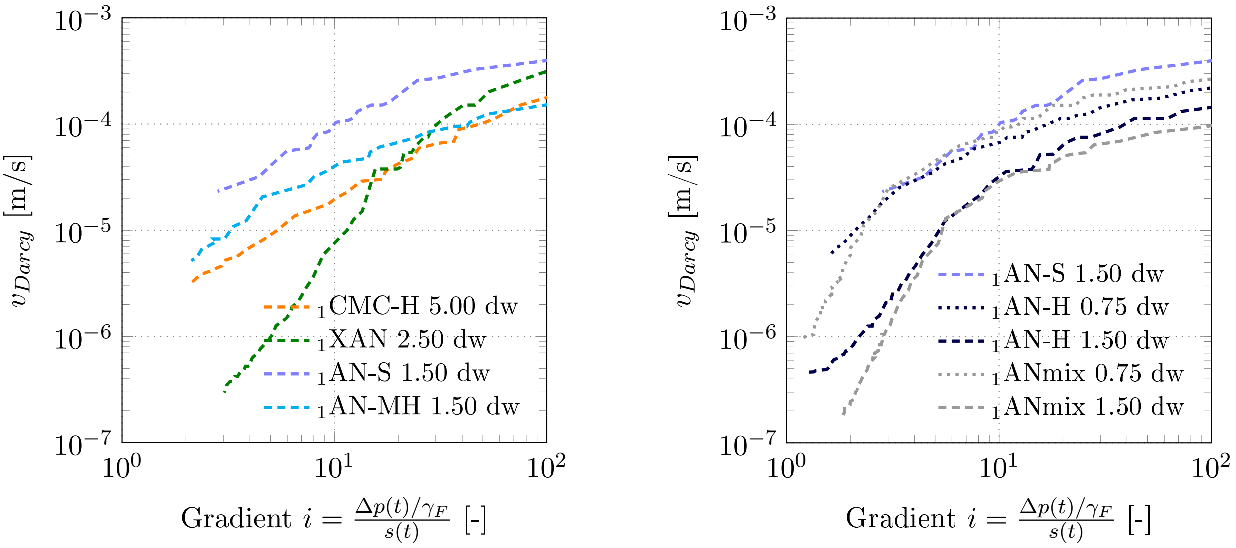

(a) (b)

Figure 3.30.: 0/2 mm – no additives: development of filter velocity with decreasing gradient

Generally, linear or nearly polygonal courses with two linear segments can be noted in this double-logarithmic visualization for all plots. It can be observed that AN-MH, AN-S, CMC-H and AN-H/ANmix show a similar inclination at higher i. The long-chain polymers AN-H/ANmix 0.75 vs. 1.50 show a significantly steeper curve at lower gradients reaching a similar inclination as XAN. The AN-H 1.50 curve shows an additional change of inclination at $i < 2$, with the slope matching the slope at higher gradients. This suggests that the flatter sections are created by Newtonian plateaus ($m = 1$) with a pronounced η_{min} plateau. The different levels result from differing κ parameters and different $\dot{\gamma}_{crit}$ values for the respective plateaus (Fig. 2.29 & 2.30). AN-MH, AN- and CMC-H seem to follow this plateau behaviour nearly along the whole gradient regime. AN-H 1.50 visibly follows the lower Newtonian plateau η_{min} until $i \approx 6$. Power law behaviour can then be assumed until $i \approx 1.5$ followed by an upper Newtonian plateau η_{min}. For XAN, it can be assumed that the power law section ranges at least between $i \approx 4$ and $i \approx 15$.

A pronounced lower Newtonian plateau η_{min} means that a minimum viscosity is already mobilized at high shear rates, wich results in a lower penetration rate (filter velocity) than assumed from pure power-law behaviour. Exemplarily quantified for XAN, extrapolating power-law behaviour from $i = 4 - 15$ towards $i \approx 40$, power-law behaviour would assume $v_{Darcy} \approx 1 \cdot 10^{-3}$ 1/s while the data suggests $v_{Darcy} \approx 1.5 \cdot 10^{-4}$ 1/s. A calculation of the penetration depth according to pure power law would therefore slightly overestimate the penetration depths near the penetration start, i.e. at low s. This will be further addressed in section 3.3.3.

Again, these results can only partly be related to rheometer data, especially concerning the found Newtonian plateau levels. When comparing an increase in concentration from AN-H 0.75 to AN-H 1.50 at least, a relatively vertical shift similarly to bulk rheology (i.e. similar m, different *kappa*) can be observed. At higher gradients, an increase in molecular weight from AN-S 1.50 towards AN-H 1.50 has the same result. AN-MH, i.e. medium molecular weight, but higher anionicity, shows a similarly favourable effect. However, the marked difference in behaviour when comparing AN-S, AN-MH and AN-H cannot be found by means of bulk rheological comparison, where the flow behaviour of AN-MH and AN-H are more closely related than AN-S vs. AN-MH. With respect to Newtonian plateaus, only AN-S and CMC-H show a marked plateau formation (η_{max}) at lower shear rates (or flow velocities) in their bulk rheological data.

The improved behaviour of ANmix towards AN-H can be explained by the effect of pore blockers contained in the mix as described by the manufaturer. Otherwise, deviations between bulk rheology and 'in-situ' rheology can only be explained by interactions between the polymer chains and the porous matrix (Fig. 2.27). Reasons for deviations with respect to bulk rheology will be further discussed in the context of capillary bundle approximations in section 3.3.3.

On the whole, it can be concluded that the penetration velocity (related to the filter velocity by n, Eq. 2.17) decreases over several decimal powers within the first hours of penetration, especially with XAN 2.5 and AN-H/ANmix 1.5 – with a significant influence of interaction mechanisms between polymer properties and soil, which cannot be immediately related to bulk rheological parameters. In this context, filter velocities decrease towards 10^{-5} m/s (3.6 cm/hr) → 10^{-7} m/s (0.036 cm/hr) in 0/2 mm soil at a pressure level of 0.15 bar. Especially the lower value can be considered near-stagnation.

0/2 mm: pressure relationships

The development of the pressure drop curvature along the soil depth with increasing penetration depth is shown in Fig. 3.34. Each pressure sensor result is given by its position x relative to the first sensor ($x_i = h_{rel,i}$) (Fig. 3.27). The 'earth wall' is located at $x = 0.9$ cm, i.e. between the first two data points, the first sensor in the sand being positioned at a depth of 2.1 cm ($h_{rel,S1} = 3$ cm). The vertical lines indicate the position of each sensor reached by the fluid with their position increasing from light gray to black, i.e. they reflect the progression of the penetration depth. The pressure drop curvatures are chosen from the points in time when the calculated penetration depth reaches the individual sensor and are therefore coloured according to the same grayscale. The pressure values of the respective sensors are given as normalized values to filter out effects from (small) deviations in total overpressure Δp created by changes in the fluid levels of the inflow and outflow containers.

For CMC-H, XAN and the full AN range, it is noticeable that the pressure drop curvature follows the penetration depth (Figs. 3.31a-3.31b, grey arrow). The course of the pressure drop is clearly nonlinear, as would be assumed for viscous flow behaviour with a shear-thinning fluid (Fig. 2.6b). The curvature affects the amount of pressure $\Delta p_{mob,wall}$ mobilized immediately at the earth wall, here defined as the pressure difference between the first two sensors. The respective value for the last displayed time step is marked in each individual figure. Apparently, the amount varies significantly between the different types of polymer, with XAN exhibiting a significantly higher value than the other types. CMC-H and especially XAN seem to stabilize at a certain value of $\Delta p_{mob,wall}$, i.e. the pressure drop immediately at the earth wall remains relatively constant after an initial drop within the first approximately 20 cm of penetration. This effect may be noted to a lower degree for the AN polymer of higher anionicity (Fig. 3.31d). The AN polymers of medium anionicity (AN-S/AN-H) show the lowest values for $\Delta p_{mob,wall}$.

When plotting the pressure drop values in relation to their relative position along the penetration depth (s_p) as illustrated in Fig. 3.32, it can be seen that the course of the pressure drop does not change significantly with increasing penetration. Fig. 3.32 shows the pressure drop curves

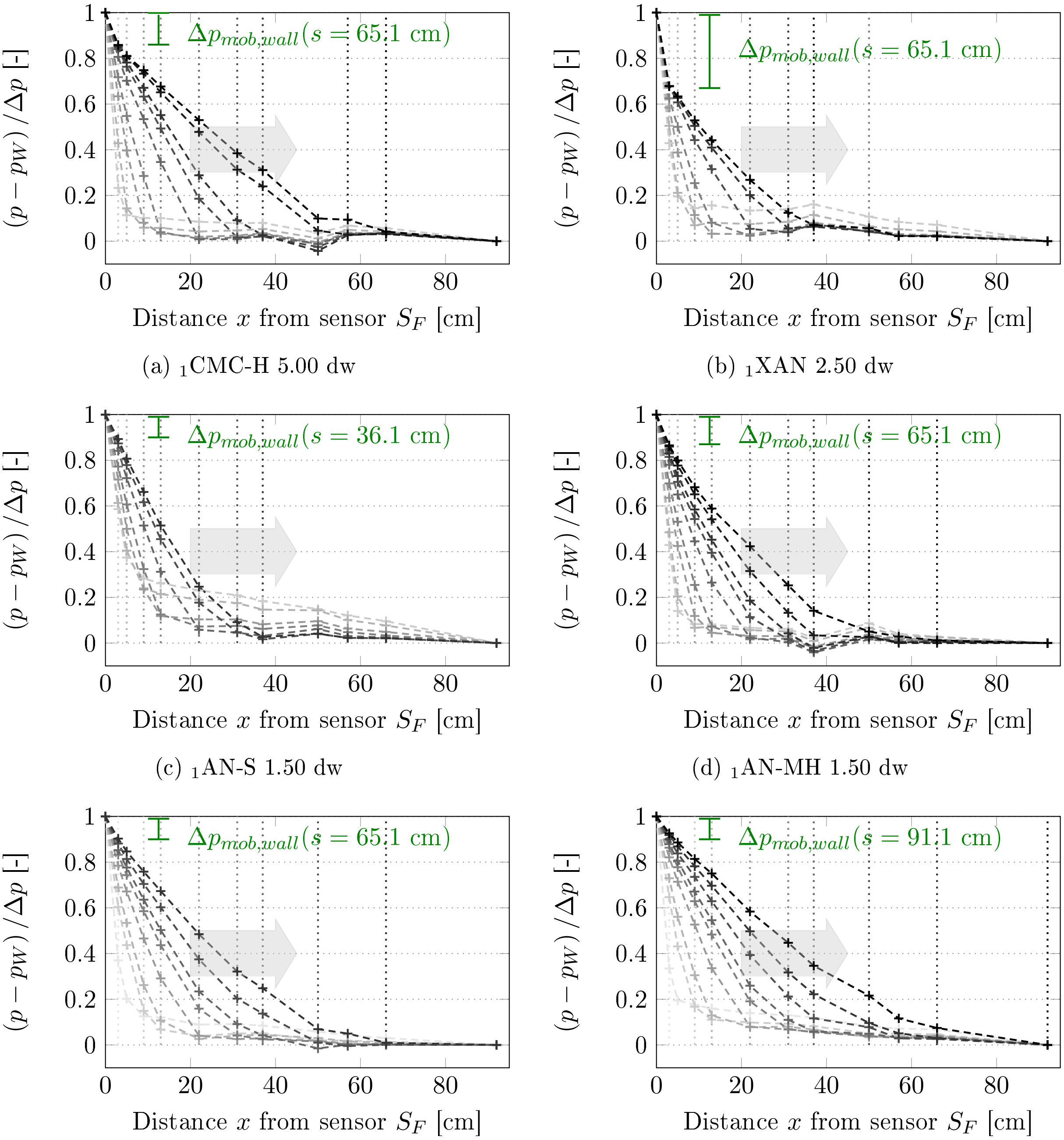

(a) $_1$CMC-H 5.00 dw

(b) $_1$XAN 2.50 dw

(c) $_1$AN-S 1.50 dw

(d) $_1$AN-MH 1.50 dw

(e) $_1$AN-H 0.75 dw

(f) $_1$AN-H 1.50 dw

Figure 3.31.: 0/2 mm – no additives – CMC-H/XAN/AN-S/AN-MH/AN-H: development of $p - p_W$ along soil depth at $\Delta p \approx 0.15$ bar (normalised)

starting from a minimum penetration of 13 cm (sensor $S4$). No significant change in pressure drop course means that characteristic curvatures could be usable for stability calculations relative to assumed penetration depths to take into account related increases in mobilized pressure from the non-linear as compared to the linear course.[5].

---

[5] Unlike Fig. 3.31, Fig. 3.32 shows the curvatures based on penetration calculation starting from the start of

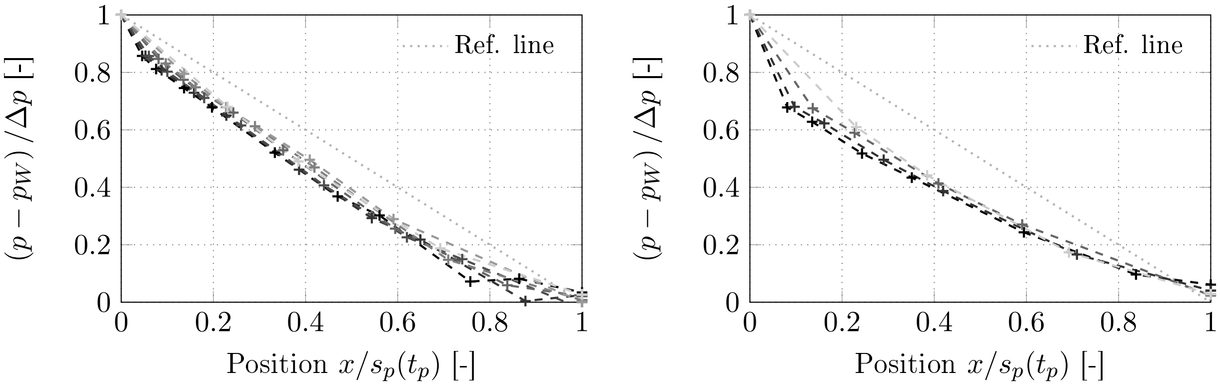

(a) $_1$CMC-H 5.00 dw (b) $_1$XAN 2.5 dw

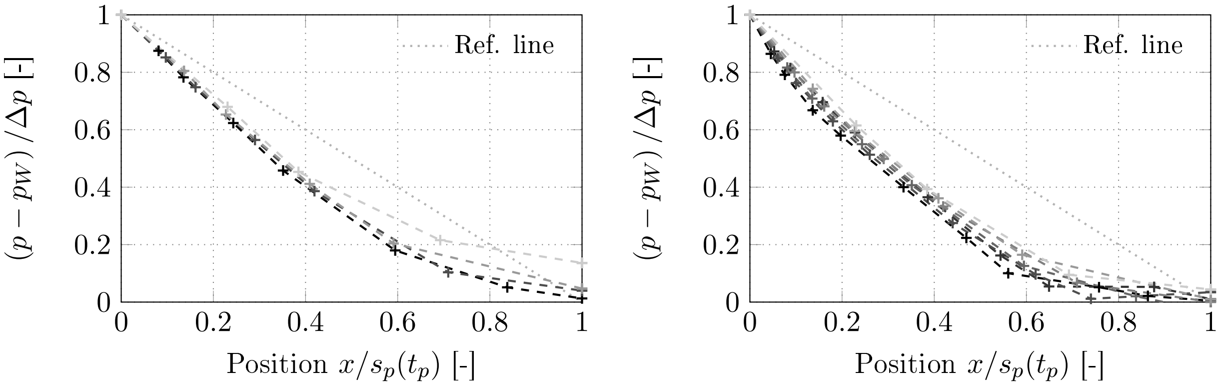

(c) $_1$AN-S 1.5 dw (d) $_1$AN-MH 1.5 dw

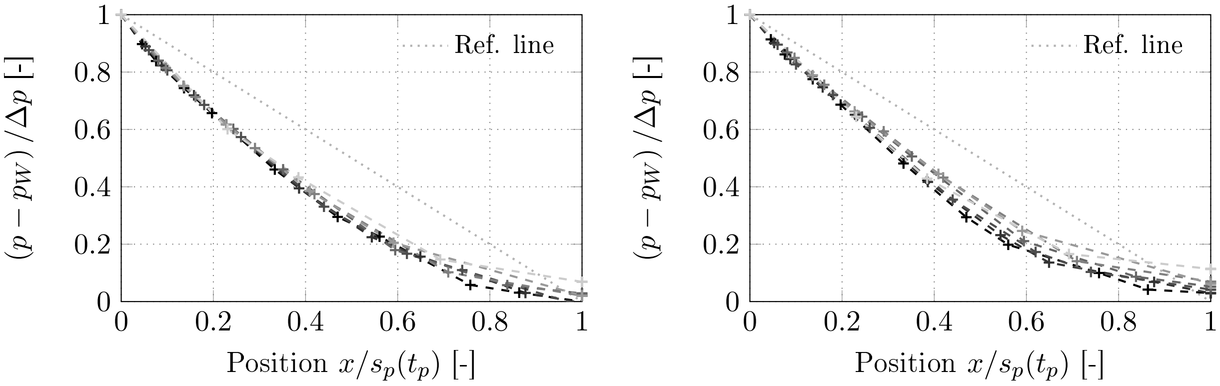

(e) $_1$AN-H 0.75 dw (f) $_1$AN-H 1.5 dw

Figure 3.32.: 0/2 mm – no additives – CMC-H/XAN/AN-S/AN-MH/AN-H: normalized pressure drop curvature along the penetration depth s_p

---

pressure transfer (s_p). Understandably, this starting point correlates better with the pressure peak points at sensor position as illustrated in appendix D.3. The respective curvatures based on s instead of s_p are given in appendix D.4 for reference. However, they are thought to be misleading in this context, because they contain effects from different inclinations of pressure drops of the sensors as shown in appendix D.3. This offset between s and s_p, i.e. between penetration and pressure transfer behaviour, needs to be taken into account when considering different curvatures during stability assessment

When comparing the normalized pressure drop curvatures for CMC-H/XAN vs. the AN range, it appears that the maximum depth of the deviation between linear and non-linear course are located immediately at the earth wall ($x \approx 0.05 - 0.1 \cdot s_p$) for the more complex polymer structures CMC-H/XAN as compared to deeper into the ground for the smaller AN chains. This suggests that the deviation for CMC-H and XAN primarily results from processes happening at the earth wall interface, e.g. a certain degree of earth wall colmation. It is interesting to note that this effect is significantly more pronounced for XAN than for CMC-H, even though CMC-H is used at double concentration compared to XAN. The remaining curvature after the initial drop runs rather linearly.

The effect of AN seemingly occurs rather along the length of the penetration or towards the end (max. deviation from reference line around $x \approx 0.6 \cdot s_p$). AN-S and both concentrations of AN-H show very similar curves, AN-MH visibly has a higher depth of deviation compared to the linear course. This suggests that the AN curvature is governed rather by degree of anionicity (inflexibility of the chain) than by concentration or molecular weight.

This differing behaviour results in a higher $\Delta p_{mob,wall}$ for CMC-H and XAN, especially compared to the AN range of medium anionicity, which is the decisive parameter for internal stability. For macrostability, however, depending on the penetration depth, employing AN may result in a higher percentage of mobilized pressure relative to their respective penetration level. This effect can be seen exemplarily at the position of $0.6 \cdot s_p$. The total mobilized pressure of CMC-H and XAN here amounts to approximately $0.7 - 0.75 \cdot \Delta p$ (linear case $0.6 \cdot \Delta p$). AN-S/AN-H reach approximately $0.8 \cdot \Delta p$ and AN-MH up to $0.9 \cdot \Delta p$. However, as the pressure drop curvature generally clearly still follows the penetration depth, the penetration rate (Fig. 3.28) remains the overall governing factor.

The ANmix solutions show a distinctly different pressure drop course with increasing penetration depth as illustrated in Fig. 3.34 and Fig. 3.33. The pressure drop curvature changes significantly starting similarly to AN-MH with a more pronounced nonlinearity than AN-H. Subsequently, membrane behaviour (increasing pressure transfer at the earth wall interface) starts developing slowly at the earth wall resulting in $\Delta p_{mob,wall}$ increasing with progressing penetration depth. Again, the polymer concentration does not seem to affect this curvature development (only the penetration rate). Fig. 3.34 illustrates this effect more clearly. Apparently, the pressure curvature initially follows the penetration depth (viscous flow, Fig. 2.6b, grayscale in Fig. 3.34),

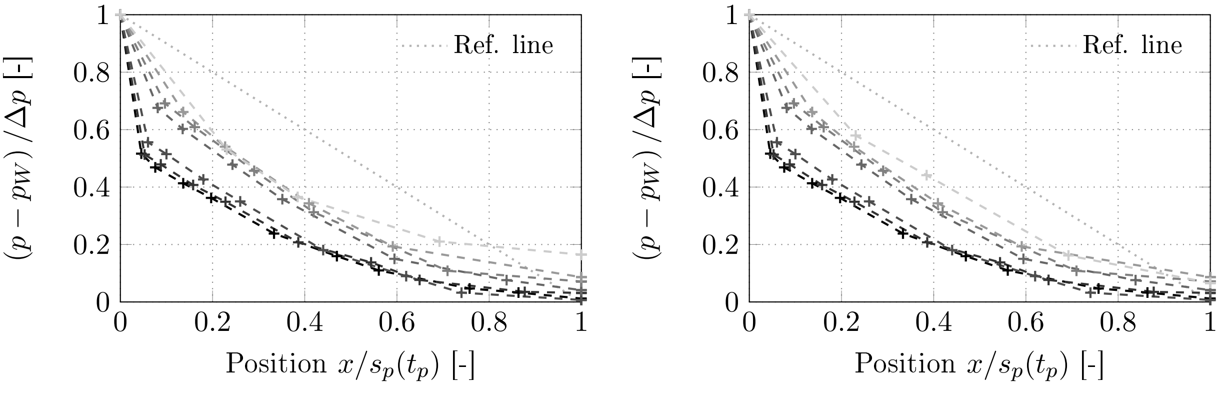

(a) $_1$ANmix 0.75 dw

(b) $_1$ANmix 1.5 dw

Figure 3.33.: 0/2 mm – no additives – ANmix: normalized pressure drop curvature along the penetration depth s_p: 0/2

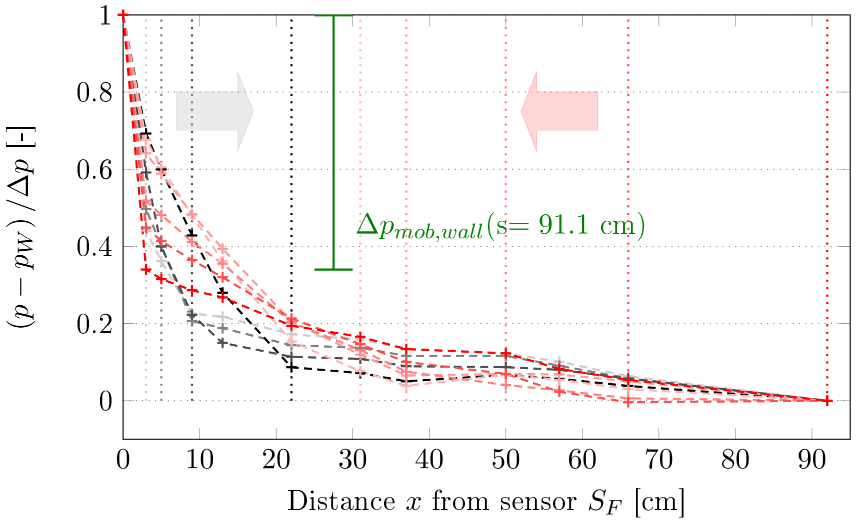

(a) $_1$ANmix 0.75 dw

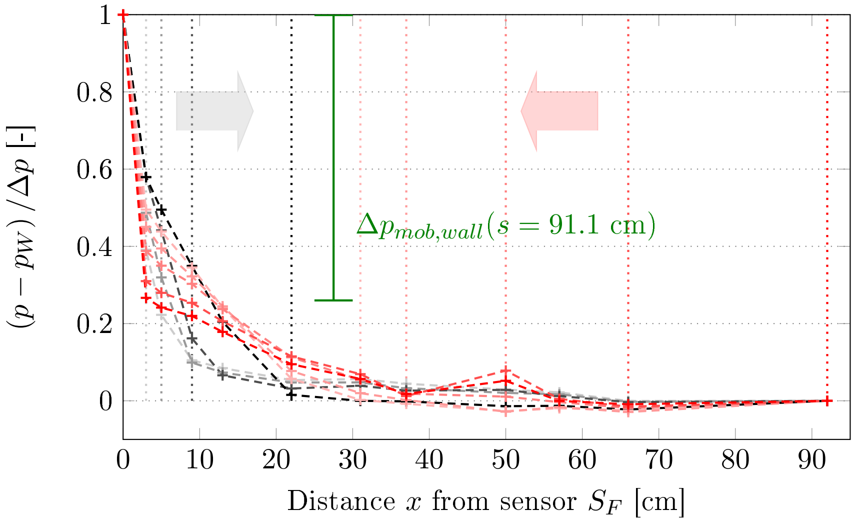

(b) $_1$ANmix 1.50 dw

Figure 3.34.: 0/2 mm – no additives – ANmix: Development of $p - p_W$ along the soil depth at $\Delta p \approx 0.15$ bar

slightly further for ANmix 0.75 than for ANmix 1.50. Then, this process reverses indicating the formation process of a pressure-absorbing earth wall membrane (Fig. 2.6c, red development in Fig. 3.34).

A quantification with respect to a mobilized earth wall pressure gradient of all polymer solutions mentioned previously is shown in Fig. 3.35 (penetration dependency) and Fig. 3.36 (time-dependency). The earth wall gradient is calculated according to Eq. 2.9 by assuming that the pore pressure drops between the filter sensor S_F and the first sensor in the sand $S1$ within the sand between the sensors of depth d_{ref} (Fig. 3.27) (Eq. 3.2):

$$f_{s0,wall} = \frac{p_F - p_{S1}}{d_{ref}} \tag{3.2}$$

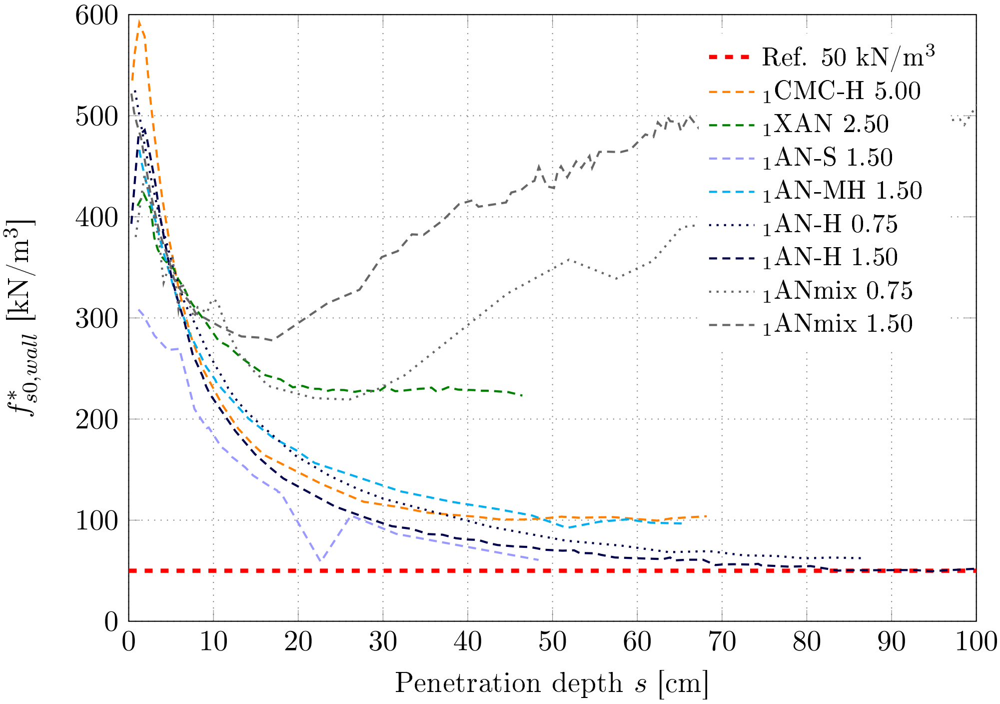

Figure 3.35.: 0/2 mm – no additives: penetration-dependency of pressure gradient at $\Delta p \approx$ 0.15 bar

A red reference line at 50 kN/m^3 is added following the quantification of the required earth wall gradient from Fig. 2.5 to visualize a critical limit (safe side, even lower for a 0/2 mm sand).

Fig. 3.35 illustrates the penetration-dependency of the mobilized earth wall gradient visible as a decreasing $f_{s0,wall}$ [6] , especially along the first cm of penetration. Following the previous observations, CMC-H, AN-MH and especially XAN show higher values. The curves of the ANmix solutions initially follow the same drop in $f_{s0,wall}$, but deviate around $s \approx 7-10$ cm reaching their lowest values of approximately 220-280 kN/m^3 around $s \approx 15-30$ cm and increasing subsequently. The subsequent increase correlates with the overall change of pressure curvature towards membrane formation and especially with a deviation from the penetration rate as compared to AN-H (fig. 3.30b).

As seen in Figs. 3.31a, 3.31b, 3.32a and 3.32b, the mobilized earth wall pressure and therefore $f_{s0,wall}$ for the polymers of natural origin visibly stagnate (or at least continue with negligible decrease) at a sufficiently high level (100 kN/m^3 for CMC-H 5 and 230 kN/m^3 for XAN 2.5) as compared to the AN range. Only AN-MH 1.50 could also be ranked similarly to CMC-H 5, but with a slightly higher decrease rate guaranteeing a sufficiently high pressure gradient for a few days at minimum. With respect to the medium level of anionicity, it can be noted that all curves reach a similarly low level of $f_{s0,wall}$ with similar penetration depths.

This effect is even more pronounced when scaled over time (Fig. 3.36), where XAN and CMC-

---

[6] The displayed earth wall gradient $f^*_{s0,wall}$ shows the pressure gradient corrected with reference to the applied overpressure level by $f^*_{s0,wall} = f_{s0,wall} \cdot \Delta p_{ref} / \Delta p_{measured}$ with $\Delta p_{ref} = 0.15$ bar. This correction is performed to exclude the influence of the changing fluid levels in the inflow and outflow containers, which are comprised in $\Delta p_{measured}$. The influence of the changing fluid heads is relatively small, but is magnified in relation to d_{ref}, which hinders an easy interpretation, in particular for values reaching the maximum possible $f_{s0,wall}$. This method is used in all following visualizations with $f_{s0,wall}$.

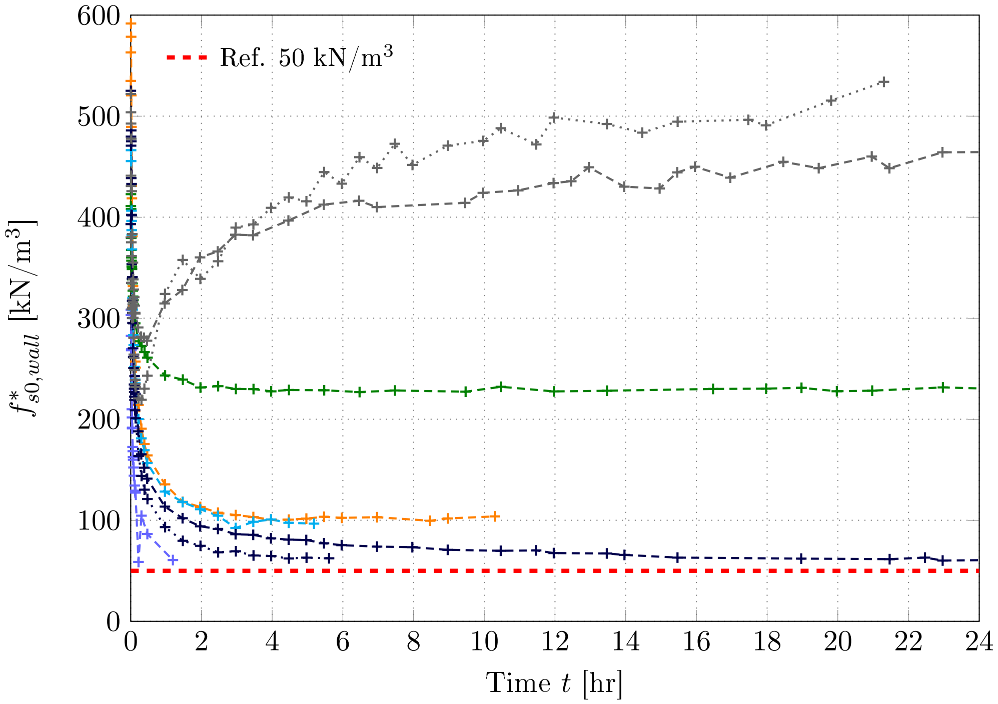

Figure 3.36.: 0/2 mm – no additives: time-dependency of pressure gradient at $\Delta p \approx 0.15$ bar

H seem to stay relatively constant after the first 2 hrs. Moreover, AN-H 0.75 and especially AN-S reach critical $f_{s0,wall}$ values significantly faster than AN-H due to lower viscosity. With ANmix, however, the higher penetration rate of ANmix 0.75 compared to ANmix 1.50 results in a slightly quicker build-up of $f_{s0,wall}$ and consequently also membrane formation, which is favourable for both internal and external stability.

In any case, both with respect to macro ($\Delta p_{mob}(t)$) and micro stability ($f_{s0,wall}(t)$), ANmix provides significantly higher pressure mobilization, with the effect even increasing over time. Especially for the stabilization of grains at the earth wall, this behaviour shows a clear advantage over its closest bulk rheological representative AN-H, for which internal stability may become critical in certain soils over time. In comparison, the safety level of CMC-H and especially XAN seems sufficiently high with negligible decrease over time even at this lower boundary pressure level of 0.15 bar, so time effects are not likely to become critical for micro stability in these soil conditions.

0.1/0.4 mm: penetration and pressure relationships

Fig. 3.37-3.40 show the results for two tests performed with fine soil material. CMC-H 2.50 and AN-H 0.75 are chosen as two representatives of the respective groups. The lower concentration range is chosen to verify whether this amount suffices in a fine soil. The two tests are compared in every plot to their closest representatives from the previous tests with 0/2 mm soil. In terms of soil characteristics, deviations between the two soils range around $d_{10} = 0.2 \rightarrow 0.15$ mm $d_{50} = 0.45 \rightarrow 0.25$ mm and around half a decimal power for the hydraulic conductivity (Fig. 3.3).

When comparing the behaviour of the two polymer types in the 0.1/0.4 mm test material, it can be noted that both penetration behaviour and pressure development range at a relatively similar level.

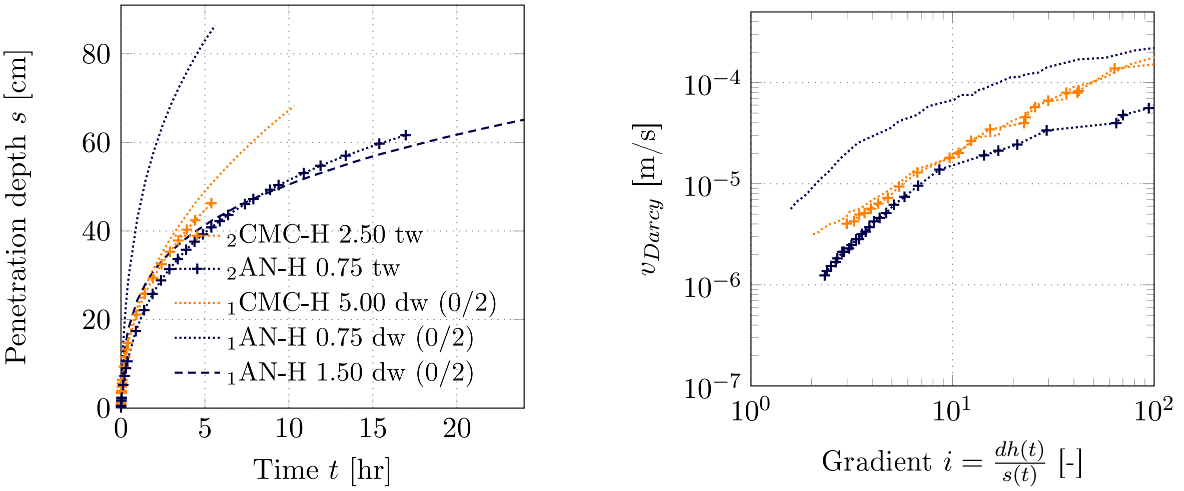

Figure 3.37.: 0.1/0.4 mm – no additives: development of penetration behaviour at $\Delta p \approx 0.15$ bar

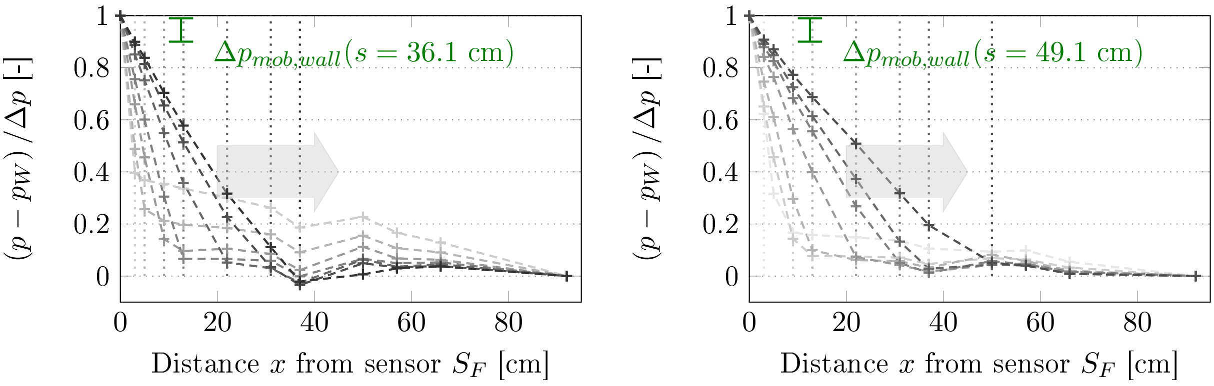

(a) $_2$CMC-H 2.50 tw

(b) $_2$AN-H 0.75 tw

Figure 3.38.: 0.1/0.4 mm – no additives – CMC-H/AN-H: development of $p - p_W$ along the soil depth at $\Delta p \approx 0.15$ bar

In comparison to the 0/2 mm tests, their penetration development matches the results of the higher concentration representative in the coarser soil material relatively well. For AN-H 0.75 in 0/2 towards AN-H 0.75 in 0.1/0.4, this amounts to a halving of the penetration depth down to ca. 40 cm at 5 hrs, even though tap water is used as mixing water instead of deionized water. A comparison within the $v - i$ plot shows a vertical shift (for AN-H nearly one decimal power) due to the decrease in soil permeability. Around $i = 3$ ($s = 50$ cm), the penetration rate ranges around $4 - 7 \cdot 10^{-}6$ m/s (1-3 cm/hr).

The pressure curvature following the penetration depth is visibly flatter in this finer soil material (Fig. 3.39). Deviations compared to a linear pressure drop now only amount to a maximum of approximately 10 %. Maybe this can be explained by conformational restrictions of the polymer chains during flow through the more narrow pore channels. This affects the earth wall pressure gradient $f_{s0,wall}$ to a larger extent for CMC-H resulting in values near the critical reference line.

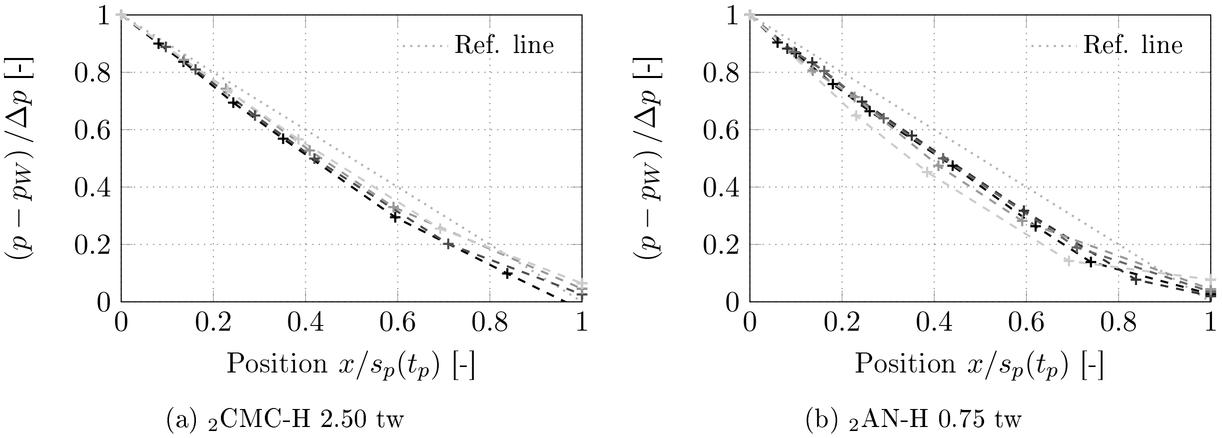

(a) $_2$CMC-H 2.50 tw (b) $_2$AN-H 0.75 tw

Figure 3.39.: 0.1/0.4 mm – no additives – CMC-H/AN-H: normalized pressure drop curvature along the penetration depth s_p: 0/2

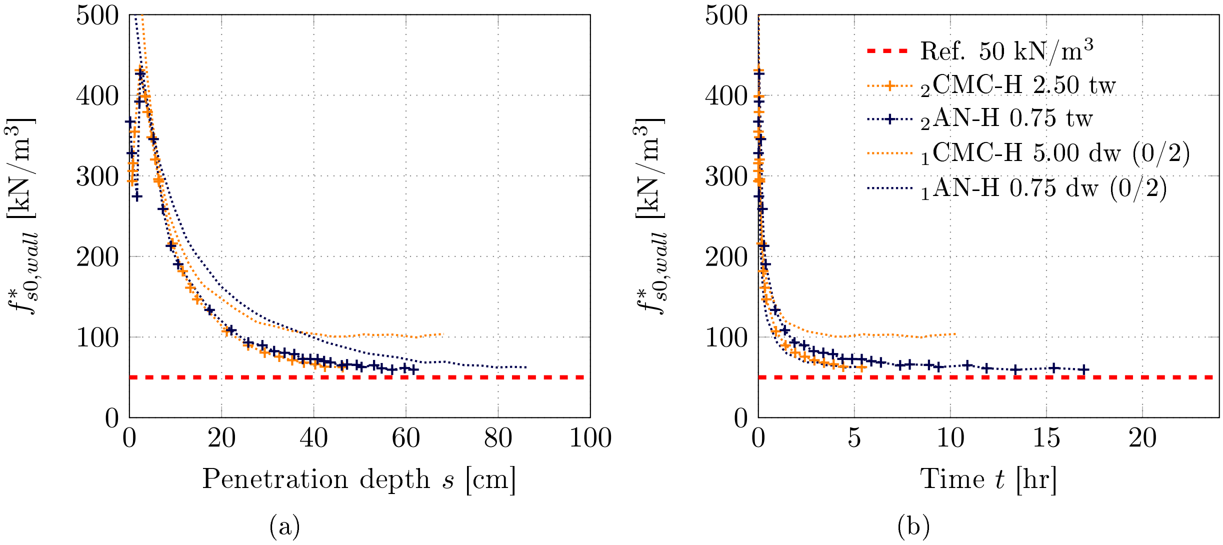

(a) (b)

Figure 3.40.: 0.125/0.355 mm – no additives: penetration- and time-dependency of pressure gradient at $\Delta p \approx 0.15$ bar

Higher pressure

The overpressure levels Δp of all tests were raised at the end of each penetration test (i.e. after different penetration times and depths) in steps from 0.15 bar up to 0.7 bar.

Tab. 3.5 gives an overview on related values, in particular the earth wall pressure gradient and the filter velocities, for Δp 0.3 bar and 0.7 bar, respectively. With increasing overpressure, $f_{s0,wall}$ increases in all cases, with a lower increase in the finer soil where the pressure curvatures are flatter. Filter velocities range in the order of 10^{-5} m/s within the first hour after increasing the pressure level.

Fig. 3.41 shows the resulting normalized pressure drop curvatures of a representative selection. It can be seen that the curvatures do not markedly change when Δp is increased, except for the earth wall pressure drop for CMC-H 5 and XAN 2.5. A pressure drop of approximately 20%

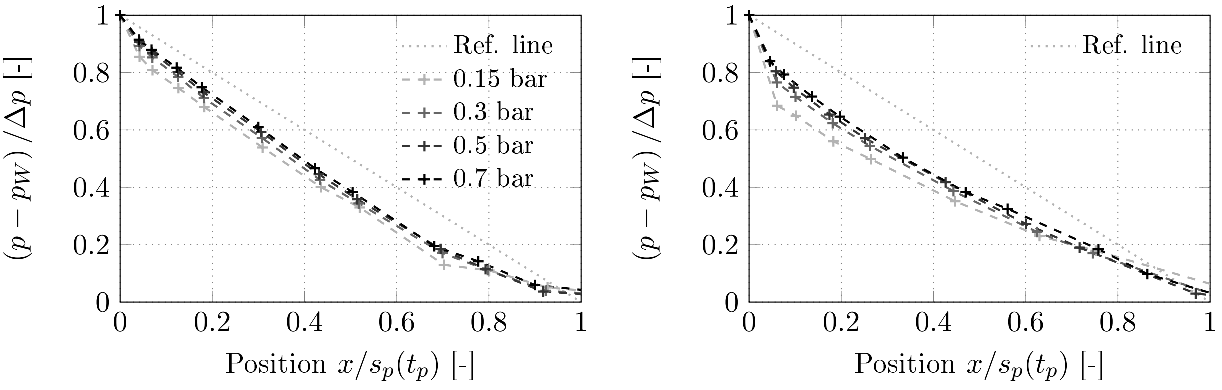

(a) $_1$CMC-H 5.00 dw

(b) $_1$XAN 2.50 dw

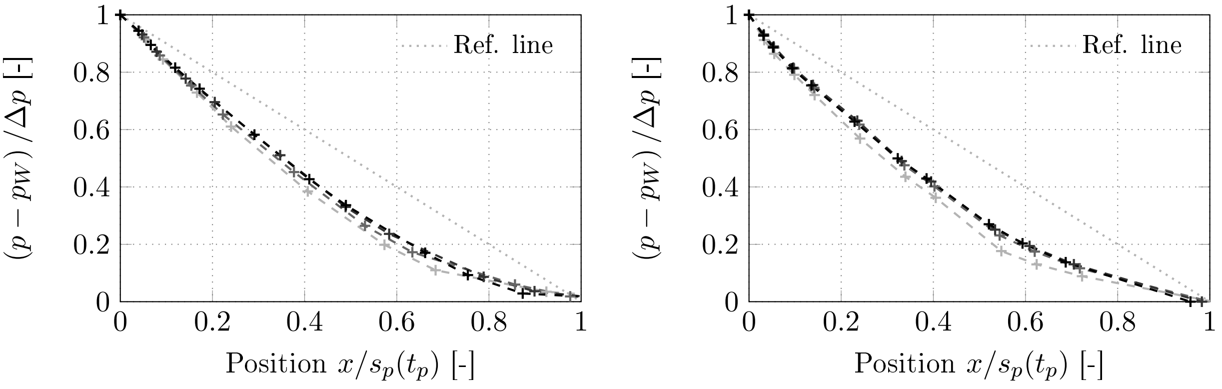

(c) $_1$AN-S 1.50 dw

(d) $_1$AN-H 0.75 dw

Figure 3.41.: 0/2 mm – no additives – normalized pressure drop curvature at higher pressure levels

immediately at the earth wall is still maintained for XAN. CMC-H still reaches approximately 10-15%. It is possible that this reduction results from the relatively sudden change of pressure levels applied during the test, i.e. it may reform. However, as a safe-side choice, the pressure drop curvatures presented here should be used as a reference for stability calculation.

Table 3.5.: No additives – pressure gradient and filter velocity ranges at higher overpressure levels (0.3 / 0.7 bar)

	soil [mm]	v_{Darcy} [m/s]	$f_{s0,wall}$ [kN/m^3]	s [cm]	t [hr]
AN-S 1.50	0/2	$0.5 \cdot 10^{-4}$ / $1.4 \cdot 10^{-4}$	110 / 180	48 / 69	1.2 / 1.45
AN-H 0.75	0/2	$1.7 \cdot 10^{-5}$ / $7.5 \cdot 10^{-5}$	100 / 230	87 / 91	5.6 / 5.7
CMC-H 5.00	0/2	$1.9 \cdot 10^{-5}$ / $2.5 \cdot 10^{-5}$	150 / 280	68 / 70	10.3 / 10.5
XAN 2.50	0/2	$0.9 \cdot 10^{-5}$ / $2.3 \cdot 10^{-5}$	320 / 530	46 / 63	46 / 47
AN-H 0.75	0.1/0.4	$0.9 \cdot 10^{-5}$ / $1.4 \cdot 10^{-5}$	70 / 160	62 / 70	17.2 / 17.9
CMC-H 2.50	0.1/0.4	$0.5 \cdot 10^{-5}$ / $2.3 \cdot 10^{-5}$	70 / 135	47 / 52	5.5 / 5.8

3.3.3. Discussion on the applicability of capillary bundle approximations

Fig. 3.42 shows the experimental results (marked as 'x' and '+') of the penetration development over time compared to their best-fit capillary bundle approximations (solid lines) based on Eq. 2.22 in combination with Eq. 2.23. The respective curve-fitting parameters are listed in Tab. 3.6. The approximations were performed in two steps

(1) Bulk rheology approximation: κ, m
(2) Capillary bundle approximation: α^*, $\dot{\gamma}_{crit,max\eta}$, $\dot{\gamma}_{crit,min\eta}$

The approximation steps are illustrated exemplarily for two tests in Fig. 3.43-3.44. The solid black lines show the experimental results for bulk rheology (a) and filter velocity (b). The remaining tests are summarized in Fig. 3.45-3.47 only with visualization of bulk vs. capillary bundle rheology. The same confrontation of rheology vs. filter velocity for these tests can be found in appendix D.5.

The blue dashed line in every rheology plot (a) shows the bulk rheological power-law approximation termed 'OdW'[7] fitted to the chosen region (step 1). Especially for the AN polymers of larger molecular weight, the bulk rheology curves were not found to follow an ideal straight line leading eventually to a Newtonian plateau as e.g. the CMC-H or the AN-S curves. It could therefore be suggested that κ and m should be defined to create average curves. However, the resulting $m_{average}$ values did not match the slope of the experimental $v - i$ data curves ((b) plots). A parameter m based on power-law approximation at high shear rates, on the other hand, was found to fit in every case. This region is not necessarily representative for the overall bulk rheology of the tested fluid (appendix C.6).

Capillary bundle approximation (step 2) comprised the determination of correction factor α^* and critical shear rates $\dot{\gamma}_{crit,max\eta}$ and $\dot{\gamma}_{crit,min\eta}$ so that penetration level $s(t)$ and respective

Table 3.6.: Power law and capillary bundle approximation parameters

Fluid	Power law [a]		Soil	Capillary bundle [b]					
	κ [Pa·s]	m [-]	d [mm]	α^* [-]	$\alpha^* \cdot \kappa$ [Pa·s]	$\dot{\gamma}_{max\eta}$ [1/s]	$\dot{\gamma}_{min\eta}$ [1/s]	η_{max} [c] [Pa·s]	η_{min} [c] [Pa·s]
XAN 2.50 dw	0.92	0.35	0/2	0.85	0.78	0.16	25	2.57	0.1
CMC-H 5.00 dw	2.00	0.42	0/2	0.25	0.5	1.8	2.5	0.36	0.29
CMC-H 2.50 tw	0.40	0.55	0.1/0.4	0.3	0.12	3.6	7	0.07	0.05
AN-H 1.50 dw	0.50	0.43	0/2	1.30	0.65	0.14	6.5	1.99	0.22
AN-H 0.75 dw	0.20	0.50	0/2	0.64	0.13	0.15[d]	6	0.33[d]	0.05
AN-H 0.75 tw	0.15	0.55	0.1/0.4	0.95	0.14	0.15[d]	5	0.33[d]	0.07
AN-MH 1.50 dw	0.50	0.43	0/2	0.48	0.24	2.9	5.0	0.13	0.1
AN-S 1.50 dw	0.80	0.35	0/2	0.45	0.36	8	11	0.09	0.08

[a] Approximation based on bulk rheological characterization (rheometer) at high shear rates
[b] Approximation based on soil permeation tests
[c] $\eta_{ref} = \kappa \cdot \dot{\gamma}_{crit,ref}^{m-1}$
[d] Assumed, not measured within the tested range

---

[7] power-law approach by Ostwald and de Waele

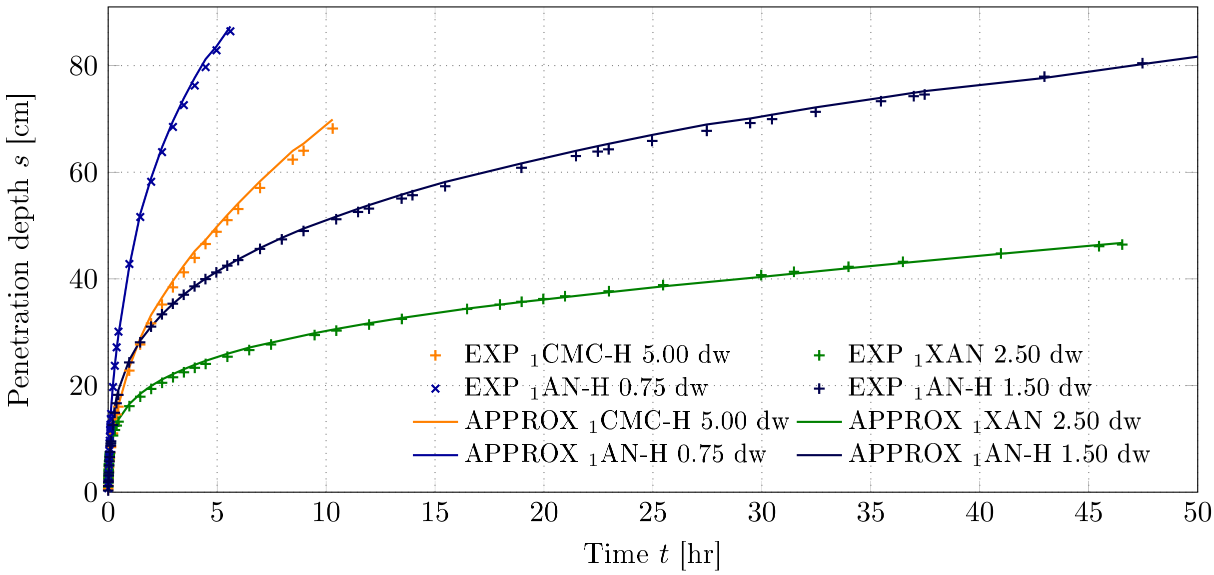

(a) 0/2 mm

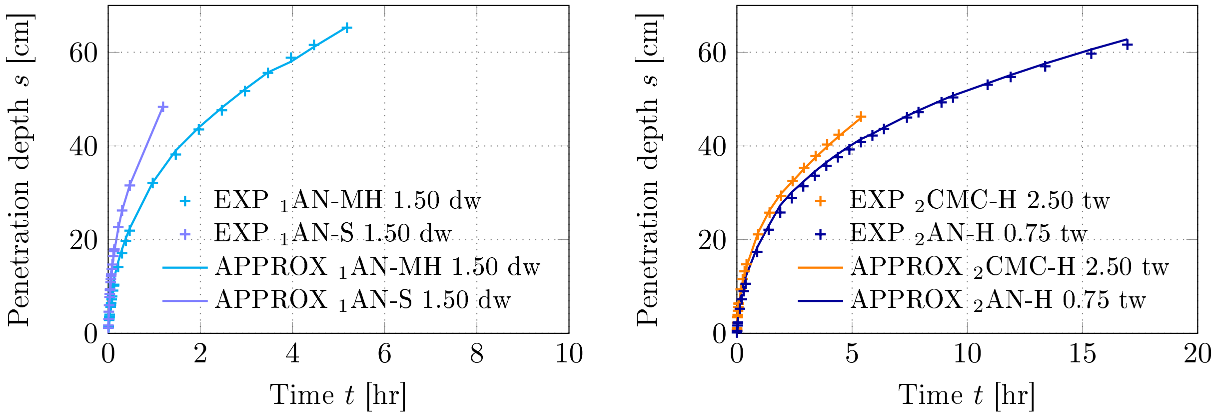

(b) 0/2 mm

(c) 0.1/0.4 mm

Figure 3.42.: Capillary bundle approximation for the penetration depth at $\Delta p \approx 0.15$ bar

penetration rates are adequately captured. This coincides with a good fit of the experimentally obtained filter velocity $v_{EXP} = \Delta s_{EXP}/\Delta t$ with v_{approx} (Eq. 2.21) and generally with the numerical derivation $\Delta s_{approx}(t)/\Delta t$ (Eq. 2.22) ((b) plots), if plateau behaviour is taken into account. The determination of Newtonian plateaus was performed on the basis of the considerations by Steinhoff (1993), but with different limit criteria for the implementation of the critical shear rates. They were implemented to immediately match the deviation in $v - i$ found with experiments. This procedure is described in appendix D.5. An exemplary display of the influence of the individual approximation parameters α^*, $\dot{\gamma}_{crit,max\eta}$ (η_{max}) and $\dot{\gamma}_{crit,min\eta}$ (η_{min}) on the resulting approximation curve for the penetration depth of XAN 2.50 can be found in appendix D.5.2. In essence, α^* creates dilution ($\alpha^* < 1$) or thickening ($\alpha^* > 1$). A lower viscosity plateau (η_{min}) modifies the approximation at the start of the penetration process (at high shear rates $\dot{\gamma}_i > \dot{\gamma}_{crit,min\eta}$). A higher viscosity plateau (η_{max}) influences the result at low flow velocities (at low shear rates $\dot{\gamma}_i < \dot{\gamma}_{crit,max\eta}$), i.e. with progressing penetration.

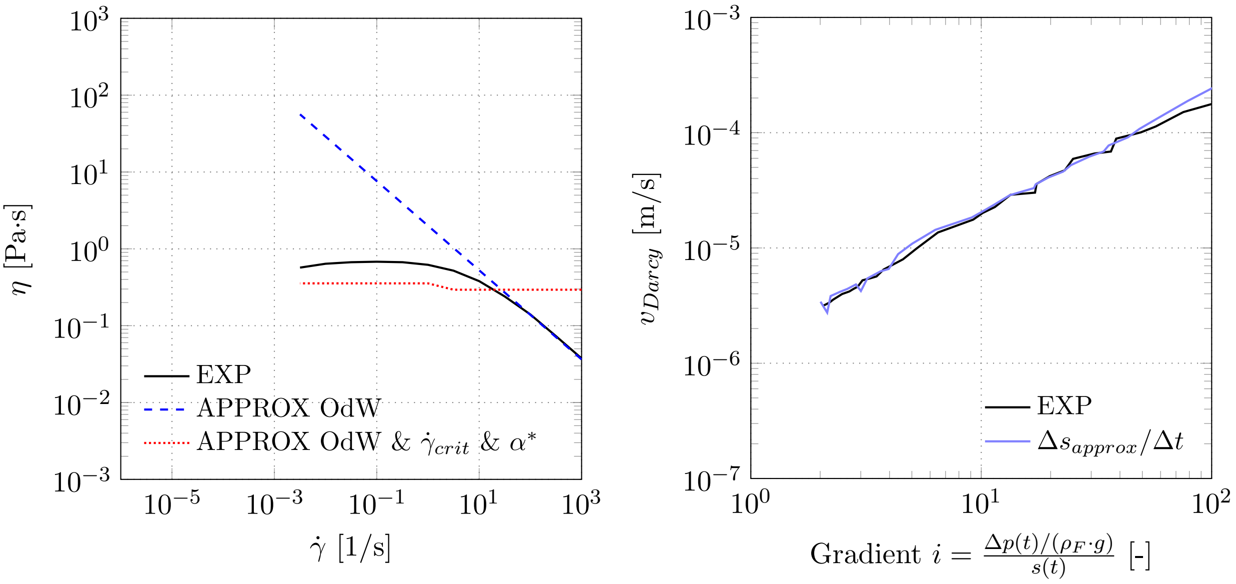

(a) Fluid rheology (b) Filter velocity

Figure 3.43.: Rheology and filter velocity approximation: 0/2 mm – $_1$CMC-H 5.00 dw

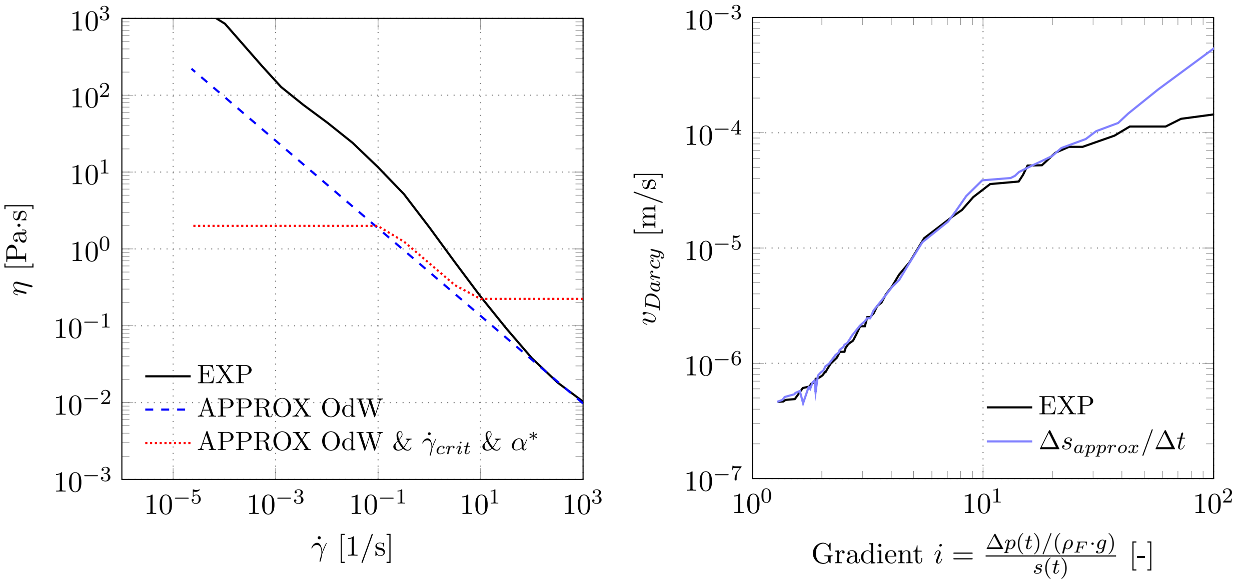

(a) Fluid rheology (b) Filter velocity

Figure 3.44.: Bulk rheology and filter velocity approximation: 0/2 mm – $_1$AN-H 1.50 dw

It can be seen in Fig. 3.42 that all experimental curves are matched relatively well, which underlines the applicability of the proportionality between s and $t^{\frac{m}{m+1}}$. α^*, $\dot\gamma_{crit,max\eta}$ and $\dot\gamma_{crit,min\eta}$ thereby seem adequate parameters to reflect deviations in polymer flow between bulk and in-pore behaviour also for an otherwise power-law approach.

For CMC-H 5 in 0/2 mm soil, a clear vertical shift can be seen between the bulk experimental and the capillary-bundle-corrected viscosity curve (Fig. 3.43). The same, though more pro-

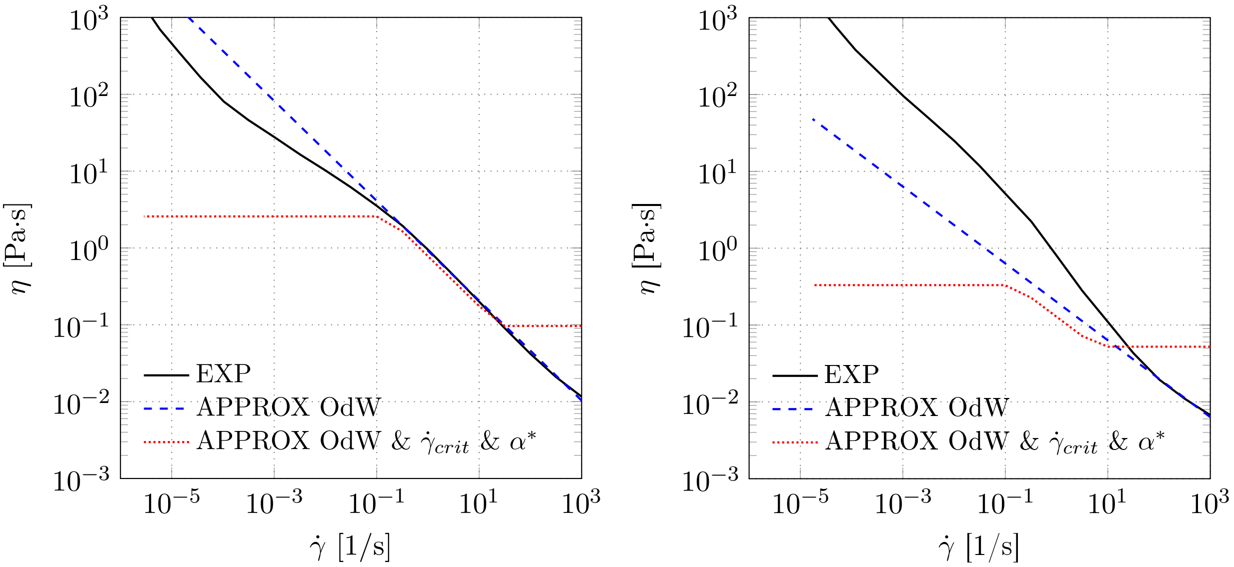

(a) $_1$XAN 2.50 dw

(b) $_1$AN-H 0.75 dw

Figure 3.45.: Bulk rheology and filter velocity approximation: 0/2 mm – fluid rheology

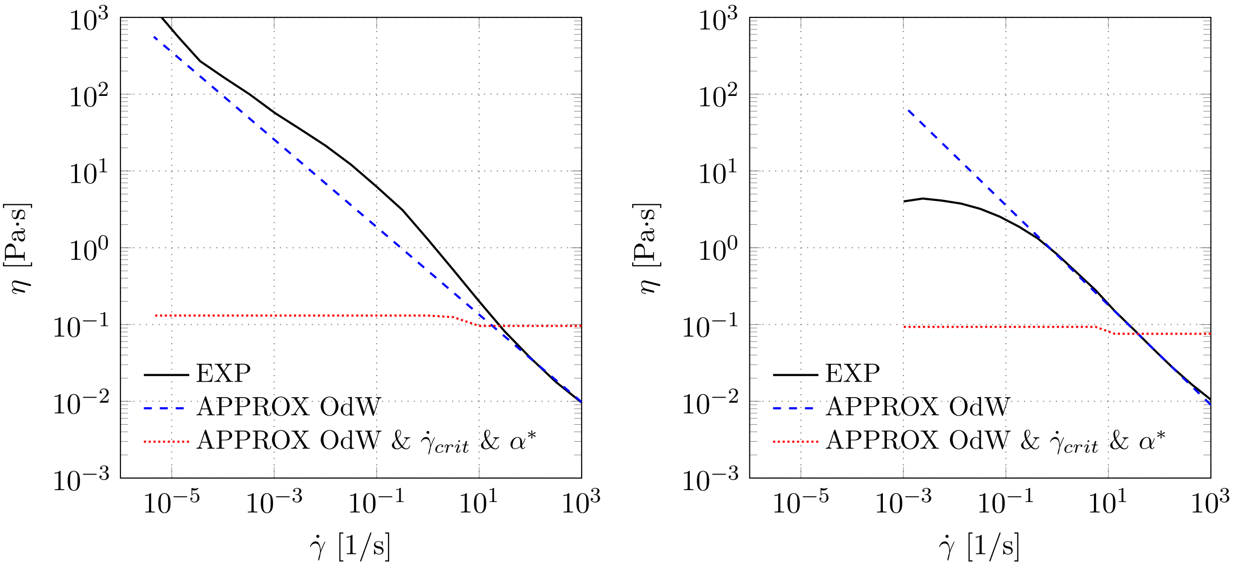

(a) $_1$AN-MH 1.50 dw

(b) $_1$AN-S 1.50 dw

Figure 3.46.: Bulk rheology and filter velocity approximation: 0/2 mm – fluid rheology

nounced, can be observed for the same polymer at lower concentration in finer soil (Fig. 3.47a). It is possible that this shift can be associated with depletion effects, according to which polymer chains arrange more towards the centre of the pores creating more dilute areas at the pore surface (section 2.3.1). A lower concentration increases the polymer mobility in the solution, which could explain why $\alpha^* \cdot \kappa$ is significantly reduced from CMC-H 5 (0.5) towards CMC-H 2.5 (0.12), despite a reduction in pore size from 0/2 towards 0.1/0.4. In the same porous environment,

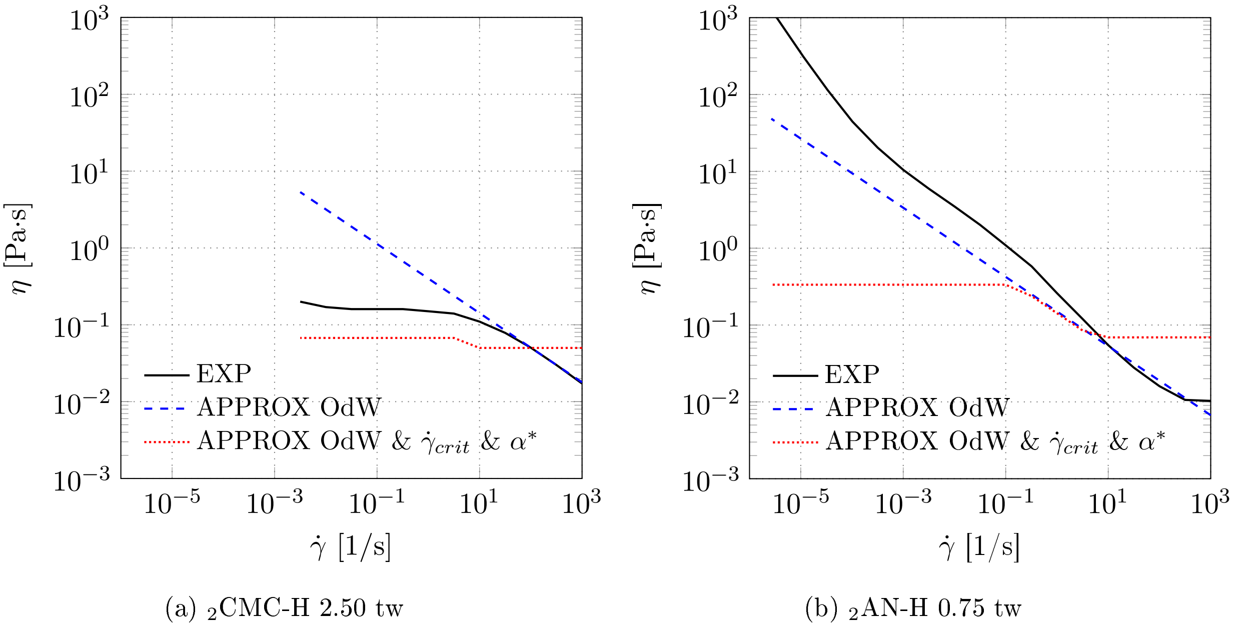

(a) $_2$CMC-H 2.50 tw

(b) $_2$AN-H 0.75 tw

Figure 3.47.: Bulk rheology and filter velocity approximation: 0.1/0.4 mm – fluid rheology

halving the concentration of AN-H from 1.50 towards 0.75, creates the similar diluting effect with $\alpha^*\kappa$ being reduced from 0.65 towards 0.13.

A direct comparison of the same polymer and concentration between the two soils (AN-H 0.75) is not immediately possible as two different types of mixing water were used, which have a significant effect on AN rheometer viscosity curves at low shear rates (Fig. C.4). But as κ is based on higher shear rates anyway, it may be assumed that comparability is possible. In any case, they reach similar values for $\alpha^* \cdot \kappa$ and the critical shear rate parameters. The conclusion may therefore be drawn that the capillary bundle parameters do not markedly change from medium to fine sand, they are rather influenced by a change in polymer concentration and polymer type.

With respect to plateau formation, it can be noted that only with CMC-H can the critical shear rate be directly associated with the respective shear rate for bulk behaviour. XAN 2.50 and the large molecular weight representative AN-H 1.50 show a relatively low value of 0.15 1/s. Higher values are clearly found with AN-S, but also significantly with AN-MH. With application of these critical shear rates, the maximum viscosity levels achieved by means of this capillary bundle approximation range around 2-3 Pa·s. It may be concluded that viscosity mobilisation (with related polymer conformation change) is indeed limited in the narrow soil pore system in comparison to the shearing environment of a rheometer or Marsh funnel. The maximum viscosity ranges seem relatively low compared to the values measurable with bulk rheology. However, compared to the bulk viscosity values of the tested bentonite suspensions with a maximum of 0.006 Pa·s at 60 g/l (C.10b), the displayed η_{max} values are still higher by a factor of 10-430.

This capillary bundle evaluation covers a broad range of gradients and can therefore be considered to be applicable to differing overpressure levels. With regard to the applicability of the achieved capillary bundle results for stability analysis, the question remains whether these results can be transferred to coarser soil materials. It is possible that the polymer-soil interaction differs when the soil pore sizes increase to a larger extent. It is equally unclear whether a larger amount of dissolved ions in solvents can still influence these parameters. These eight tests can be considered useful as a first reference.

3.3.4. Addition of quartz mineral grains

The influence of quartz mineral addition on the penetration and pressure transfer behaviour was studied based on 12 penetration tests. Quartz powder or a sequence of quartz grains were applied at concentrations of 1-160 g/l, i.e. at a maximum support fluid density of $\rho_{F,max} \approx 1.1$ g/cm^3. The quartz grains fractions are named according to Tab. 3.2. The following variations were considered:

- amount of additive (4 tests, 0/2 mm soil, with CMC-H)
    - ◇ $\mathrm{S}_{XS} = 1$ g/l
    - ◇ $\mathrm{S}_{XS} = 5$ g/l
    - ◇ $\mathrm{S}_{XS} = 10$ g/l (2x)
- type of polymer (5 tests, 0/2 mm soil, additive $\mathrm{S}_{XS} = 20$ g/l)
    - ◇ CMC-H
    - ◇ XAN
    - ◇ AN range with molecular weight variation (AN-S vs. AN-H)
    - ◇ synthetic mix polymer (ANmix)
- soil permeability (3 tests)
    - ◇ 0.5/1.2 mm soil, CMC-H & $\mathrm{S}_{XS/S} = 2x10$ g/l
    - ◇ 3/5 mm soil, XAN & $\mathrm{S}_{XS/G} = 4x40$ g/l (2x)

Fig. 3.48-3.61 summarize the results. If available, they are compared to the closest representative curves without additives from section 3.3.2. The visualizations are again differentiated into penetration and pressure relationships. Most tests presented here were performed for a longer duration than 24 hrs to determine the stability of the formed filter cakes over time without additional fines material available.

Overall, in the context of interpretation of the results presented below, it should be noted that the added grains will already settle in part in the inflow container before test start. Therefore, the amount of grains reaching the sand interface will be slightly lower. The concentration levels can therefore be considered a safe-side indication.

Penetration relationships

Fig. 3.48 shows the effect of the amount of quartz powder addition exemplarily with CMC-H 2.50 compared to CMC-H 5 without additive. It can be seen that a concentration of $\mathrm{S}_{XS}1$ seems to have no marked effect on the penetration behaviour with only a shift between CMC-H 2.50 and CMC-H 5 owing to the difference in polymer concentration. An increase to $\mathrm{S}_{XS}5$, however, shows a clear deviation of the penetration behaviour within the first 5-10 min leading to a near stagnation below 20 cm of penetration depth due to formation of a filter cake at the sand interface (Fig. 3.61). This filter cake is still visibly permeable to a certain extent with its permeability increasing to a certain extent after a few hours. A further increase in quartz concentration to 10 g/l decreases the maximum penetration depth and stabilizes the filter cake. Repeated testing (2 blue curves) further shows a small variability in the testing results, but 10-15 cm of penetration depth can still be considered relatively close and small. A likely explanation for the deviation is the homogeneity of the mixture, which results from not perfectly distributing the small quartz grains within the solution. Larger aggregates sink faster in the inflow container reducing the concentration reaching the sand. As all particles settle over time, the filter cake can

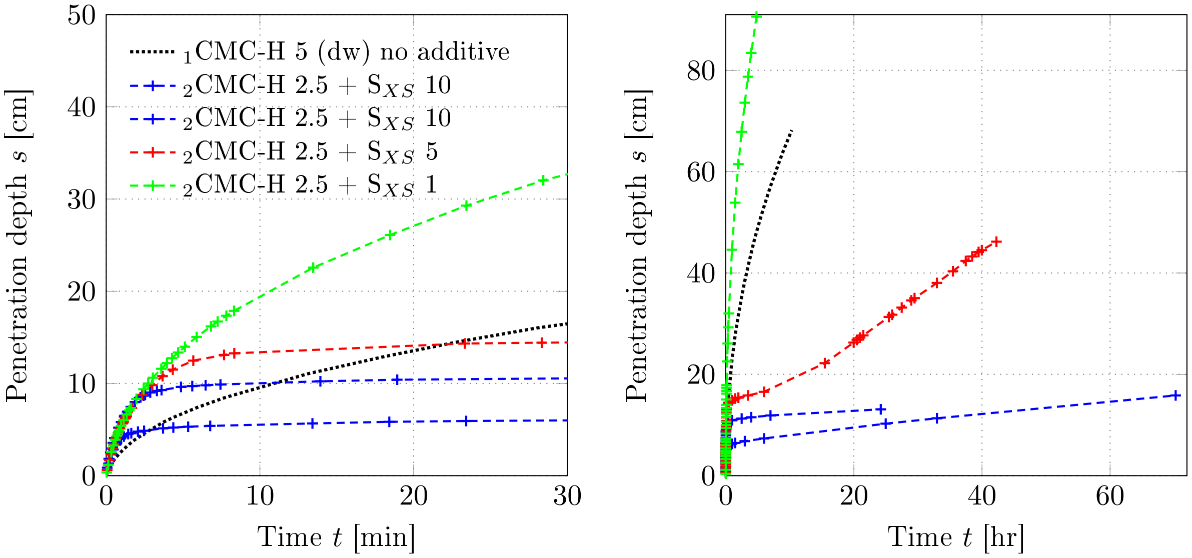

Figure 3.48.: 0/2 mm – variation of additive concentration – $_2$CMC-H tw: penetration behaviour

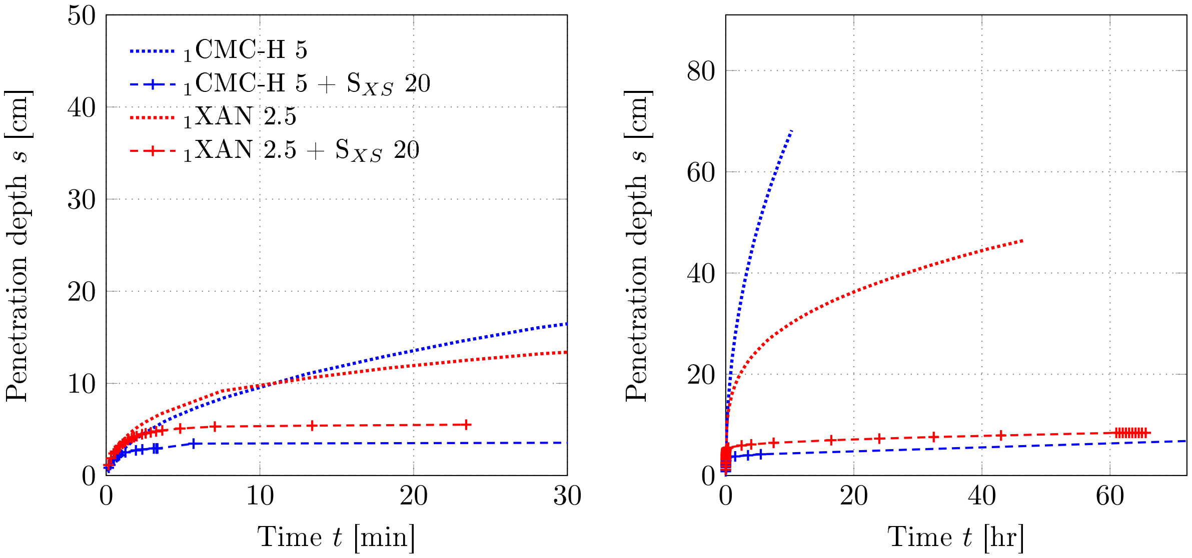

Figure 3.49.: 0/2 mm – quartz addition – CMC-H/XAN: penetration behaviour (dw)

only be built during the initial filtration and colmation process when the penetration velocity significantly surpasses the settling velocity of the grains. When the filter cake is formed and the penetration rate is significantly reduced, the fines concentration of the polymer solution consequently decreases and fewer and fewer grains reach the sand interface in this testing device with upwards flow. This underestimates the availability of fines as compared to real conditions.

A comparison of the effect of different polymer types was performed at a quartz powder concentration of 20 g/l, which is still considered relatively low with $\rho_F \approx 1.01$ g/l. It can be noted that the maximum penetration level for XAN 2.5, CMC-H 5 (Fig. 3.49) is comparably lower with a visibly less permeable filter cake. This can be attributed both to the increased fines concentration and the higher polymer concentration. A higher concentration level of XAN

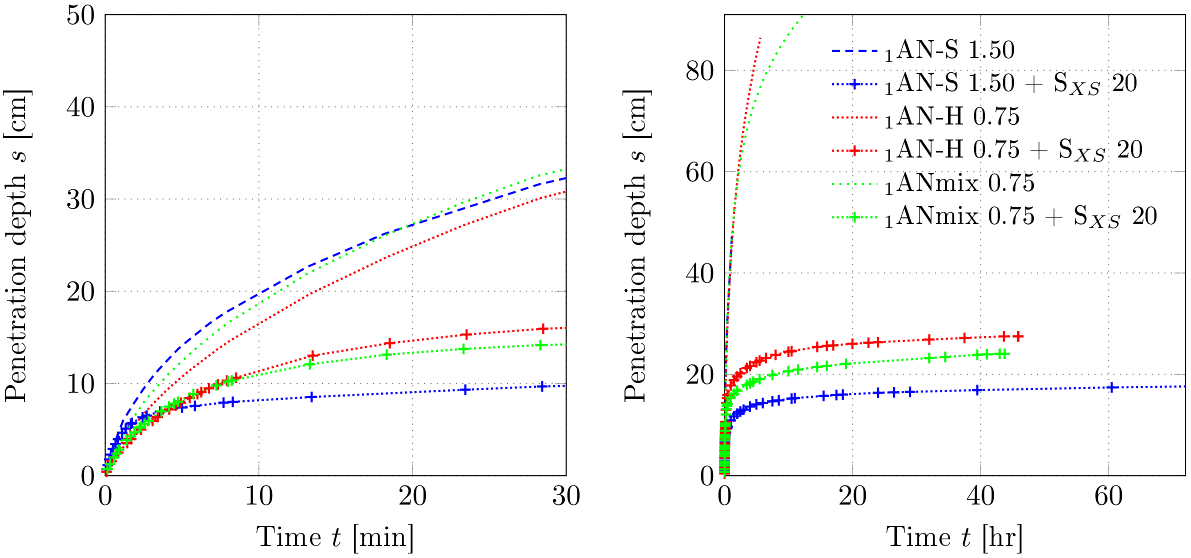

Figure 3.50.: 0/2 mm – quartz addition – AN-S/AN-H/ANmix: penetration behaviour (dw)

or CMC-H increases the fines carrying capacity and its viscosity, which concerns filter cake permeability.

The synthetic polymer products AN-S, AN-H and ANmix (Fig. 3.50) all show higher maximum penetration depths. It is possible that the effect can be attributed to testing tolerances. However, it is plausible that, for AN-S, this can be attributed to the lower fines carrying capacity. As quartz powder, even with small amounts of water, is not easily dispersed in AN solutions with long chains, it is possible that the actual fines concentration in AN-H and ANmix is slightly lower. Moreover, fines are not as available (given away as freely due to chain interactions) for colmation in these fluids. Furthermore, filter cake formation with the synthetic polymers takes significantly more time than with XAN or CMC-H (several hours). This is particularly interesting as the initial penetration rate of the tested AN products is higher as it is governed by the penetration behaviour of the respective 'clean' polymer solution (Fig. 3.28). In this context, CMC-H and XAN can be considered more effective.

Coarse sand (0.5/1.2 mm) and gravel (3/5 mm) were chosen to test the applicability of grain size distributions of fines in more critical (more permeable) ground conditions. The tests were performed with CMC-H and XAN only, because the AN polymers were not found to create colmation as effectively with larger fines fractions. This will be further addressed in the context of the larger property variation (V-S tests). Fig. 3.51 shows that a concentration of 20 g/l is still effective in creating a full filter cake in coarse sand with a reasonable maximum level of penetration depth. This can be partly attributed to the larger fines fraction (S_S). The lower fraction (S_{XS}), however, is still necessary to effectively block the soil pores. A broader quartz sequence necessary for gravel is equally effective, but a larger fines concentration is necessary to reach a similar maximum penetration level. An increase in soil permeability clearly leads to a quicker filter cake formation due to the increased penetration rate at penetration start.

Fig. 3.52-3.53 give an overview on the $v-i$ development of all tests with quartz grain addition. The visualizations show that the filter cake formation can be clearly seen as a deviation from the $v-i$ curve without additives. The lowest percentage of quartz addition (Fig. 3.52a CMC-H 2.5 + S_{XS} 1) shows no marked filter cake formation. In fact, a clear vertical shift can be

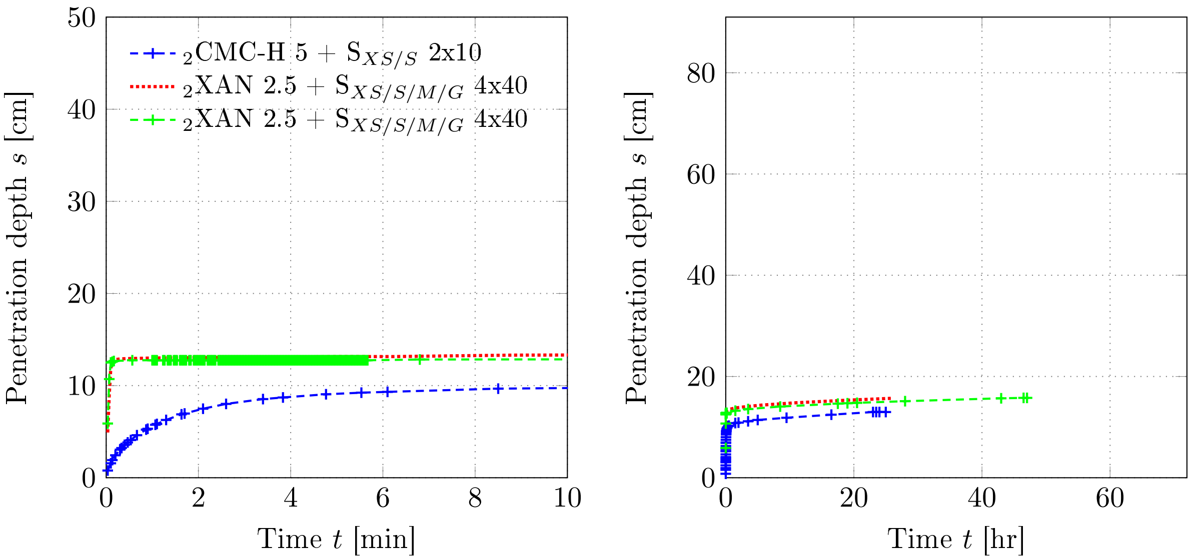

Figure 3.51.: Quartz sequence addition in 0.5/1.2 (CMC-H) and 3/5 (XAN): penetration behaviour (tw)

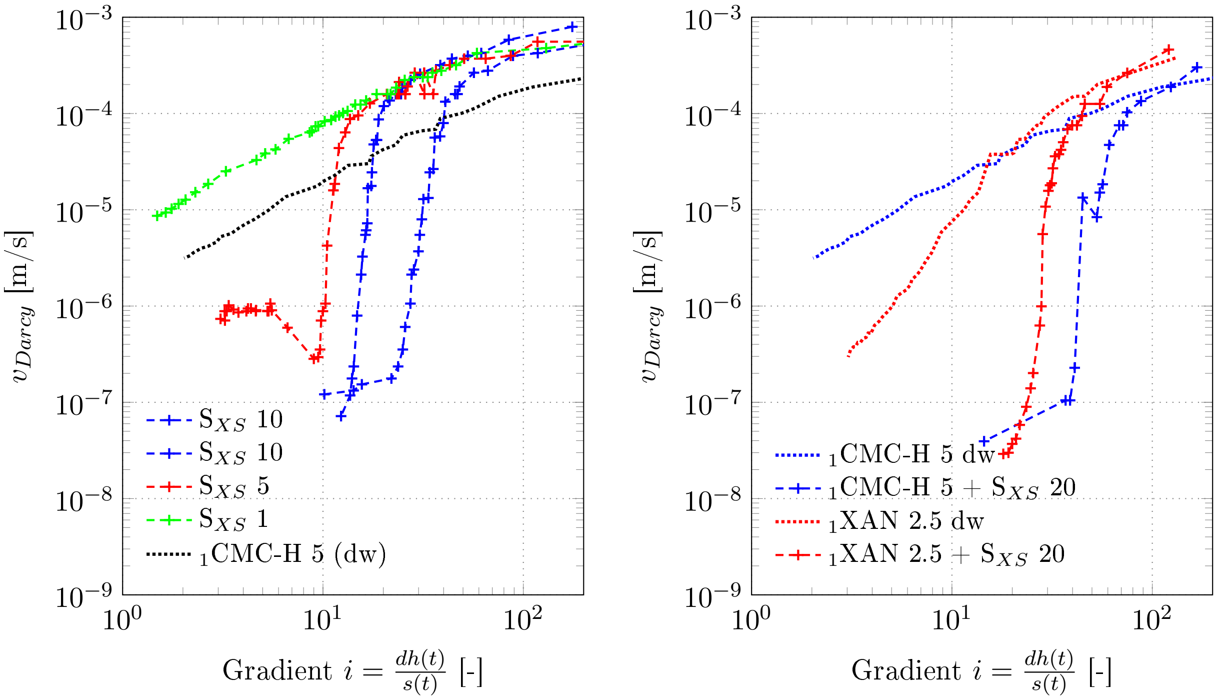

(a) $_2$CMC-H 2.50 tw – 0/2 mm

(b) $_1$CMC-H 5 / $_1$XAN 2.5 in 0/2 mm (tw)

Figure 3.52.: Variation of soil, polymer type and quartz additives: filter velocity with decreasing gradient (1)

noted compared to CMC-H at double concentration, which can be attributed to viscosity effects entirely. An increase of fines concentration to S_{XS} 5 already reduces the filter velocity, i.e. the

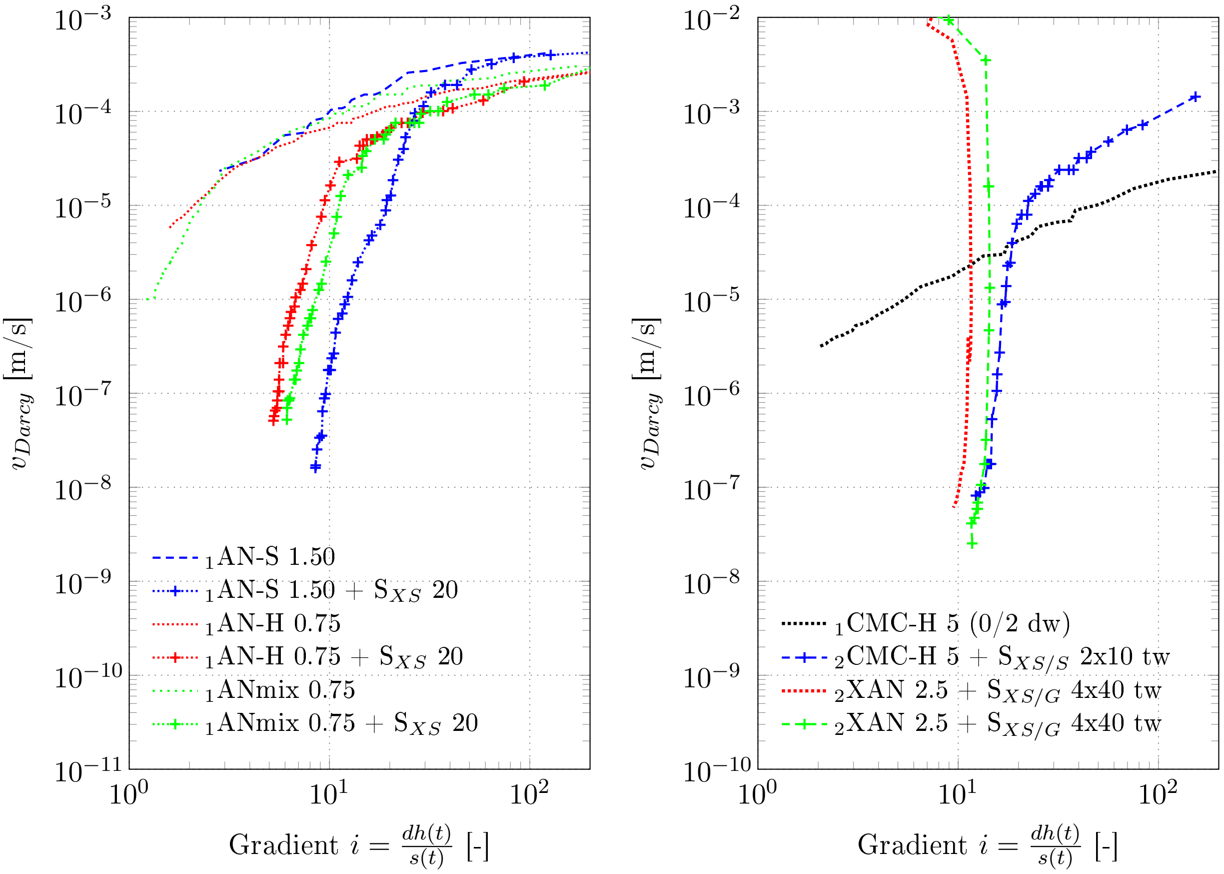

(a) $_1$AN-S/$_1$AN-H/$_1$ANmix in 0/2 mm (dw)

(b) $_2$CMC-H in 0.5/1.2 mm – $_2$XAN in 3/5 mm (tw)

Figure 3.53.: Variation of soil, polymer type and quartz additives: filter velocity with decreasing gradient (2)

residual filter permeability, to around $0.5 - 1 \cdot 10^{-6}$ 1/s stabilizing at $1 \cdot 10^{-6}$ 1/s. That is, even though the filter cake is not perfectly formed, it does not destabilize over time, it merely stabilizes at a higher residual filter cake permeability. Higher fines concentrations result in filter velocities stabilizing at at least one decimal power lower and in some cases even decreasing further over time. This colmation effect can also be reached in gravel.

Pressure relationships

Colmation is also clearly visible in the development of the pore pressure transfer to the ground, as can be seen in Fig. 3.54-3.55. In all cases, the effect of colmation manifests immediately at the earth wall and not, as could be suspected, along the full penetration depth.

Even S_{XS} 1 g/l (Fig. 3.54a) shows a starting colmation after approximately 40-50 cm of penetration depth, despite no marked changes for the penetration behaviour. This results in a pressure drop of approximately 30 % at 90 cm of penetration depth increasing slightly further with increasing penetration.

In every case, $\Delta p_{mob,wall}$ successively increases once the colmation takes effect on the pressure development. Thus remaining pressure curvature behind the colmating zone for CMC-H 2.5 +

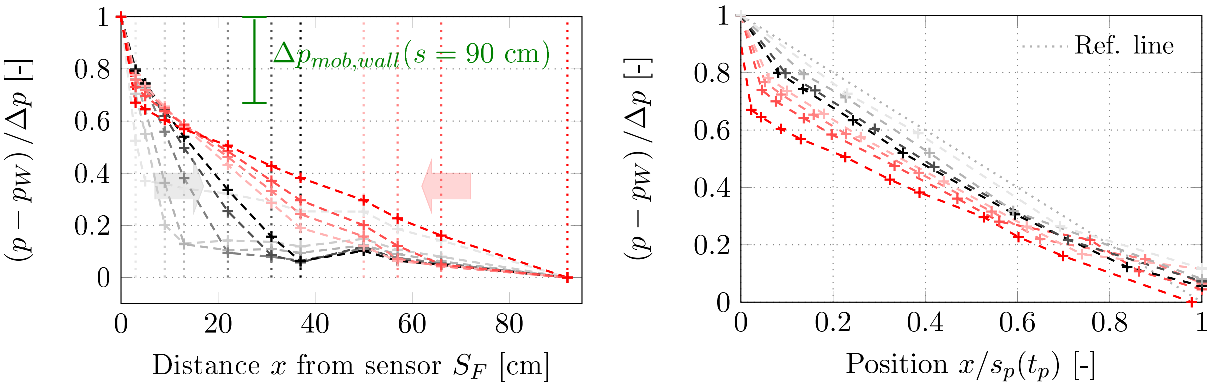

(a) $_2$CMC-H 2.50 (tw) + S$_{SX}$ 1 g/l

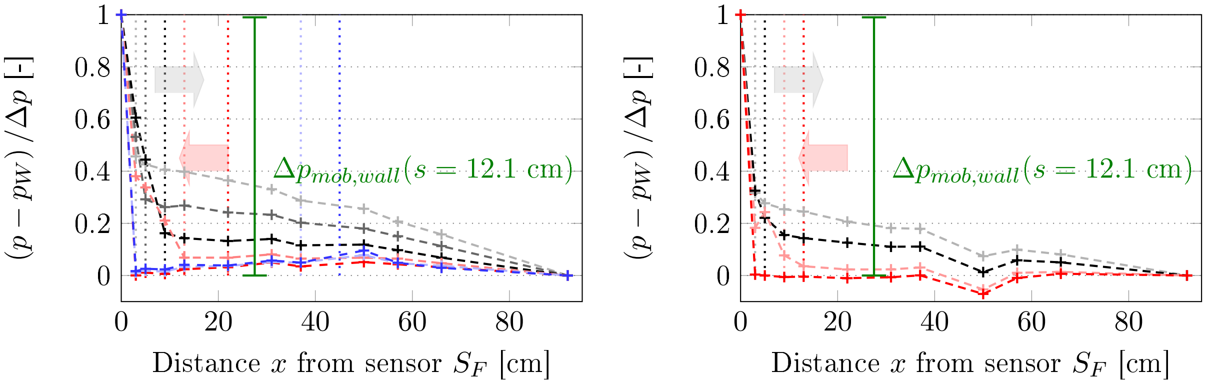

(b) $_2$CMC-H 2.50 (tw) + S$_{SX}$ 5 g/l (left) vs. S$_{SX}$ 10 g/l (right)

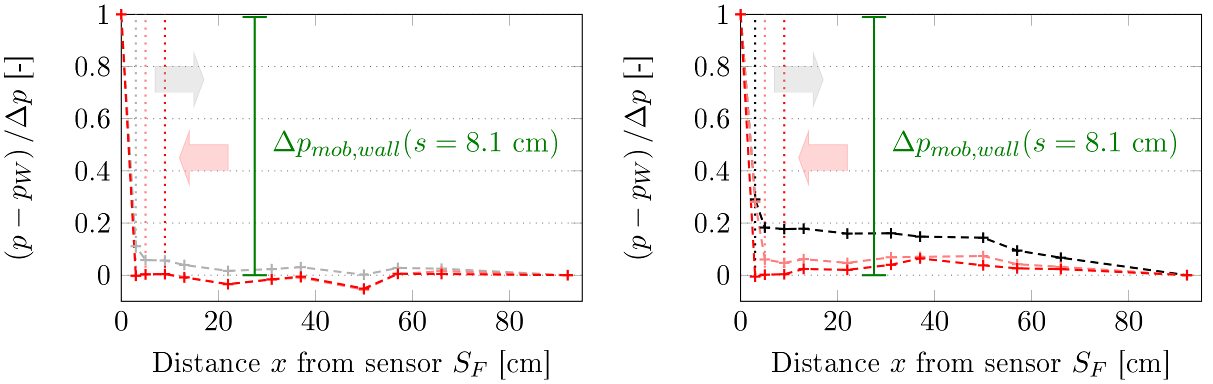

(c) S$_{SX}$ 20 g/l with $_1$CMC-H 5 (left) vs. $_1$XAN 2.5 (right) (dw)

Figure 3.54.: 0/2 mm – quartz addition – CMC-H/XAN: development of $(p - p_W)/\Delta p$ along the soil depth at $\Delta p \approx 0.15$ bar

S$_{XS}$ 1 is still moderately non-linear and is suspected to be similar in the other cases. Owing to the low penetration depths in the other cases, the actual curvature cannot be determined.

With 5 g/l of quartz powder, the main colmation process happens around 13-20 cm starting at around 60 % of pressure drop and quickly reaching full pressure transfer at the earth wall. The subsequent increase in filter cake permeability observed previously results in an additional

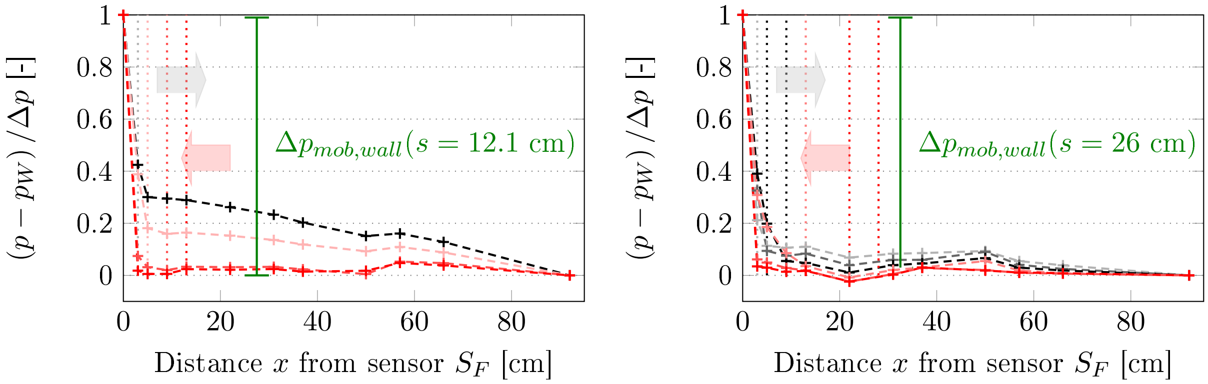

(a) $_1$AN-S 1.50 + S$_{SX}$ 20

(b) $_1$AN-H 0.75 + S$_{SX}$ 20

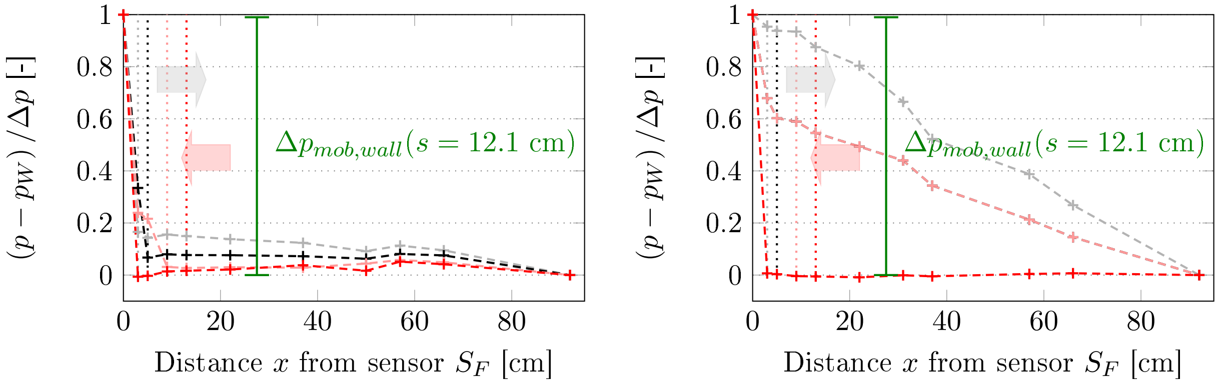

(c) $_2$CMC-H 5 + S$_{XS/S}$ 2x10 in 0.5/1.2

(d) $_2$XAN 2.5 + S$_{XS/G}$ 4x40 in 3/5

Figure 3.55.: Development of $(p-p_W)/\Delta p$ along the soil depth at $\Delta p \approx 0.15$ bar (tw) (2)

20-30 cm of penetration depth, but manifests only as a slight decrease of the mobilized pressure at the interface within a time period of 30 hrs down to 98 % (marked in blue).

An increase in fines concentration to 10 g/l already results in a full pressure transfer at the earth wall even below 10 cm of penetration. The same effect or faster can be observed with CMC-H 5 and XAN 2.50 at higher quartz concentration and soil permeability (Fig. 3.54c & Fig. 3.55c-3.55d). The long-chain polymer AN-H (Fig. 3.55b) needs a higher level of penetration depth to fully form the colmation zone. With the first 10 cm of penetration 70 % of Δp are transferred between the first two sensors and 95 % around 20 cm of penetration.

Fig. 3.56-3.57 show the dependency of the earth wall pressure gradient (Eq. 3.2) on time, displayed over the first 30 min of penetration (left) and over a maximum time span of 72 hrs (right). The red and black dashed lines show man/max values. The red line represents the critical reference line for 50 kN/m^3, the black line shows the maximum possible pressure gradient at $\Delta p = 0.15$ bar based on Eq. 3.2. It can be seen that the maximum level is reached eventually with all tests (except with S$_{XS}$ 1) with only marginal deviations over time when this level is reached. This reflects full pressure transfer at the earth wall.

Like the penetration behaviour, the development of $f_{s0,wall}$ with loaded fines initially follows the development of the curves of the same polymer at equal polymer concentration without fines, until the colmation process takes effect. An increase in the amount of fines then leads to an earlier deviation. With the polymers of natural origin, $f_{s0,wall,max}$ is reached within 5-20 min

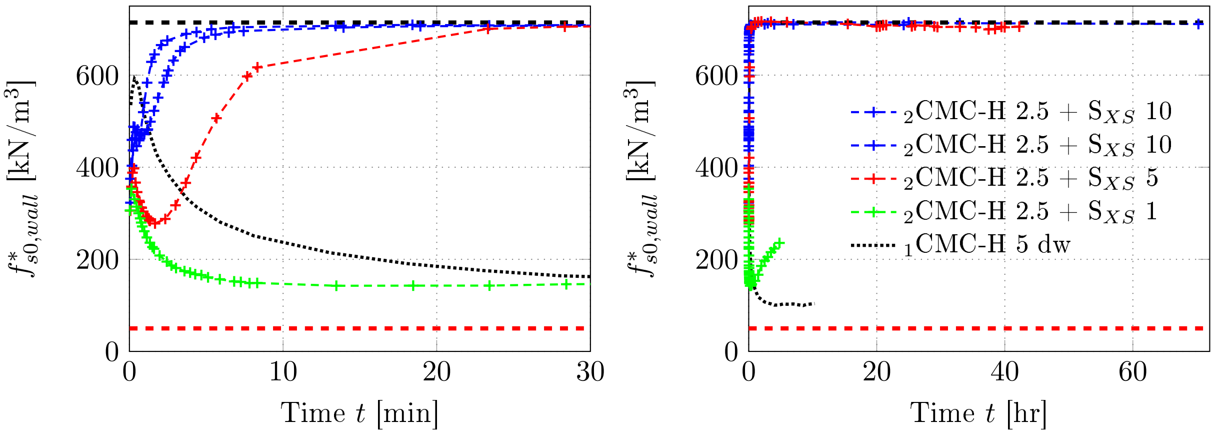

(a) CMC-H: variation of additive concentration (tw)

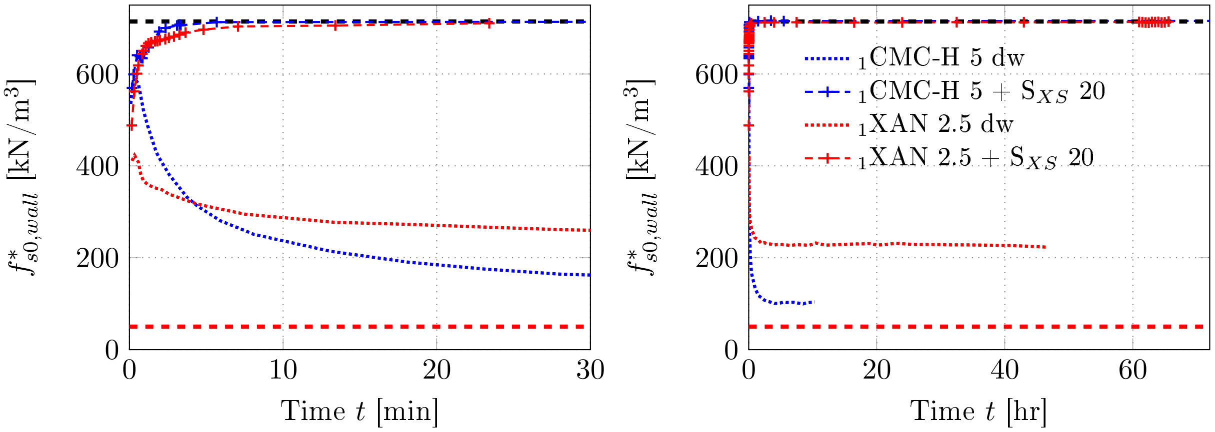

(b) CMC-H vs. XAN (dw)

Figure 3.56.: 0/2 – quartz addition – time dependency of pressure-gradient at $\Delta p = 0.15$ bar (1)

in sand and instantly in gravel depending on the amount of fines and the penetration rate. AN-S behaves similarly. AN-H and ANmix take significantly longer, as was already observed in the context of pressure curvature development. This cannot be attributed to the penetration rate as 'clean' XAN 2.50 and CMC-H 5 penetrate significantly slower than AN-H 0.75 or ANmix 0.75. Consequently, $f_{s0,wall,min}$ (at around 5-7 min for AN-H) reaches a comparably lower value than the respective minimum reached with CMC-H or XAN with the same added amount of additives.

However, in general, it is evident that the minimum earth wall gradient $f_{s0,wall,min}$ in all cases stays significantly above the critical level. Even a small amount as low as $\mathrm{S}_{XS} = 1$ g/l with CMC-H 2.50 already results in a sufficiently high level of $f_{s0,wall,min}$ above 100 kN/m^3. This shows that even a very small amount of fines taken up by the support fluid from the native ground can significantly increase the stability against the removal of grains from the earth wall in medium sand (Fig. 3.56a). In gravel, colmation happens so fast that no drop in $f_{s0,wall}$ can be measured.

It can be concluded that micro stability is not critical in all tested environments with added fines, even when considering an additional safety factor of 2. Long stand-up times do not markedly change the safety level, even though the filter cake needs to be stabilized vertically

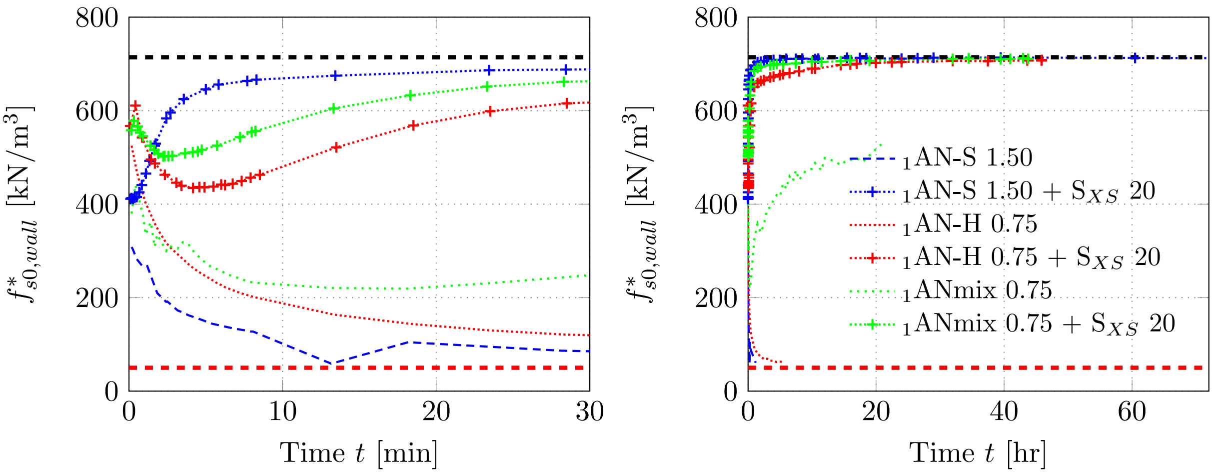

(a) 0/2: AN-S/AN-H/ANmix (dw)

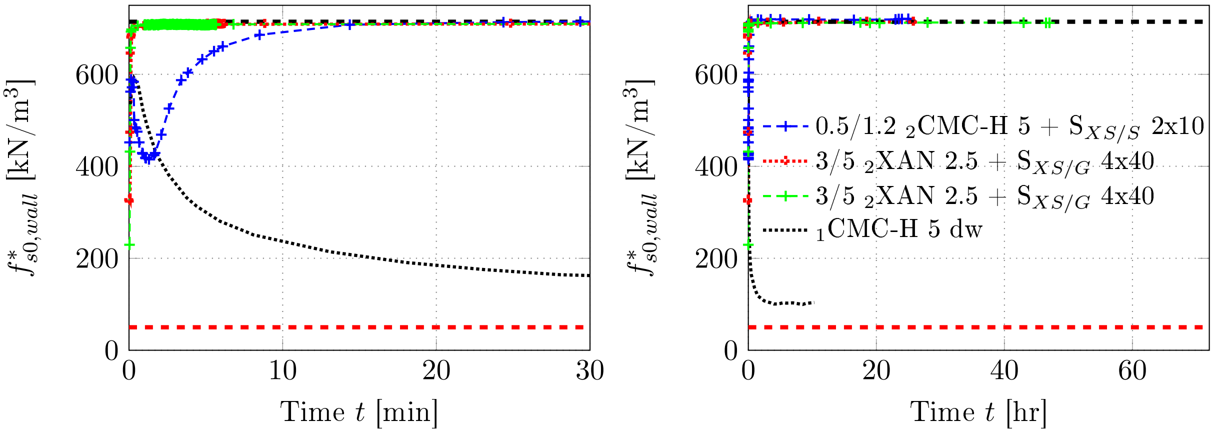

(b) 0.5/1.2: CMC-H | 3/5: XAN (tw)

Figure 3.57.: Time dependency of pressure-gradient at $\Delta p = 0.15$ bar (2)

in this testing device. This suggests that the colmated fines are fixed in the filter cake and do not easily settle. Only the test with $S_{XS} = 5$ g/l showed a small destabilizing effect after some hours, but the effect is seemingly insignificant with respect to the reached level of $f_{s0,wall}$.

For macro stability, the development of $\Delta p_{mob,wall}$ ($= p_F - p_{S1} = f_{s0,wall} \cdot d_{ref}$) with increasing penetration depth is essential for an evaluation of total mobilizable pressure, as $p_{mob,wall}$ also dictates the percentage of pressure transferred behind the colmation zone. Fig. 3.58-3.59 show a comparison of the development of the normalized mobilized earth wall pressure with the development of the filter velocity with increasing penetration depth. The figures reveal that the relevant penetration depths determining the development of $p_{mob,wall}$ coincide with the areas of deviation of v_{Darcy}. In particular, the critical penetration depth, at which the mobilized pressure at the earth wall reaches its minimum $\Delta p_{mob,wall,min}$, i.e. where colmation starts to take effect, matches relatively well the start of deviation of the $v - i$ curve with fines from the curve without fines (if the first 1-2 cm of penetration are ignored). Full pressure mobilization is reached around $v_{Darcy} \approx 1 \cdot 10^{-7}$ m/s, i.e. with a decrease in permeability of several decimal powers.

The decisive parameters $s_{crit,1}$ for the start of colmation and $s_{crit,2}$ for the completion of

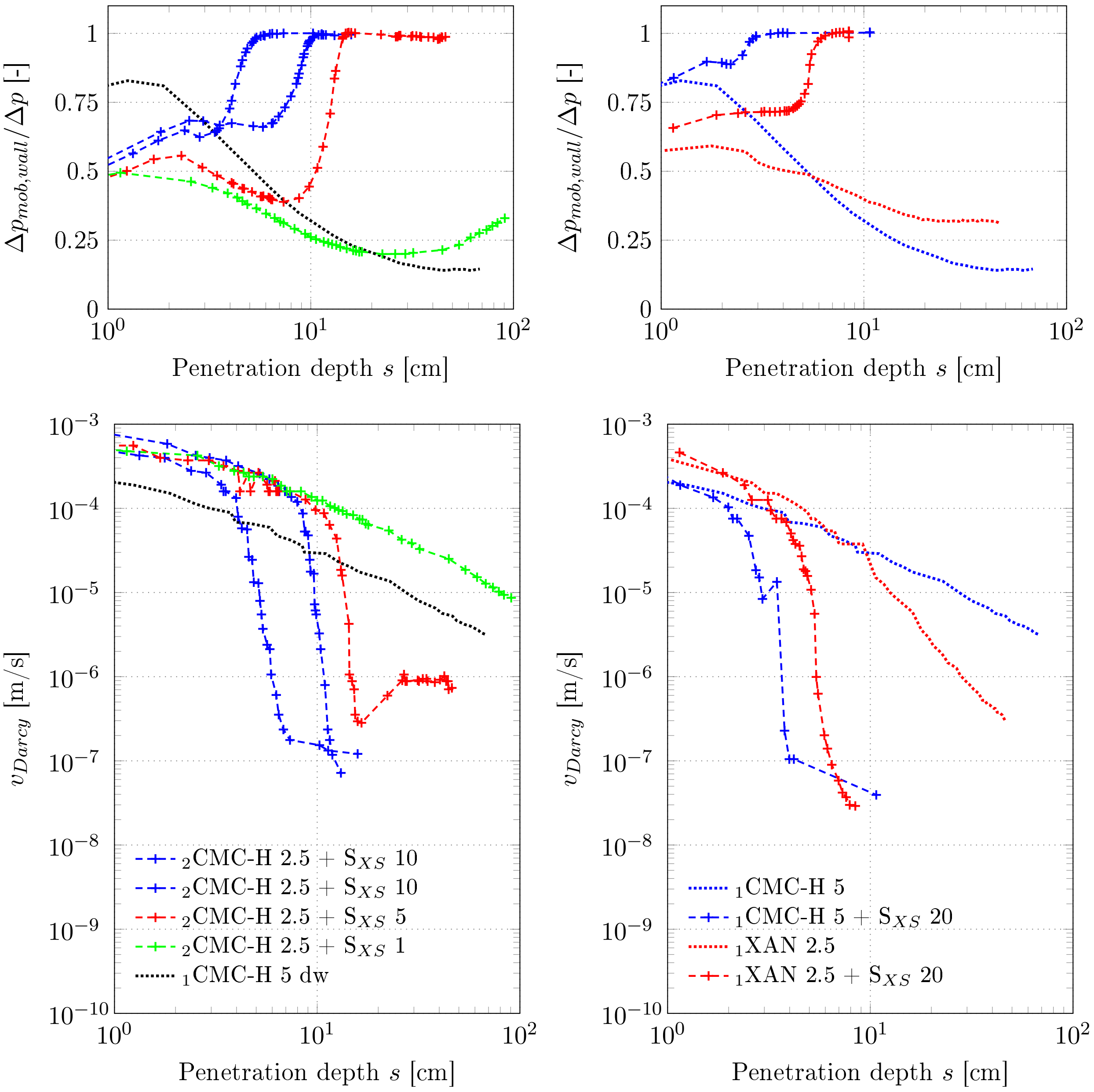

(a) $_2$CMC-H tw: variation of additive concentration (tw)

(b) CMC-H vs. XAN (dw)

Figure 3.58.: 0/2 – quartz addition – CMC-H/XAN: $\Delta p_{mob,wall}$ vs. v_{Darcy} at $\Delta p = 0.15$ bar

membrane formation are summarized in Tab. 3.7 for all tests with quartz mineral addition. It can be noted that the minimum mobilizable earth wall pressure $\Delta p_{mob,wall,crit,1}$ at a penetration depth $s_{crit,1}$ exceeds $0.5\Delta p$ in all cases except for the lowest quartz concentration and gravel. Evaluation of $s_{crit,2}$ emphasizes that XAN and CMC-H are more suitable for the usage of colmation effects with quartz grains than AN-H.

Stability evaluation can be based on these characteristic limit values (with consideration of a certain variation factor due to the limited repetition) as they reflect both the minimum mobilizable earth wall pressure and the maximum reference level for full pressure mobilization. This

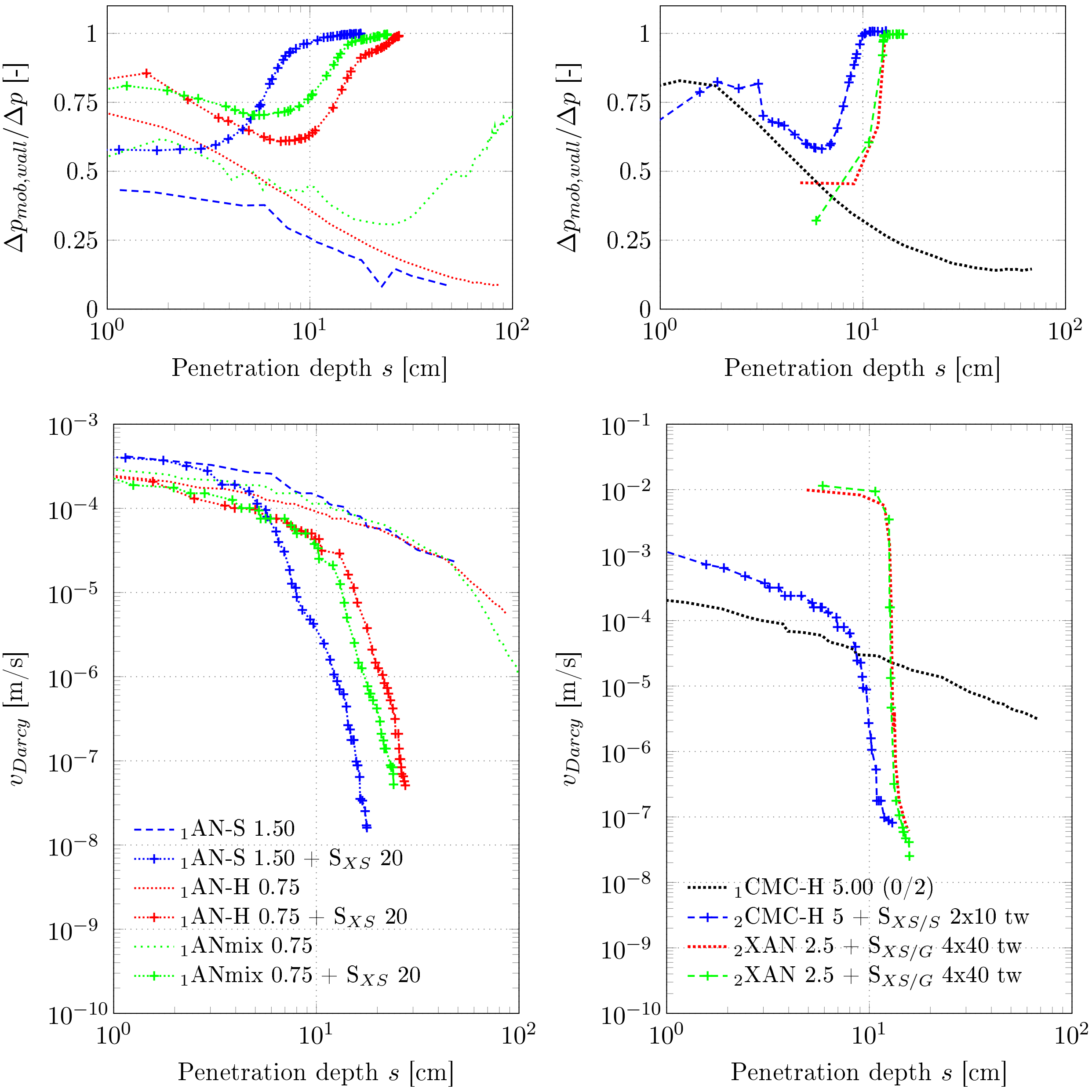

(a) AN-S/AN-H/ANmix dw in 0/2

(b) $_2$CMC-H tw in 0.5/1.2 mm vs. $_2$XAN tw in 3/5 mm

Figure 3.59.: 0/2 – 0.5/1.2 – 3/5: $\Delta p_{mob,wall}$ vs. v_{Darcy} at $\Delta p = 0.15$ bar

will be closer evaluated in section 4.1.

A further increase in pressure after several hours showed that membrane behaviour is equally effective at overpressure levels between 0.3 bar and 0.7 bar. Fig. 3.60 shows two examples.

In the context of further evaluation with small-scale tests (V-S), it can be assumed that the colmation effects encountered here can also be studied by means of small soil fractions as colmation happens at the earth wall.

Table 3.7.: Characteristic values for pressure-penetration relationships with quartz mineral grain addition and full membrane formation

Fluid	Additive	Soil [mm]	$s_{crit,1}$ [cm]	$\frac{\Delta p_{mob,wall,crit,1}}{\Delta p}$ [-]	$s_{crit,2}$ [cm]	$\frac{\Delta p_{mob,wall,crit,2}}{\Delta p}$ [-]
$_2$CMC-H 2.5 tw	S$_{XS}$ 5	0/2	9	0.4	14	1
$_2$CMC-H 2.5 tw	S$_{XS}$ 10	0/2	3-6	0.63-0.68	6-10	1
$_1$CMC-H 5 dw	S$_{XS}$ 20	0/2	2	0.87	4	1
$_1$XAN 2.5 dw	S$_{XS}$ 20	0/2	3	0.77	7	1
$_1$AN-S 1.5 dw	S$_{XS}$ 20	0/2	2	0.6	18	1
$_1$AN-H 0.75 dw	S$_{XS}$ 20	0/2	7	0.62	28	1
$_1$ANmix 0.75 dw	S$_{XS}$ 20	0/2	7	0.73	25	1
$_2$CMC-H 5 tw	S$_{XS/S}$ 2x10	0.5/1.2	6	0.62	11	1
$_1$XAN 2.5 tw	S$_{XS/G}$ 4x40	3/5	8	0.45	14	1

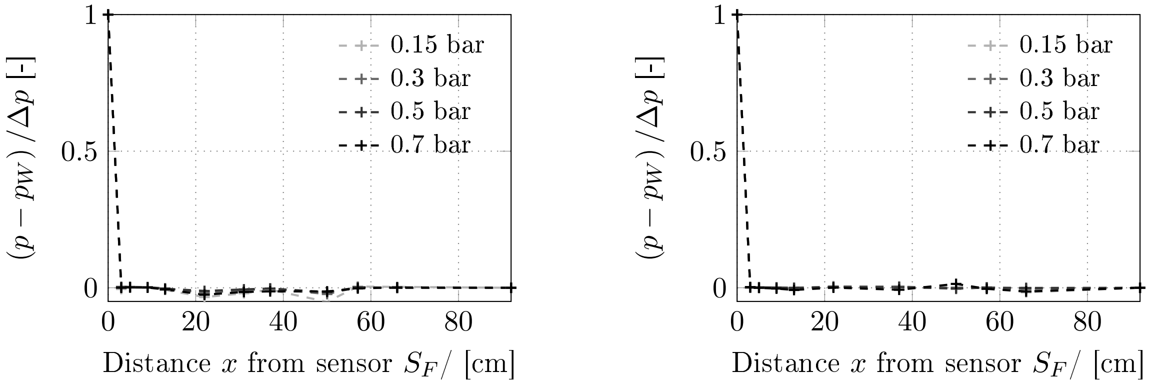

(a) CMC-H + S$_{XS}$ 20 in 0/2

(b) $_2$XAN 2.50 tw in 3/5

Figure 3.60.: Quartz mineral additives – normalized pressure drop curvature at higher pressure levels – examples

Filter cake formation

Fig. 3.61 shows six representative pictures of the filter cakes formed with quartz mineral addition within approximately 24 hrs. It is evident that the filter cakes formed with the polymers of natural origin are thinner (max. 1 mm) than the cakes formed with AN-S or AN-H (a few mm). The first row shows the effect of an increase of quartz powder concentration. It can be noted that the filter cake thickness slightly increases. This explains the lower cake permeability and higher stability with 10-20 g/l compared to only 5 g/l. The effect of an addition of a distribution of quartz mineral fines can be seen in Fig. 3.61f. It matches the assumption of the colmation process from Fig. 2.31, according to which the larger pores are blocked successively first by the larger fractions and successively decreasing to the last layer of quartz mineral grains. Appendix D.4 shows additional pictures of filter cakes.

The generally small filter cake thickness can be explained by an effective colmation combined with viscosity and solution stability effects. As long as the polymer solution is relatively stable, it does not easily release water for filtration. The high viscosity in the environment of the small pores created through the colmation process creates a low permeability. At low flow velocities, the settling velocity of the fines surpasses the inflow velocity, so the grains settle instead of accumulating at the cake, especially with upwards flow. Filter cake formation and stability will further be discussed in sections 3.5 & 3.6, where fluid-soil contact is direct and horizontal.

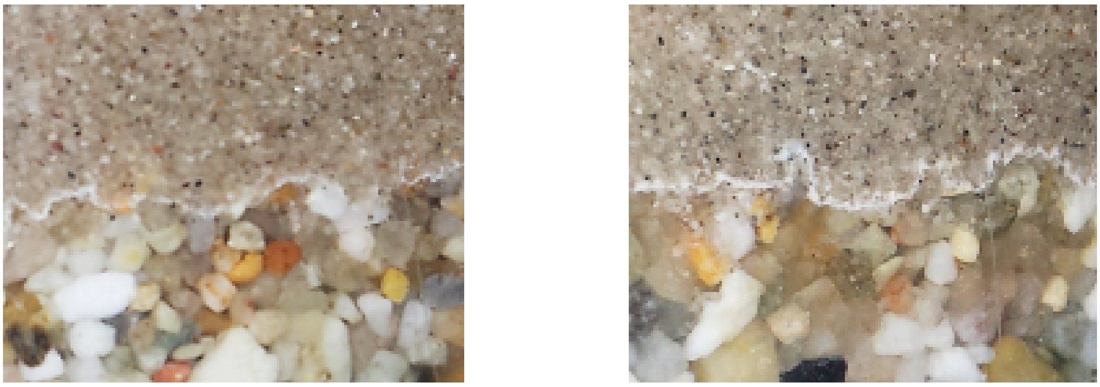

(a) CMC-H 2.5 +S_{XS} 5 (b) CMC-H 2.5 +S_{XS} 10

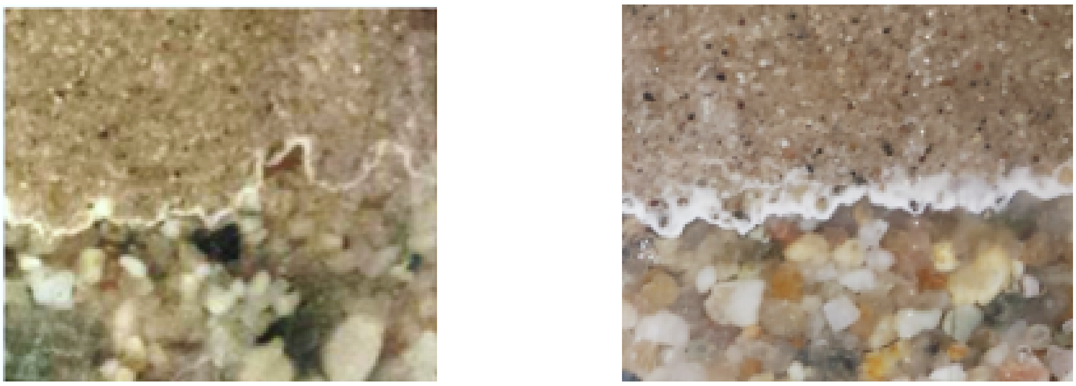

(c) CMC-H 5 + S_{XS} 20 (d) AN-S 1.5 +S_{XS} 20

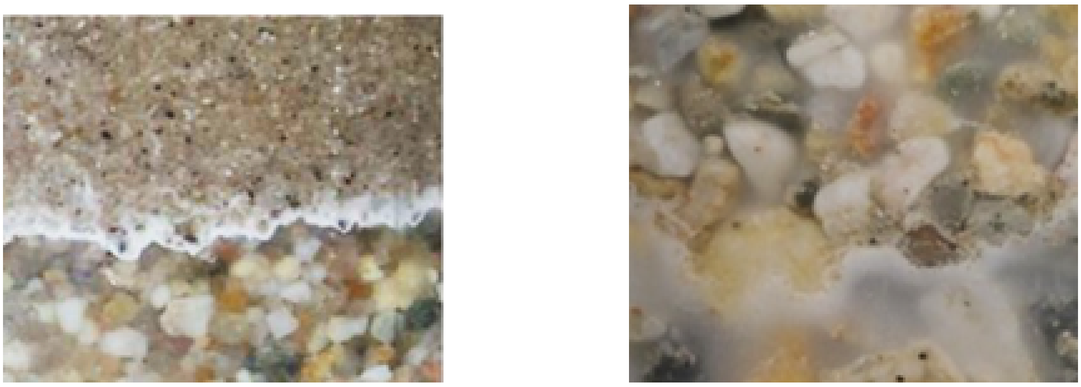

(e) AN-H 0.75 + S_{XS} 20 (f) XAN 2.5 + $S_{XS/G}$ 4x40

Figure 3.61.: Filter cakes with quartz mineral additives

3.3.5. Addition of bentonite suspension

The pressure-penetration relationships with the addition of bentonite suspension were analysed exemplarily for CMC-H 5 in comparison to AN-H 0.75 / ANmix 0.75 to emphasize the very different effect this type of addition can have. Fig. 3.20 showed a clear flock-formation with AN-H and ANmix, but not in CMC-H. Therefore, CMC-H is tested with the finer sand material (0/2 mm) and the AN products are tested in coarse sand (0.5/1.2 mm).

Fig. 3.62 shows a possible filter cake formation for CMC-H vs. AN-H and a visualization of the differences in solution. The first picture for AN-H is taken during penetration. It can be seen that the bentonite suspension flocks orient according to the direction of flow when passing through the granular filter. After 24 hr, no clear cake can be seen, but instead a certain blur indicating that bentonite flocks have filtered. No visible effect can be seen for CMC-H. The solution mix does not indicate any flocks and no agglomeration of bentonite is visible.

(a) AN-H 0.75 + B 5

(b) CMC-H 2.5 +B 5

Figure 3.62.: Filter cakes with bentonite suspension addition

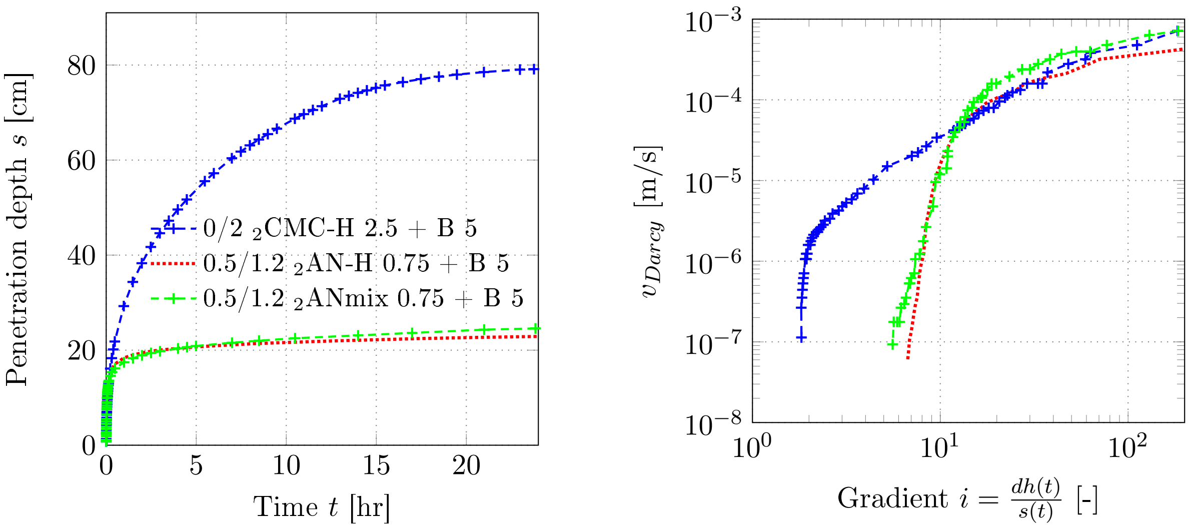

(a) Penetration depth

(b) Filter velocity

Figure 3.63.: Bentonite suspension as additive – penetration behaviour

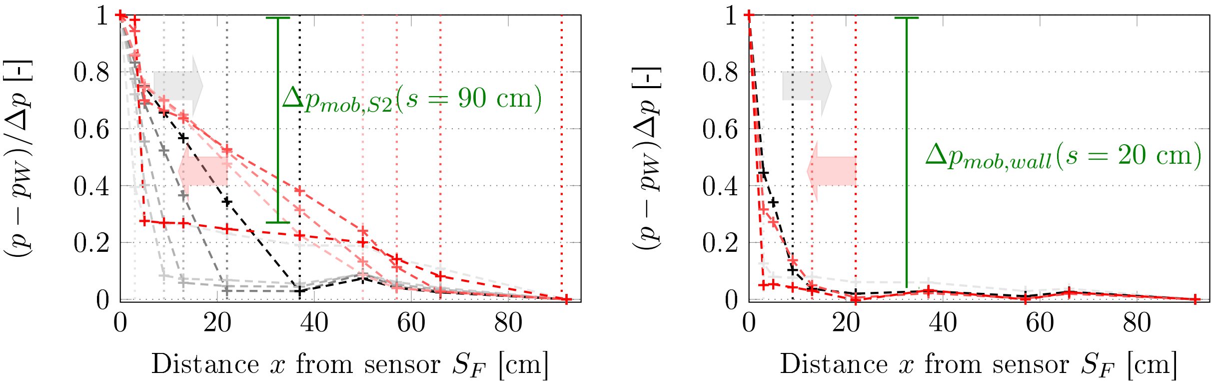

(a) ${}_2$CMC-H 2.5 + B 5 in 0/2

(b) ${}_2$AN-H 0.75 + B 5 in 0.5/1.2

Figure 3.64.: 0/2 – 0.5/1.1 – addition of bentonite suspension– CMC-H/AN-H: development of $p - p_W$ along the soil depth at $\Delta p \approx 0.15$ bar (tw)

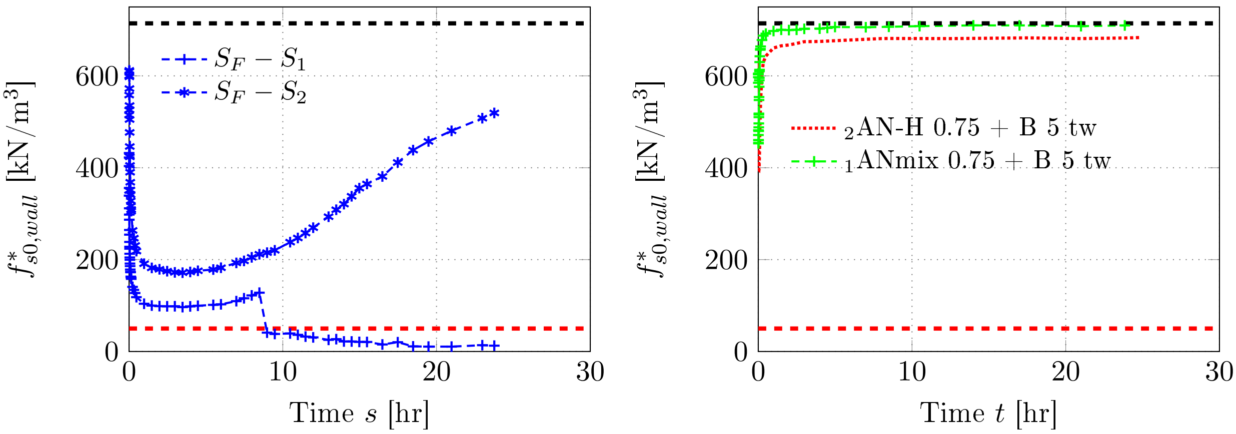

(a) ${}_2$CMC-H 2.5 + B 5 in 0/2

(b) ${}_2$AN-H 0.75 + B 5 vs. ${}_1$ANmix 0.75 + B 5 in 0.5/1.2

Figure 3.65.: Addition of bentonite suspension – CMC-H/AN-H/ANmix: time dependency of the earth wall pressure gradient at $\Delta p = 0.15$ bar

Fig. 3.63 gives an overview on the penetration behaviour of the three tested products. It can be seen that the fluids with the synthetic long-chain polymers stagnate relatively quickly and at a similar level. The CMC-H mix penetrates relatively far, but eventually also shows a certain degree of stagnation.

Fig. 3.64 shows the related pressure drop development for CMC-H+B and AN-H as a representative for AN-H/ANmix. In accordance with the penetration behaviour, pressure drops relatively quickly for AN-H 0.75 + B 5. With CMC-H, viscous flow seems to proceed until around 40-50 cm of penetration. Then an increased pressure transfer starts to form at the earth wall. However, between 60-90 cm of penetration depth, this pressure drop is formed not between the first two sensors, but between sensors S_1 and S_2 in sand. The filter cake formation apparently stretches along a broader area behind the earth wall. Nonetheless, still a considerable pressure drop of over 70 % is noticeable at a penetration depth of approximately 90 cm.

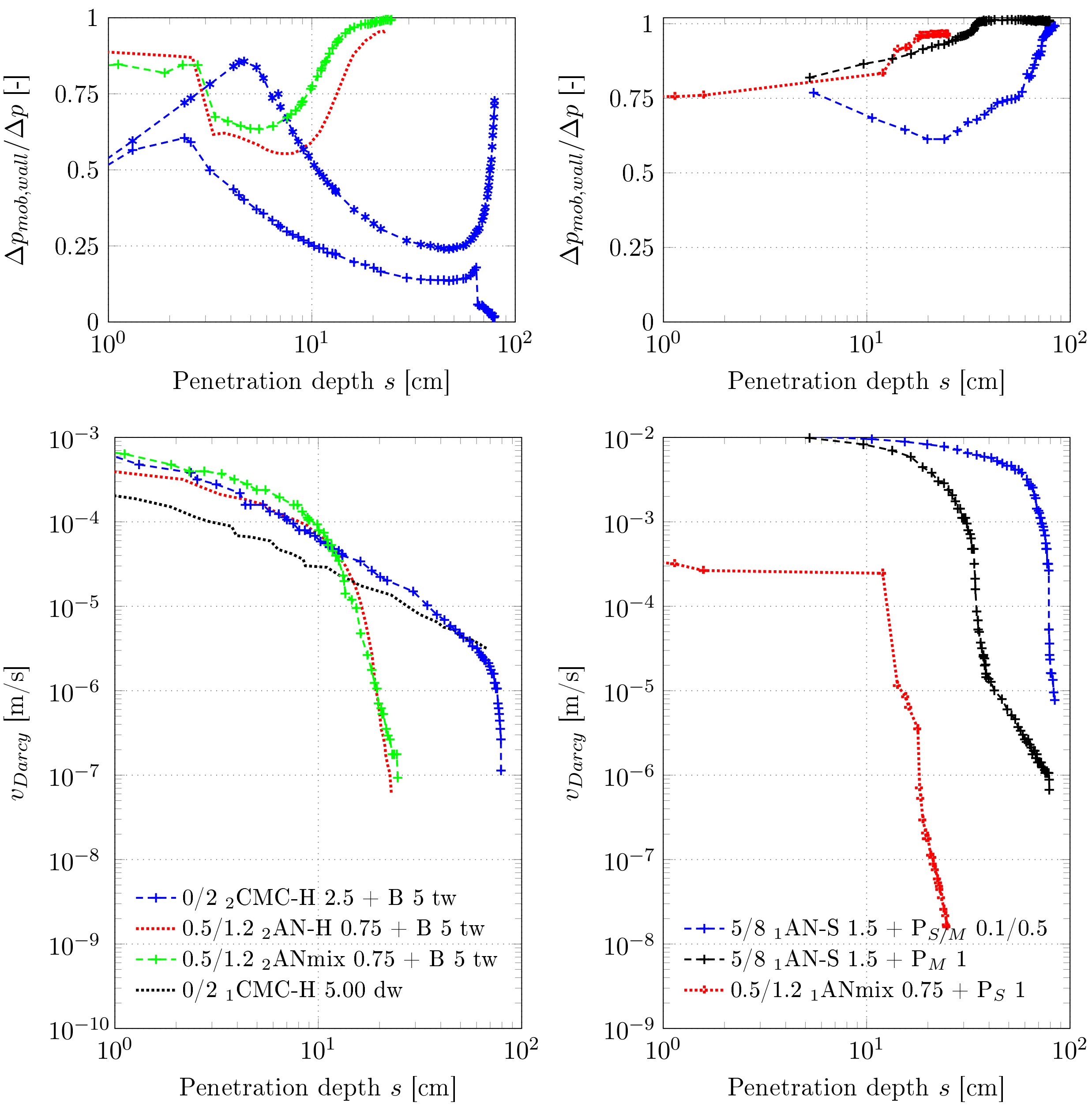

(a) 0.5/1.2 – CMC-H/AN-H/ANmix + B 5

(b) 0.5/1.2 ANmix vs. 5/8 AN-S with hydrogel

Figure 3.66.: Bentonite suspension and hydrogel addition – $\Delta p_{mob,wall}$ vs. v_{Darcy} at Δp = 0.15 bar

This effect is further illustrated in Fig. 3.65, which shows the development of the earth wall pressure gradient over time. An earth wall gradient calculated based on the mobilized pressure between S_F and S_2 is also displayed for comparison for the CMC-H mix ($d_{ref,S2}$ = 4.1 cm). It can be observed that $f_{s0,wall}$ drops continuously for the CMC-H mix over the first approximately 5 hr while the mixes with the synthetic polymers show a relatively quick increase due to the filter cake formation.

Fig. 3.66a shows a comparison of mobilized earth wall pressure and filter velocity for the three

Table 3.8.: Characteristic values for pressure-penetration relationships with bentonite suspension addition and membrane formation

Fluid	Additive	Soil [mm]	$s_{crit,1}$ [cm]	$\frac{\Delta p_{mob,wall,crit,1}}{\Delta p}$ [-]	$s_{crit,2}$ [cm]	$\frac{\Delta p_{mob,wall,crit,2}}{\Delta p}$ [-]
$_2$AN-H 0.75 tw	B 5	0.5/1.2	7	0.55	25	0.96
$_1$ANmix 0.75 tw	B 5	0.5/1.2	5	0.64	25	1

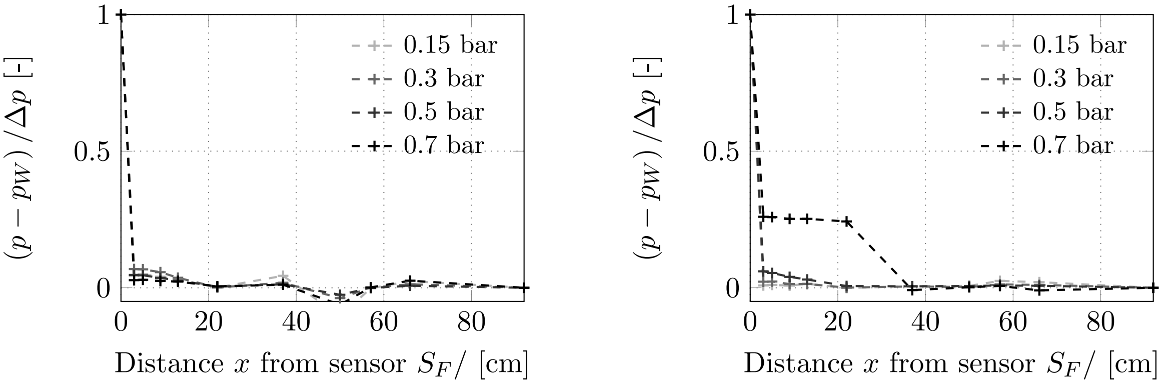

(a) $_2$AN-H 0.75 + B 5 tw

(b) $_1$ANmix 0.75 tw

Figure 3.67.: Bentonite suspension addition with AN – normalized pressure drop curvature at higher pressure levels

tests. For AN-H and ANmix with bentonite flocks, the same behaviour as found before with quartz mineral addition can again be observed. Characteristic deviations in the filter velocity development can be linked to changes in the mobilized earth wall pressure. Maximum pressure mobilization is reached when the filter velocity drops several decimal powers and reaches a value of approximately $1 \cdot 10^{-7}$ m/s. This amounts to 96-100 %. Tab. 3.8 summarizes the results accordingly. A subsequent stepwise increase of the overpressure level (Fig. 3.67) showed that the created earth wall filter cakes are stable until 0.5 bar.

For CMC-H, it is clearly visible that the addition of bentonite grains has a favourable effect on the penetration behaviour of CMC-H. However, filter cake formation does not seem stable at a reliable level in this test, so conclusions cannot safely be drawn. In any case, the effect of bentonite addition is less effective by far compared to an addition of quartz powder at the same concentration. This can probably be related to the good miscibility of CMC-H solutions with bentonite suspensions. The mix is relatively homogeneous, so it is likely that the bentonite grains mainly work as grains. With their smaller size compared to quartz grains, they are understandably less effective.

For AN-H solutions, however, adding bentonite suspensions into solution seems a more effective method than the addition of quartz grains. It can be easily mixed, it can even be mixed directly in hole (as has already been performed on construction sites). The addition of quartz grains to AN solutions of high molecular weight is significantly more difficult in comparison.

3.3.6. Addition of polymeric grains

The tests with polymeric grains displayed here represent the first tests performed with this material (with a 1-element column), so they do not reflect the best combinations of concentrations. They are still displayed here to highlight the general behaviour with these grains. A broader investigation on the addition of polymeric grains is given in section 3.5.

The three tests comprise one test with a relatively viscous fluid (ANmix 0.75) in coarse sand and two tests in gravel with the low-molecular AN representative AN-S 1.5. The small polymeric fraction P_S was used for the coarse sand material at a concentration of 1 g/l, which can be considered relatively high as elaborated in section 3.2.4. The two tests in gravel were performed with two different combinations of polymeric grain fractions.

Fig. 3.68-3.70 & 3.66b and Tab. 3.9 summarize the results for penetration and pressure relationships.

In particular, it can be seen that stagnation and full pressure mobilization immediately at the earth wall occurs in all cases, but at significantly different penetration levels. In coarse sand, a penetration level similar to the equivalent test with bentonite flocks is reached. The grain sizes and quantities chosen for gravel do not create reasonable maximum penetration depths and filtration rates at low levels yet. These polymeric grains are deformable to a certain extent, so it could be assumed that they are able to block certain pores more effectively than quartz grains. Apparently though, this effect is not pronounced enough for an aqueous grain of medium size (P_M) to fully block the gravel pores for filtration of the dissolved low-molecular weight AN with relatively low viscosity values. It can be assumed that a range of grains also containing a significant amount of smaller fractions prove more effective in this context (section 3.5). The amount of 0.1 g/l used for the first AN-S test does not suffice.

An increase in overpressure levels was only performed for one test, which showed stability for all tested levels (Fig. 3.70). But it can be assumed that the result is transferable to other applications with hydrogel addition as the type of grain does not change and this concerns the general stability towards pressure of the aqueous grain.

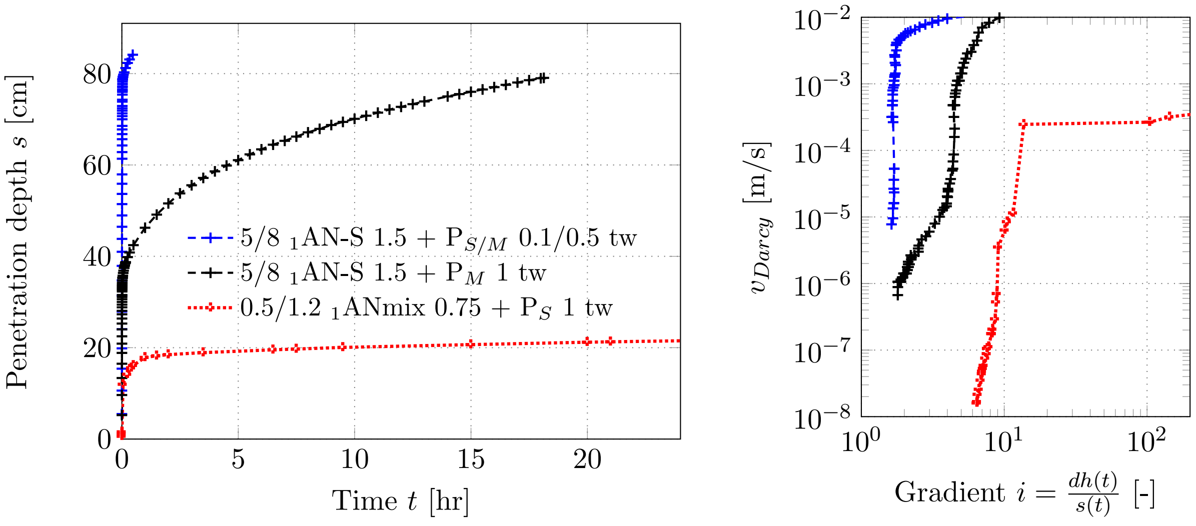

(a) Penetration depth

(b) Filter velocity

Figure 3.68.: Hydrogels as additive – penetration behaviour

It can be concluded that aqueous grains are generally usable as pore blockers for coarser material. (The tested range cannot be used for finer material as no fine polymeric grains could be obtained). It cannot be guaranteed, however, that they are as effective as rough quartz mineral grains in penetrating into the ground without the favourable conditions encountered in this device due to the slippery surface of the grains. Therefore, particular focus will be laid on polymeric grains with regard to horizontal penetration tests (section 3.5).

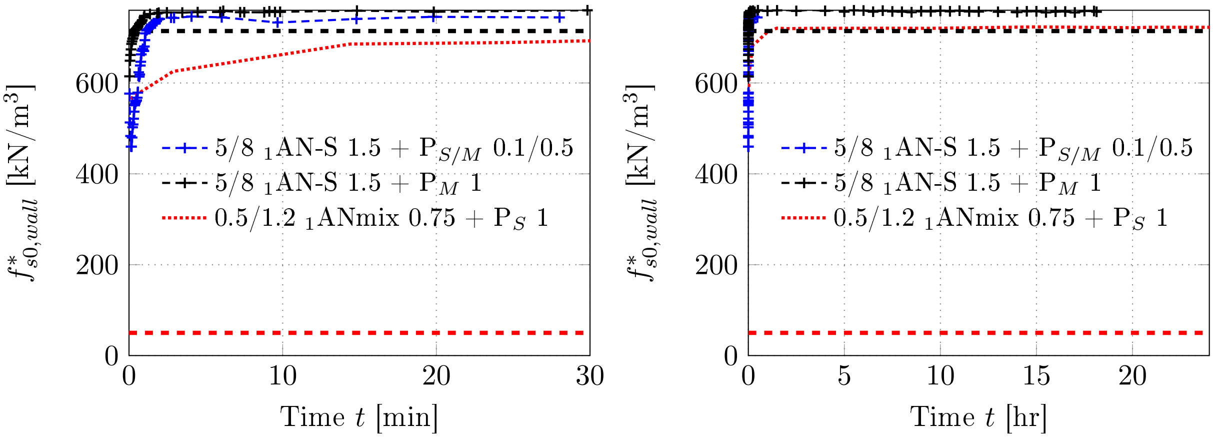

Figure 3.69.: 0/2 – 0.5/1.2 – 5/8 – addition o polymeric grains: time dependency of the earth wall pressure gradient at $\Delta p = 0.15$ bar

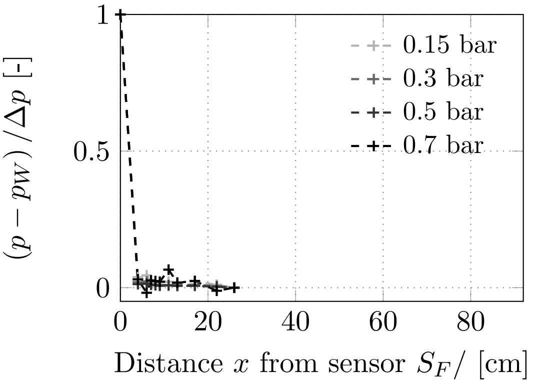

Figure 3.70.: AN-H 0.75 + P_S 1 – normalized pressure drop curvature at higher pressure levels

Table 3.9.: Characteristic values for pressure-penetration relationships with polymeric grain addition and membrane formation

Fluid	Additive	Soil [mm]	$s_{crit,1}$ [cm]	$\frac{\Delta p_{mob,wall,crit,1}}{\Delta p}$ [-]	$s_{crit,2}$ [cm]	$\frac{\Delta p_{mob,wall,crit,2}}{\Delta p}$ [-]
$_1$AN-S 1.50 tw	P$_{S/M}$ 0.1/0.5	5/8	5	0.61	85	1
$_1$AN-S 1.50 tw	P$_M$ 1	5/8	20	0.80	35	0.96
$_1$ANmix 0.75 tw	P$_S$ 1	0.5/1.2	1	0.75	25	0.97

3.4. Results: vertical penetration – small scale (V-S)

3.4.1. General

The following subsections summarize parameter studies performed by means of small-scale tests (V-L) in order to

- determine characteristic grain diameters $d_{ref,visc}$ which can be related to this flow behaviour as equivalent values for pore sizes (in the sense of d_{10} for bentonite suspensions),
- analyse the flow behaviour of viscous base polymers in different porous environments,
- analyse combinations of soils and granular additives with regard to maximum penetration depths,
- determine characteristic grain diameters $d_{ref,add}$ as a reference for the choice of adequate size fractions and amounts of granular additives for effective colmation,
- conclude suitability matrices as a basis for quantification of related characteristic penetration depths $s_{crit,1}$ and especially $s_{crit,2}$.

If not otherwise stated, the tests were generally performed at $\Delta p = 0.15$ bar to be relatable to V-L testing. Due to the narrow size of the testing device, soil pluviation resulted in a slightly higher porosity than with V-L tests ($n = 0.39$), which is taken into account during comparison.

The tests without granular additive addition comprise a total of 55 tests performed as downwards flow tests to create direct contact between fluid and soil (Fig. 3.2a). A total of 77 upwards flow tests were performed with variation of granular additives (Fig. 3.2b). These tests focus on a variation of

- polymer types: mainly CMC-H, XAN, AN-H and AN-S at both concentrations
- granular additives: quartz mineral sequences vs. bentonite suspension

3.4.2. Soil classification for viscous flow

In order to classify the grain size distributions (GSD) used in the large-scale tests (V-L) within the soil fraction diameter ranges tested in this section (V-S), the V-L and the V-S tests without additives are compared with respect to their filter velocities at similar gradients. The V-L gradient $i_{V-L} = \Delta h(t)/s(t)$ decreases with increasing penetration at relatively constant pressure level ($h(t) \approx const.$). The V-S tests are performed at the same pressure level, but with a smaller soil sample length ($L_{V-S} = 5$ cm $\rightarrow i_{V-S} \approx const.$). The behaviour should therefore be equivalent at approximately 4-6 cm of penetration depth.

Fig. 3.71-3.72 display a comparison of the penetration rates differentiated by polymer type and polymer concentration. Each coloured cross marks the filter velocity obtained from one V-S test with downwards flow at $\Delta p = 0.15$ bar at approximately full soil penetration ($s = 5$ cm $\rightarrow i \approx 30$) ordered with respect to the mean diameters d_{mean} of the penetrated soil fractions. The horizontal lines show the filter velocities obtained from V-L tests at similar gradient and adapted by taking into account porosity differences between V-S and V-L. It can be noted that the two V-L tests with finer grained soil (0.125/0.355 mm) match the lower boundary of the similar 0.125/0.25 mm soil fraction relatively well.

Based on comparison of the points of intersection of the V-S trends (marked in gray) and the V-L reference lines (black), it can be seen that $d_{mean} \approx 0.33$ mm represents a reasonable reference value for all tests with 0/2 mm sand and CMC-H, XAN and AN-S, which reflects the d_{30} value of the soil. The permeation behaviour for AH-H seems to be more closely related

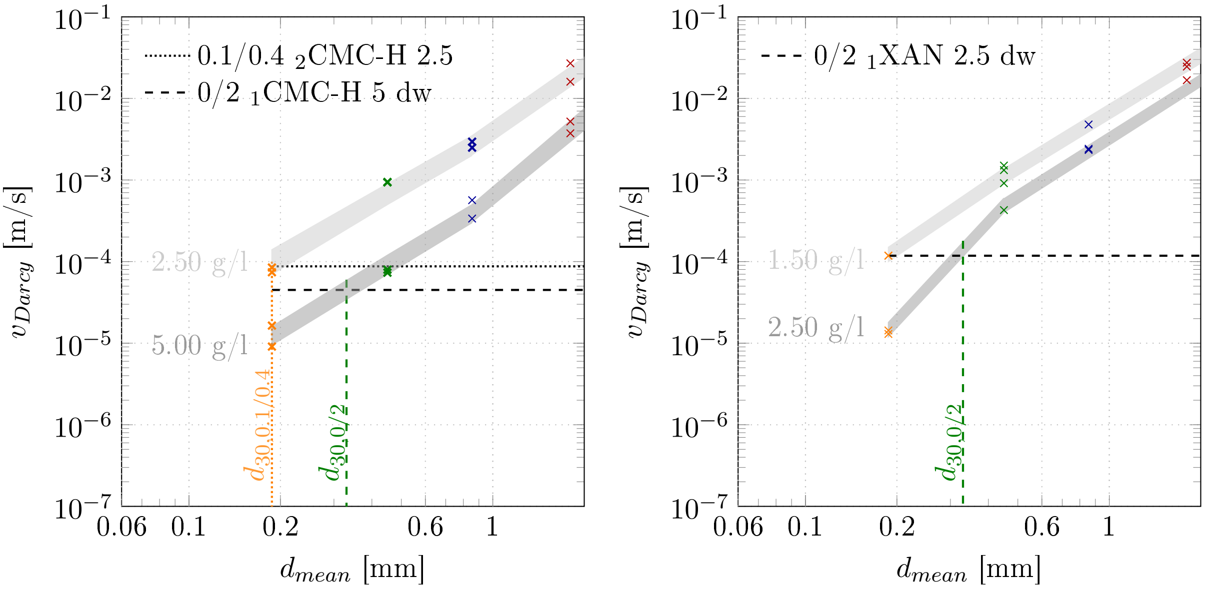

(a) $_2$CMC-H tw

(b) $_2$XAN tw

Figure 3.71.: CMC-H/XAN: V-S filter velocity along GSD at ca. 5 cm penetration depth with V-L classification

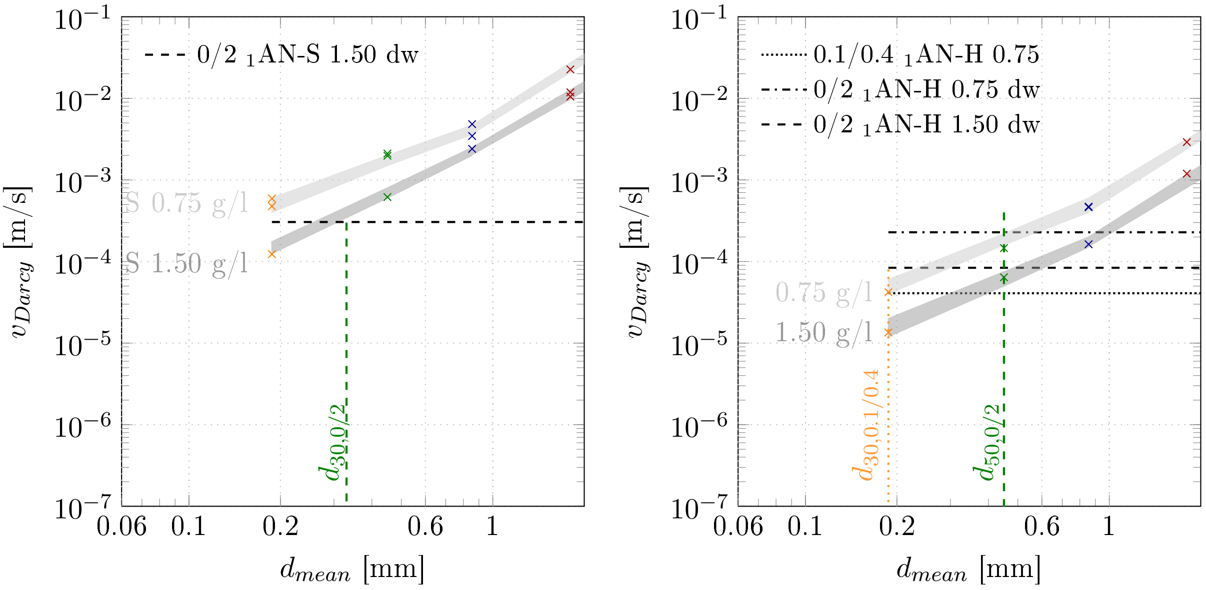

(a) $_1$AN-S tw

(b) $_2$AN-H tw

Figure 3.72.: AN-S/AN-H: V-S filter velocity along GSD at ca. 5 cm penetration depth with V-L classification

to $d_{50} = 0.45$ mm. Polymer concentration or solvent type do not seem to have a pronounced influence on this relation.

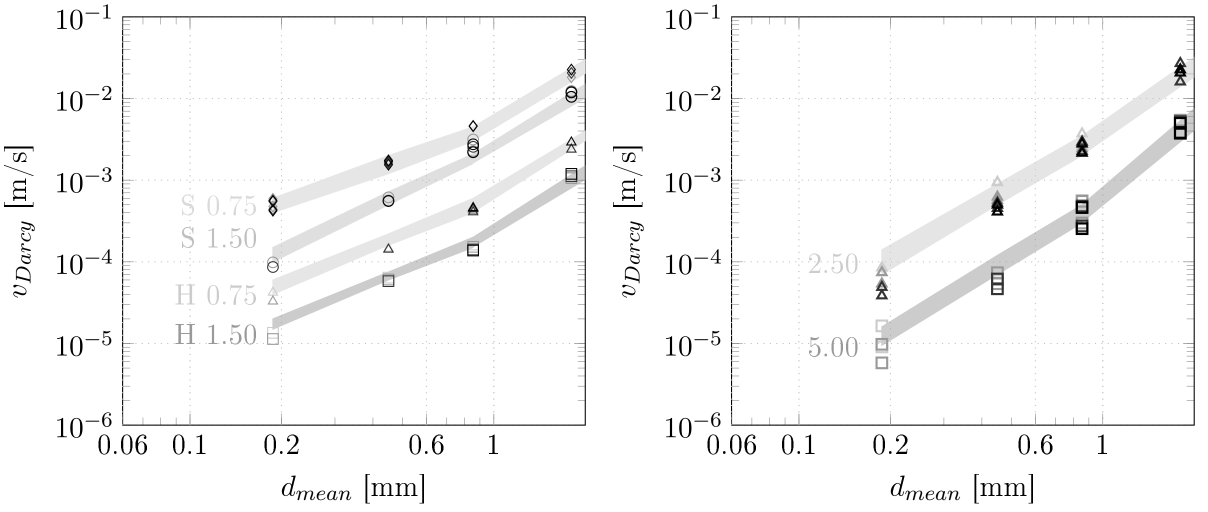

(a) $_2$AN-S/$_2$AN-H tw

(b) $_2$CMC-H tw

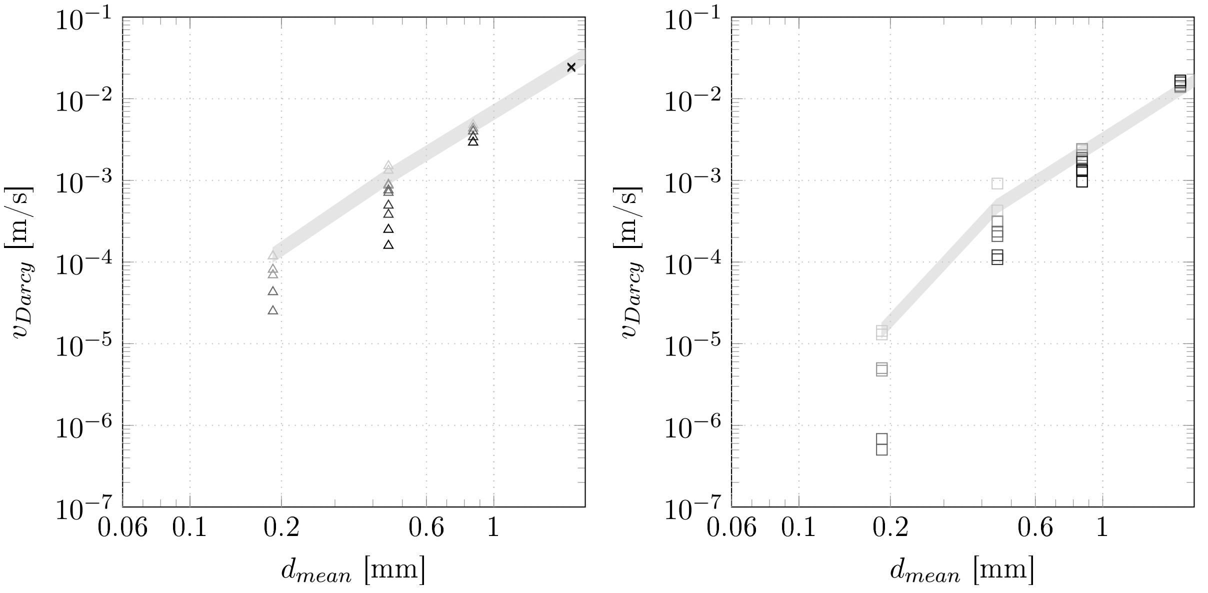

(c) $_2$XAN 1.5 tw

(d) $_2$XAN 2.5 tw

Figure 3.73.: Development of the filter velocity with progressing penetration at $\Delta p = 0.15$ bar for differing soil fractions

3.4.3. Viscous flow and micro-colmation at soil fractions

Fig. 3.73 compares the development of the curves shown in the previous section with progressing penetration (from light gray to black) at $\Delta p = 0.15$ bar and constant gradient (maximum volume used: 2 L, gradient $i \approx 30$). It therefore illustrates effects of micro-colmation at the earth wall. In accordance with the observations from V-L testing, these results show largely differing degrees of decreases in filter velocity, especially in finer soil fractions. The behaviour can be summarized as follows:

$$\text{XAN} >>>> \text{CMC-H} >> \text{AN-H} > \text{AN-S}.$$

For AN-S, no change in filter velocities is visible for the whole tested soil range, a very slight change can be noted for the higher concentration. AN-H shows a small decrease with progressing penetration in fine sand (0.125/0.355). CMC-H shows a more pronounced decrease in fine sand and moderate effects in coarser material. In contrast, XAN exhibits a significant decrease in filter velocity with progressing penetration. This micro-colmation effect increases with decreasing soil grain diameter (i.e. pore size). In 1.6/2 mm soil, the effect can be considered negligible. At maximum level, it reaches over one decimal power for the higher polymer concentration in fine sand. The last (darkest) points mark 20 cm of equivalent penetration depth $s_{eq} = \sum V/(A \cdot n)$ with $\sum V$ the cumulated outflow volume and A and n soil cross section and porosity, respectively [8].

Aside from micro-colmation, Fig. 3.73 shows that the filter velocities related to their respective porous environment (equivalent to d_{mean}) decrease faster with CMC-H and XAN with decreasing soil grain size compared to AN. A change in concentration and molecular weight leads to a vertical shift of the connected curve. It is therefore likely and conclusive that this effect can be related to the size of the respective polymer chains. XAN has the most complex structure, i.e. thickest backbone, followed by CMC-H. AN chains are comparably thin. The difference between CMC-H and XAN is probably also enhanced by their differing viscosity values. In this case, micro-colmation reduces the effective pore size available for flow and flow rates will consequently reduce faster with XAN owing to its higher viscosity.

It is unclear whether these large reductions in filter velocity found with XAN in fine sand can be related to a significant amount of pressure drop at the earth wall. It is clearly a factor explaining the increased drop in pressure observed for XAN (and to a certain extent for CMC-H) already in medium grained sand. However, in any case, these results can be used as an indicator for estimated penetration rates in different soil conditions. As these tests are performed at constant gradient, it can be assumed that they can be transferred to higher overpressure conditions as well. In real conditions, exemplarily, $i \approx 30$ and $s = 20$ cm would reflect an overpressure level of $\Delta p = 0.6$ bar (resp. $\Delta H = 6$ m hydrostatic difference between support fluid and groundwater head).

3.4.4. Colmation with quartz grains or bentonite suspension at soil fractions

Fig. 3.74-3.77 show the development of the filter velocity v_{Darcy} with increasing equivalent penetration depth s_{eq} differentiated by polymer type, polymer concentration and type of additive. The tested soil fractions are marked by colour:

0.125/0.25	orange	1.6/2	red
0.4/0.5	green	2.8/4	olive
0.71/1	blue	5.6/6.3	lilac

The main additive and soil variation was performed based on CMC-H, XAN and AN-H. The influence of molecular weight (AN-H/-M/-S) and anionicity (AN-H/AN-M/AN-MH) was performed with 0.71/1 mm as reference soil. The addition of bentonite suspension was tested with

---

[8] The equivalent penetration s_{eq} term will be also used in the following subsections as it is considered easier to relate to as the cumulated outflow mass $\sum_m$ or outflow volume $\sum_V$. At 5 cm soil sample depth, $\sum_V = V_0$ ($V_0 = n \cdot V$ total pore volume) and $s_{eq} = s$. It can therefore be considered as an extrapolated penetration depth at constant gradient. Hence, the actual penetration depth s into ground of larger depth is lower at the same pressure level, because then the gradient depends on the penetration depth. For the determination of critical depths $s_{crit,1}/s_{crit,2}$ with colmation, the results should be comparable as the penetration depth depends mainly upon the penetrated volume and fines concentration and not on the pressure level.

CMC-H and the AN range. Appendix 3.4 shows a selection of filter cake pictures from the performed tests.

For the first four soils, the development of the filter velocity without the addition of fines from upwards flow testing is plotted as a solid line without marks if available. It can be seen in all cases that penetration with fines starts at similar flow rate levels. This verifies the comparability of upwards and downwards flow and is in accordance with the flow behaviour observed during V-L testing.

With regard to quartz mineral addition, it can be observed that polymer support fluids based on CMC-H (Fig. 3.74a, 3.74b, 3.74d) and XAN (Fig. 3.75) are able to form stable filter cakes in all tested soils. In this respect, the level of stagnation varies with varying additive concentration and choice of the maximum additive diameter. Two tests at higher overpressure level performed exemplarily with CMC-H (Fig. 3.74a) show that the start of deviation from viscous flow as well as the stagnation level do not depend upon the overpressure level.

With CMC-H, it can be observed that stagnation can be reached with relatively small amounts of quartz powder even in coarse sand (0.71/1, blue). This effect is possibly attributed to the CMC-H chains enlarging the effective grain size of the powder, more pronounced at larger polymer concentration. This would explain that doubling the polymer concentration leads to a halving of the equivalent penetration depth from 80 cm to 40 cm. With increasing soil grain diameter, larger additive sizes reduce the penetration depth. With the example of 1.6/2 mm soil (red) and CMC-H 5 (Fig. 3.74b) it can be seen that neither only S_{XS} nor S_S alone work sufficiently well in forming stagnation. Only in combination a stagnation can be reached. This underlines the importance of a grain size distribution from larger fractions down to quartz powder for a filter cake to be formed.

With a significant increase in the total amount of fines and an adequate grain size distribution (equal amounts of each fraction), even 5.6/6.3 mm gravel (lilac) can be stabilized. In the tested cases, $4x80 = 320$ g/l were used, which reflects a fluid density as high as 1.2 g/cm^3, resulting in an equivalent penetration depth of 50 cm. This depth, however, cannot immediately be transferred. The estimated penetration depth should be considerably lower. The large (and reproducible) penetration depths measured here are significantly influenced by wall effects due to the small diameter of the testing device (4 cm). It is assumed that the penetration depths are reflected adequately for the four finer soils ($d \leq 2$ mm) as the formed filter cakes were relatively even compared to the filter cakes formed in the two coarsest materials.

The addition of bentonite suspension with CMC-H (Fig. 3.74c) seems moderately effective for fine sand[9]. However, it still creates a significantly larger penetration depth than quartz addition.

For XAN, similar conclusions can be drawn as compared to CMC-H. With respect to applicable additive sizes and related penetration depths, certain differences can be found. In fine sand, penetration depths seem comparable, they are probably not largely influenced by polymer concentration. The penetration depth in the medium sand fraction (green) is slightly lower with XAN 1.5 than with CMC-H 2.5 despite equal additive type and concentration. In coarse sand (blue), on the other hand, the penetration depth with quartz powder and higher XAN concentration matches the penetration depth of the lower CMC-H concentration, i.e. they show the same penetration depth at the same polymer concentration. In gravel, CMC-H 5 and XAN 2.50 can again be matched as the penetration depth here largely depends on the carrying capacity of the solutions with respect to the additives.

---

[9] An increase in bentonite concentration towards 10-20 g/l already changes the overall behaviour of the fluid towards a modified bentonite suspension. For these suspensions, significantly lower amounts of CMC-H are necessary.

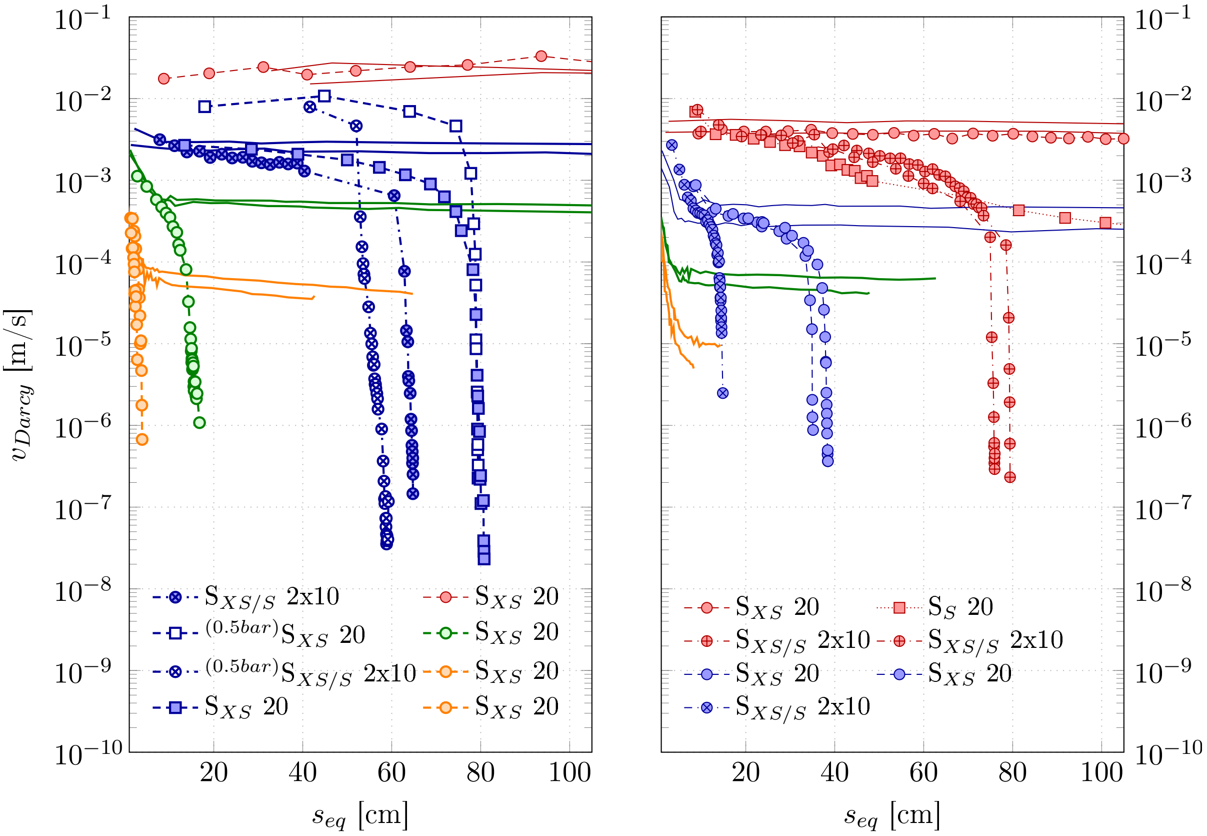

(a) CMC-H 2.5 with S variation

(b) CMC-H 5 with S variation

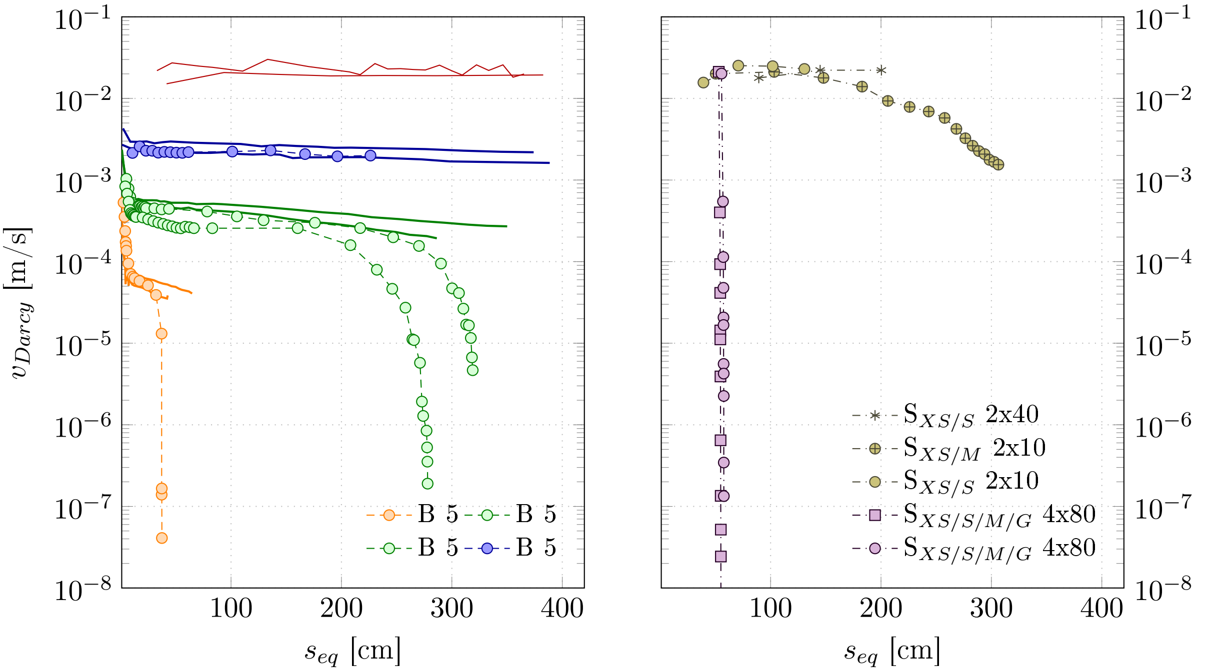

(c) CMC-H 2.5 + B 5

(d) CMC-H 5 with S variation

Figure 3.74.: Penetration development of $_2$CMC-H tw with quartz mineral or bentonite suspension addition

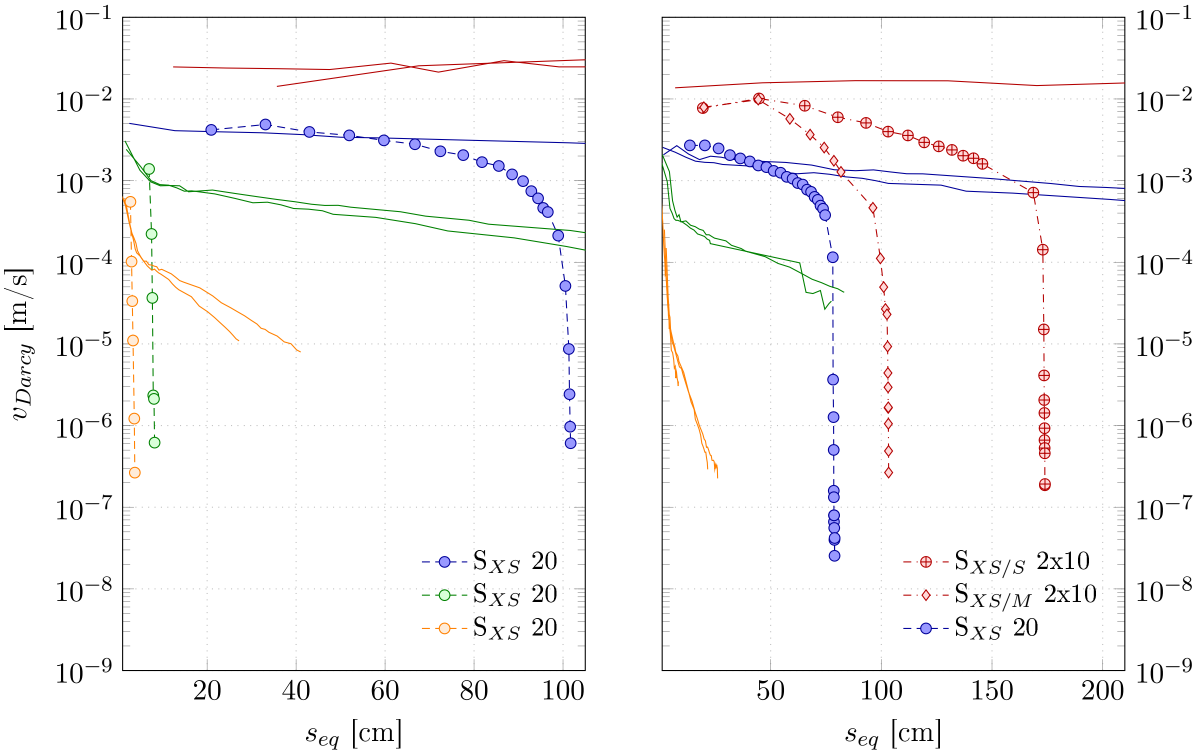

(a) XAN 1.5 with S variation

(b) XAN 2.5 with S variation

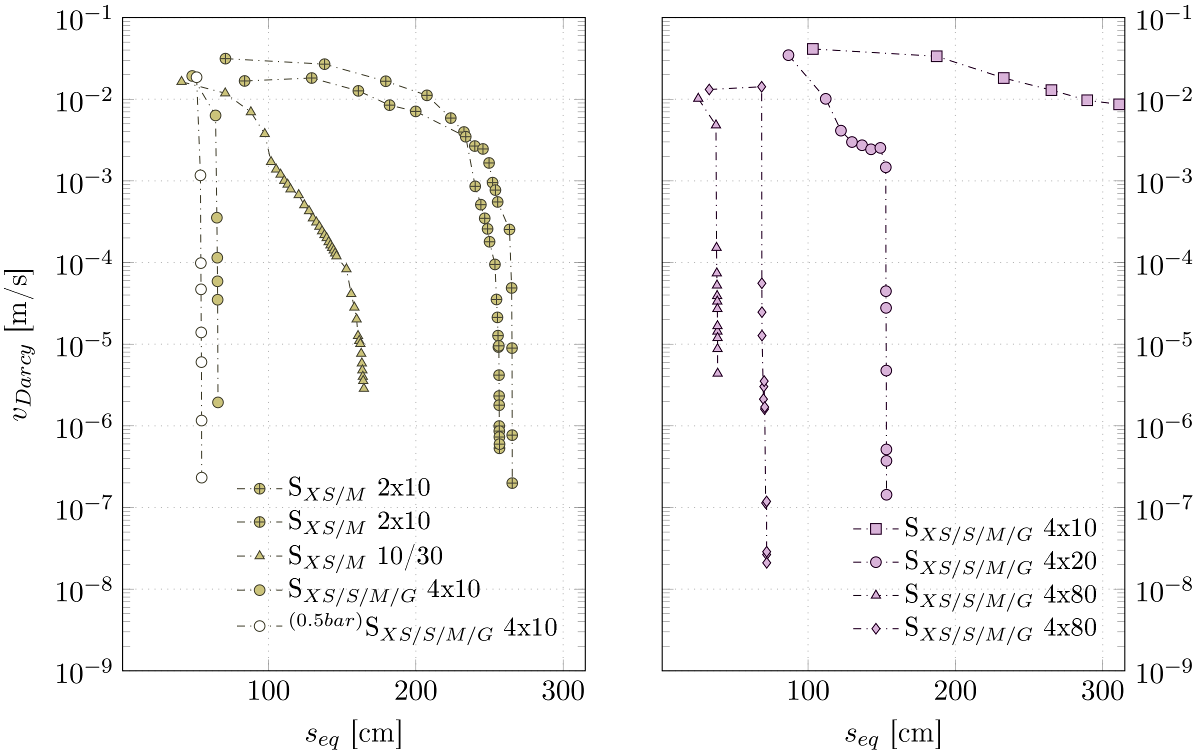

(c) XAN 2.5 with S variation

(d) XAN 2.5 with S variation

Figure 3.75.: Penetration development of $_2$XAN tw with quartz mineral addition

In contrast to CMC-H and XAN, AN-H (Fig. 3.76a - 3.76b) visibly only functions well with quartz powder addition (S_{XS}). If a larger fraction (S_S) is introduced into the mix for coarse sand (blue), no improvement can be observed, rather the opposite. Even though the fluid can technically carry S_S relatively well, it apparently does not release this group of granular material to a sufficient extent to be available for colmation. AN-S (Fig. 3.76d) shows no improvement with the addition of larger additives either, but this can be related more to the lower carrying capacity of the solution, which results in less granular additives reaching the soil surface.

When comparing the influence of different molecular weights with pure quartz powder addition in coarse sand, it can be observed that slightly better results can be achieved with high and low molecular weight than with medium molecular weight (AN-M), though with a certain uncertainty with respect to the tolerance of the results. It could, however, be rationalised by the observation that it is relatively similarly difficult to disperse the quartz grains in AN-H and AN-M as compared to AN-S, but the carrying capacity of AN-H is superior to AN-M and the availability of grains for colmation is superior for AN-S. The influence of anionicity (AN-M vs. AN-MH) is tested by means of one example (Fig. 3.76c). This suggests that an increase in anionicity improves the colmation behaviour.

Overall, it can be concluded for these synthetic polymers that sequence addition of different sizes of quartz grains in order to reduce the penetration depth is not applicable. The application of quartz mineral grains is possible, but is less effective with AN than with XAN or CMC-H.

The addition of bentonite suspension (Fig. 3.77), on the other hand, proves very effective. It reaches its limits with AN of high molecular weight in coarse sand, no stagnation can be observed in 1.6/2 mm sand. A combination of quartz grains and bentonite suspension (Fig. 3.77a) does not markedly influence this mix. This is plausible as the grains are still not easily provided by the solution. However, the functionality of this polymer-bentonite mix highly depends upon the polymer chain length. It takes no effect with AN-S, works moderately well with AN-M and successfully with AN-H and ANmix. It does not seem to be controlled by concentration as tests with 0.75 g/l and 0.375 g/l show the same results (Fig. 3.77a). However, tests at different pressure levels show moderately larger penetration depths.

A modification of the mixing water was additionally performed to study its effect on the formation of these bentonite flocks. 1 g/l of Na_2CO_3 (25 %) was added to the mixing water to increase pH level to 10. No effect was observed for AN-H, but a significant effect was noted for AN-M. The AN-M curves already show a large variance with no clear stagnation level. Only a higher degree of anionicity (AN-MH) seems to show a stable stagnation level. Modifying the mixing water seemed to significantly impact the effectiveness of the formed flocks. Moreover, the addition of NaOH (equally resulting in pH 10 of the mixing water) was tested at the same concentration. It can be seen that this, too, probably even to a larger degree, affects the formation of these flocks. The hydroxy groups (OH^-) chemically degrade the polymer chain to a certain extent, making it nearly as ineffective as AN-S with respect to the formation of these flocks. This displays that the usage of this bentonite flocking effect needs to be closely controlled if used, especially with synthetic polymers at medium chain length.

Altogether, this parameter study on soil fractions shows that the penetration behaviour up to gravel can be largely influenced by granular additives. With the two polymers of natural origin, quartz mineral grains have proven to be effective in creating stagnation if adequately fitted with respect to concentration and size distribution to the relevant soil fraction. As the filter cakes are relatively thin, it is unclear how stable these cakes are towards agitation from the excavation tool. Filter cakes with finer soil are probably less sensitive to movement as they are stabilized by polymer chains to a certain extent (micro-colmation, adsorption, etc.).

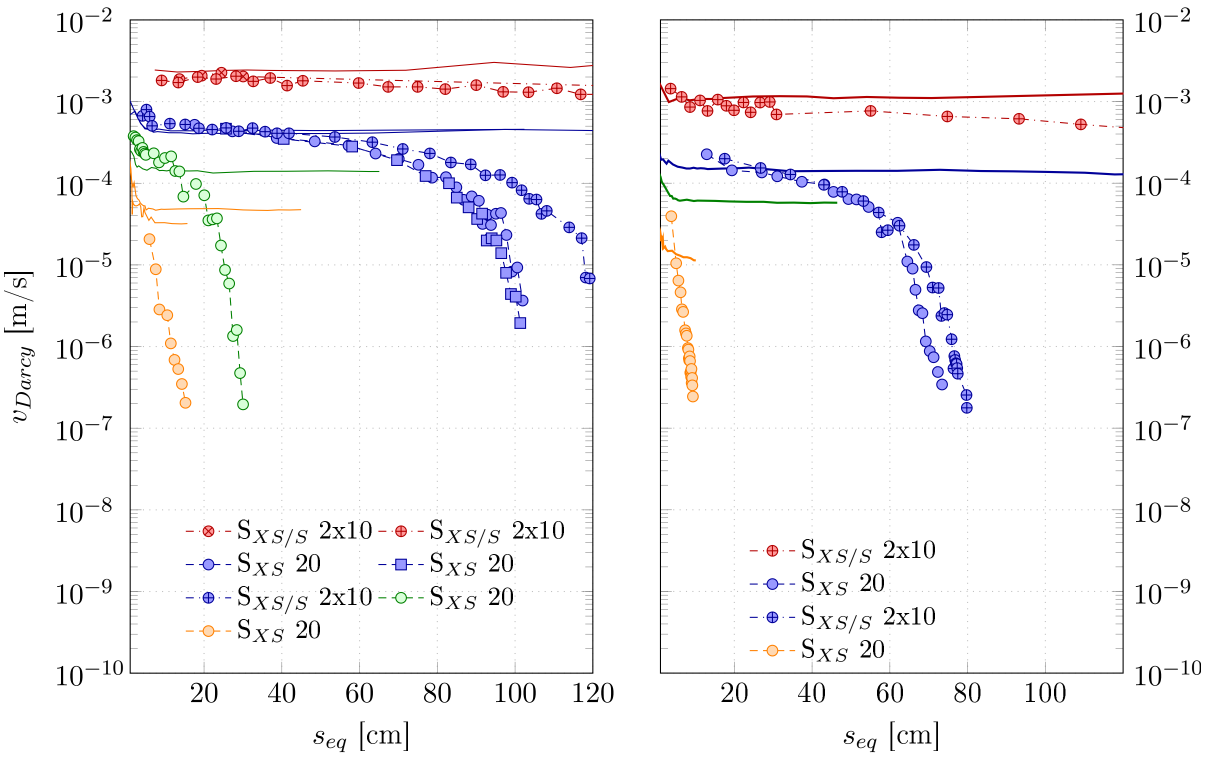

(a) AN-H 0.75 with S variation

(b) AN-H 1.5 with S variation

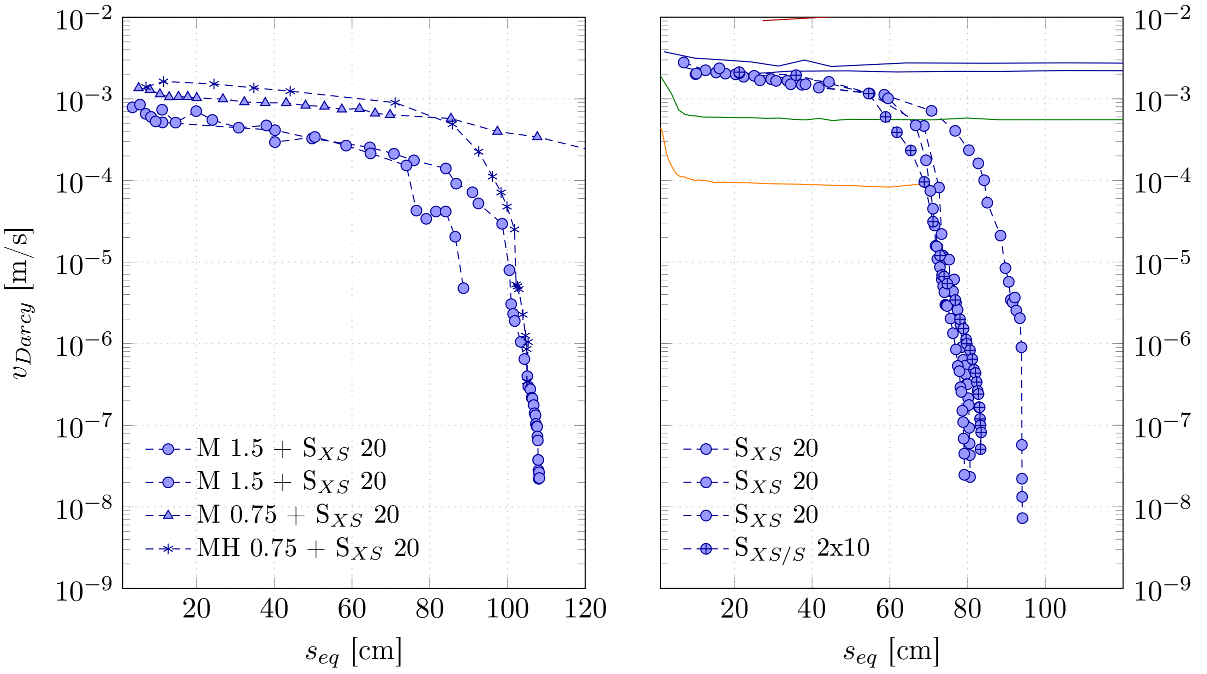

(c) AN-M 0.75/1.5 & AN-MH 0.75 with S_{XS}

(d) AN-S 1.5 with S variation

Figure 3.76.: Penetration development of AN range and ANmix (tw) with quartz mineral addition

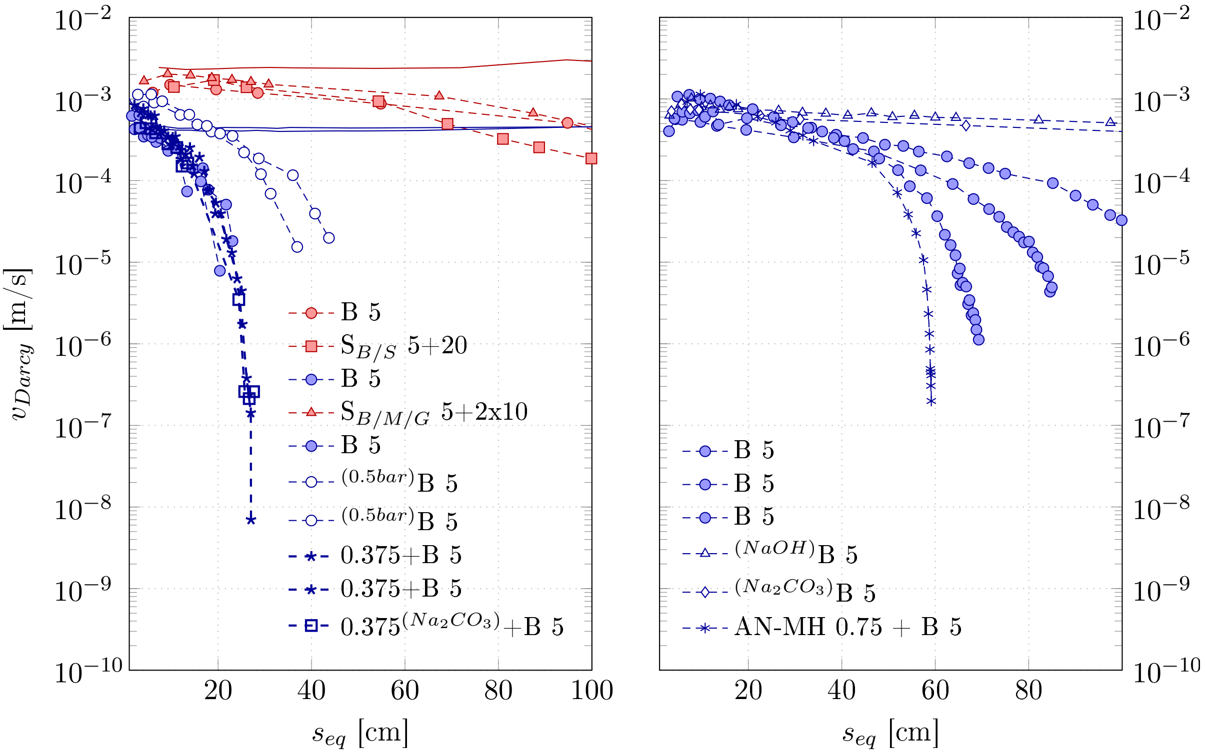

(a) AN-H 0.75 with B 5

(b) AN-M 0.75 with B 5

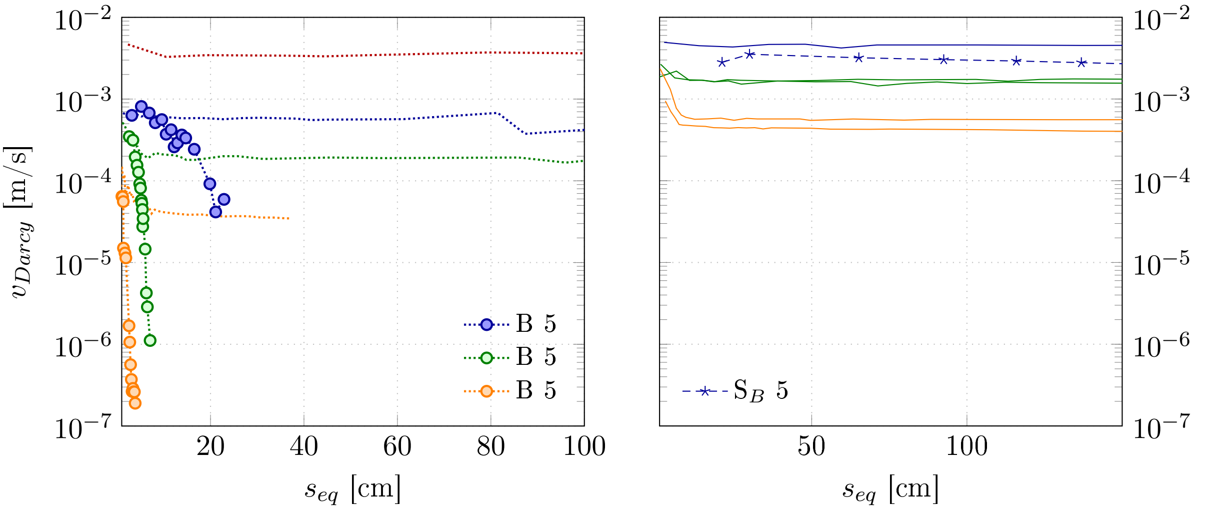

(c) ANmix 0.75 with B 5

(d) AN-S 0.75 with B 5

Figure 3.77.: Penetration development of AN range / ANmix (tw) with bentonite suspension addition

For AN polymers, quartz powder addition can be troublesome and is therefore mainly recommended at lower molecular weights, but it also functions at high molecular weights. The higher molecular weight AN products function particularly well in combination with bentonite suspensions at low concentration. In coarse sand, high molecular weight AN polymers need to be applied. Care must be taken with respect to the influence of the mixing water or similar. For coarser soil fractions, AN polymers could to be complemented with polymeric grains. Their effectiveness will be discussed in section 3.5.

Tab. 3.10-3.11 (V-S) summarize a selection of this test range with penetration depths below 1 m and stagnation.

Table 3.10.: CMC-H/XAN: characteristic values for penetration with stagnation with quartz mineral or bentonite suspension addition (V-S test)

Fluid	Additive	Soil [mm]	$s_{crit,1}$ [cm]	$s_{crit,2}$ [cm]
CMC-H 2.50 tw	S_{XS} 20	0.125/0.25	1-2	3-4
CMC-H 2.50 tw	B 5	0.125/0.25	30	37
CMC-H 2.5 tw	S_{XS} 20	0.4/0.5	8	17
CMC-H 2.5 tw	S_{XS} 20	0.71/1	40	80
CMC-H 2.5 tw	$S_{XS/S}$ 2x10	0.71/1	30	60-70
CMC-H 5 tw	S_{XS} 20	0.71/1	10	35-40
CMC-H 5 tw	$S_{XS/S}$ 2x10	0.71/1	30	15
CMC-H 5 tw	$S_{XS/S}$ 2x10	1.6/2	35	75-80
CMC-H 5 tw	$S_{XS/S/M/G}$ 4x80	5.6/6.3	<50 [a]	<50[a]
XAN 1.50 tw	S_{XS} 20	0.125/0.25	1-2	3-4
XAN 1.50 tw	S_{XS} 20	0.4/0.5	6	8-9
XAN 2.50 tw	S_{XS} 20	0.71/1	50	80
XAN 2.50 tw	$S_{XS/S/M/G}$ 4x10	2.8/4	<50 [a]	<55 [a]
XAN 2.50 tw	$S_{XS/S/M/G}$ 4x80	5.6/6.3	<25 [a]	<40 [a]

[a] overestimated

Table 3.11.: AN range: characteristic values for penetration with stagnation with quartz mineral or bentonite suspension addition (V-S test)

Fluid	Additive	Soil [mm]	$s_{crit,1}$ [cm]	$s_{crit,2}$ [cm]
AN-H 0.75 tw	S_{XS} 20	0.125/0.25	5	18
AN-H 0.75 tw	S_{XS} 20	0.4/0.5	15	30
AN-H 1.5 tw	S_{XS} 20	0.125/0.25	7	10
AN-H 0.375 tw	B 5	0.71/1	10	27 [a]
AN-H 0.75 tw	B 5	0.71/1	10	27 [a]
AN-H 1.5 tw	S_{XS} 20	0.71/1	40	80
AN-MH 0.75 tw	B 5	0.71/1	25	60 [a]
AN-S 1.5 tw	S_{XS} 20	0.71/1	40	80-95
ANmix 0.75 tw	B 5	0.125/0.25	1-2	3-4 [a]
ANmix 0.75 tw	B 5	0.4/0.5	4	7 [a]

[a] at 0.15 bar

3.4.5. Soil and polymer classification for colmation

Section 3.4.2 has shown that the flow behaviour of viscous base fluids in soil can be classified with reference to the characteristic soil grain diameters d_{30} or d_{50}.

Based on a comparison of Tab. 3.10-3.11 (V-S) and Tab. 3.7 & Tab. 3.8 (V-L) with Tab. 3.10 (soil), it can be concluded that this classification also matches colmation sufficiently well as the following summary shows:

V-L:	AN-H 0.75 dw + S_{XS} 20	0/2 ($d_{50} = 0.45$):	$s_{crit,2} = 28$ cm
V S:	AN-H 0.75 tw + S_{XS} 20	0.4/0.5:	$s_{crit,2} = 30$ cm
V-L:	AN-H 0.75 tw + B 5	0.5/1.2 ($d_{50} = 0.86$):	$s_{crit,2} = 25$ cm
V-S:	AN-H 0.75 tw + B 5	0.71/1:	$s_{crit,2} = 27$ cm
V-L:	CMC-H 2.5 tw + S_{XS} 10	0/2 ($d_{30} = 0.33$):	$s_{crit,2} = 6 - 10$ cm
V-L:	CMC-H 5 dw +S_{XS} 20	0/2 ($d_{30} = 0.33$):	$s_{crit,2} = 4$ cm
V-S:	CMC-H 2.5 tw + S_{XS} 20	0.125/0.25:	$s_{crit,2} = 3 - 4$ cm
V-S:	CMC-H 2.5 tw + S_{XS} 20	0.4/0.5:	$s_{crit,2} = 17$ cm
V-L:	CMC-H 2.5 tw +B 5	0/2 ($d_{30} = 0.33$):	$s_{crit,2} \approx 100 - 120$ cm
V-S:	CMC-H 2.5 tw + B 5	0.125/0.25:	$s_{crit,2} = 37$ cm
V-S:	CMC-H 2.5 tw + B 5	0.4/0.5:	$s_{crit,2} = 280 - 320$ cm

In order to give an estimate on relations to the Terzaghi filter criteria (section 2.3.3), the following Tab. 3.12 summarise the ratios from V-S testing with quartz mineral additives, which were found to lead to stagnation with CMC-H or XAN. It can be seen that the stable ratio factor named F for mechanical filter stability can range significantly above 4-5, which is the respective value for pure grain filtration. The difference can be probably attributed to enlarged effective grain sizes through polymer adsorption.

Table 3.12.: Quartz additive matrix – CMC-H / XAN

	Quartz mineral additive				Stable ratios $d_{max,add} = d_{soil}/F$
Soil	0/0.125	0.125/0.25	$0.4/0.5^{a)}$	$0.71/1^{a)}$	$F_{applied}$
0.125/0.25	(X)	–	–	–	5
0.4/0.5	X	(X)	–	–	7-10
0.71/1	X	(X)	–	–	5-20
1.6/2	X	X	(X)	X/(X)	2-10
2.8/4	X	X	X	(X)	7.5
5.6/6.3	X	X	X	X	7.0

X necessary, (X) recommended, – not applicable

[a)] Higher polymer dosage (5 g/l) recommended to ensure suspendability

3.5. Results: horizontal penetration – plane (H-P)

General

The following testing regime comprising 26 tests was chosen in order to evaluate the transferability from V-S and V-L towards horizontal flow with direct soil-fluid contact and related filter cake formation.

With respect to mineral fines, a range of soils and quartz mineral sequences was tested for the polymers of natural origin (mainly CMC-H as a representative). Variation with synthetic base polymers comprised the comparison of quartz powder vs. bentonite suspension addition exemplarily for AN-H/ANmix. Subsequently, the addition of different compositions of aqueous grains was tested in varying ground conditions with CMC-H, AN-H/ANmix and AN-M. The tested soils are coloured in accordance with Fig. 3.10 (and with their closest representative soil fractions used for V-S testing).

0/2	green	3/5	olive
0.5/1.2	blue	3/8	cyan (50% 3/5, 50% 5/8)
1/3	red	5/8	lilac

Penetration behaviour

Fig. 3.78-3.79 show the development of the cumulated outflow over time. In this respect, 4000 g represent approximately 29 cm of penetration depth based on average calculation.

Concerning the addition of mineral additives (Fig. 3.78), it can be noted that the penetration behaviour matches the behaviour found with V-S and V-L testing very well. A quantitative comparison is given in Tab. 3.13. The average penetration depths obtained with bentonite

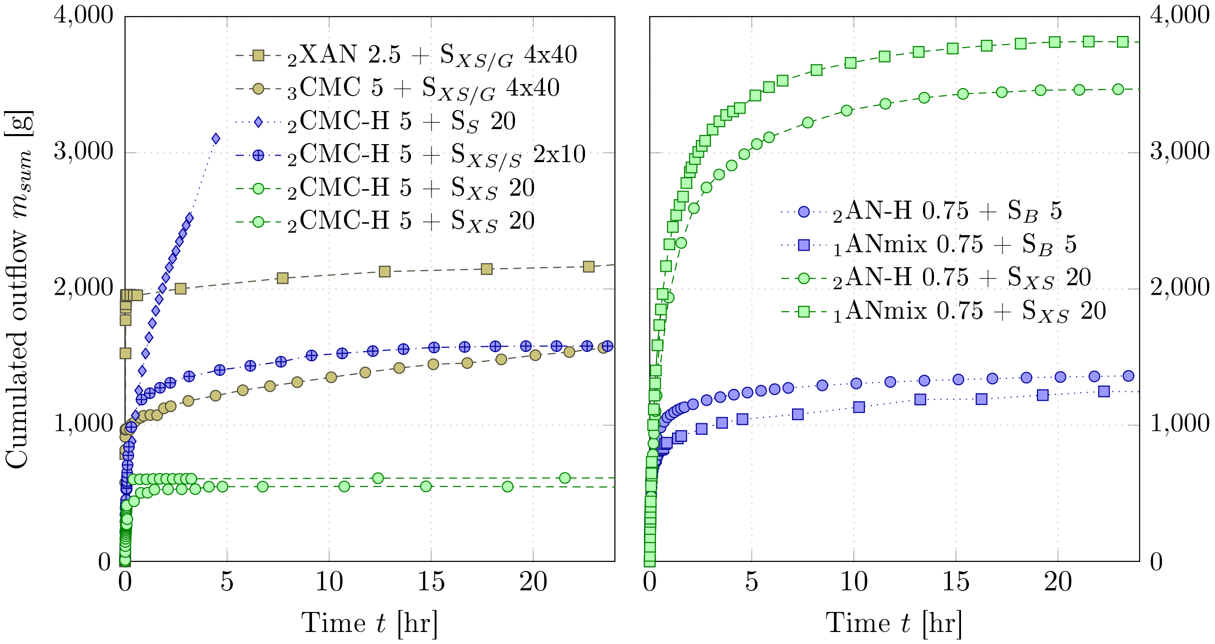

(a) Polymers of natural origin

(b) Synthetic polymers

Figure 3.78.: Plane model penetration test with mineral load (tw)

Table 3.13.: H-P vs. V-L: Maximum penetration depths with mineral additives

Testing device	Soil	Fluid	s_{max} [cm]
V-L	0/2	$_1$CMC-H 5 dw + S$_{XS}$ 20	4
H-P	0/2	$_2$CMC-H 5 tw + S$_{XS}$ 20	4-4.5 (545-620 g)
V-L	0.5/1.2	$_2$CMC-H 5 tw + S$_{XS/S}$ 2x10	11
H-P	0.5/1.2	$_2$CMC-H 5 tw + S$_{XS/S}$ 2x10	11 (1580 g)
V-L	3/5	$_2$XAN 2.5 tw + S$_{XS/G}$ 4x40	14
H-P	3/5	$_2$XAN 2.5 tw + S$_{XS/G}$ 4x40	16 (2185 g)
H-P	3/5	$_2$CMC-H 5 tw + S$_{XS/G}$ 4x40	11.5 (1585 g)
V-L	0/2	$_1$AN-H 0.75 dw + S$_{XS}$ 20	28
H-P	0/2	$_2$AN-H 0.75 tw + S$_{XS}$ 20	25 (3470 g)
V-L	0/2	$_1$ANmix 0.75 dw + S$_{XS}$ 20	25
H-P	0/2	$_1$ANmix 0.75 dw + S$_{XS}$ 20	28 (3810 g)
V-L	0.5/1.2	$_2$AN-H 0.75 tw + B 5	25
H-P	0.5/1.2	$_2$AN-H 0.75 tw + B 5	10 (1360 g)
V-L	0.5/1.2	$_1$ANmix 0.75 tw + B 5	25
H-P	0.5/1.2	$_1$ANmix 0.75 tw + B 5	9 (1255 g)

Table 3.14.: H-P vs. V-L: Maximum penetration depths with aqueous grains

Testing device	Soil	Fluid	s_{max} [cm]
V-L	0.5/1.2	$_1$ANmix 0.75 tw + P$_S$ 1	22
H-P	0.5/1.2	$_1$ANmix 0.75 tw + P$_S$ 1	9 (1180 g)
H-P	0.5/1.2	$_1$AN-M 0.75 tw + P$_S$ 1	21 (2885 g)
V-L	5/8	$_2$AN-S 1.5 tw + P$_M$ 1	80
H-P	5/8	$_2$AN-H 0.5 tw + P$_M$ 0.8	112 (15.4 kg)

suspension addition are even below what was tested in V-L. This can possibly be explained by the low overpressure applied with this device (0.025 bar). In addition and to underline the findings from V-S testing, one test with CMC-H 5 in coarse sand (0.5/1.2 mm) was performed with a quartz sequence addition (S$_{XS/S}$) vs. only sandy grains (S$_S$) at cumulated same concentration. The results displayed in Fig. 3.78a clearly show the importance of the smaller grain fraction (or more generally of grain sequences from a maximum required grain size to quartz powder) in adequately sealing the earth wall. No stagnation could be measured by only applying S$_S$ = 0.125/0.25 mm.

Aqueous grain addition covered a broader range of variation (Fig. 3.79) with coarse sand to gravel. Tab. 3.14 gives a comparison of V-L vs. H-P testing with relatable mixes. It can be

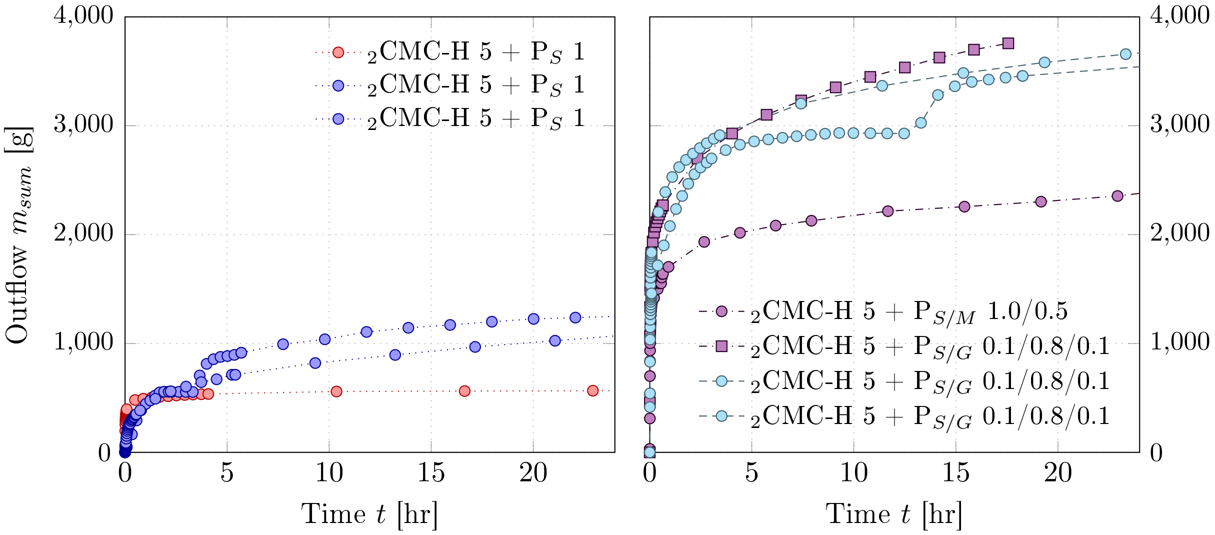

(a) Sand and gravel sand

(b) Gravel

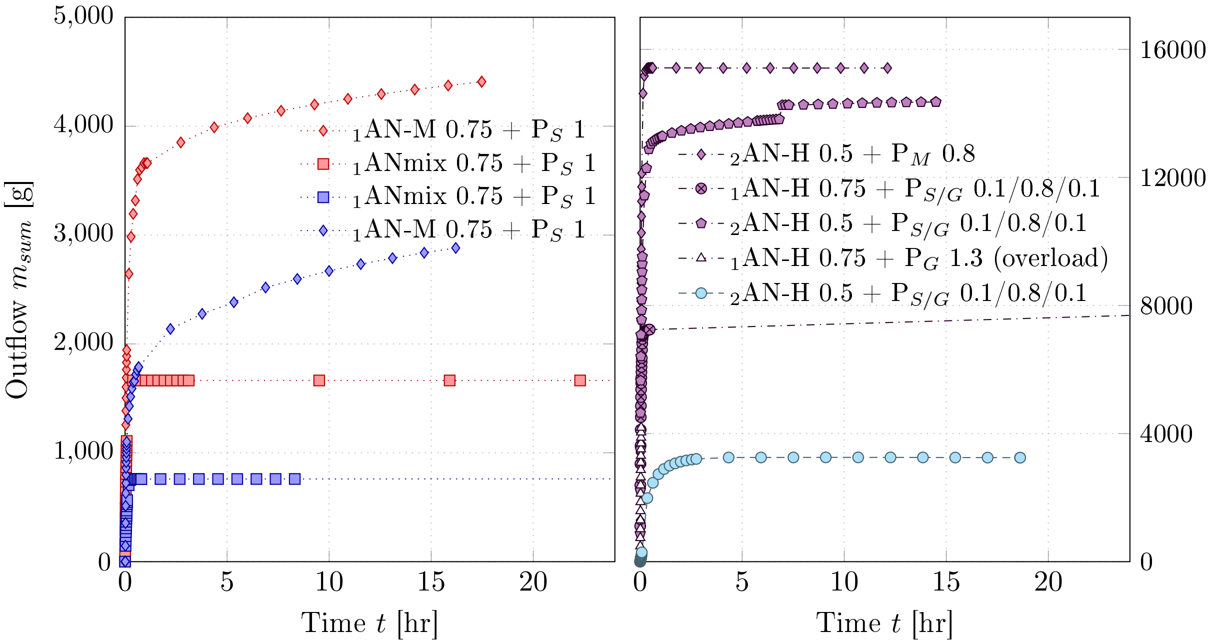

(c) Sand and gravel sand

(d) Gravel

Figure 3.79.: Plane model penetration test with SAP load (tw)

seen that the V-L tests generally seem to produce higher penetration depths in combination with the synthetic base polymers. It is likely that this, too, is mainly related to the significant overpressure difference. It can be rationalized that the rough surfaces of the mineral grains are more easily trapped at the earth wall for colmation. In contrast, aqueous bentonite flocks or aqueous polymeric grains may 'slip away' more easily at higher pressure level. This 'slippery' effect is also visible with uncharacteristic deviations of certain curves in Fig. 3.79. They were created by refilling of the fluid level, which apparently influenced the stability of the aqueous filter cake.

Relative comparisons of penetration depths and the overall behaviour obtained with this testing device, however, are still meaningful when considered at scale. It can be concluded based on Fig. 3.79 that aqueous polymeric grains can be used both for synthetic base polymers and for polymer bases of natural origin. In this respect, CMC-H 5 even seems more effective than the synthetic products, especially when the polymeric grain sequences do not adequately match the soil conditions.

For coarse sand (blue) to gravel sand (red), CMC-H and ANmix show comparable results with P_S addition, though inversed concerning their deviation (Δm_{sum}=500-1000 g $\sim s_{average} = 4 - 7$ cm). AN-M, in comparison, proves less effective. This can possibly be related to thinner (compared to CMC-H) and shorter (compared to ANmix, so less interactions) chains. In 5/8 mm gravel (scale difference in Fig. 3.79d!), CMC-H 5 needs significantly lower fluid volumes than AN-H at $P_{S/M/G} = 0.1/0.8/0.1$. In this respect, it can be seen that an increase in finer grains (P_S) nearly halves the penetration depth (Fig. 3.79b).

Moreover, a comparison of this aqueous grain mix to single fractions use was performed with AN-H (Fig. 3.79d). It can be seen that with solely applying large grains (P_G), which do not adequately match the soil pores, clearly no effect can be achieved. In fact, a significant increase in the lower water level was observed during flow initiation. The medium fraction, however, resulted in further penetration than with the addition of a small fraction of finer grains. But eventually, a filter cake was built. This effect could never be observed with quartz mineral grains within the tested ranges and can be probably attributed to the behaviour of these aqueous grains. One possible explanation could be that the grains were in fact not fully swollen at test start even though intended. Consequently, they could penetrate the soil more easily and then swell further, which more effectively seals the ground. Or, enough penetration eventually pressed enough grains into the soil, which is possible as they are moderately flexible. The former effect can be considered a useful effect on site, but cannot be safely calculated.

Generally, the following conclusions can be drawn. The behaviour of quartz mineral grains is clearly immediately transferable from vertical testing at higher overpressure and with granular filter material to horizontal testing at low overpressure with direct fluid-soil contact. All mixes except for CMC-H 5 + S_S were able to stabilize the small earth wall section and maximum penetration depths compared between V-L and H-P are very close. Bentonite flocks and polymeric grains have also proven to be applicable for horizontal penetration and filter cake formation. However, the effect of filtration in this context seemingly depends upon overpressure levels to a certain extent. Higher overpressure may result in a moderately higher maximum level of penetration for these types of grains. Moreover, an adequate grain size distribution with enough small fractions has proven to be favourable for effective colmation.

Filter cakes

In the context of filter cake stability, especially with respect to the influence of movement during excavation, the following Fig. 3.80-3.84 give a representative overview on filter cake types observed with this testing device.

Generally, it can be seen that the filter cakes formed with quartz minerals are relatively thin (<1 mm), especially the filter cakes with the polymers of natural origin XAN/CMC-H are only barely visible and even thinner (externally) than observed during V-L testing. This can be clearly attributed to wall effects with V-L testing. In sand (Fig. 3.80), CMC-H (or equally XAN) forms a visibly stable thin layer around the larger sand grains. As the grain surface is still clearly visible, it may be assumed that this cake will not have a significant influence on wall friction

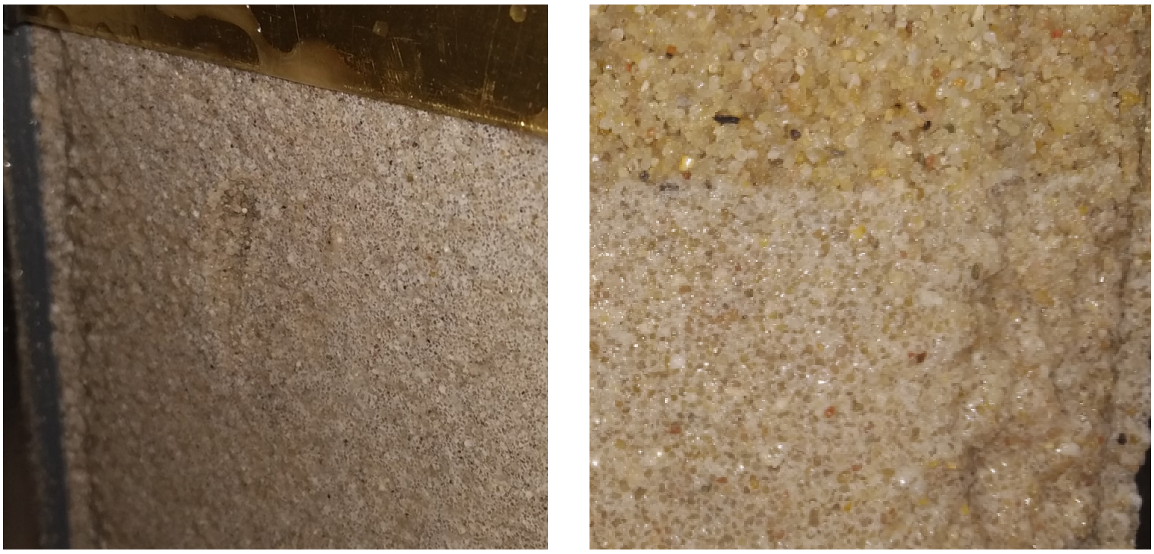

Figure 3.80.: H-P filter cake CMC-H with quartz powder (left) and quartz powder and fine sand (right)

mobilization of the later structure. Moreover, the polymer penetration and membrane formation have formed a certain degree of cohesion between the particles at the earth wall, which will possibly markedly contribute to internal stability.

In gravel (5/8 mm) (Fig. 3.81), these cohesion effects do not seem possible. Consequently, the equally thin filter cake easily breaks once the overpressure is reduced. It will likely easily reform if adequate grains are available, but otherwise it may be considered potentially unstable towards agitation. With enough overpressure, it is, however, perfectly stable.

The filter cake formed by AN polymers and quartz powder (Fig. 3.82) is clearly thicker, but still < 1 mm in thickness. It seems to have formed more like an external filter cake, but the same cohesion effect could be observed here, which additionally stabilizes the earth wall locally.

The filter cakes produced by aqueous grains, bentonite flocks or polymeric grains, are visibly thicker and more diffuse. In this respect, the deformable bentonite flocks seem to interconnect the grains and thereby equally locally stabilize them as above. The polymeric grains seem to form a rather thick external wall in combination with the viscous base fluid with a certain degree of internal clogging. In these illustrated soil conditions it may be possible that the viscous aqueous polymeric grain layer can be moved by an excavation tool. This 'peeling' effect showing an easily removable front formed by polymeric grains can be seen in Fig. 3.84 (left). However, it is possible that this external wall reflects the remaining filtration material rather than the main pressure-absorbing membrane.

Especially with AN-based polymers, which create a more slimy surface, it is unclear how the filter cake will interact with concrete placement. Generally, for temporary stability under fluid support, all filter cakes in sand seem relatively stable against agitation from excavation. Gravel soil could be potentially unstable.

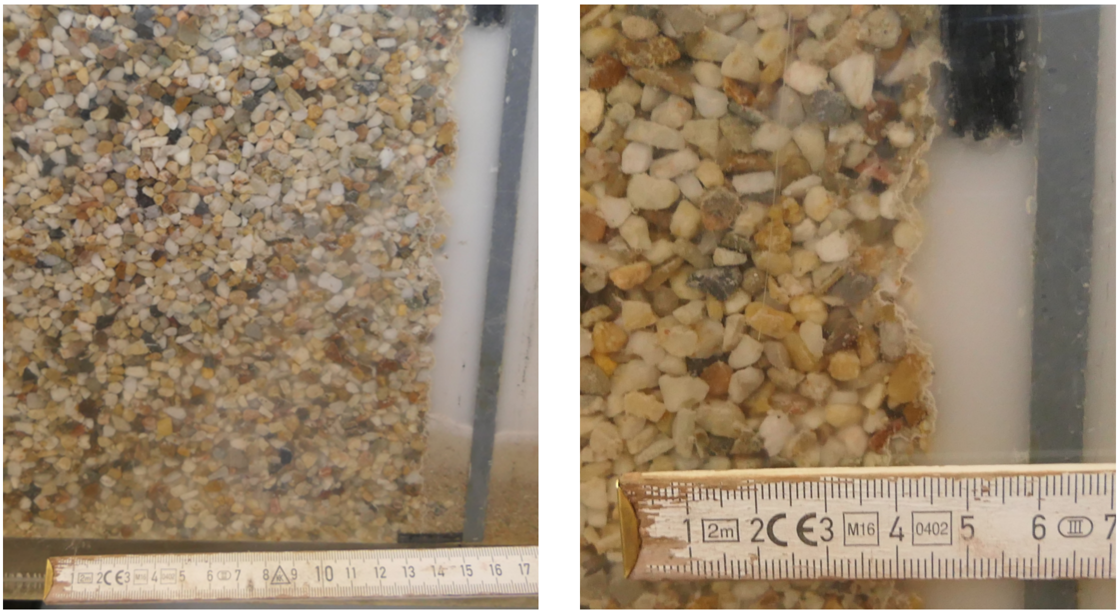

Figure 3.81.: H-P filter cake CMC-H with quartz sequence in gravel

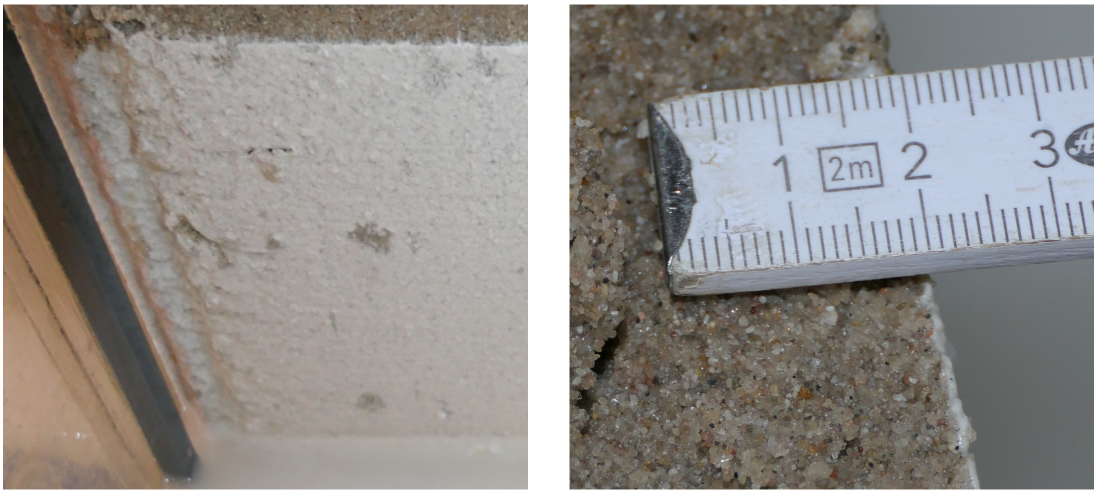

Figure 3.82.: H-P filter cake AN-H/Anmix with quartz powder

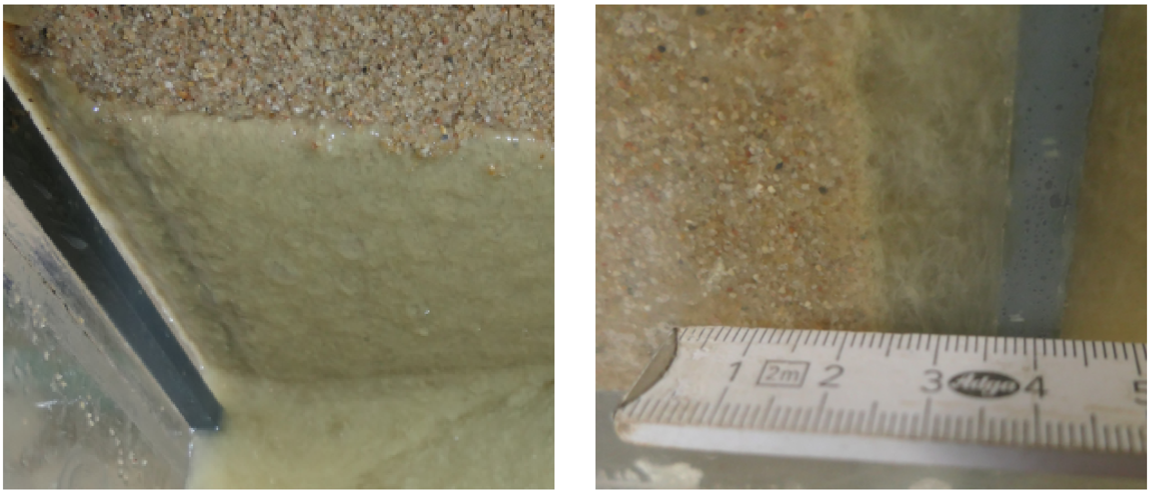

Figure 3.83.: Filter cake with bentonite flocks (AN-H/ANmix)

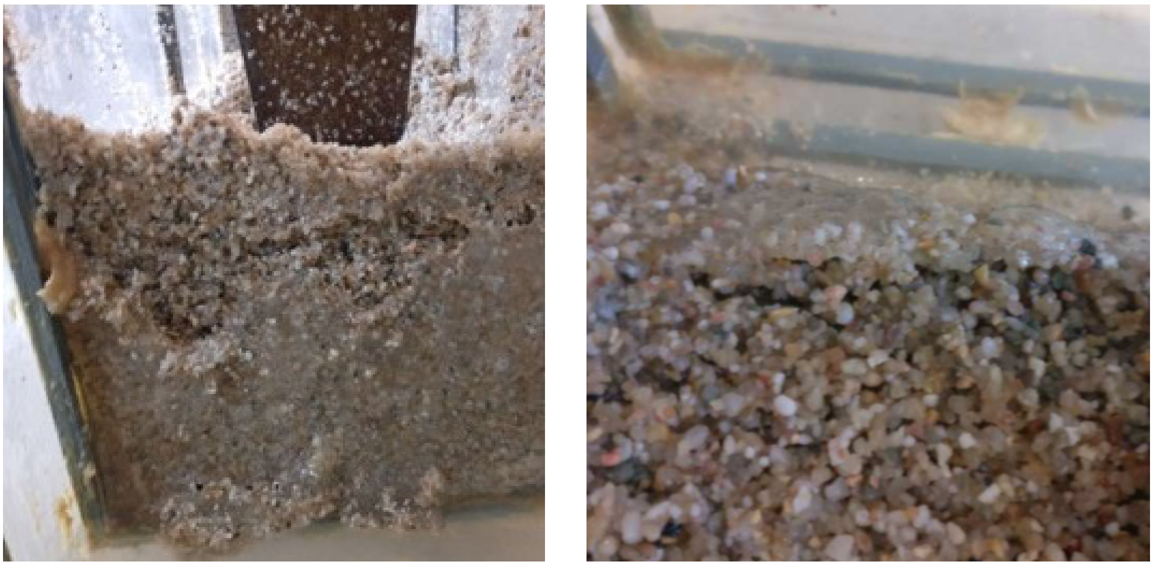

Figure 3.84.: Filter cake with polymeric grains (AN-H/CMC-H)

3.6. Results: horizontal penetration – radial (H-R)

Four exemplary circular test piles were produced in order to analyse the effect of aqueous grains on the final filter cake. Tab. 3.15 summarizes the results with regard to bulk rheology and penetrated volume. Fig. 3.85-3.87 give an impression on skin and filter cakes after concreting and removal of surrounding soil.

Average penetration values (assuming the same penetration depth along the height) based on penetrated volume are indicated as $s_\varnothing$. The penetrated volume is differentiated as initial volume for filter cake formation and subsequent volume for filtration. The Marsh values are given with indication of maximum deviations to reflect homogeneity of the mixes. The homogeneous mixes were performed with the mixing device shown in Fig. 3.5. The other two mixes show considerably higher deviations due to problems during mixing.

Firstly, it can be noted that the obtained penetration depths can all be categorized as relatively low. The results with 0.5/1.2 mm soil match the results obtained from plane penetration with H-P testing relatively well despite higher overhead (approximately 1.25 m). It needs to be noted in this context that the curvature of the pressure drop in this radial case should be even steeper due to radial penetration, i.e. pressure should drop more rapidly. Moreover, in the case of bentonite suspension addition, a certain piping effect started after filter cake formation, which resulted in a certain drop in overhead due to the rise of some fluid between the fluid-containing pipe and the soil. This indicated a relatively impermeable filter cake, but could also be the reason for the lowest level of subsequent penetration depth.

The penetration depth calculated for $_1$ANmix in gravel is astonishingly low. This can be attributed to a certain degree to the mixing process which produced a relatively thick mix. Moreover, it is possible that not properly dissolved polymer aggregates functioned as small polymeric pore blockers and that the P_M products were not yet fully swollen at penetration start.

With respect to resulting skin optics, it can generally be noted that the concrete surfaces in all cases are sufficiently well formed. The figures can be considered representative. They show the transition zone between cased (top) and fluid-supported (bottom) areas. Differences between these zones were observed in all cases. It was found that the surrounding soil was easier to remove along the fluid-supported fractions (visible especially in Fig. 3.85b and 3.86a). It may be concluded that the surface film created by the viscous polymer solution is not entirely removed,

Table 3.15.: Radial model penetration tests – overview

Soil fraction	Polymer [g/l]	Additive [g/l]	Marsh 1L $\varnothing^{\Delta_{max,+}}_{\Delta_{max,-}}$ [s]	Bulk visc. $\eta_{\dot{\gamma}=1\cdot10^{-3}}$ [Pa·s]	Penetrated volume $V_{init} + V_{subs} = V_{tot}$ ($s_\varnothing$) [l] ([cm])
0.5/1.2	$_2$CMC-H 5	P_S 1	$72^{+25\%}_{-21\%}$	0.8	27+13=40 (14.5 cm)
0.5/1.2	$_2$AN-H 1	P_S 1	$260^{+4\%}_{-2\%}$	19	37+7=42 (15.0 cm)
0.5/1.2	$_1$ANmix 0.75	B 5	$295^{+2\%}_{-3\%}$	6	20.5+0.5=21 (8.5 cm)
5.6/8	$_1$AN-Mix 1	P_M 2	$153^{+41\%}_{-33\%}$	22	37+2=39 (14.2 cm)

(a) Pile ${}_2$CMC-H 5

(b) Pile ${}_2$AN-H 1

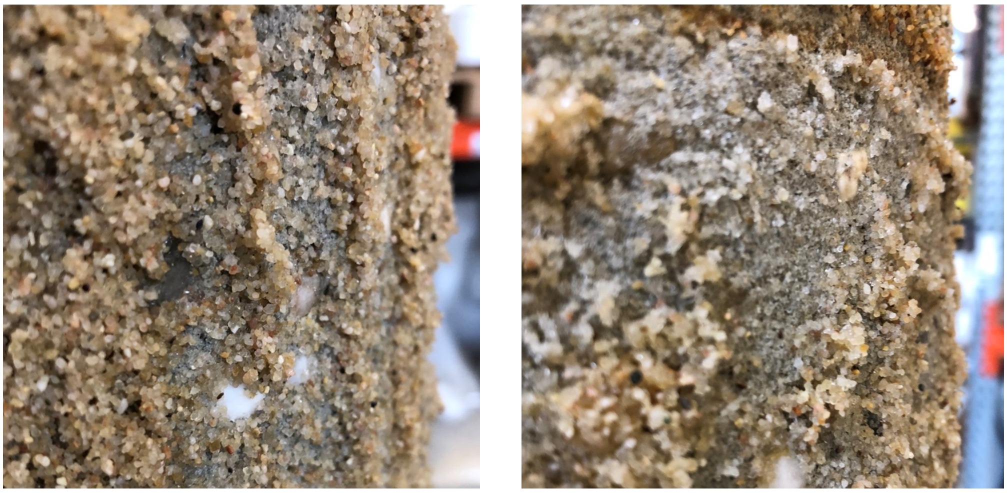

(c) Exemplary details

Figure 3.85.: Skin and filter cake: 0.5/1.2 -CMC-H/AN-H with P_S 1 (tw)

which may have a negative effect on the mobilizable skin friction at the soil/concrete interface. The pile toes are not shown, but they were found even without any visible filter cake depositions or badly spread concrete. Only the pile produced with ${}_2$AN-H (Fig. 3.85 centre) showed a small intrusion at the transition zone between soil contact and pipe (Fig. 3.85, centre left). This can be attributed to the device restrictions creating a low concrete overhead during the last concreting step when the pipe is pulled up. As overheads are usually higher, this effect may be neglected

(a) Pile (b) Detail

Figure 3.86.: Skin and filter cake: 5/8 $-_1$ANmix 1 + P_M 1 (tw)

here.

The formed filter cakes are clearly thicker and denser than was observed during H-P testing. This effect is also common for bentonite suspensions as described e.g. by Arwanitaki (2009). The skin of the piles executed with polymeric grains is still covered with a certain amount of aqueous grains. In this respect, the two piles concreted in 0.5/1.2 mm soil with P_S both show a relatively small amount, only a few grains can still be located, the filter cake has clearly been removed to a significant degree by the rising concrete. The larger polymeric grains used for gravel are still present in a considerable quantity (Fig. 3.86b). This may be explained by the geometrical roughness of the soil, which impedes the removal of these grains through upwards flowing concrete to a larger degree. While the low percentage of remaining grains in 0.5/1.2 mm soil will have no significant influence on the mobilizable skin friction, the same cannot be said for the gravel soil. The possibility that these grains are chemically degraded at some point should be considered as this could reduce the mobilizable friction.

The pile concreted with bentonite suspension addition is visibly covered with a thin gum-like bentonite-polymer layer similar to a filter cake created by means of polymer-modified bentonite. It is rather difficult to remove, but it can still be considered flexible to a certain degree, so its is unclear to what extent this type of filter cake influences the mobilizable skin friction.

It can be concluded that the application of these types of additives can produce filter cakes, whose effect on skin friction is not clear. It can be said, however, that concrete can remove, solidify or drain the filter cake formed during fluid support. It is likely that this happens to a larger degree with higher concrete overpressure.

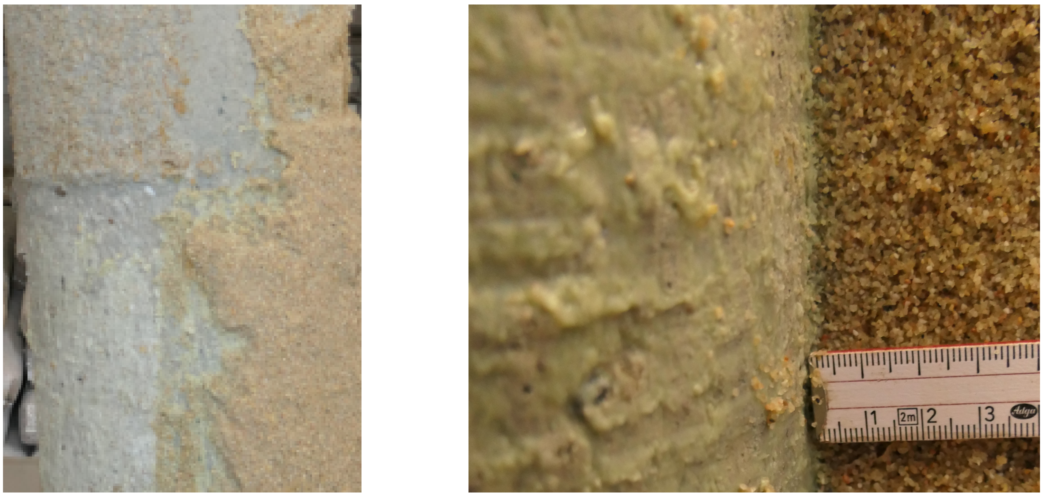

(a) Pile (b) Cut

(c) Filter cake residues

Figure 3.87.: Skin and filter cake: 0.5/1.2 $-_{1}$ANmix 0.75 + B 5 (tw)

3.7. Conclusions from soil penetration testing

The experimental investigation has shown that the penetration behaviour of viscous polymer solutions into non-cohesive soil is governed by interaction mechanisms between these two systems, which can be associated with the effective grain diameters d_{30} or d_{50} of the subsoil and the specific structure of each polymer type (complexity, anionicity, etc.).

In this regard, the penetration behaviour of pure viscous base products can be generally classified as 'viscous penetration', i.e. with a pressure drop curvature following the successively advancing penetration depth rather independently of the overpressure level (Δp_{max} investigated: 0.7 bar). This curvature is moderately non-linear and characteristic to the specific conformation the individual polymer type can form within the specific porous medium. Consequently, the nonlinearity to the pressure drop is not as pronounced in finer soil fractions with comparably narrow pore channels likely limiting the conformational flexibility of the polymer chains.

Accordingly, polymer bulk rheological characterisation cannot be immediately transferred to this 'in-situ' situation. However, by taking into account correction factors enabling a vertical shift (dilution) and pronounced plateau formation, it was found possible to relate high-shear-rate bulk rheological behaviour to the in-situ rheology observed by means of capillary bundle approximations. In this context, it was observed that the capillary bundle parameters ($\alpha^*, \dot{\gamma}_{crit,\eta min}, \dot{\gamma}_{crit,\eta max}$) do not markedly change from medium to fine sand, but that they are rather influenced by changing polymer concentration and polymer type.

In addition to this viscous flow behaviour, a certain micro-colmation effect was observed in finer soil material with CMC-H and especially XAN during V-L and V-S testing. This resulted in a steeper decrease of measured penetration depths with decreasing representative grain diameter as found with AN polymers and a moderately higher pressure transfer immediately at the earth wall associated with higher mobilizable earth wall gradients.

The analysis of the effect of granular additives on the colmation behaviour and related support pressure mobilization generally matched with practical experience in the sense that the presence of relatively small amounts of fines was found to significantly influence maximum penetration depths and the effectiveness of pressure transfer in many cases.

Especially the polymers of natural origin were found the be very effective in combination with quartz granular material in easily taking up and dispersing fines and forming thin and sufficiently sticky filter cakes in sand relatively quickly, if the grain size fractions necessary for colmation were present to a sufficient degree. In accordance with filtration theory, for colmation to take full effect and enable full pressure transfer, the additive grain size fraction must contain a distribution of fractions down to quartz powder at equal individual fraction concentrations. Otherwise, i.e. e.g. if the smallest grain size fractions are missing, the penetration behaviour will slow down to a certain degree but not sufficiently well to visibly stagnate. On the other hand, with suitable grain size distributions, formed filter cakes were found stable at all tested overpressure levels.

In this regard, it was observed that an effective filter cake formation process follows a characteristic behaviour describable by two critical penetration depth parameters $s_{crit,1}$ and $s_{crit,2}$. In an initial phase, the flow behaviour follows the development of the curves of the same polymer at equal polymer concentration without fines, until the colmation process takes effect $s_{crit,1}$. This deviation point from viscous flow behaviour visible in $v-s$ or $v-i$ plots coincides with the starting increase of pressure transfer at the earth wall. Here, a significant decrease in v of several decimal powers can be related to full pressure mobilization at the earth wall with formation of a filter cake. An increase in the amount of fines leads to an earlier deviation and quicker stagnation.

It was further found that even a very small amount of fines taken up by the support fluid from the native ground can already create a marked filtration effect and thus significantly increase the stability against the removal of grains from the earth wall (tested for 1 g/l of quartz fines in medium sand). Likewise, a synthetic manufacturer mix was found to already contain a certain amount of additives to create a certain degree of colmation zone. However, in both cases, this effect cannot be safely taken into account as it is not pronounced enough to be reflected as a marked change in filter velocity. This, however, conversely shows that a significant decrease in filter velocity with the presence of fines is a strong indicator for full pressure transfer through filter cake formation.

These observations were generally also made for AN polymers in combination with quartz powder. However, as these polymers do not easily take up quartz fines and effectively release them for colmation (at at least medium molecular weight values), this method is not suggested for this group of polymers. Instead, they were found to function well with addition of bentonite suspension at low concentration as this mix forms aqueous flocks, more effectively with larger molecular weight. Aqueous polymeric grains, too, were found to be applicable at least to coarser soil materials with all tested polymer types. If stagnation occurred, both categories were found to exhibit the same behaviour with respect to these critical penetration depth levels as polymers of natural origin with quartz minerals. However, stability at high pressure levels was not found to be guaranteed in all cases.

With respect to the characteristics of formed filter cakes, it was observed that they are relatively thin and seemingly stable against mechanical agitation at least in sand material owing to a certain cohesion created by the polymer film connecting the filter cake. They are therefore generally considered not to be detrimental to the following concreting stage if fluid and based are properly cleaned beforehand. However, clearly, a clean polymer solution would be favourable in this regard. Likewise, it cannot be ruled out that especially bentonite flocks and polymeric grains may create adverse effects for final skin resistance as gum-like remains were found to a marked degree after concreting, even though the rising concrete seemingly removed a significant amount of the soft filtration remains of the filter cake.

Overall, it can be concluded based on this experimental investigation that it is indeed possible to relate soil properties and specific polymer characteristic to values, which can be used for stability design. Moreover, it may indeed be possible to take into account the positive effect of fines suspended anyway in the support fluid, e.g. from previously excavated layers. However, current testing methods cannot adequately reflect the requirements which have to be met regarding adequate grain size distributions and amounts of fines.

4. Stability conclusions

4.1. Stability concept

On the basis of the previous investigation, stability considerations can be differentiated into two categories:

(1) viscous flow with 'clean' polymer solutions and
(2) colmation effects with granular additives

In this context, the concept presented below focusses on the determination of

- the characteristic support force S_k based on the mobilizable pressure Δp_{mob} within the failure body (related to f_{s0}),
- the characteristic mobilizable earth wall pressure gradient $f_{s0,wall,k}$ and especially
- the critical time t_{crit} defining the worst and therefore decisive case.

to be applied within the general stability concept described in section 2.1.2.

4.1.1. Viscous flow

With viscous flow, the pressure drop curvature continuously follows the penetration depth s, but the penetration rate also decreases with increasing s. Consequently, stability can only be guaranteed for a limited time interval with s_{max} representing the critical state, i.e.

$$t_{crit} = T_{max} = t(s_{max})$$

An adequate safety level should therefore not only take into account material deviations, but also a sufficient tolerance on time to be defined for the respective application.

A realistic prediction of the time-dependent penetration behaviour of the support fluid into soil is essential. This can be provided for by an analytical formulation based on capillary bundle models or by means of soil penetration tests, also from comparable soil-polymer combinations. For capillary bundle models, bulk rheological parameters cannot be applied without correction factors considering the specific interaction between soil and polymer. Otherwise, the penetration depth could be underestimated by far. Capillary bundle parameters for common polymer products and medium to fine sand are provided in section 3.3.3.

For a given point in time, a penetration depth can then be derived and a linear pressure drop can be assumed as a conservative approach for the pressure drop curvature. For fine to medium grained sand, the curvatures displayed in Fig. 4.2-4.3 can be used to take into account the non-linearity of the pressure drop. They are based on the previous experimental investigations and on the assumption that the curvature depends upon relations between the polymer chain and the porous environment and not on the polymer concentration. Three sections with linear course are assumed to simplify subsequent calculations. As these curvatures are based on s_p, a constant correction factor Δs is suggested for the determination of the input parameter s_p with

$\Delta s_{XAN} = \Delta s_{CMC} = 2$ cm and $\Delta s_{AN} = 5$ cm (Eq. 4.1). This stretches the displayed curvatures. It is yet unclear how different overpressure levels affect these values.

$$s_p = s + \Delta s \tag{4.1}$$

With a given penetration formulation and related curvature, the mobilizable pressure can be determined, which forms the basis of micro- and macro stability consideration. Fig. 4.1 summarizes the determination of the mobilizable pressure for macro stability, i.e. for the calculation of the support force $S_k(t, \vartheta)$ (Eq. 4.2).

$$S_k(t, \vartheta) = \int \Delta p_{mob}(t, \vartheta) d\tilde{z} \tag{4.2}$$

For a given slip surface angle ϑ and time t, the following parameters need to be determined in order to calculate the effective support force:

(1) the course of the penetration depth along $\tilde{z}$ (Fig. 4.1 blue illustration)
(2) the points of intersection between penetration level and slip surface to differentiate areas of full pressure transfer ($s_p(z_i) < l(z_i)$) and areas of partial pressure transfer (Fig. 4.1 $\tilde{z}_{crit}$)
(3) the percentage of Δp_{mob} based on a linear pressure drop curvature or based on Fig. 4.2-4.3 (example Fig. 4.1 yellow line)
(4) the resulting course of Δp_{mob} along $\tilde{z}$

The mobilized support pressure transferred to the slip body for the example in Fig. 4.1 should then amount to the area marked in orange. The horizontally hatched area represents the amount of Δp transferred to the soil outside the failure body. This concept can be equally applied to

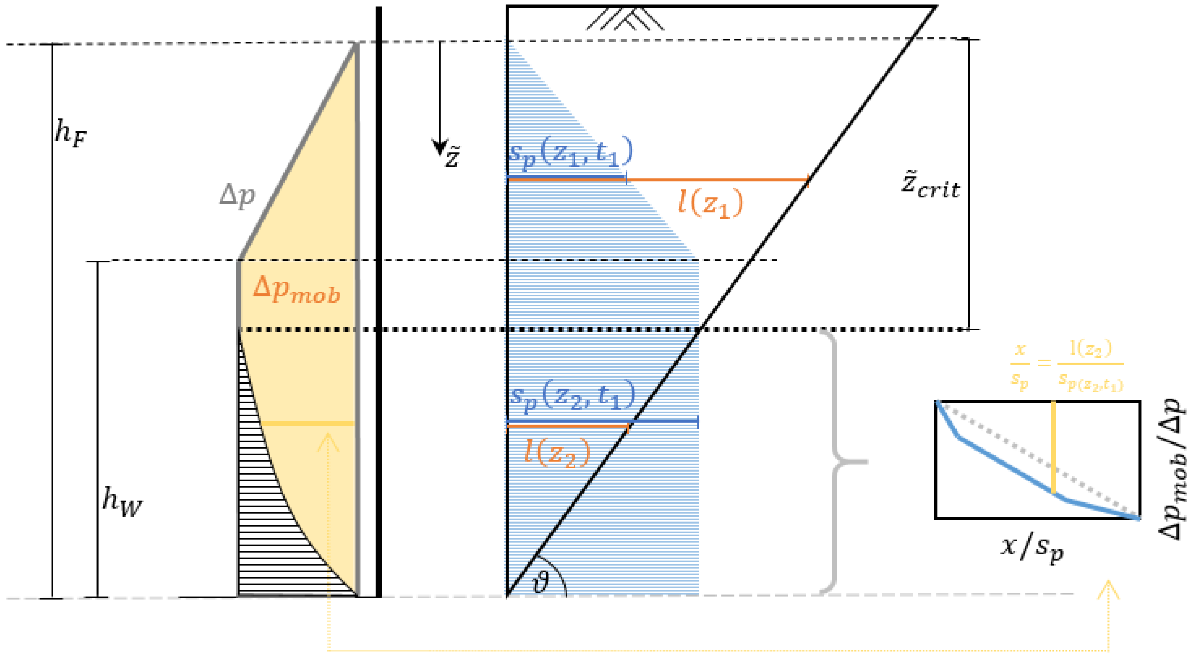

Figure 4.1.: Macro stability: determination of Δp_{mob} for a given penetration course s at time t_1 and slip surface angle ϑ and homogeneous soil conditions

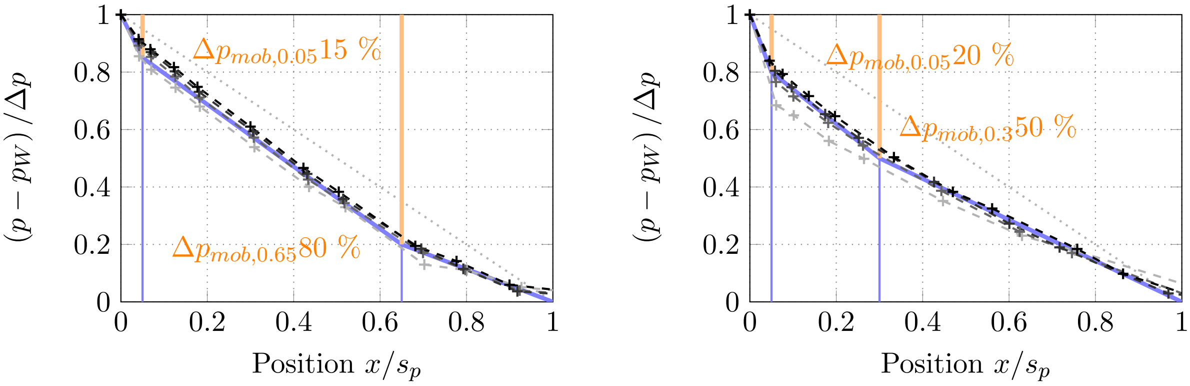

(a) CMC-H (b) XAN

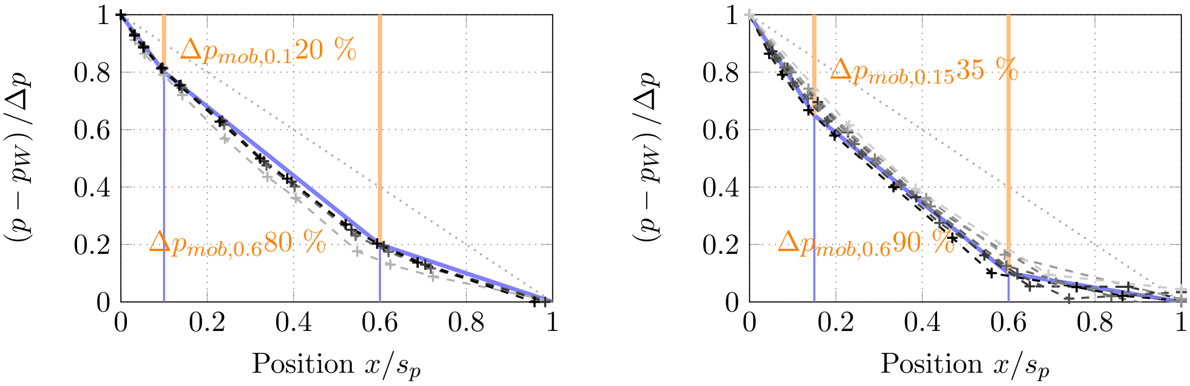

(c) AN-S/AN-H (d) AN-MH

Figure 4.2.: Idealized pressure drop curvatures and mobilized pressure: medium

layered soil conditions. With a more permeable intermediate layer, it is possible that several $\tilde{z}_{crit}$ need to be defined.

As explained in section 2.1.2, an iterative process is necessary to determine the critical values for ϑ and S for the given time t as both earth pressure and support force depend upon ϑ.

For micro stability the earth wall pressure gradient can be determined in accordance with the procedure used to interpret the experimental data. That is, a minimum reference depth of $b = 2$ cm is suggested to determine the earth wall gradient based on Δp_{mob} following Eq. 2.7 [1]. The respective mobilized earth wall pressure $\Delta p_{mob,wall}$ can then be determined based on a linear pressure drop curvature or Fig. 4.2-4.3 with $x = b$. Consequently, for micro stability, it suffices to verify the earth wall pressure gradient at the level of maximum penetration depth $\tilde{z}(s_{max})$, i.e. (Eq. 4.3):

$$f_{s0,wall,crit,k}(t) = f_{s0,wall,crit,k}(t, \tilde{z}(s_{max})) = \frac{\Delta p_{mob,2\ cm}}{b} \tag{4.3}$$

This method can be used iteratively to determine critical stand-up times for all excavation levels based on either the micro or the macro criterion failing. For fine and medium sand and based on the capillary bundle parameters and idealized pressure drop curvatures, this iteration

---

[1] Higher values for b are possible as a safe-side choice, but lower values should only be applied with knowledge about guaranteed support pressure mobilization along this depth. $b = 2$ cm represents the limit value guaranteed by the experimental tests performed within the scope of this work.

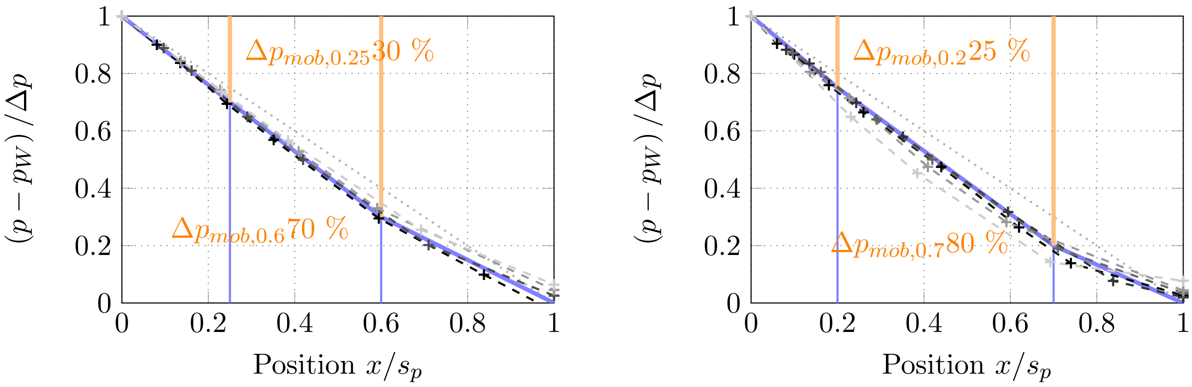

(a) CMC-H

(b) AN-S/-H

Figure 4.3.: Idealized pressure drop curvatures and mobilized pressure: fine sand

Table 4.1.: Increase factor $f_{s0,wall,lin}/f_{s0,wall,lin}$ for micro stability for fine and medium sand based on Fig. 4.2-4.3

Soil	CMC-H	XAN	AN-S/AN-H	AN-MH
Medium sand	$0.15/0.05 = 3$	$0.2/0.05 = 4$	$0.2/0.1 = 2$	$0.35/0.15 = 2.3$
Fine sand	$0.3/0.25 = 1.2$		$0.25/0.2 = 1.25$	

process can be solved numerically for a chosen resolution of $\tilde{z}$, which facilitates the otherwise still complex analysis.

Furthermore, for fine and medium sand and the tested polymers types, the earth wall pressure gradient can be derived directly from the linear calculation ($f_{s0,wall,lin} = \Delta p/s_p$) by means of a correction factor based on Fig. 4.2-4.3 as shown in Tab. 4.1. Thus, the increase factor f_{nonlin} of $f_{s0,wall}$ towards a linear calculation ranges between 1.2 and 4 for fine to medium sand, if the respective non-linearity of the pressure drop curvature is taken into account. With reference to the visualization of reachable values for $f_{s0,wall,req,d}$ (Fig. 2.5), it can be concluded that the design value for the required earth wall pressure gradient for medium to fine sand amounts to max. $f_{s0,wall,req,d} = 25$ kN/m^3 ($\varphi' > 30$ °, $\gamma'' \leq 12$ kN/m^3). With $\gamma_G = 1.00$ (GEO-3), this leads to a critical penetration depth (Eq. 4.4)

$$s_{p,crit,micro} = f_{nonlin} \cdot \frac{\Delta p}{25} \cdot 100 \tag{4.4}$$

with Δp in [kPa] and $s_{p,crit,micro}$ in [cm]. For medium sand and a minimum overpressure level of 0.15 bar, $s_{p,crit,micro}(\Delta p = 15\,\text{kPa}) = 3.3–6.7$ m based on Tab. 4.1, for fine sand, $s_{p,crit,micro}(\Delta p = 15\ \text{kPa}) = 2.0 - 2.1$ m (given that no further safety factor is considered). It can be assumed that macro stability is critical at an earlier stage ($s_p < 2$ m). Therefore, micro stability is not likely to be the critical case. Safety levels in this regard are further discussed in section 4.3.

4.1.2. Colmation

When colmation is considered, critical stability states depend on characteristic penetration depths during the formation of the filter cake. Once the filter cake is formed, full pressure drop at the earth wall can be assumed, i.e. internal stability is guaranteed and $\Delta p_{mob} = \Delta p$. The remaining filter cake permeability was not found to markedly impact pressure transfer at the filter cake. Consequently, the critical time for stability is related to the filter cake formation, i.e. it requires a sufficient amount of colmated solids. It is therefore more accurately described by a critical penetration depth s_{crit} independently of time. The time t_{crit} related to s_{crit} depends on the overpressure level Δp_{max}. With a higher overpressure level, the same s_{crit} is reached faster.

Two methods have been found plausible for the determination of the critical penetration depth s_{crit} in this context, which depend upon two characteristic penetration depths during the formation of the filter cake:

- $s_{crit,1}$ reflects the transfer between viscous flow behaviour and the start of the colmation process
- $s_{crit,2}$ reflects the penetration depth at which the filter cake can be considered fully formed

The dependency of $\Delta p_{mob,wall}$ on $s_{crit,1}$ and $s_{crit,1}$ is explained in Fig. 4.4. The first limit criterion $s_{crit,1}$ can be interpreted as an $s_{visc,max}$ with pressure mobilization following viscous flow behaviour. It therefore represents the state of minimum pressure mobilization at the earth wall (defined by depth b in Fig. 4.4). During $s_{crit,1} < s(t) < s_{crit,2}$, $\Delta p_{mob,wall}$ increases and only the remaining $\Delta p_{mob,rest} = \Delta p - \Delta p_{mob,wall}$ follows the penetration depth until $s_{crit,2}$ is reached.

The critical state for micro stability therefore is $s_{crit,1}$. $\Delta p_{mob,wall}(s_{crit,1})$ can be determined as described in the previous section based on a type-specific curvature of the pressure drop with $s_p = s_{crit,1} + \Delta s$ and $x = b$.

As a safe-side choice, macro stability can then be determined based on a fixed non-linear curvature independently of time as shown in Fig. 4.4c with one intermediate level at $x = b$ with its pressure drop value $\Delta p_{mob,wall}(s_{crit,1})$ defined by the course at $s_{crit,1}$ as described in the previous paragraph. For simplicity or as the determination of a definite $s_{crit,1}$ may not be possible, a linear pressure drop could even be assumed until $s_{crit,2}$ as a safe-side criterion. This corresponds to the approach by DIN 4126:2013 with $s = s_{crit,2}$. The pressure gradient along s is then constant with f_{s0} according to Eq. 4.5.

$$f_{s0,wall,crit,k} = f_{s0,lin,crit,k} = \frac{\Delta p}{s_{crit,2}} \tag{4.5}$$

The calculation of the mobilized pressure for a given depth $x = l(z)$ based on a linear pressure drop along $s_{crit,2}$ is then trivial and the iteration process for macro stability reduces to finding

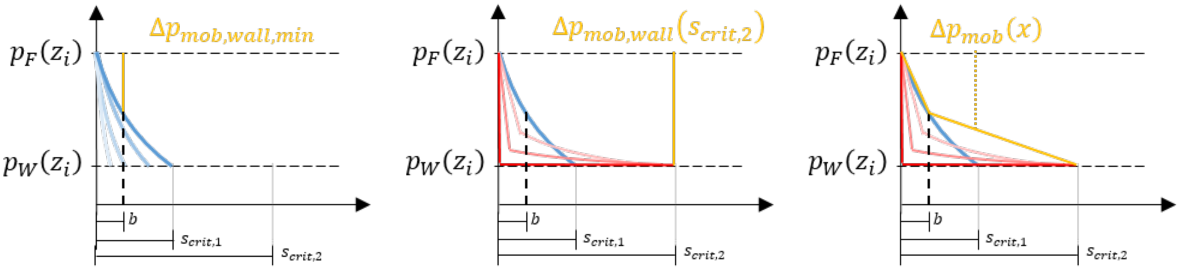

(a) Limit for viscous flow: $s_{crit,1}$

(b) Limit for membrane formation: $s_{crit,2}$

(c) Suggested curvature for macro stability

Figure 4.4.: Filter cake and membrane formation during colmation and critical penetration parameters

ϑ_{crit}. This approach is particularly recommended for small penetration depths $s_{crit,2}$, e.g. below 50 cm, as it significantly simplifies the calculation and reduces the impact of underestimated penetration depths, which is particularly critical at lower penetration depths combined with a non-linear pressure drop curvature.

This concept, however, is based on the assumption that $s_{crit,2}$ and possibly $s_{crit,1}$ are known. Three methods are suggested for the determination of these parameters:

(1) classification of the targeted soils within available data from penetration testing in the form of suitability matrices (e.g. Tab. 3.10-3.11 or Tab. 3.7) to obtain $s_{crit,2}$ and $s_{crit,1}$ with reference to similarity of the following parameters
 - ▪ soil: porosity n, grain diameter d_{30} (XAN/CMC-H polymers) or d_{50} (AN polymers)
 - ▪ viscous base polymer solution: type (molecular weight M_W relevant for AN), polymer concentration, mixing water chemistry
 - ▪ granular additive: type, size distribution, concentration of each fraction (for bentonite flocks defined by the viscous base polymer)

(2) penetration testing with upwards flow (similarly to V-S) with the targeted soils and polymers and a variation of fines concentration similarly to the basis for (1)
(3) comparable experience values based on previous testing according to (2)

The following Tab. 4.2-4.3 summarize suitable polymer-additive combinations as a reference. On site, adequate testing needs to be performed in order to ensure the availability of the needed grain size distribution and amount of fines. This will be addressed in section 4.3. Section 4.2 quantifies this stability concept by means of an example with parameter variation.

Table 4.2.: Additive matrix – CMC-H/XAN

d_{30} [mm]	Quartz grains	Bentonite suspension	Polymeric grains
0.125/0.25	++	+	–
0.4/0.5	++	o	–
0.71/1	+	–	o
1.6/2	+	–	+
2.8/4	o$^{a)}$	–	+
5.6/6.3	o$^{a)}$	–	+

+ recommended, o possible, – not applicable; $^{a)}$ influence of excavation tools on filter cake unclear

Table 4.3.: Additive matrix – AN-S/-M/-H

d_{50} [mm]	Quartz grains	Bentonite suspension	Polymeric grains
0.125/0.25	+/o$^{a)}$/o$^{a)}$	o/+/+	–
0.4/0.5	+/o$^{a)}$/o$^{a)}$	–/o/+	–
0.71/1	–/o$^{a)}$/o$^{a)}$	–/o/+	o
1.6/2	–	–	+
2.8/4	–	–	+
5.6/6.3	–	–	+

+ recommended, o possible, – not applicable; $^{a)}$ difficult to disperse

4.2. Exemplary calculation

Fig. 4.5 shows the results of an exemplary calculation for viscous penetration based on the stability concept presented in the previous sections. The following parameters are used (similar to V-L test XAN 2.5 dw 0/2, but with higher overpressure):

Type	diaphragm wall
Depth guide wall	1.2 m
Polymer solution:	XAN 2.5
Capillary bundle parameters:	$\kappa^* = 0.78$
	$m = 0.35$
	$\dot{\gamma}_{crit,\eta min} = 25$ 1/s
	$\dot{\gamma}_{crit,\eta max} = 0.16$ 1/s
Soil:	medium sand
	$n = 0.3625$
	$k_W = 3.1 \cdot 10^{-4}$ m/s
Overpressure:	$\Delta p = 0.25$ bar
Exemplary slip angle:	$\vartheta_i = 68$ °
Exemplary excavation depth	5 m
Time frame:	5/10/24/72 hr

The failure body for this exemplary slip angle and the penetration depths for the selected time steps are shown in Fig. 4.5a. The penetration depths were calculated by means of the capillary bundle concept applied in section 3.3.3. Fig. 4.5b displays the applied overpressure Δp along the depth of the excavation (black) in comparison to the mobilizable pressure thereof for the first and the last time step. The dashed lines represent the linear approach, the solid lines take into account the non-linear curvature of the pressure drop along the penetration depth. These Δp_{mob} curves deviate from Δp where the penetration depth exceeds the boundary of the failure body for the respective time step. It can be noted that the additionally mobilizable proportion from taking into account the non-linearity of the pressure drop is clearly visible, but not particularly pronounced. Consequently, the resulting characteristic support force S_k (integral of Δp_{mob} along the earth wall) is increased only slightly. In this respect, Fig. 4.5c illustrates the development of the support force mobilized within the failure body with reference to the total transferred force (based on Δp) over time. It can be clearly seen that S_k decreases over time due to the progressing penetration depth. However, nearly 80 % of the total applied overpressure can still be mobilized within the failure body with the chosen support fluid. In this respect, the difference between the linear and the non-linear calculation amount to approximately 7 %. The influence of the curvature on the decisive earth wall pressure gradient (Fig. 4.5d) is more pronounced by far. While the linear calculation reaches critical levels (25 kN/m^3), taking into account the actual curvature gives a significant safety level. Moreover, the levels for S_k and $f_{s0,wall}$ do not decrease over time as in the viscous case.

Fig. 4.6 shows the results of a small parameter variation based on the previous example (displayed in black) to visualise the impact of a certain degree of tolerance especially with respect to the estimated corrected power-law flow parameters m and κ^* ($= \alpha^* \cdot \kappa$). Again, the dashed lines represent linear calculation, the solid lines are based on curvature evaluation. The parameter variation comprises a deviation of 10 % for each parameter except for k_W (factor 2), which is mainly visualised to illustrate the effect of different ground conditions. The red reference lines represent the case of colmation as tested during V-L testing with 20 g/l of quartz fines and

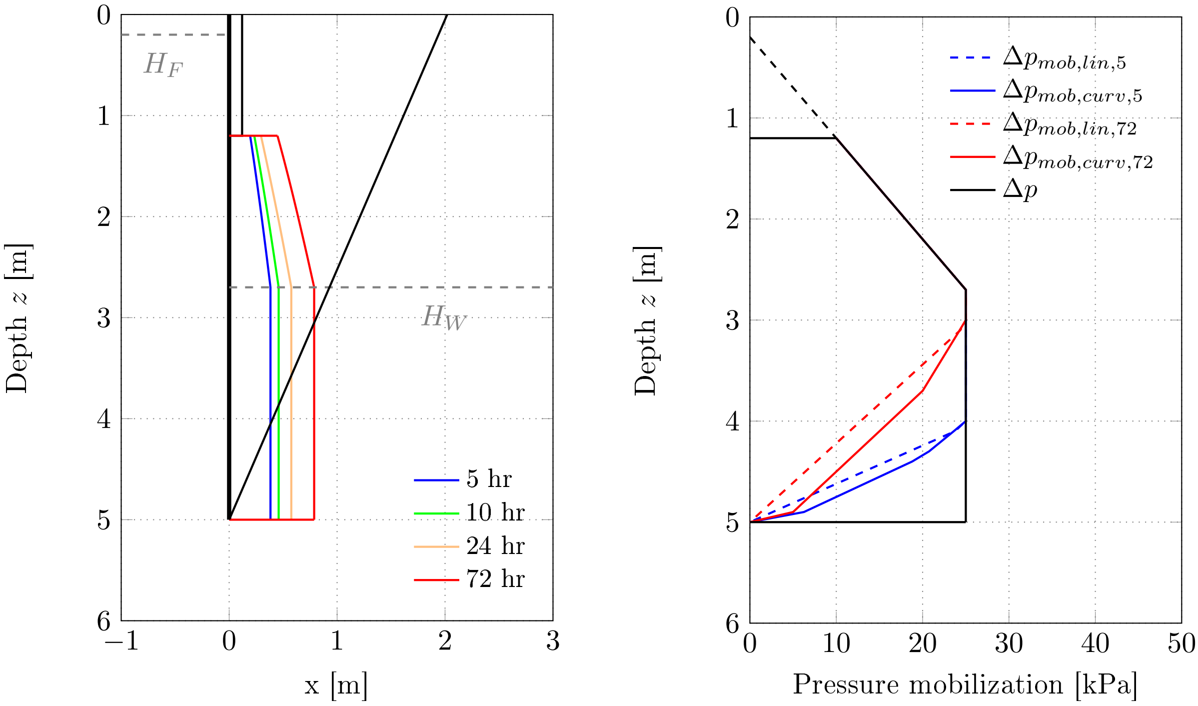

(a) Geometry

(b) Δp_{mob}

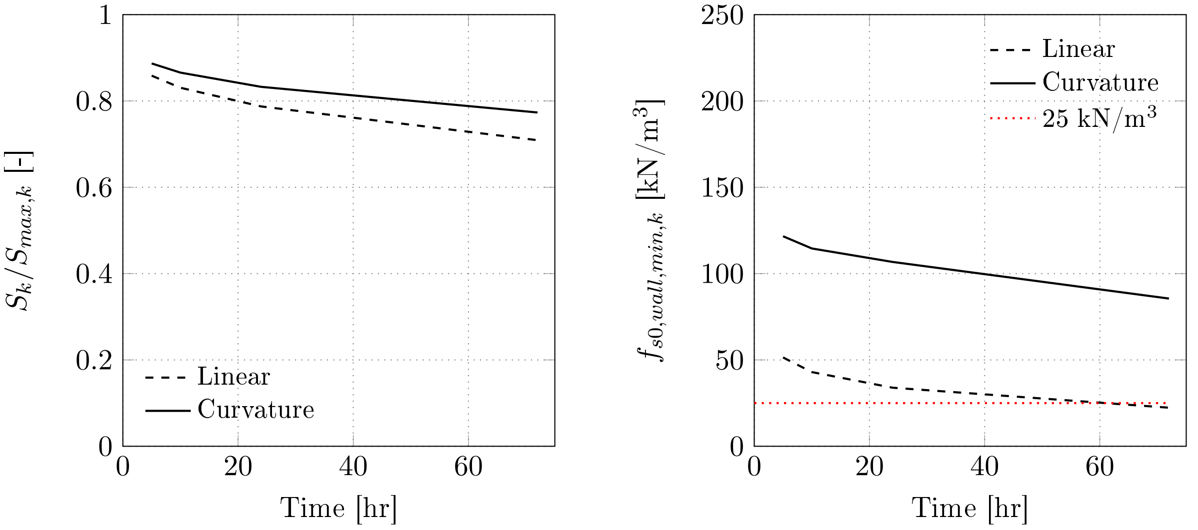

(c) Support force ($S_{max,k} = 83.75$ kN/m)

(d) Min. earth wall pressure gradient (z_{ref} =top)

Figure 4.5.: Stability concept – example

$s_{crit,2} = 7$ cm. They are calculated conservatively, i.e. based on a linear pressure drop along $s_{crit,2}$ (Eq. 4.5). Despite not taking into account the non-linearity of the pressure drop, approximately 97 % of the maximum support force can be mobilized with this approach due to the small penetration depth (Fig. 4.6a & Fig. 4.6b). The related earth wall pressure gradient is still sufficiently elevated. Moreover, the safety level does not decrease over time as with viscous penetration as the displayed level is considered the critical level independently of time.

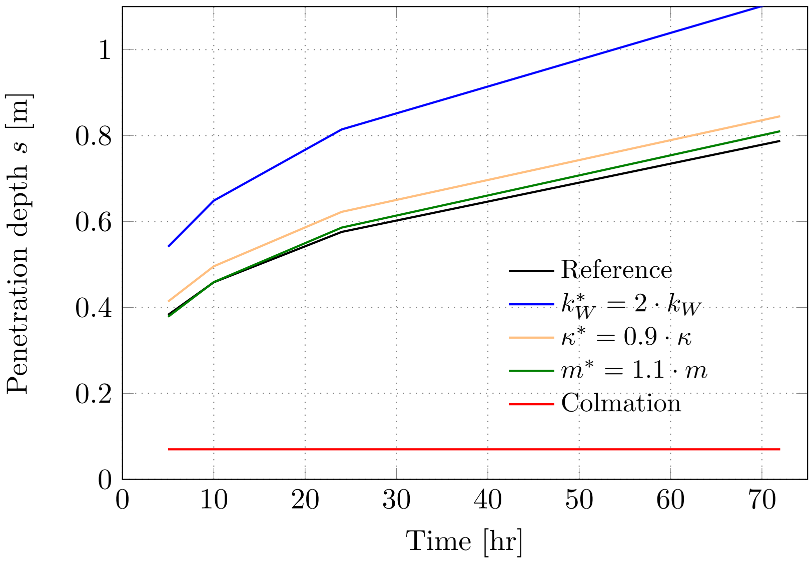

(a) Penetration depth at $z = 5$ m

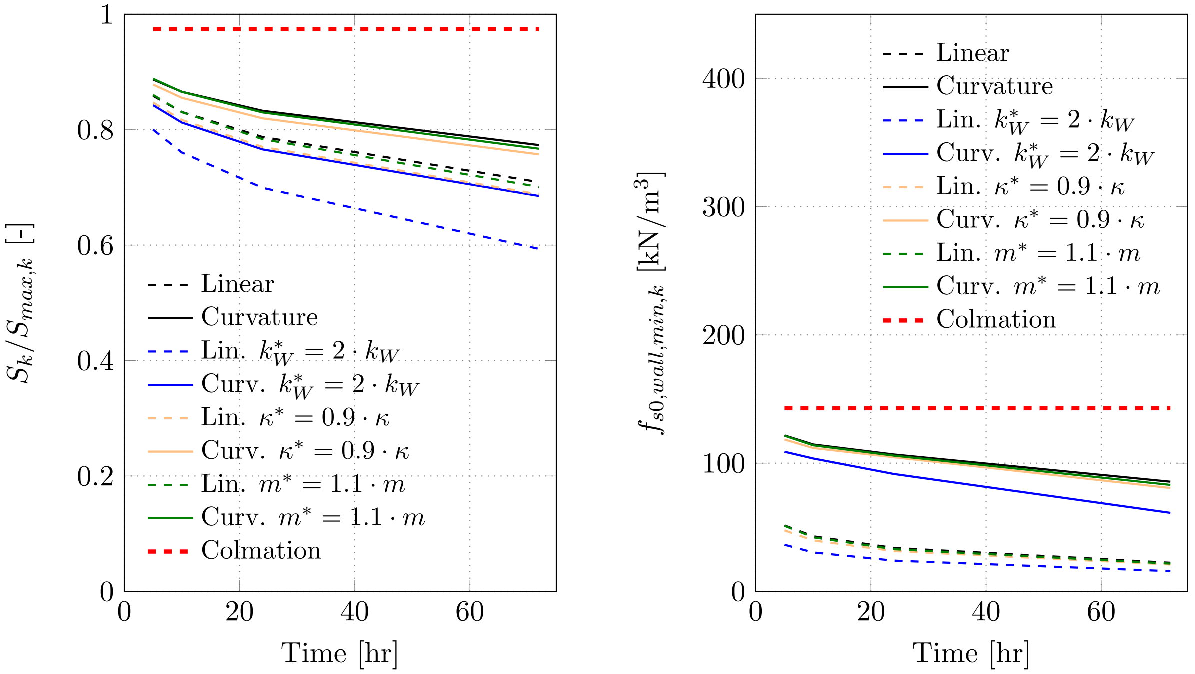

(b) Support force ($S_{max,k} = 83.75$ kN/m)

(c) Min. earth wall pressure gradient (z_{ref} =top)

Figure 4.6.: Stability concept: example – parameter variation

The parameter variation displayed here is considered adequate to capture normal deviations. The results for both the characteristic support force and the characteristic earth wall pressure gradient do not seem significantly influenced by these chosen deviations. A maximum deviation of 5-10 % can be considered to capture these variations including the variation produced by k_W.

4.3. Safety levels

The experimental investigations, which form the foundation of this concept, have covered a broad range of soil-polymer-additive combinations with a few repetition tests. The repetition tests show a relatively good repeatability, but still a certain variability. In order to account for these uncertainties and differing conditions encountered on site, a multiplicator for S_k in the sense of η_F for bentonite suspensions in the order of 0.9 is suggested based on the exemplary parameter variation in the previous section. In the case of relatively small penetration depths targeted for colmation, it may be reasonable to add a constant safety factor for the critical reference depths, on which the colmation concept is based. $\Delta s = 5$ cm is suggested based on evaluation of the experimental tests if the curvature calculation is used (instead of the conservative linear approach), because this approach is more sensitive to deviations (due to the non-linearity). However, these parameters should be considered as a first estimation. The variability of parameters at construction sites with polymer application cannot be captured by the present study.

With respect to micro stability, it needs to be noted that the related stability verification does not take into account any effects related to an increase in cohesion between the particles provided by the viscous polymer, which was observed with all tests in sand, particularly with synthetic polymers of high molecular weight. In addition to a certain clogging effect within the soil, a small external filter cake in the form of a very thin polymer film additionally provides local support for individual grains when colmation is considered. This behaviour is considerably different to what is known from bentonite suspensions as these do not possess this pronounced degree of viscosity and the possibility of entanglements as polymer chains.

It can therefore be assumed that the safety level is significantly underestimated even without considering testing variability with respect to the value for s. It may therefore be concluded that, in the case of sand material, this calculative concept for micro stability is already conservative by itself and does not require further safety correction.

This increase in apparent cohesion may also contribute to macro stability to a certain extent. However, it is unclear how far this influence reaches into the ground and how to quantify this observation along a larger depth. It should therefore not be taken into account for macro stability, but rather be considered as an additional (incalculable) safety level.

4.4. Discussion on testing methods for quality control on site

Quality control on site should be based on relatively simple testing methods which can be easily and quickly performed on site. The necessary properties for fluid support comprise two main aspects

(1) in-situ viscosity
(2) suspendability of the correct size fraction and amount of necessary granular additive (only for colmation)

A combination of Marsh funnel and filter testing is suggested to control a relatively constant level of viscosity. Marsh funnel testing does not provide any viscosity values, which can be immediately related to flow parameters. However, it seems a good estimate to control any change in fluid behaviour based on a reference value unique to each polymer type. Power-law parameters can be determined based on simple viscometer testing, as the capillary bundle analysis found that bulk viscosity values at high shear rates around 100-500 1/s are related to in-situ parameters. This can be considered a relatable basis for stability calculation beforehand, but it may not be necessary for quality control on site.

Filter testing seems a reasonable tool to verify that the flow behaviour tested by means of a Marsh funnel is not overestimated by the presence of fines creating a soil-water mix rather than a stable support fluid. If filter testing gives a significantly different time for the saturation of the filter paper, this suggests that the mix is not stable anymore as it contains a significant amount of free water. It is suggested to use a larger filter paper than recommended by the guideline DVGW W 116:2019. This test is even more important in swelling ground conditions to verify the capability of water retention of the support fluid.

If colmation of quartz mineral fines is considered within the stability concept, most likely for XAN or CMC-H, then quality control must equally comprise the testing of the grain size distribution of the contained fines and their respective concentration. This may be performed by regular sieving and areometer evaluation and at higher concentration by means of the mud balance. Sieving may be performed to determine the amount of necessary sand fractions.

Areometer tests with 1 l of support fluid for an individual test may then additionally provide the remaining density after settlement of the larger grain fractions, which is a good indicator for the amount of finer material contained in the fluid. A minimum of three mixes should be tested in order to guarantee the reliability of the results.

Moreover, in order for sieving of the additives to give reliable results, the sieve must be cleaned of polymer which may block the sieves. Also, the polymer solution needs to be diluted significantly or viscosity broken down by chemical additive addition. Exemplary testing with CMC-H 5 tw + $S_{XS/G}$ 4x10 of fines (0/0.125, 0.125/0.25, 0.4/0.5, 0.71/1 [mm]) showed that dilution to a polymer concentration of 0.5 g/l (i.e. addition of 9 l to 1 l of CMC-H 5) gave the correct results for the medium to coarse sand fractions. The same test wiht XAN 2.5 tw showed that the amount of sand fines may be reproduced until 0.125/0.25 mm with a dilution down to 0.17 g/l (i.e. the addition of 14 l of water to 1l l of XAN 2.5). Polymeric grain sizes range around sizes of sand and gravel, so they may equally be controlled by dilution sieving.

The effectiveness of bentonite flocks from addition of bentonite suspensions into polymer solutions of long-chain synthetic AN products cannot as easily be determined. The aqueous flocks can be visually evaluated, large flocks must be visible. However, this may not provide sufficient reliability, so it may be useful to perform penetration index tests, e.g. by means of a filter press filled with the relevant soil material. As aqueous grains from bentonite suspensions do not settle, downwards flow testing can be performed. In the best case, this filter press should reflect pressure levels as encountered on site. Pressure levels within the experimental investigations presented before never exceeded 1 bar (i.e. 10 m level difference). It can therefore not be concluded that higher pressure levels create the same penetration and filtration behaviour, especially for aqueous grains from bentonite suspension addition.

5. Overall concluding remarks

5.1. Summary and interpretation

Water-soluble polymers are used more and more frequently around the world as a support fluid basis for pile drilling and diaphragm walling as well as for tunnel construction as a promising alternative to clay suspensions. Reasons for the application of polymer solutions are diverse. They may be related e.g. to environmental requirements, operational or economic advantages or the assumption of improved soil-concrete skin friction mobilization and concrete quality for the final structure. However, polymer solutions are not always applied with success, as parameters and testing methods for quality control on site are still the subject of research and not state-of-the-art. Moreover, the stabilizing behaviour of polymer solutions is not yet sufficiently understood theoretically to result in a quantitative prediction and safe classification of mobilizable support during fluid-supported earth wall stabilization. Against this background, a broad theoretical and experimental investigation was performed within the scope of this work in order to improve the understanding of the polymer category with respect to its impact on penetration behaviour and support mobilization during temporary earth-wall stabilization.

Summary of the theoretical context – section 2

Following section 2.1.2, generally, three failure mechanisms need to be considered for a calculative quantification of earth wall stability, of which two are influenced by the penetration behaviour of the support fluid and therefore potentially depend upon time: micro (internal) and macro (external) stability. Additionally, swelling problems in clay may have to be taken into account, e.g. related to a potential loss of integrity of the ground or clogging effects. As elaborated in section 2.1.3, these can be enhanced with certain support fluids, but equally controlled and reduced by an adequate choice of support fluid chemistry.

With physicochemical stability guaranteed, the analytical stability concept underlying DIN 4126:2013 can be used to assess micro and macro stability. It can be employed for all considered fields of application by taking into account the respective earth wall geometry, overpressure level and spatial earth pressure approaches available for each field as listed exemplarily in section 2.1.2. However, knowledge on pressure-penetration relationships was found to be lacking for polymer support fluids, firstly as a basis for the definition of worst-case scenarios for each failure mechanism, secondly to quantify pressure mobilization within the critical failure body (Δp_{mob}) in the assessment of macro stability and locally ($f_{s0,wall}$) at the earth wall in the assessment of micro stability.

Specifications for the calculation of critical penetration depths and related pressure variables given in DIN 4126:2013 reflect empirical parameters specifically defined for 'clean' bentonite suspensions and can therefore not be applied directly to polymer solutions. They base upon the definition of a support fluid shear strength mobilizable at rest, i.e. when the suspension stagnates in the pore channels due to its yield strength, which is related to a critical grain diameter d_{10}. This parameter is considered representative to reflect the interaction between soil and bentonite suspension. Both variables cannot be transferred to polymer solutions as their penetration behaviour is rather defined by viscosity values significantly higher than for bentonite, but with negligible shear strength at low shear rates (or at rest) (sections 2.2.2 & 3.2.2).

The approach by Steinhoff (1993) therefore suggested the prediction of time-dependent penetration depths and related pressure mobilization based on polymer bulk rheology in combination with basic capillary bundle models and the assumption of a linear pressure drop along the predicted penetration depth. This approach was generally found to be relatively complex and conservative compared to experience from construction sites. Furthermore, experience from construction sites suggests that the uptake of fines by the support fluid may in certain cases be decisive in realizing effective support mobilization.

It could be concluded that categorization into viscous flow behaviour vs. colmation provides a reasonable basis for the analysis of pressure-penetration relationships, related interaction mechanisms and possible subsequent classification by means of laboratory experiments.

As a basis for the choice of suitable polymer products for variation, section 2.2 showed that the polymer category comprises a broad range of components, which are not necessarily commonly associated with this term and which can provide a large variability both of natural or synthetic origin. Polymeric base products useful for support fluids therefore need to be grouped according to their supportive use as viscosifiers, pore blockers and clay swelling inhibitors with different requirements for each category (section 2.2.1). While the bulk properties of groups of polymeric materials, especially of viscosifiers, are relatively well understood, it is less broadly investigated how they behave in the narrow pores of a soil matrix, and especially whether bulk parameters can be used to describe processes at pore scale, which are essential for the classification of penetration behaviour in the targeted fields of application, e.g. in the context of capillary bundle approximations (section 2.3.1, 2.3.2). With respect to colmation effects, it was further found that criteria are needed to guarantee this effect both in terms of effective filtration, i.e. here reduction in penetration rate nearing stagnation, and membrane behaviour, i.e. full pressure transfer, if they are to be considered for stability. A geometric classification was therefore suggested comparable to Terzaghi's filter criterion referring to mechanical filter stability for the choice of adequate granular material sizes to be added in coarse-grained soils (section 2.3.3).

Summary of laboratory results, classification and stability – sections 3-4.3

Based on these conclusions, a laboratory concept was developed to experimentally assess these open questions based on four different soil penetration testing devices and prior material classification with focus on bulk rheology and fluid stability of the viscous base products and granular additive characterization for pore blocking. The experimental investigations indeed revealed certain characteristic relationships between viscous base solutions, granular additives and soil properties. Based on the experimental investigation on viscous flow in non-cohesive soil (section 3.3.2-3.3.3 & 3.4.2), it is concluded that the in-situ viscosity is governed by interactions between the specific structure of each polymer type and the porous soil matrix. These mechanisms can be associated with:

- effective grain diameters d_{30} (CMC-H/XAN) and d_{50} (AN) of the subsoil,
- characteristic moderately nonlinear pressure drop curvatures, which follow the penetration depth with a small offset, for CMC-H and XAN, they seemingly take into account a certain degree of micro-filtration at the earth wall,
- characteristic capillary bundle correction parameters (α^*, $\gamma_{crit\dot{,}min\eta}$ and $\gamma_{crit\dot{,}max\eta}$) based on bulk rheological characterisation at high shear rates (around 100-500 1/s), which mainly result in a vertical shift (dilution) and more pronounced Newtonian plateaus than are found

with bulk rheology and are clearly influenced by polymer type and concentration.

Subsequently, the colmation behaviour was investigated taking into account quartz mineral grains, aqueous bentonite flocks and aqueous polymeric grains as granular material. It could be shown that the polymers of natural origin CMC-H and XAN function considerably well with quartz mineral grains in creating stagnation with complete pressure drop at the earth wall in soils ranging from medium sand to gravel, if the amount and size distribution of the granular additives were adequately fitted (sections 3.3.4 & 3.4.4). The formed filter cakes were found to be stable at all tested pressure levels (0.15-0.7 bar). Successful small-scale tests were implemented within a suitability matrix, which showed that applicable ratios of $F = d_{soil,ref}/d_{max,add}$ with reference to Terzaghi's mechanical filter criterion can in some cases reach factors $F > 10$ (Tab. 3.12). Filter cake evaluation (section 3.5) indicates that this colmation process in sand creates a rather sticky, dense and cohesive inner filter cake that is not easily removed by mechanical agitation.

With the large-chain AN representative AN-H, bentonite flocks created by shortly dispersing (or just pouring into one another) bentonite suspension at low concentration (10 g/l) into the AN polymer solution .... to be the optimal colmation material. The formation of these flocks here highly depends upon the viscous base polymer applied, so it can only safely be assured for AN-H and only to a smaller degree for AN-M (sections 3.2.4 & 3.3.5). These flocks create a gum-like, but thin filter cake similar to that for polymer-modified bentonite, which is not entirely removed by rising fresh concrete (section 3.6). The related effect on the shear resistance of the created contact zone requires further investigation regarding wall friction. Aqueous polymeric grains (hydrogels) as a possible choice for all types of viscous base polymers for coarser subsoils to be supported were found to work moderately well and also raised questions concerning the resulting quality of the contact zone (sections 3.3.6, 3.5 and 3.6).

With respect to classification of colmation mechanisms for stability regardless of the type of granular additive, the laboratory investigations showed that the process can be described by two characteristic penetration depths. At these points, the penetration velocity deviates clearly, which coincides with changes in pressure transfer from viscous penetration ($s_{crit,1}$) to membrane formation ($s_{crit,2}$). With a significant decrease in penetration velocity of several decimal powers at $s_{crit,2}$, it can be derived that the membrane is fully built. Supported by comparison between V-L and V-S testing, it could be concluded that:

- $s_{crit,1}$ and $s_{crit,2}$ can be obtained from simple (small-scale) soil penetration testing (preferably upwards flow) and that
- these parameters reflect the critical times for stability and can therefore form the basis of stability calculations formulated independently of time.

A stability concept differentiating between the two categories:

(1) viscous flow with 'clean' pure polymer solutions (time-dependent)
(2) colmation (with full membrane formation) by means of granular additives (independently of time)

was derived on this basis (section 4.1). The first category still essentially follows the approach developed by Steinhoff (1993), i.e. it still formulates stability verification in terms of critical stand-up times, but additionally enables the consideration of the non-linearity of the pressure drop curvature for the three types of polymers investigated. This significantly increases the mobilizable pressure gradient at the earth wall and therefore micro stability. With respect to the implementation of capillary bundle models for the prediction of penetration depths in this regard, it is considered important to use adequately corrected capillary bundle parameters, e.g. based on Tab. 3.6. Otherwise, especially with respect to dilution effects, these approaches may underestimate penetration depths, which is critical for stability.

The stability approach suggested for colmation is considerably simpler as it does not require the variation of time steps. It is based on the evaluation of small-scale penetration tests (or comparable experience values) with reference soil material chosen related to the effective diameters d_{30} (CMC-H/XAN) or d_{50} (AN) of the targeted ground conditions. Moreover, suitability matrices were provided with recommendations on granular additive types for a given polymer type and the related effective grain diameter of the subsoil (section 4.1.2).

Summary of testing methods for quality control – section 4.4

Taking into consideration the critical stability parameters described above, typical and additional testing methods for construction sites were evaluated with respect to their suitability in assuring the functionality of polymer support fluids to provide sufficient stabilizing qualities (section 4.4). The following devices were found suitable in this regard:

- viscosity
    - Marsh funnel
    - filter paper test (ring apparatus, preferably with larger filter paper)
- colmation
    - appropriate sieves
    - areometer (for lower concentrations of fines)
    - mud balance (for higher concentrations of fines)
    - e.g. Bauer filter press filled with soil and fluid (for bentonite flocks)

The Marsh funnel test is considered sufficient to monitor changes in the fluid behaviour, even if rheological parameters cannot be directly derived. The filter paper test is considered suitable to verify the chemical stability of the fluid mix linked to viscosity, which would be considerably different for a soil-water-slurry than for a functioning fluid. It therefore seems suitable as a complement to Marsh testing, which may not be able to differentiate in this regard.

The testing range suggested for colmation effects envisages at ensuring the correct grain size distribution and amount of each necessary fraction. For sieving to be applicable, the polymer solutions need to be sufficiently diluted (or chemically broken) so that the sieving results do not overestimate the available sizes of the grain fractions.

Conclusions and perspective

Polymer support fluids can still be considered a relatively new and growing field in geotechnical engineering applications, especially in Germany. In this context, the presented investigations were targeted at drawing a conclusive picture of the diversity of applicable polymers and their interaction mechanisms with the ground. It was shown that the polymer category can provide a broad range of useful properties and products, which need to be differentiated in order to clarify the respective base mechanisms. Examples for viscosifiers in this respect are the formation of flocks with addition of bentonite suspensions in certain boundary conditions only or their differing reaction with respect to the dispersibility of fines. Yet, only three polymer types and one mixed product were tested in detail. They represent the most commonly applied product range. The obtained results can therefore be considered relatively well applicable to practical application in this respect. The tested variability in polymer types allows a certain degree of transferability to other types of polymers as well. The large number of tests and the relatively good coherence despite differing testing conditions are considered a sufficient basis to conclude that the main results are robust and relatable for both practical and calculative stability-related considerations.

As far as the implementation within standards is concerned, it is still suggested that these experimental results are evaluated against a range of experiences from construction sites based on the refined focus on necessary parameters gained with this study. This would provide a more solid basis for the quantification of parameter variability, which can be influenced e.g. by operational handling at construction sites.

The presented investigation tried to critically evaluate the obtained results e.g. with respect to different excavation techniques where possible. However, a detailed discussion on every attended field is considered to be beyond the scope of this work, which focusses rather on the basal understanding of underlying mechanisms as a first step.

However, it can be generally concluded that polymer support fluids are a promising alternative to bentonite suspensions. Reluctance with respect to the application of these types of support fluids in Germany is thought to mainly be related to a lacking understanding of the working mechanisms, especially with respect to the predictability of penetration depths and related polymer concentrations needed. It is hoped that the present work can provide a basis for reevaluation in this regard in combination with the procedure initiated and framed by Lesemann (2010) in the context of environmental impact analysis.

5.2. Related topics

Loaded bentonite suspensions

Owing to their yield strength, bentonite suspensions are usually loaded with fines during excavation, which requires the application of complex treatment plants to subsequently remove these fines from the fluid, e.g. for regeneration. They may even be considered more capable of carrying and subsequently filtering fines at the earth wall than polymer solutions because of this property. Arwanitaki (2009) found a sufficient amount of sand in filter cakes taken from construction sites, which were found to significantly influence the shear resistance of the formed filter cake. Thienert (2011) found a marked reduction of maximum penetration depths of bentonite suspensions resulting from the presence of sand particles.

However, the analytical design approach in Germany for bentonite suspensions DIN 4126:2013 bases on 'clean' suspensions only. Favourable impacts from suspended fines are not taken into account. It can be suspected that this impact can be considered based on the same concept as loaded polymer solutions. First laboratory penetration tests with fines addition have shown that it is indeed possible to predict stagnation effects based on geometric criteria for the choice of suitable granular additives. In this context, it can be assumed that the lowest fraction necessary for polymer solutions (quartz powder) is not needed, as the bentonite grains themselves provide a minimum filterable size. Taking into account these effects could prove cost-effective and favourable with respect to stability calculations.

Polymer-modified clay suspensions

Polymer modification of bentonite is a common procedure to improve the properties of activated bentonite, e.g. by means of low-molecular weight CMC (CMC-L) or low-molecular weight synthetic additives (section 2.2.5). The interaction mechanism explaining the positive effect of certain polymers on bentonite suspensions is referred to as 'steric stabilization'. It is also accompanied by an increase in salt stability, as Jasmund and Lagaly (1993) stated.

Apart from low-molecular weight polymeric additives, regular CMC-H has also proven to be suitable to enhance bentonite suspension properties (own laboratory tests). Medium molecular weight synthetic polymers AN-M are also applied[1]. In this context, suitable concentrations range around 0.4-0.5 g/l of polymer with 10-30 g/l of bentonite suspension. The resulting product then behaves similarly to a bentonite suspension of higher concentration, i.e. the polymer addition reduces the amount of bentonite needed to reach a certain shear strength level.

It remains to be answered what concentration combinations of polymer vs. bentonite are needed for the mix to either be governed by polymer solution or by bentonite suspension behaviour, or possibly even destabilize at a certain concentration ratio as described by Jasmund and Lagaly (1993).

Swelling-related stability

The swelling inhibition effect of viscous polymer solutions is often explained by their low water activity values, i.e. a good water retention capacity and general solution stability. This parameter is linked to the measurements performed with filter testing. It would be helpful to be able to quantify this water activity level achievable with these solutions and to relate it to respective filter test propagation times. This way, this test could be used more precisely for problematic

---

[1] Ref.: Laurent Giuranna (SNF), personal communication, July 9, 2020

soils, also as a form of an on-site quality control technique for the support fluid, if the respective water activity of the soil can be equally determined.

Final stability – skin friction

The mobilizable skin friction is an important factor for stability calculations of the final concrete structure. First laboratory tests from literature suggest that the mobilizable skin friction with clean polymer solutions is superior to bentonite suspensions as they do not form filter cakes (Lam, Jefferis, and Martin, 2014b). It can be expected that the skin friction is comparably lower when bentonite flocks or aqueous grains are used for colmation. On the other hand, the geometric roughness of the excavated earth wall may govern the mobilizable skin friction between concrete surface and soil (Arwanitaki, 2009).

However, even though the support with CMC-H/XAN and quartz mineral grains seemingly creates negligibly thin filter cakes, it cannot be assured that skin friction can be fully mobilized due to the presence of polymers. No shear tests have been performed with loaded polymer solutions yet.

A suitable testing device for shear testing after previous horizontal penetration was developed by Arwanitaki (2009) for bentonite suspensions. Filter cake shear tests by means of this testing device will be performed within the scope of a subsequent project in order to systematically analyse the effect of load on the skin friction of both bentonite suspensions and polymer solutions to allow for a direct comparison.

Bibliography

Alagha, L., S. Wang, L. Yan, Z. Xu, and J. Masliyah (2013). "Probing adsorption of polyacrylamide-based polymers on anisotropic basal planes of kaolinite using quartz crystal microbalance". In: *Langmuir* 29.12, pp. 3989–3998. DOI: `10.1021/la304966v`.

Alexanderson, M. (2001). "Construction of a cable tunnel ID 2-6 Vibhavadi". In: *Proceedings of the 5th international symposium on microtunnelling.* Bauma, Munich, pp. 139–147.

Anagnostou, G. (2007). "Zur Problematik des Tunnelbaus in quellfähigem Gebirge". In: vol. 154. German. Schweizerische Gesellschaft für Bodenmechanik und Fundationstechnik, pp. 1–10.

Anagnostou, G. and K. Kovarí (1994). "The face stability of slurry-shield-driven tunnels". In: *Tunnelling and underground space technology* 9.2, pp. 165–174. DOI: `10.1016/0886-7798(94)90028-0`.

Anderson, R. L., I. Ratcliffe, H. C. Greenwell, P. A. Williams, S. Cliffe, and P. V. Coveney (2010). "Clay swelling – a challenge in the oilfield". In: *Earth-Science Reviews* 98.3-4, pp. 201–216. DOI: `10.1016/j.earscirev.2009.11.003`.

API RP 13D:2017. *Rheology and hydraulics of oil-well drilling fluids.* Standard.

Araújo, P. H., C. Sayer, R. Giudici, and J. G. Poço (2002). "Techniques for reducing residual monomer content in polymers: A review". In: *Polymer Engineering & Science* 42.7, pp. 1442–1468. DOI: `10.1002/pen.11043`.

Arwanitaki, A. (2009). *Über das Kontaktverhalten einer Zweiphasenschlitzwand und nichtbindigen Böden.* Vol. 41. Schriftenreihe des Lehrstuhls für Grundbau, Boden und Felsmechanik. phD thesis, German. Ruhr-Universität Bochum, Germany.

Baille, W. (2014). *Hydro-mechanical behaviour of clay – significance of mineralogy.* Vol. 53. Schriftenreihe des Lehrstuhls für Grundbau, Boden und Felsmechanik. phD thesis, German. Ruhr-Universität Bochum, Germany. ISBN: 2190-3255.

Balhoff, M. T. and K. E. Thompson (2006). "A macroscopic model for shear-thinning flow in packed beds based on network modeling". In: *Chemical Engineering Science* 61.2, pp. 698–719. DOI: `10.1016/j.ces.2005.04.030`.

Barnes, H. A., J. F. Hutton, and K. Walters (1989). *An introduction to rheology.* 3. Amsterdam New York: Elsevier. ISBN: 9780444871404.

Barvenik, F. W. (1994). "Polyacrylamide characteristics related to soil applications". In: *Soil Science* 158.4, pp. 235–243. DOI: `10.1097/00010694-199410000-00002`.

BeMiller, J. N. (2019). *Carbohydrate chemistry for food scientists.* London: WP AACC International Press. ISBN: 9780128134382.

Berkovitz, B. C. and C. S. Long (1995). "Use of polymer slurries for drilled shaft construction". In: *Proceedings of the 31st Symposium on Engineering Geology and Geotechnical Engineering*, pp. 17–23.

Bird, R. B., W. E. Stewart, and E. N. Lightfoot (2007). *Transport phenomena.* Rev. 2. ed. New York: Wiley. ISBN: 9780470115398.

Blake, F. C. (1922). "The resistance of packing to fluid flow". In: *Transactions of the American Institute Chemical Engineers* 14, pp. 415–421.

Bol, G. M., S.-W. Wong, C. J. Davidson, and D. C. Woodland (1994). "Borehole stability in shales". In: *SPE Drilling & Completion* 9.02, pp. 87–94. DOI: `10.2118/24975-pa`.

Borghi, F. X. (2006). “Soil conditioning for pipe jacking and tunnelling”. PhD thesis. University of Cambridge. DOI: `10.17863/CAM.19109`.

Brax, M., C. Buchmann, and G. E. Schaumann (2017). “Biohydrogel induced soil-water interactions: how to untangle the gel effect? A review”. In: *Journal of Plant Nutrition and Soil Science* 180.2, pp. 121–141. DOI: `10.1002/jpln.201600453`.

Brazel, C. S. and S. L. Rosen (2012). *Fundamental principles of polymeric materials.* John Wiley & Sons.

Broere, W. (2015). “On the face support of microtunnelling TBMs”. In: *Tunnelling and Underground Space Technology* 46, pp. 12–17. DOI: `10.1016/j.tust.2014.09.015`.

Buja, H.-O. (2009). *Handbuch der Baugrunderkennung.* German. Vieweg-Teubner. DOI: `10.1007/978-3-8348-9994-1`.

Burbaum, U., T. Böhme, and I. Sass (2011). “Hydroschildvortrieb im Lauenburger Ton: Untersuchungen zur Adhäsivität des Baugrunds”. In: *geotechnik* 34.2. German, pp. 108–114. DOI: `10.1002/gete.201000011`.

Butscher, C., T. Mutschler, and P. Blum (2015). “Swelling of clay-sulfate rocks: A review of processes and controls”. In: *Rock Mechanics and Rock Engineering* 49.4, pp. 1533–1549. DOI: `10.1007/s00603-015-0827-6`.

Caenn, Ryen, H. C. H. Darley, and George R. Gray (2017). *Composition and properties of drilling and completion fluids.* 7th ed. Elsevier. DOI: `10.1016/c2015-0-04159-4`.

Cannella, W. J., C. Huh, and R. S. Seright (1988). “Prediction of xanthan rheology in porous media”. In: *SPE Annual Technical Conference and Exhibition.* Society of Petroleum Engineers. DOI: `10.2118/18089-ms`.

Carman, P. C. (1937). “Fluid flow through granular beds”. In: *Transactions of the Instituion of Chemical Engineers* 15, pp. 150–166.

Carraher Jr., Charles E. (2018). *Carraher’s polymer chemistry.* 10th ed. Boca Raton, FL: CRC Press, Taylor & Francis Group. ISBN: 9781498737388.

Carreau, R. J. (1968). *Rheological equations of state from molecular network theories: PhD thesis.* Madison: University of Wisconsin.

Caulfield, M. J., G. G. Qiao, and D. H. Solomon (2002). “Some aspects of the properties and degradation of polyacrylamides”. In: *Chemical Reviews* 102.9, pp. 3067–3084. DOI: `10.1021/cr010439p`.

Chauveteau, G (1986). “Fundamental criteria in polymer flow through porous media and their importance in the performance differences of mobility-control buffers”. In: *Water Soluble Polymers* 213, pp. 227–268.

Chauveteau, G. and N. Kohler (1984). “Influence of microgels in polysaccharide solutions on their flow behavior through porous media”. In: *Society of Petroleum Engineers Journal* 24.03, pp. 361–368. DOI: `10.2118/9295-pa`.

Choy, Tuck (2016). *Effective medium theory : principles and applications.* 2nd ed. Oxford: Oxford University Press. ISBN: 9780191015182.

Christopher, R. H. and Stanley Middleman (1965). “Power-law flow through a packed tube”. In: *Industrial & Engineering Chemistry Fundamentals* 4.4, pp. 422–426. ISSN: 0196-4313. DOI: `10.1021/i160016a011`.

Coulomb, C. A. (1773). *Essai sur une application des règles des maximis et minimis a quelques problèmes de statique relatifs à l’architecture.* Vol. 7. Mémoires de Mathématique et de Physique par divers savans. French, printed 1776, held 1773. Paris: Académie Royale des Sciences, pp. 343–382.

Dai, C. and F. Zhao (2018). "Drilling Fluid Chemistry". In: *Oilfield Chemistry.* Singapore: Springer, pp. 21–84. DOI: `10.1007/978-981-13-2950-0_2`.

Darcy, H. (1856). *Les fontaines publiques de la ville de Dijon: Exposition et application des principes à suivre et des formules à employer dans les questions de distribution d'eau.* French. Paris: Victor Dalmont.

DAUB-SSWG (2005). "Recommendations for static analysis of shield tunnelling machines". In: *Tunnel* 7. German/English, pp. 44–59.

Derjaguin, B. V. and Landau, L. D. (1941). "The theory of stability of strongly charged lyophobic sols and the adhesion of strongly charged particles in solutions of electrolyte". In: *Acta Physicochimica U.S.S.R.* 14, pp. 633–662.

DIBt:2009. *Grundsätze zur Bewertung der Auswirkungen von Bauprodukten auf Boden und Grundwasser – Teil 1.* Standard. German. Berlin: Deutsches Institut für Bautechnik. DOI: `10.1002/dibt.200930029`.

DIN 38414-S4:1984. *German standard methods for the examination of water, waste water and sludge; sludge and sediments (group S); determination of leachability by water (S 4).* Standard. Deutsches Institut für Normung, Beuth Verlag.

DIN 4126:1986. *Cast-in-situ concrete diaphragm walls; design and construction.* Standard. Deutsches Institut für Normung, Beuth Verlag.

DIN 4126:2013. *Stability analysis of diaphragm walls; German version.* Standard. Deutsches Institut für Normung, Beuth Verlag.

DIN 4127:2014. *Earthworks and foundation engineering - Test methods for supporting fluids used in the construction of diaphragm walls and their constituent products; German version.* Standard. Deutsches Institut für Normung, Beuth Verlag.

DIN 51562-1:1999. *Messung der kinematischen Viskososität mit dem Ubbelohde-Viskosimeter – Teil 1: Bauform und Durchführung der Messung.* Standard. German. Deutsches Institut für Normung, Beuth Verlag.

DVGW W 116:2019 (2019). *Application of drilling fluid additives for the construction of water and monitoring wells with flush drilling methods.* Standard. German. Bonn, Germany: Deutscher Verein des Gas- und Wasserfaches e. V.

DWA-A 161:2014 (2014). *Arbeitsblatt DWA-A 161 – Statische Berechnung von Vortriebsrohren.* Standard. German. Hennef, Germany: Deutsche Vereinigung für Wasserwirtschaft, Abwasser und Abfall e.V.

EA-P:2013 (2013). *Recommendations on Piling (EA-Pfähle).* Standard. Translation of 2nd edition EA-Pfähle 2012, German version. DOI: `10.1002/9783433604113`.

EAB:2013 (2013). *Recommendations on Excavations EAB.* Standard. Translation of the 5th German Edition. DOI: `10.1002/9783433603970`.

Ejezie, J. O., S. A. Jefferis, C. Lam, M. Sedighi, and S. M. Ahmad (2020). "Permeation behaviour of PHPA polymer fluids in sand". In: *Géotechnique*, pp. 1–10. DOI: `10.1680/jgeot.18.p.353`.

EN 12457-4:2003. *Characterization of waste - Leaching; Compliance test for leaching of granular waste materials and sludges - Part 4: One stage batch test at a liquid to solid ratio of 10 l/kg for materials with particle size below 10 mm (without or with limited size reduction); German version EN 12457-4:2002.* Standard. Deutsches Institut für Normung, Beuth Verlag.

EN 1536:2015. *Execution of special geotechnical work - Bored piles; German version EN 1536:2010 + A1:2015.* Standard. Deutsches Institut für Normung, Beuth Verlag.

EN 1538:2015. *Execution of special geotechnical work - Diaphragm walls; German version EN 1538:2010 + A1:2015.* Standard. Deutsches Institut für Normung, Beuth Verlag.

EN 1997-1:2014 (2014). *Eurocode 7: Geotechnical design - Part 1: General rules; German version EN 1997-1:2004 + AC:2009 + A1:2013.* Standard. Deutsches Institut für Normung, Beuth Verlag.

EN 206:2017 (2017). *Concrete - Specification, performance, production and conformity; German version EN 206:2013+A1:2016.* Standard. Deutsches Institut für Normung, Beuth Verlag.

EN ISO 17892-11:2019. *Geotechnical investigation and testing – Laboratory testing of soil – Part 11: Permeability tests; German version EN ISO 17892-11:2019.* Standard. Deutsches Institut für Normung, Beuth Verlag.

EN ISO 17892-4:2017. *Geotechnical investigation and testing – Laboratory testing of soil – Part 4: Determination of particle size distribution; German version EN ISO 17892-4:2016.* Standard. Deutsches Institut für Normung, Beuth Verlag.

Fannin, J. (2008). "Karl Terzaghi: from theory to practice in geotechnical filter design". In: *Journal of Geotechnical and Geoenvironmental Engineering* 134.3, pp. 267–276. DOI: `10.1061/(asce)1090-0241(2008)134:3(267)`.

Farrokhrouz, M. and M. R. Asef (2013). *Shale engineering - mechanics and mechanisms.* CRC Press. ISBN: 978-0-203-84791-6.

Fawell, P. (2017). "Solid-liquid separation of clay tailings". In: *Clays in the Minerals Processing Value Chain.* Ed. by M. Grafe, C. Klauber, A. J. McFarlane, and D. J. Robinson. Cambridge University Press, pp. 327–380. DOI: `10.1017/9781316661888.010`.

Feng, Y., R. Tabary, M. Renard, C. Le Bon, A. Omari, and G. Chauveteau (2003). "Characteristics of microgels designed for water shutoff and profile control". In: *International Symposium on Oilfield Chemistry.* Society of Petroleum Engineers. DOI: `10.2118/80203-ms`.

Ferapontov, N. B., M. G. Tokmachev, and A. N. Gagarin (2009). "The properties of water in solutions of hydrophilic polymers". In: *Russian Journal of Physical Chemistry A* 83.8, pp. 1321–1325. DOI: `10.1134/s0036024409080135`.

FHWA-NHI-10-016:2010 (2010). *Drilled shafts: Construction procedures and LRFD design methods.* Tech. rep. United States. Federal Highway Administration.

Floset CE 130 XF 35. *Safety Data Sheet (exemplarily for the AN polymer viscosifier range).* SNF, France, 29 June 2016.

Frey, S. and P. Schmaeh (2019). "The role of mechanized shaft sinking in international tunnelling projects". In: *Tunnels and Underground Cities: Engineering and Innovation meet Archaeology, Architecture and Art.* CRC Press, pp. 2119–2128.

Ghannam, M. T., M. Y. Selim, A. Y. Zekri, and N. Esmail (2019). "Flow characteristics of xanthan solutions and their crude oil emulsions in terms of thixotropic behavior". In: *Petroleum Science and Technology* 37.11, pp. 1279–1288. DOI: `10.1080/10916466.2019.1566363`.

Gholami, R., H. Elochukwu, N. Fakhari, and M. Sarmadivaleh (2018). "A review on borehole instability in active shale formations: Interactions, mechanisms and inhibitors". In: *Earth-Science Reviews* 177, pp. 2–13. DOI: `10.1016/j.earscirev.2017.11.002`.

Goodhue, K. and M. Holmes (1997). *Polymeric earth support fluid compositions and method for their use.* U.S. Patent 5,663,123.

Gulrez, S. K. H., S. Al-Assaf, and G. O. Phillips (2011). "Hydrogels: methods of preparation, characterisation and applications". In: *Progress in Molecular and Environmental Bioengineering - From Analysis and Modeling to Technology Applications.* InTech. DOI: `10.5772/24553`.

Haugwitz, H.-G. and M. Pulsfort (2018). "Pfahlwände, Schlitzwände, Dichtwände". In: ed. by Karl Joseph Witt. 8. German. Wiley Online Library, pp. 823–907.

Hawkes, C. D., P. J. McLellan, W. C. Maurer, and C. G. Ruan (2000). “Wellbore instability in shales: a review of fundamental principles and GRI-funded research”. In: *GRI Final Report* 99.0025.3, A2–A4.

Heinz, A. (2006). “Modifizierte Bentonitsuspensionen für geotechnische Bauverfahren in Böden hoher Durchlässigkeit”. de. German. PhD thesis. DOI: `10.3929/ETHZ-A-005274662`.

Hirasaki, G. J. and G. A. Pope (1974). “Analysis of factors influencing mobility and adsorption in the flow of polymer solution through porous media”. In: *Society of Petroleum Engineers Journal* 14.04, pp. 337–346. ISSN: 0197-7520. DOI: `10.2118/4026-PA`.

Horn, M. (1961). “Horizontaler Erddruck auf senkrechte Abschlussflächen von Tunnelröhren”. In: *Referate zum Thema 'Unterirdische Bauwerke'*, pp. 7–16.

Huder, J. and G. Amberg (1970). “Quellung in Mergel, Opalinuston und Anhydrit”. In: *Schweizerische Bauzeitung* 88.43, pp. 975–980.

ICE-SPEARWall:2016. *ICE specification for piling and embedded retaining walls.* Standard. ICE Publishing, London.

Jagur-Grodzinski, J. (2009). “Polymeric gels and hydrogels for biomedical and pharmaceutical applications”. In: *Polymers for Advanced Technologies*, pp. 27–47. DOI: `10.1002/pat.1504`.

Janssen, H. A. (1895). “Versuche über Getreidedruck in Silozellen”. In: *Zeitschrift des Vereins Deutscher Ingenieure* 39.35, pp. 1045–1049.

Jasmund, K. and G. Lagaly (1993). *Tonminerale und Tone: Struktur, Eigenschaften, Anwendungen und Einsatz in Industrie und Umwelt; German.* German. Steinkopff Verlag, Darmstadt.

Jefferis, S. A. and C. Lam (2013). “Polymer support fluids: use and misuse of innovative fluids in geotechnical works”. In: *Proceedings of the 18th International Conference on Soil Mechanics and Geotechnical Engineering.* Presses des Ponts, Paris, France, pp. 2–6.

Jouenne, S., A. Klimenko, and D. Levitt (2016). “Tradeoffs between emulsion and powder polymers for EOR”. In: *SPE Improved Oil Recovery Conference.* Society of Petroleum Engineers, pp. 1–14. DOI: `10.2118/179631-ms`.

Karimi, M. and M. R. Naimi-Jamal (2019). “Carboxymethyl cellulose as a green and biodegradable catalyst for the solvent-free synthesis of benzimidazoloquinazolinone derivatives”. In: *Journal of Saudi Chemical Society* 23.2, pp. 182–187. DOI: `10.1016/j.jscs.2018.06.007`.

Kirsch, A. (2010). “Experimental investigation of the face stability of shallow tunnels in sand”. In: *Acta Geotechnica* 5.1, pp. 43–62. DOI: `10.1007/s11440-010-0110-7`.

Klein, L. and C. Moormann (2015). “Design of deep excavations under consideration of spatial earth pressure”. In: *Proceedings of the XVI ECSMGE - Geotechnical Engineering for Infrastructure and Development.* ICE Publishing, pp. 613–618.

Klemm, D., B. Heublein, H.-P. Fink, and A. Bohn (2005). “Cellulose: fascinating biopolymer and sustainable raw material”. In: *Angewandte Chemie International Edition* 44.22. German, pp. 3358–3393. DOI: `10.1002/anie.200460587`.

Kolymbas, D. (2008). *Tunnelling and tunnel mechanics: a rational approach to tunneling.* 2nd ed. Berlin, Heidelberg, Germany: Springer. ISBN: 978-3-540-28500-7. DOI: `10.1007/978-3-540-28500-7`.

Kozeny, J. (1927). “Über kapillare Leitung des Wasser im Boden: Aufstieg, Versickerung und Anwendung auf die Bewässerung”. In: *Sitzungsberichte der Wiener Akademie der Wissenschaften* 136. German, pp. 271–306.

Lam, C. and S. Jefferis (2015a). “An investigation of possible yield stress and thixotropy in polymer excavation-support fluids”. In: *Proceedings of the XVI ECSMGE – Geotechnical Engineering for Infrastructure and Development.* ICE Publishing, pp. 3183–3188. DOI: `10.1680/ecsmge.60678`.

Lam, C. and S. Jefferis (2018). *Polymer support fluids in civil engineering.* London: ICE Publishing.

Lam, C. and S. A. Jefferis (2014). "The use of polymer solutions for deep excavations: Lessons from Far Eastern experience". In: *HKIE Transactions* 21.4, pp. 262–271.

– (2015b). "Performance of bored piles constructed using polymer fluids: lessons from European experience". In: *Journal of Performance of Constructed Facilities* 30.2, p. 04015024.

Lam, C., S. A. Jefferis, and K. G. Goodhue Jr. (2010). "Observations on viscosity reduction of PHPA polymer support fluids". In: *Deep Foundations and Geotechnical In Situ Testing.* American Society of Civil Engineers. DOI: `10.1061/41106(379)23`.

Lam, C., S. A. Jefferis, and C. M. Martin (2014a). "Effects of polymer and bentonite support fluids on concrete-sand interface shear strength". In: *Géotechnique* 64.1, p. 28.

– (2014b). "Effects of polymer and bentonite support fluids on concrete–sand interface shear strength". In: *Géotechnique* 64.1, pp. 28–39. DOI: `10.1680/geot.13.p.012`.

Lam, C., S. A. Jefferis, T. P. Suckling, and V. M. Troughton (2015). "Effects of polymer and bentonite support fluids on the performance of bored piles". In: *Soils and Foundations* 55.6, pp. 1487–1500.

Larson, R. (1999). *The structure and rheology of complex fluids.* New York: Oxford University Press. ISBN: 9780195121971.

Lechner, M. D., K. Gehrke, and E. H. Nordmeier (2014). *Makromolekulare Chemie: Ein Lehrbuch für Chemiker, Physiker, Materialwissenschaftler und Verfahrenstechniker.* Berlin, Heidelberg: Springer Spektrum. ISBN: 978-3-642-41769-6.

Lei, M., W. Huang, J. Sun, Z. Shao, T. Wu, J. Liu, and Y. Fan (2020). "Synthesis of carboxymethyl chitosan as an eco-friendly amphoteric shale inhibitor in water-based drilling fluid and an assessment of its inhibition mechanism". In: *Applied Clay Science* 193, p. 105637. DOI: `10.1016/j.clay.2020.105637`.

Lei, M., L. Liu, Y. Lin, C. Shi, W. Yang, C. Cao, and Y. Liu (2019). "Research progress on stability of slurry wall trench of underground diaphragm wall and design method of slurry unit weight". In: *Advances in Civil Engineering* 2019, pp. 1–19. DOI: `10.1155/2019/3965374`.

Lesemann, H. (2010). "Anwendung polymerer Stützflüssigkeiten bei der Herstellung von Bohrpfählen und Schlitzwänden". German. PhD thesis. Technische Universität München.

Lesemann, H. and G. Schwab (2015). "Flüssigkeitsstützung in der Wüste – Gründungs-pfähle für den Kingdom Tower in Jeddah". In: *Vorträge zum 22. Darmstädter Geotechnik-Kolloquium.* Mitteilungen des Institutes und der Versuchsanstalt für Geotechnik der Technischen Universität Darmstadt. German, pp. 169–178.

Lesemann, H., N. Vogt, and M. Pulsfort (2016). "Analytical stability checks for diaphragm wall trenches and boreholes supported by polymer solutions". In: *Proceedings of 13th Baltic Sea geotechnical conference.* 10.3846/13bsgc.2016.035. Lithuania: Vilnius Gediminas Technical University Press Technika, pp. 231–238.

Levy, G. J. and D. N. Warrington (2015). "Polyacrylamide addition to soils: impacts on soil structure and stability". In: *Functional polymers in food science.* John Wiley & Sons, Inc., pp. 9–31. DOI: `10.1002/9781119108580.ch2`.

Liao, W. A. and D. R. Siems (1990). "Adsorption characteristics of PHPA on formation solids". In: *SPE/IADC drilling conference.* Society of Petroleum Engineers.

Lieske, W., S. Tripathy, W. Baille, and T. Schanz (2020). "An alternative approach for determining suction of polyethylene glycols for soil testing". In: *Géotechnique Letters* 10.1, pp. 45–49. DOI: `10.1680/jgele.19.00017`.

Lioliou, M. G., C. A. Paraskeva, P. G. Koutsoukos, and A. C. Payatakes (2006). “Calcium sulfate precipitation in the presence of water-soluble polymers”. In: *Journal of Colloid and Interface Science* 303.1, pp. 164–170. DOI: `10.1016/j.jcis.2006.07.054`.

Mesri, G., M. C. Pakbaz, and A. F. Cepeda-Diaz (1994). “Meaning, measurement and field application of swelling pressure of clay shales”. In: *Géotechnique* 44.1, pp. 129–145. DOI: `10.1680/geot.1994.44.1.129`.

Metodiev, A. (2013). “Electric properties of carboxymethyl cellulose”. In: *Cellulose - fundamental aspects*. InTech. DOI: `10.5772/56935`.

Mielenz, P. and O. Mielenz (2016). “Polymere für Stützflüssigkeiten im Spezialtiefbau”. In: *bbr – Leitungsbau, Brunnenbau, Geothermie – Spezial Bohrtechnik/Spezialtiefbau* 8, pp. 42–49.

MMB:2013. *Merkblatt Materialtransport im Boden – BAW-Merkblätter und -Richtlinien*. Technical bulletin. German. Karlsruhe: Bundesanstalt für Wasserbau.

Mobley, S., K. Costello, and G. Mullins (2018). “The effect of slurry type on drilled shaft cover quality”. In: *DFI Journal* 11.2-3, pp. 91–100.

Müller-Kirchenbauer, H. (1977). “Stability of slurry trenches in inhomogeneous subsoil”. In: *9th International conference on soil mechanics and foundation engineering*, pp. 125–132.

Murtaza, M., M. S. Kamal, S. M. S. H., and M. Mahmoud (2020). “Clay swelling inhibition using novel cationic gemini surfactants with different spacers”. In: *Journal of Surfactants and Detergents*. DOI: `10.1002/jsde.12420`.

Nagashiro, W. and T. Tsunoda (1977). “Degradation of polyacrylamide molecules in aqueous solutions by high-speed stirring”. In: *Journal of Applied Polymer Science* 21.4, pp. 1149–1153. DOI: `10.1002/app.1977.070210427`.

Navarrete, R.C., R.E. Himes, and J.M. Seheult (2000). “Applications of xanthan gum in fluid-loss control and related formation damage”. In: *SPE Permian basin oil and gas recovery conference*. Society of Petroleum Engineers. DOI: `10.2118/59535-ms`.

Ostwald, W. (1929). “Über die rechnerische Darstellung des Strukturgebietes der Viskosität”. In: *Kolloid-Zeitschrift* 47.2. German, pp. 176–187. ISSN: 0303-402X. DOI: `10.1007/BF01496959`.

Ouyang, Y., S. Jefferis, and P. Wiltcher (2018). “A major infrastructure project and the formation of the UK’s largest rotary pile under polymer support fluid”. In: *Proceedings of the DFI-EFFC international conference on deep foundations and ground improvement*. Rome, pp. 541–550.

Oyen, M. L. (2013). “Mechanical characterisation of hydrogel materials”. In: *International Materials Reviews* 59.1, pp. 44–59. DOI: `10.1179/1743280413y.0000000022`.

Patel, A., S. Stamatakis, S. Young, and J. Friedheim (2007). “Advances in inhibitive water-based drilling dluids – can they replace oil-based muds?” In: *International Symposium on Oilfield Chemistry*. Society of Petroleum Engineers. DOI: `10.2118/106476-ms`.

Peppas, N. A., B. V. Slaughter, and M. A. Kanzelberger (2012). “Hydrogels”. In: *Polymer science: A comprehensive reference*. Elsevier, pp. 385–395. DOI: `10.1016/b978-0-444-53349-4.00226-0`.

Pimentel, E. (2003). “Swelling behaviour of sedimentary rocks under consideration of micromechanical aspects and ist consequences on structure design”. In: *Geotechnical Measurements and Modelling: Proceedings of the 8th International Symposium, Karlsruhe, Germany, 23-26 September, 2003*. Ed. by O. Natau, E. Fecker, and E. Pimentel. Taylor & Francis, pp. 367–374. ISBN: 9789058096036.

Praetorius, S. and B. Schößer (2017). *Bentonite Handbook*. Wilhelm Ernst & Sohn. DOI: `10.1002/9783433606520`.

Prakash, K. and A. Sridharan (2004). “Free swell ratio and clay mineralogy of fine-grained soils”. In: *Geotechnical Testing Journal* 27.2, pp. 220–225. DOI: `10.1520/gtj10860`.

Pulsfort, M., B. Walz, and M. Faes (1988). “Großbohrpfähle Durchmesser 3,20 m bis 60 m Länge”. In: *Bautechnik* 65.8. German, pp. 253–256.

Quainoo, A. K., B. M. Negash, C. B. Bavoh, T. O. Ganat, and B. N. Tackie-Otoo (2020). “A perspective on the potential application of bio-inhibitors for shale stabilization during drilling and hydraulic fracturing processes”. In: *Journal of Natural Gas Science and Engineering* 79. DOI: `10.1016/j.jngse.2020.103380`.

Rankine, W. J. M. (1857). “On the stability of loose earth”. In: *Philosophical Transactions of the Royal Society of London* 147, pp. 9–27.

Ruppert, F.-R. (1980). “Bentonitsuspensionen für die Schlitzwandherstellung”. In: *Tiefbau, Ingenieurbau, Straßenbau* 22.8. German, pp. 684–686.

SC VIS HVP. *Safety Data Sheet.* Clariant, France, 13 June 2016.

SC XGUM. *Safety Data Sheet.* Clariant, France, 13 June 2016.

Schroefl, C. and V. Mechtcherine (2014). “Chemical aspects of superabsorbent polymers for use in cement-based mortars: a rewiew”. In: *Proeedings of the International RILEM Conference on Application of Superabsorbent Polymers and Other New Admixtures in Concrete Construction.* Ed. by V. Mechtcherine and C. Schroefl. Dresden, Germany: RILEM Publications, Bagneux, France, pp. 25–35. ISBN: 978-2-35158-148-3.

Semar, O., K. J. Witt, and R. J. Fannin (2010). “Suffusion evaluation – comparison of current approaches”. In: *Scour and Erosion.* American Society of Civil Engineers. DOI: `10.1061/41147(392)24`.

SFG:2019 (2019). *Guide to support fluids for deep foundations.* Tech. rep. EFFC/DFI Support Fluid Task Group.

Sievert, T., A. Wolter, and N.B. Singh (2005). “Hydration of anhydrite of gypsum (CaSO4.II) in a ball mill”. In: *Cement and Concrete Research* 35.4, pp. 623–630. DOI: `10.1016/j.cemconres.2004.02.010`.

Skauge, A., N. Zamani, J. Gausdal Jacobsen, B. Shaker Shiran, B. Al-Shakry, and T. Skauge (2018). “Polymer flow in porous media: relevance to enhanced oil recovery”. In: *Colloids and Interfaces* 2.3, p. 27. DOI: `10.3390/colloids2030027`.

Slurryshield PBS. *Material Safety Data Sheet.* KB International, USA, 08 June 2011.

SlurrySMART. *Material Safety Data Sheet.* KB International, USA, 26 April 2010.

Sorbie, K. S. (1991). *Polymer-improved oil recovery.* Glasgow: Blackie. ISBN: 0-216-92693-9.

Sridharan, A. and K. Prakash (2016). “Expansive soil characterisation: an appraisal”. In: *INAE Letters* 1.1, pp. 29–33. DOI: `10.1007/s41403-016-0001-9`.

Steiger, R. P. and P. K. Leung (1992). “Quantitative determination of the mechanical properties of shales”. In: *SPE Drilling Engineering* 7.03, pp. 181–185. DOI: `10.2118/18024-pa`.

Steinhoff, J. (1993). *Standsicherheitsbetrachtungen für polymergestützte Erdwände: Zugl.: Wuppertal, Univ., Diss.* Vol. 13. Grundbau, Bodenmechanik und unterirdisches Bauen. phD thesis, German. Wuppertal. ISBN: 3-925795-14-6.

Sterling, R. L. (2020). “Developments and research directions in pipe jacking and microtunneling”. In: *Underground Space* 5.1, pp. 1–19. DOI: `10.1016/j.undsp.2018.09.001`.

Stieß, M. (2009). *Mechanische Verfahrenstechnik – Partikeltechnologie 1.* 3rd ed. German. Springer Berlin Heidelberg. DOI: `10.1007/978/3-540-32552-9`.

Stocker, M. and B. Walz (2003). “Bored piles, diaphragm walls, cut-off walls”. In: *Geotechnical engineering handbook, 3: elements und structures.* Ed. by Ulrich Smoltcyk. Berlin: Ernst & Sohn, pp. 409–450. ISBN: 3-433-01451-5.

Stokes, Sir G. G. (1850). “On the effect of internal friction of fluids on the motion of pendulums”. In: *Transactions of the Cambridge Philosophical Society – Part II.* Vol. 9. Read December 9, 1850, printed 1851, pp. 8–106.

Suter, J. L., P. V. Coveney, R. L. Anderson, H. C. Greenwell, and S. Cliffe (2011). “Rule based design of clay-swelling inhibitors”. In: *Energy & Environmental Science* 4.11, p. 4572. DOI: `10.1039/c1ee01280k`.

Theng, B. K. G. (2012). *Formation and properties of clay-polymer complexes.* Amsterdam: Elsevier. ISBN: 9780080885278.

Thienert, C. (2011). *Zementfreie Mörtel für die Ringspaltverpressung beim Schildvortrieb mit flüssigkeitsgestützter Ortsbrust.* Vol. 31. Berichte des Lehr- und Forschungsgebietes Geotechnik. phD thesis, German. Shaker. ISBN: 9783844001679.

Trombetta, G., C. Di Bona, and E. Grazi (2005). “The transition of polymers into a network of polymers alters per se the water activity”. In: *International Journal of Biological Macromolecules* 35.1-2, pp. 15–18. DOI: `10.1016/j.ijbiomac.2004.11.002`.

VanGinkel, C. G. and S. Gayton (1996). “The biodegradability and nontoxicity of carboxymethyl cellulose (DS 0.7) and intermediates”. In: *Environmental Toxicology and Chemistry* 15.3, pp. 270–274. DOI: `10.1002/etc.5620150307`.

Verst, R. and M. Pulsfort (2017). “Reduction of soil swelling effects in pipe jacking and shield tunnelling using polymer solutions as support fluid”. In: *Proceedings of the IV international conference on computational methods in tunneling and subsurface engineering – EURO:TUN 2017.* Ed. by G. Hofstetter, K. Bergmeister, J. Eberhardsteiner, G. Meschke, and H. F. Schweiger. Innsbruck, Austria: Universität Innsbruck, pp. 505–512. ISBN: 978-3-903030-35-0.

– (2018). “Zur Funktionsweise von Polymerlösungen als Stütz- und Schmierflüssigkeiten von porösen Medien für den Tunnel- und Spezialtiefbau”. In: *Tagungsband zur 3. Deutschen Bodenmechanik-Tagung 2018 – in memoriam Professor Tom Schanz.* publication in progress, German. Universität Bochum.

Verwey, E. J. W. and J. Th. G. Overbeek (1948). *Theory of the stability of lyophobic colloids – the interaction of sol particals having an electric double layer.* Amsterdam: Elsevier.

von Terzaghi, K. (1936a). “A fundamental fallacy in earth pressure computations”. In: *Journal of the Boston Society of Civil Engineers* 23.2, pp. 328–336.

– (1936b). “Distribution of lateral pressure on sand on the timbering of cuts”. In: *Proceedings of the first International Conference on Soil Mechanics and Foundation Engineering.* Cambridge, Massachussetts, USA, pp. 211–215.

– (1936c). “The shearing resistance of saturated soils and the angle between the planes of shear”. In: *International Conference on Soil Mechanics and Foundation engineering.* Ed. by A. Casgrande, P. C. Rutledge, and Watson; J. D. Cambridge, Massachussetts, USA: Harvard University press, pp. 54–56.

– (1943). “Earth pressure on temporary supports in cuts, tunnels and shafts”. In: *Theoretical Soil Mechanics.* John Wiley & Sons, Inc., pp. 182–215. DOI: `10.1002/9780470172766.ch10`.

Walz, B. (1978). “An examination of some theories of earth pressure on shaft linings: Discussion”. In: *Canadian Geotechnical Journal* 15.3, pp. 438–440. DOI: `10.1139/t78-045`.

Walz, B. and K. Hock (1987). *Berechnung des räumlich aktiven Erddrucks mit der modifizierten Elementscheibentheorie.* Vol. 6. Grundbau, Bodenmechanik und unterirdisches Bauen. German. Wuppertal: University of Wuppertal.

Ward, T. C. (1981). “Molecular weight and molecular weight distributions in synthetic polymers”. In: *Journal of Chemical Education* 8.11, pp. 867–879.

Weiß, F. (1967). *Die Standfestigkeit flüssigkeitsgestützter Erdwände.* Bauingenieur-Praxis 70. German. Ernst & Sohn.

Wheeler, P. (2003). “Clear as mud”. In: *New Civil Engineer.*

Wilson, M. J . and L. Wilson (2014). “Clay mineralogy and shale instability: an alternative conceptual analysis”. In: *Clay Minerals* 49.2, pp. 127–145. DOI: `10.1180/claymin.2014.049.2.01`.

Witt, K.J. (2018). “Hydraulisch bedingte Grenzzustände”. In: ed. by K. J. Witt. 8. German. Wiley Online Library, pp. 821–862. DOI: `10.1002/9783433607312`.

Wittke, M. (2006). “Design, construction, supervision and long-term behaviour of tunnels in swelling rocks”. In: *Proceedings EUROCK 2006: Multiphysics coupling and long-term behaviour in rock mechanics.* Liège, pp. 211–216.

Xie, G., P. Luo, M. Deng, J. Su, Z. Wang, R. Gong, J. Xie, S. Deng, and Q. Duan (2017). “Investigation of the inhibition mechanism of the number of primary amine groups of alkylamines on the swelling of bentonite”. In: *Applied Clay Science* 136, pp. 43–50. DOI: `10.1016/j.clay.2016.11.005`.

Xiong, B., R. D. Loss, D. Shields, T. Pawlik, R. Hochreiter, A. L. Zydney, and M. Kumar (2018). “Polyacrylamide degradation and its implications in environmental systems”. In: *npj Clean Water* 1.17, pp. 1–9. DOI: `10.1038/s41545-018-0016-8`.

Yong, R. N. (1999). “Soil suction and soil-water potentials in swelling clays in engineered clay barriers”. In: *Engineering Geology* 54.1-2, pp. 3–13. DOI: `10.1016/s0013-7952(99)00056-3`.

Yoo, C. and Y.-S. Han (2019). “Effect of drilling fluid on concrete-soil/rock interface shear strength in seawater drilling environment”. In: *Marine Georesources & Geotechnology* 37.8, pp. 936–944.

Yu, J., J. G. Shi, P. F. Dang, A. I. Mamedov, I. Shainberg, and G.J. Levy (2012). “Soil and polymer properties affecting water retention by superabsorbent polymers under drying conditions”. In: *Soil Science Society of America Journal* 76.5, pp. 1758–1767. DOI: `10.2136/sssaj2011.0387`.

Zhang, L.-M. (1999). “Inhibitive properties of amphoteric, water-soluble cellulosic polymers on bentonite swelling”. In: *Colloid & Polymer Science* 277, pp. 282–284. DOI: `10.1007/pl00013757`.

Zitha, P. L. J., G. Chauveteau, and L. Léger (2001). “Unsteady-state flow of flexible polymers in porous media”. In: *Journal of colloid and interface science* 234.2, pp. 269–283.

Zohourian, M. M. and K. Kabiri (2008). “Superabsorbent polymer materials: A review”. In: 17.6, pp. 451–477.

Zumsteg, R., A.M. Puzrin, and G. Anagnostou (2016). “Effects of slurry on stickiness of excavated clays and clogging of equipment in fluid supported excavations”. In: *Tunnelling and Underground Space Technology* 58, pp. 197–208. DOI: `10.1016/j.tust.2016.05.006`.

Appendix

A. Basic equations at capillary and soil level

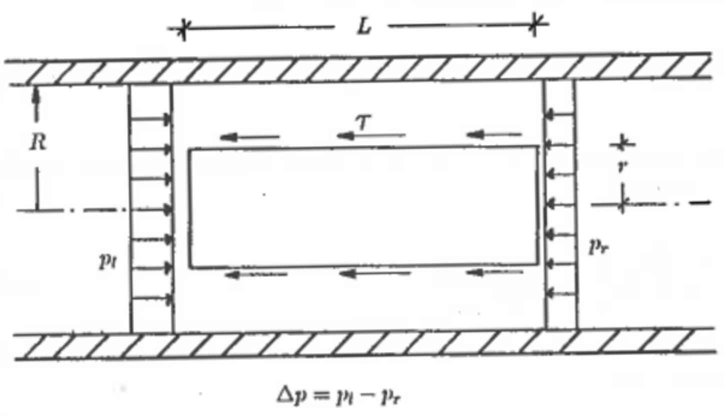

Figure A.1.: Force balance at pipe level (Steinhoff, 1993)

Force balance at pipe level according to Fig. A.1:

$$\tau = \frac{\Delta p \cdot r}{2 \cdot L} \tag{A.1}$$

Bulk rheology of a Newton fluid:

$$\tau = \eta \cdot \dot{\gamma} \tag{A.2}$$

Definition of wall shear rate:

$$\dot{\gamma}_{wall} = \dot{\gamma}(r = R) = -\frac{dv}{dr} \tag{A.3}$$

Combination:

$$-\frac{dv}{dr} = \frac{\Delta p \cdot r}{2 \cdot L \cdot \eta} \tag{A.4}$$

Integration & initial condition $v(r = R) = 0$:

$$v(r) = \frac{\Delta p}{4 \cdot L \cdot \eta} \cdot \left(R^2 - r^2\right) \tag{A.5}$$

Integration along pipe:

$$\dot{Q} = \int_0^R v(r) \cdot 2 \cdot \pi \cdot r dr = \frac{\Delta p \cdot \pi \cdot R^4}{8 \cdot L \cdot \eta} \tag{A.6}$$

Average velocity definition (Hagen-Poiseuille equation):

$$\bar{v} = \frac{\dot{Q}}{\pi \cdot R^2} = \frac{\Delta p \cdot R^2}{8 \cdot L \cdot \eta} \tag{A.7}$$

B. Materials

B.1. Polymers

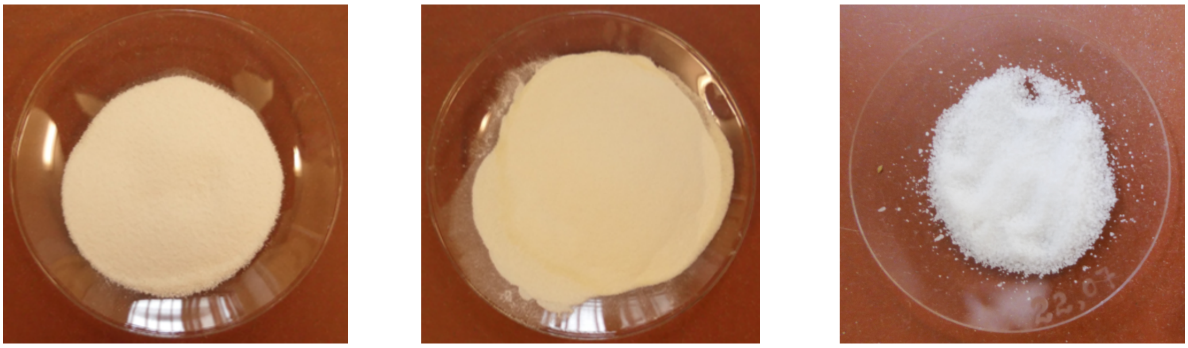

(a) CMC-H (b) XAN (c) AN range

(d) AN-Hmix (e) SAP S (f) SAP M

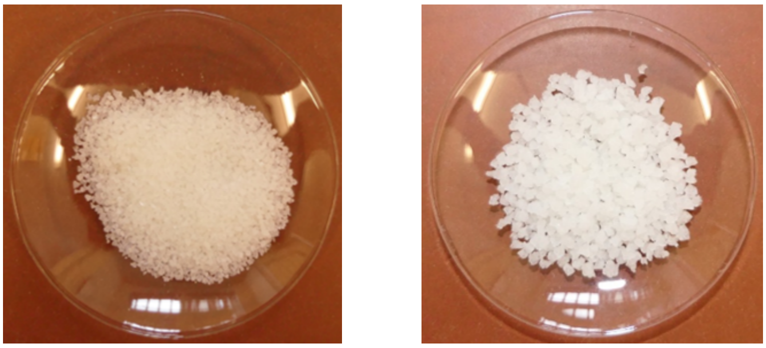

(g) SAP G (h) SAP L

Figure B.1.: Polymer granules – viscosifier (top) and superabsorber (bottom)

(a) AN-H 0.75 + S_{XS} – mixed dry, $\Delta t = 10$ min between images

(b) CMC-H 2.5 + S_{XS} – mixed dry, $\Delta t = 10$ min between images

(c) AN-H 0.75 & 0/0.1 mm – mixed in solution, $\Delta t = 10$ min between images

(d) CMC-H 2.5 & 0/0.1 mm – mixed in solution, $\Delta t = 10$ min between images

Figure B.2.: Influence of method of insertion of quartz powder (S_{XS})

B.2. Fluid mixing devices

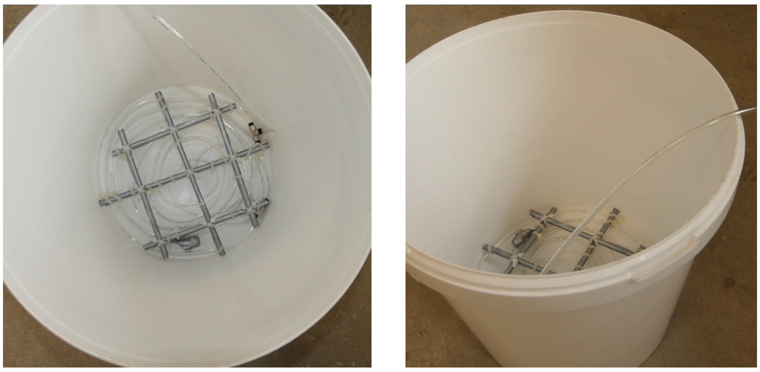

(a) Small container (ca. 20 l fluid)

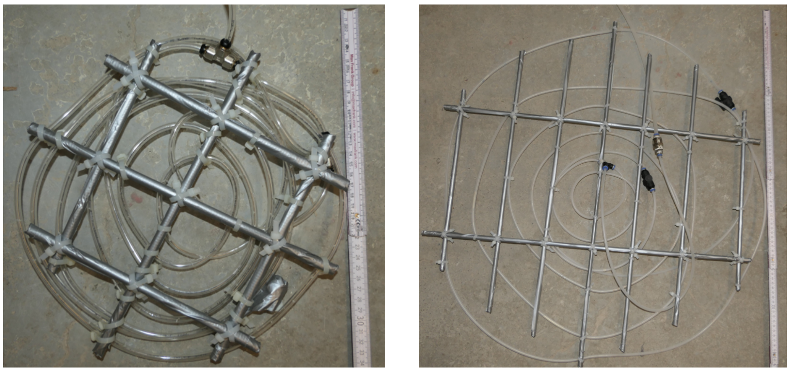

(b) Removable air supply pipes

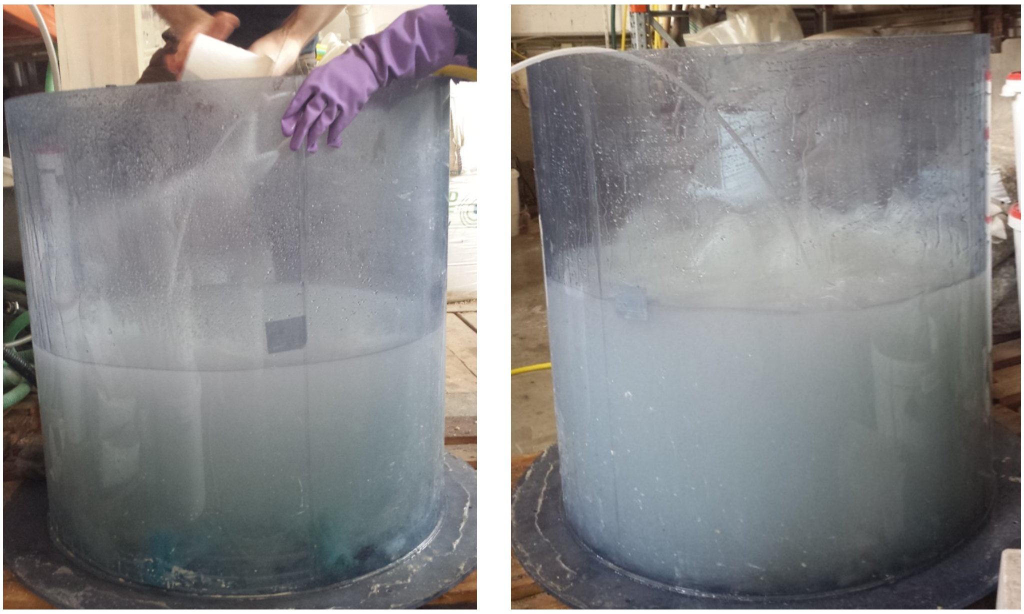

(c) Large container (ca. 200 l fluid)

Figure B.3.: Polymer fluid mixing devices for larger quantities

B.3. Concrete mix design

Table B.1.: Mix design of the concrete used for H-R

Component	Specification	Mix design	
Water	Wuppertal tap water	197.0	kg/m^3
Cement	CEM III/B 42,5 N-LH/SR(na)	370.0	kg/m^3
Fly ash	Hard coal fly ash	60.0	kg/m^3
Aggregate	0/16 mm quartz sand/gravel	1692.2	kg/m^3
Superplasticiser	Polycarboxylate ether	0.20-0.25(a)	% (w/w)
SUM		2319.2	kg/m^3

(a) Usage with a target flow spread category F5

C. Bulk rheology

C.1. Rheometer properties

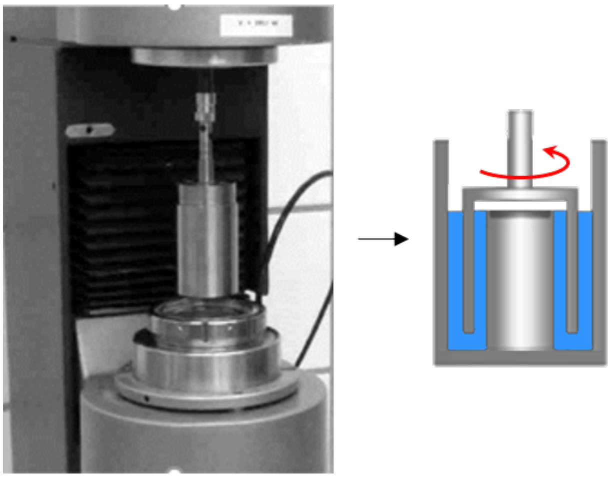

Figure C.1.: RS 600 rheometer with double-gap geometry

Rheometer	Rheostress RS600, with temperature control unit
Measuring geometry	DG43Ti double-gap cylinder
A factor	3723.000 Pa/Nm
M factor	31.080 (1/s)/(rad/s)
Inertia moment I	$3.513 \cdot 10^{-5}$ kg·m^2
Torque range	0.1 μNm - 200000 μNm
Angular velocity range	$1 \cdot 10^{-7}$ 1/min - 1500 1/min
Gap	5.1 mm
Volume	11.5 ml
Radius gap 1	$R_i = 17.750$ mm, $R_a = 18.350$ mm
Radius gap 2	$R_i = 20.990$ mm, $R_a = 21.700$ mm
Shear rate range	3.255^{-7} 1/s - 4882.04 1/s
Shear stress range	0.0003723 Pa - 744.6 Pa
Viscosity range (min - max)	$7.626e \cdot 10^{-8}$ Pa·s - $2.28778 \cdot 10^{9}$ Pa·s
Viscosity range (10·min - max/10)	7.626^{-7} Pa·s - $2.28778 \cdot 10^{8}$ Pa·s
Viscosity range (optimal)	0.1525 Pa·s - 1143.89 Pa·s

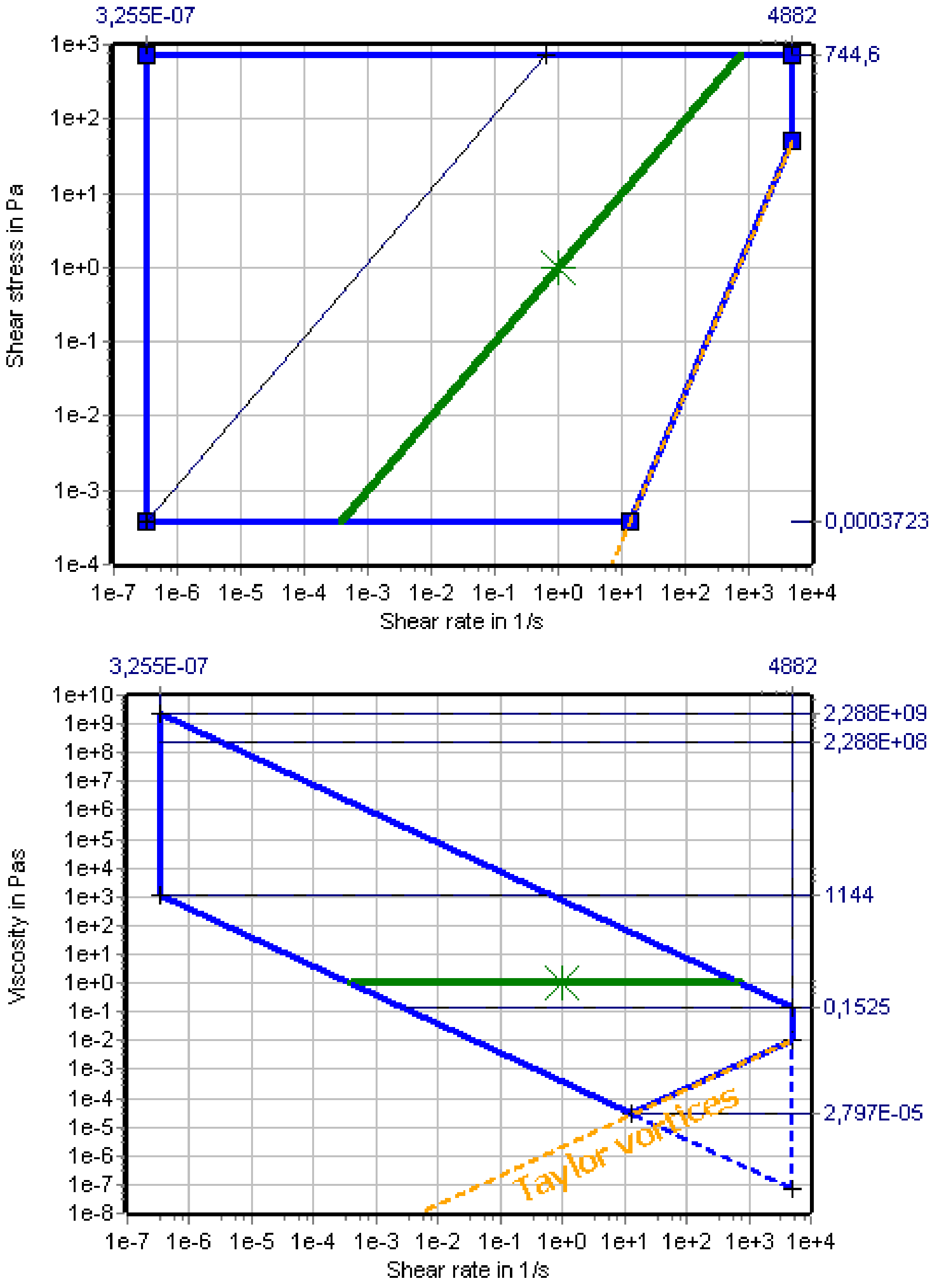

Figure C.2.: Measurement range (Manufacturer info)

C.2. Rheometer interpretation

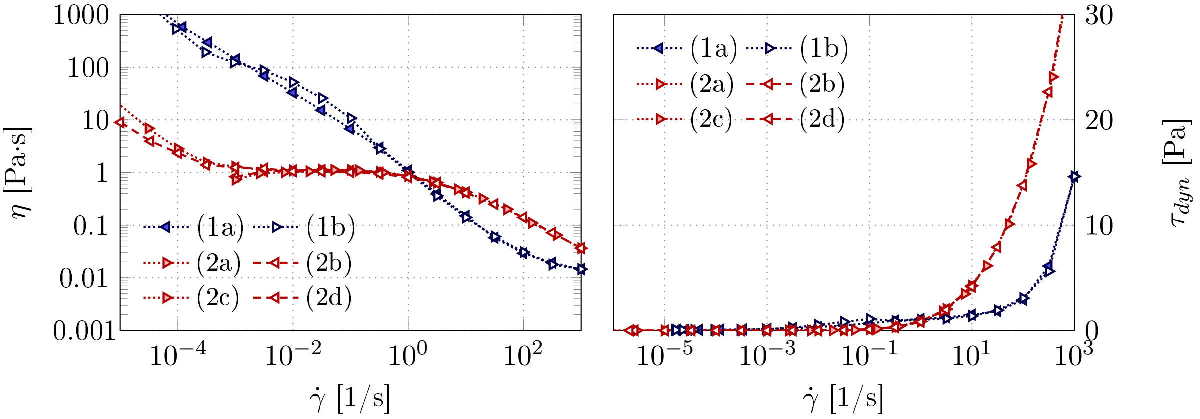

(a) Raw output

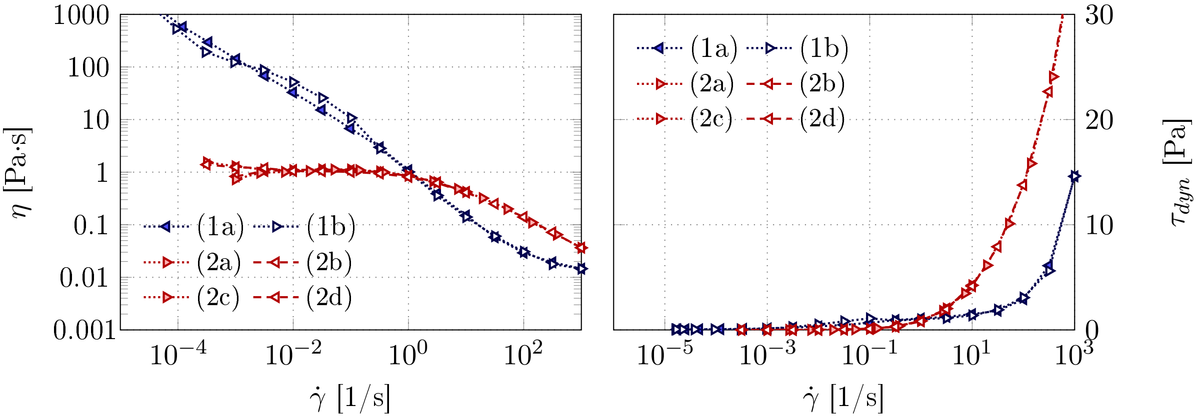

(b) Clearing based on rheometer measurement range according to Fig. C.2

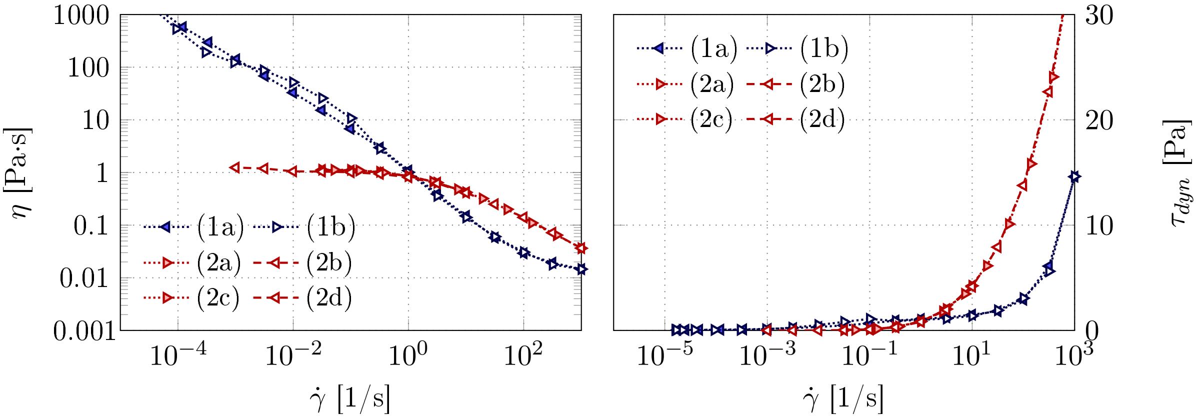

(c) Viscosity plateau clearing (at low viscosity levels)

Figure C.3.: Rheometer interpretation – two exemplary measurement interpretations

C.3. Bulk rheological characterization – boundary effects

Fig. C.4 shows the variability of rheometer bulk viscosity results as influenced by the type of solvent (tap water tw vs. deionized water dw), storage conditions and supply charge (indicated by preceding numbers). It is illustrated that the influence of dissolved ions increases with decreasing

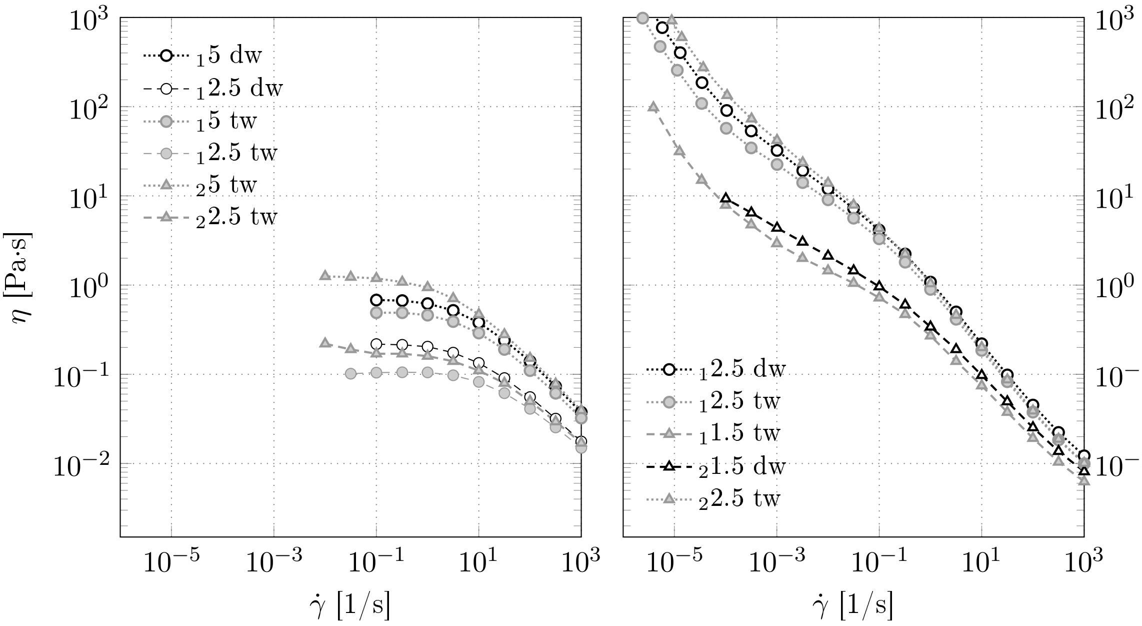

(a) $_{1/2}$CMC-H

(b) $_{1/2}$XAN

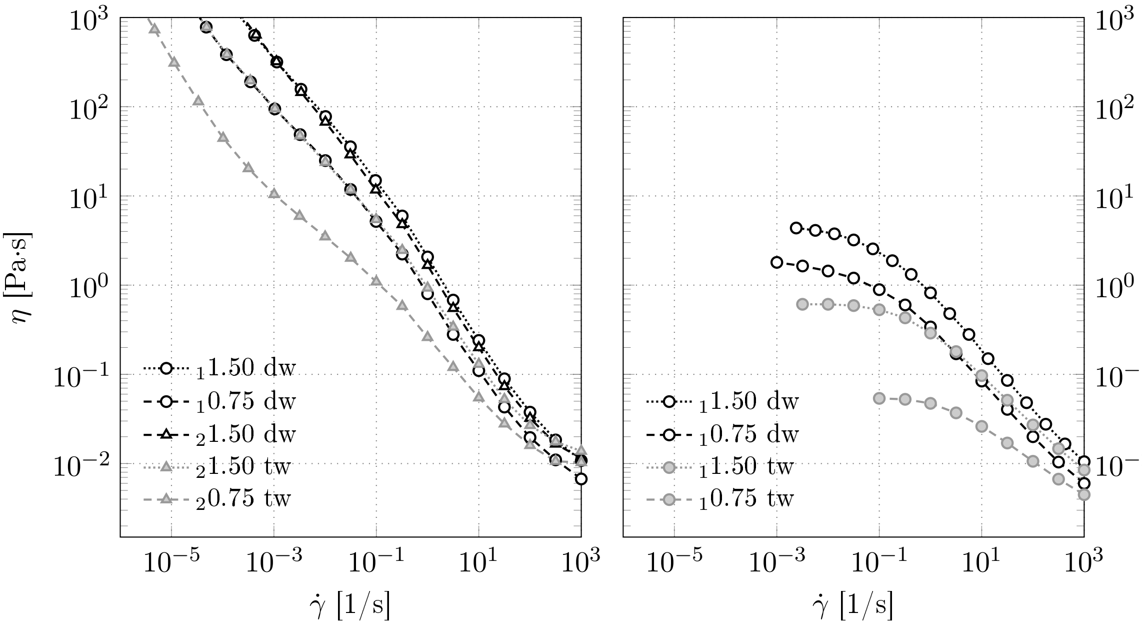

(c) $_{1/2}$AN-H

(d) $_1$AN-S

Figure C.4.: Viscosity results – influence of environmental conditions: type of solvent, storage and supply charge shear rate and polymer concentrations in the double-logarithmic viscosity plot. With respect to chain length (A-S vs. AN-H), the impact is higher with smaller chain length. ANmix is not displayed, but behaves similarly to AN-H. In comparison between CMC-H and XAN at the same concentration (2.5 g/l), the effect of dissolved ions is higher with CMC-H than with XAN.

Deviations between the first and the second supply charge of CMC-H and XAN in equal solvent and at equal concentration can be explained by biological or chemical degradation processes during storage and an influence of air humidity (storage age difference ca. 1.5 years). In these cases, the effect of degradation during storage surpasses the impact of dissolved ions. The synthetic products were applied with shorter storage time resulting in smaller deviations between the different supply charges.

The deviation increase at lower shear rates can be explained by the influence of both degradation and dissolved ions on the polymer chain length. The polymer chain length becomes insignificant at high shear rates, when the polymer chains are stretched to a maximum and arranged in parallel. With increasing concentration, a constant amount of dissolved ions has a smaller effect. The polymer composition of XAN visibly makes the polymer more stable against the influence of ions.

Fig. C.5 displays the evolution of solution viscosity over time for CMC-H, XAN and AN-H (as a representative of the synthetic group) for an exemplary mixture each. Fig. C.6 shows a comparison of viscosity values at $\dot{\gamma} = 10^{-3}$ 1/s with Marsh outflow times at 1 l of the same polymer solutions over time. The influence of the type of solvent is also evaluated in Fig. C.6 for CMC-H and XAN as these are considered to be more easily degraded over time than the synthetic polymers. The figures show that CMC-H and AN-H are relatively stable even after one month. However, small deviations can already be measured around 4-7 days. The XAN

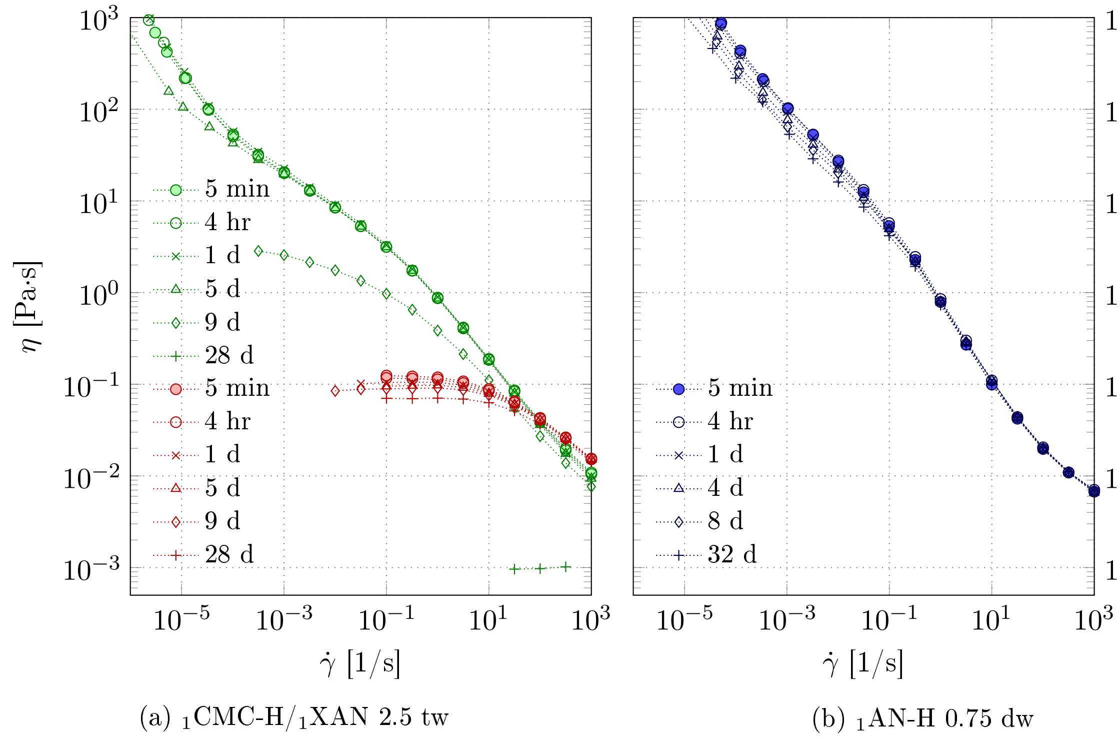

(a) $_1$CMC-H/$_1$XAN 2.5 tw

(b) $_1$AN-H 0.75 dw

Figure C.5.: Degradation of solution viscosity curves show gull degradation within 28 days as expected, as XAN is classified as biodegradable. A marked and then a significant degradation is already noted after 5 and 9 days, respectively.

Generally, a comparison of rheometer and Marsh results (Fig. C.6) shows that this degradation tendency is visible in both representations indicating comparable applicability of both measuring techniques in this regard.

Fig. C.7-C.8 show an evaluation of the influence of shear history, rheometer measurement repeatability and thixotropy for XAN, CMC-H and both AN-H and AN-S to reflect the influence of polymer chain length. The rheometer measurements for this purpose are performed in six stages. The first four stages are executed at low shear with an upper boundary at $\dot{\gamma}_{max} = 10$ 1/s, which represents the maximum shear rate the polymers were exposed to during mixing (max. 550 rpm = 9.2 1/s). The measurements with stepwise increase in shear rate $\dot{\gamma}$ ($\triangleright$) are marked by dotted lines, measurements with stepwise decrease in $\dot{\gamma}$ ($\triangleleft$) are marked by dashed lines. The upwards stages 2 and 3 are preceded by a pause of $\Delta t = 10$ min for thixotropy evaluation.

Bentonite suspension at 40 g/l is displayed for comparison showing a distinct shear stress plateau around $\tau = 3.4$ Pa stable until $\dot{\gamma} \approx 2$ 1/s and an increase in mobilised shear resistance after 10 min pause up to $\tau = 5.5$ Pa.

Before detailed comparison of each stage, it can already be noted that the lower viscosity solutions CMC-H and AN-S do not show any variability resulting from the different stages, i.e. no influence of shear history, decreasing or increasing shear rate or any thixotropic effect.

AN-H and XAN, however, do show an influence of shear history, but no significant dependency on time (thixotropy). The first stage (‘up 1’) serves for even distribution of the fluid in the measuring geometry and therefore deviates from the following stage curves for the polymer solutions of higher viscosity (XAN and AN-H), which do not spread as easiliy in the double gap geometry. The second downwards curve (‘down 2’) resumes the downwards curve of the preceeding downwards stage precisely revealing no influence of shear history so far and reflecting the accuracy of the rheometer measurement. Both upwards stages 2 and 3 follow comparable paths with only slight measuring deviations. These upwards stages also reveal a temporary increase and then decrease of τ around $\dot{\gamma} = 10^{-2} - 10^{0}$ 1/s for both XAN and AN-H in the shear stress plot, though more pronounced with the synthetic polymer. This behaviour leads to a moderate deviation from the ideal power law straight line in the double-logarithmic plot in this range and could be considered as a very moderate plateau formation. This effect is also found – though flatter – in downwards measurements with synthetic polymers at high-viscosity levels displayed in Fig. 3.15.

The final upwards and subsequent downwards stage then reveal a certain degree of shear degradation. This takes effect as a constant viscosity shift over the whole shear rate range for AN-H similar to a drop in concentration, while for XAN the change is visible as a deviation increasing with decreasing shear rate.

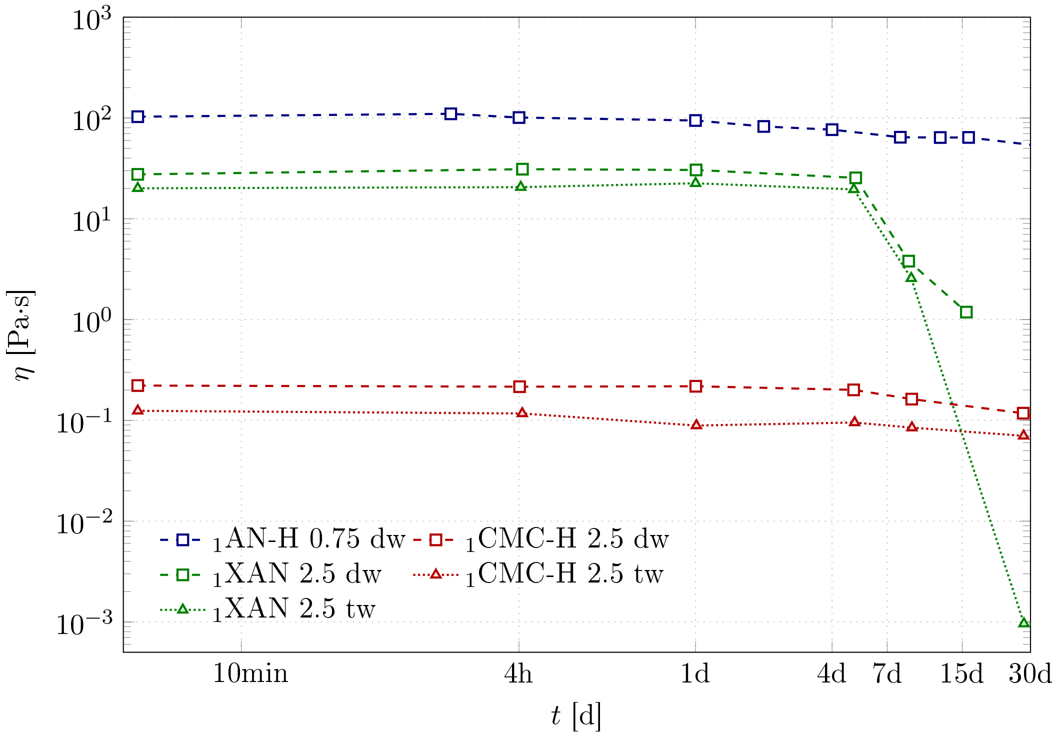

(a) Viscosity at $\dot{\gamma} = 10^{-3}$ 1/s

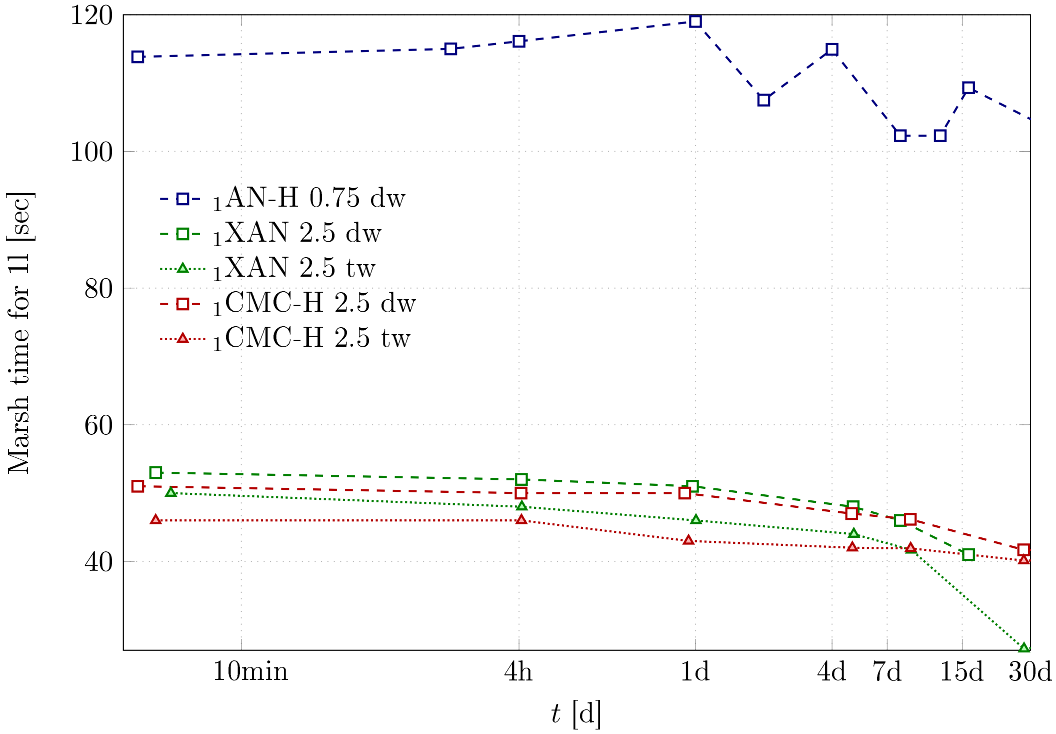

(b) Marsh outflow time at 1 l

Figure C.6.: Rheometer vs. Marsh – degradation in solution

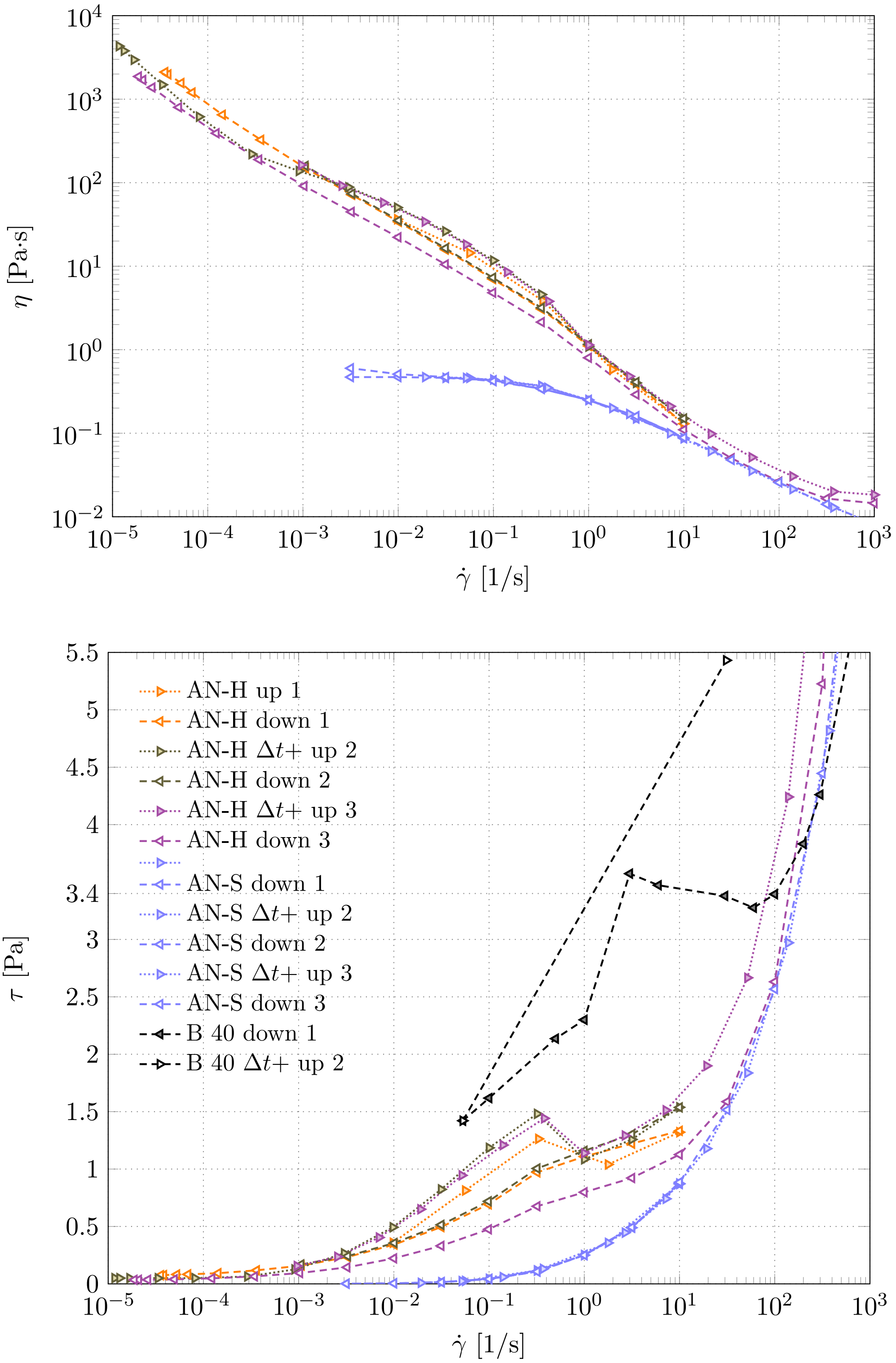

Figure C.7.: Shear history, repeatability and thixotropy – $_2$AN-H 1.5 tw & $_2$AN-S 1.5 tw

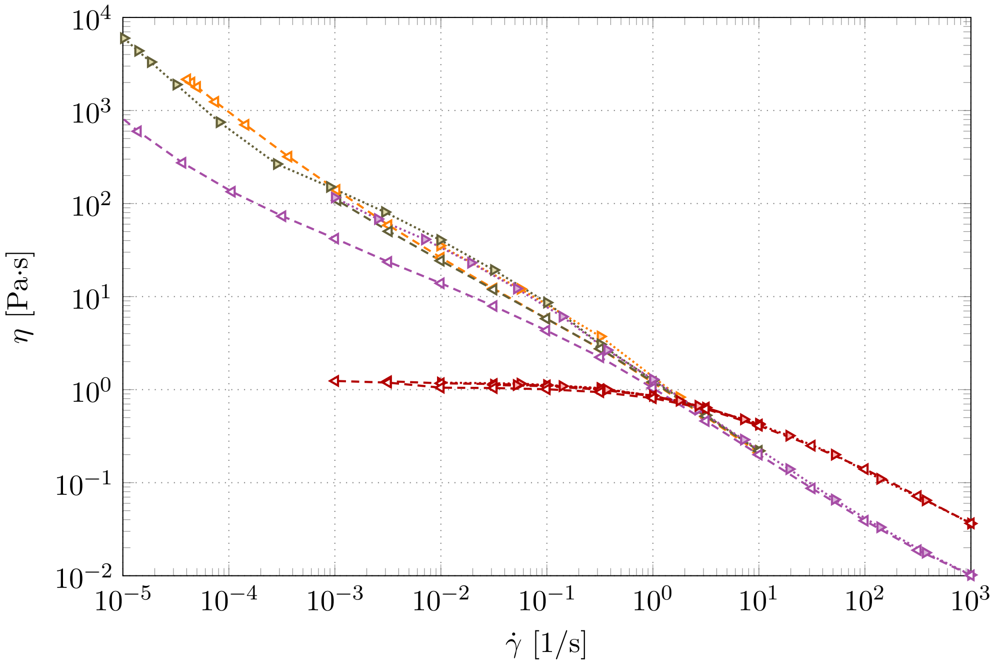

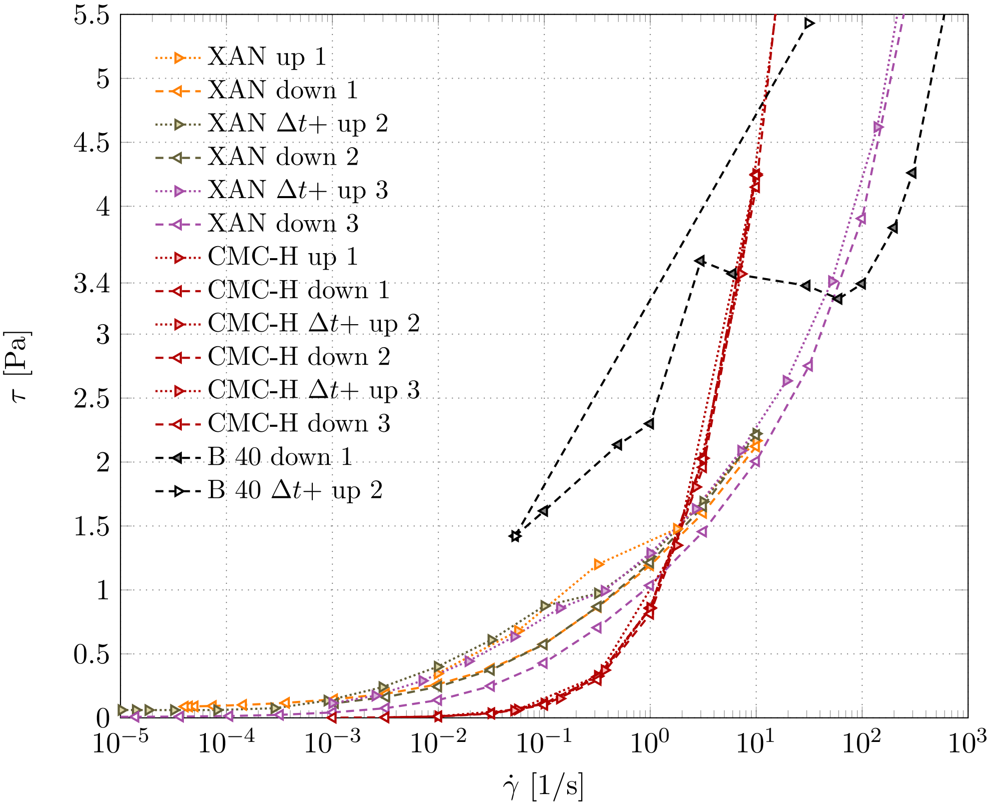

Figure C.8.: Shear history, repeatability and thixotropy – $_2$XAN 2.5 tw & $_2$CMC-H 5 tw

C.4. Influence of polymer granule size

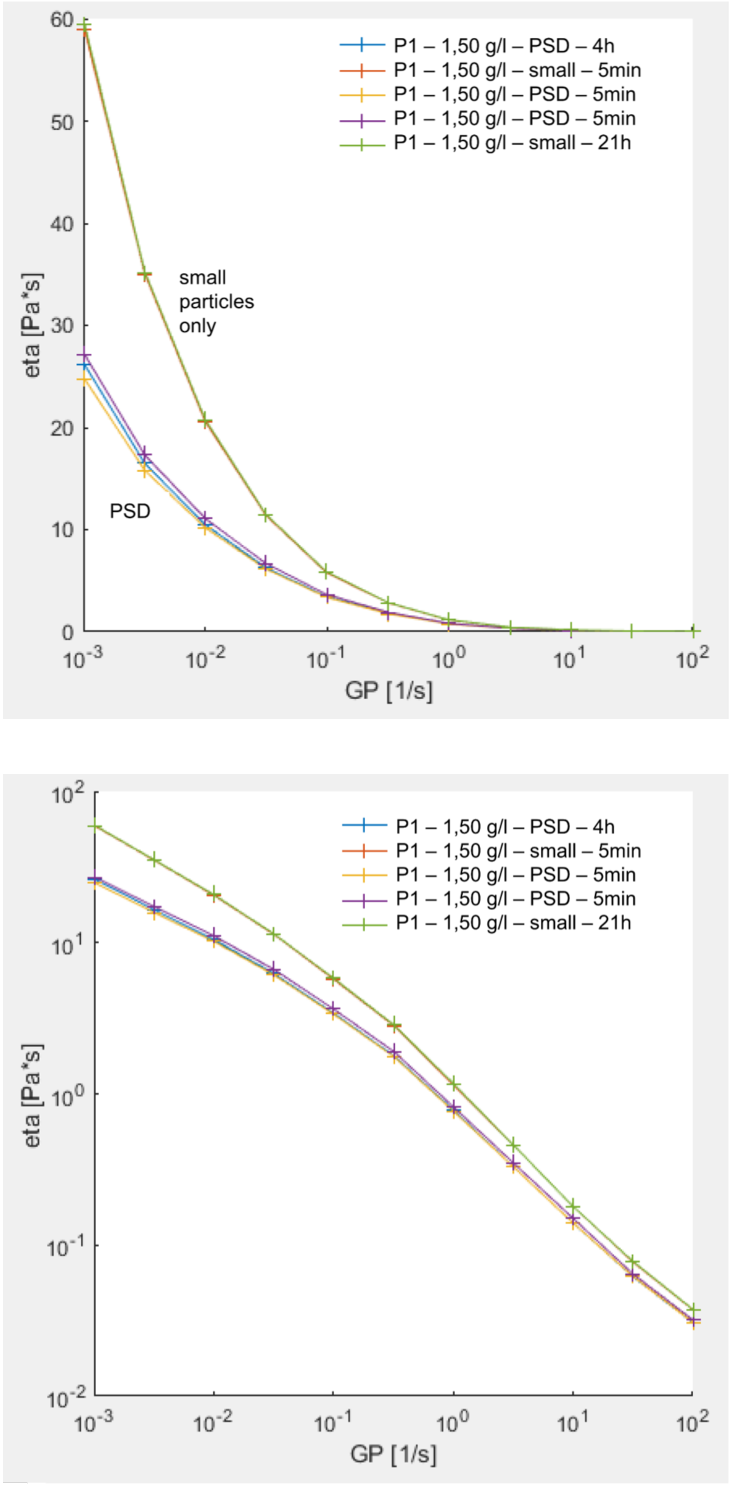

Figure C.9.: Effect of polymer granule size on rheometer viscosity curve of AN polymer

C.5. Bingham approximation

The bentonite suspensions were tested by means of a rotational rheometer with double-gap geometry at controlled shear rate (CR) with τ gradient control (see section 3.1.3). The experimental results are given in Fig. C.10a (black) showing the values obtained with stepwise decrease of the shear rate $\dot{\gamma}$. The blue lines show the Bingham approximation (Eq. C.1)

$$\tau_{Bingham} = \tau_0 + \eta_B \cdot \dot{\gamma} \tag{C.1}$$

evaluated based on the experimental values of τ_{exp} obtained at $\dot{\gamma} = 1000$ 1/s and $\dot{\gamma} = 300$ 1/s[1] with η_B as the respective secant modulus (Eq. C.2) (Fig. C.10b, blue)

$$\eta_B = \frac{\Delta\tau}{\Delta\dot{\gamma}} = \frac{\tau_{exp}\left(\dot{\gamma} = 1000\right) - \tau_{exp}\left(\dot{\gamma} = 300\right)}{1000 - 300} \tag{C.2}$$

and the related intercept (Eq. C.3)

$$\tau_0 = \tau_{exp}\left(\dot{\gamma} = 300\right) + \eta_B \cdot 300 \tag{C.3}$$

The viscosity η as displayed in Fig. C.10b (black) is calculated based on the experimental values τ_{exp} for $\dot{\gamma} \in [300, 1000]$ according to Eq. C.4.

$$\eta_{exp} = \frac{\tau_{exp} - \tau_0}{\dot{\gamma}_{exp}} \tag{C.4}$$

Fig. C.10a illustrates that the Bingham model accurately describes the bulk rheology of these bentonite suspensions for shear rates around $\dot{\gamma} = 200 - 1000$ 1/s. However, the experimental results show a shear stress plateau formation for shear rates above $\dot{\gamma} = 0$ 1/s, i.e. it can only be underestimated by the shear strength parameter τ_0 as determined according to Bingham. This deviation increases with increasing bentonite concentration.

The shear stress values obtained by means of these shear tests are designated as dynamic values τ_{dyn} as they are obtained at controlled shear rates. Shear resistance is measured as resistance against movement (torque), i.e. no true “static” values can be obtained. However, if the shearing velocity induced by the rotor is small enough, thixotropic effects may be rendered possible, which could then influence the registered values and be reflected in the measured plateau. However, it should be noted that these test results are linked to the used geometry, i.e. they can be indicative of a certain behaviour and may be transferred to similar shearing conditions (e.g. pipe flow).

---

[1] Similarly to the approach according to API RP 13D:2017, which bases on the viscometer readings at 1022 1/s and 511 1/s respectively, but adjusted to take into account the full measured shear range

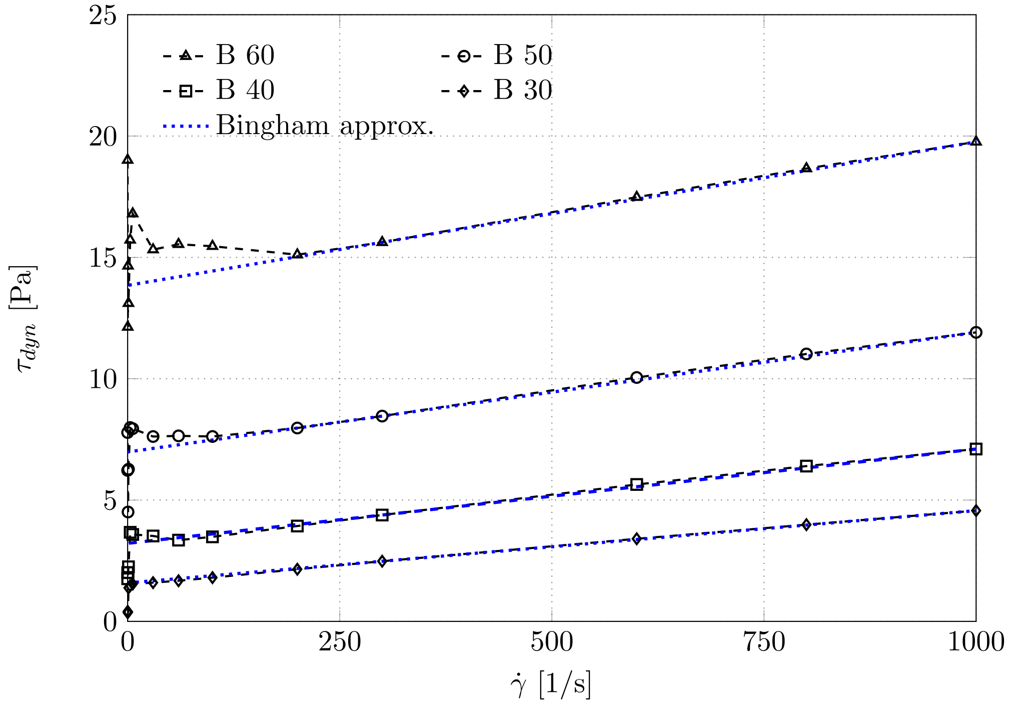

(a) Shear stress

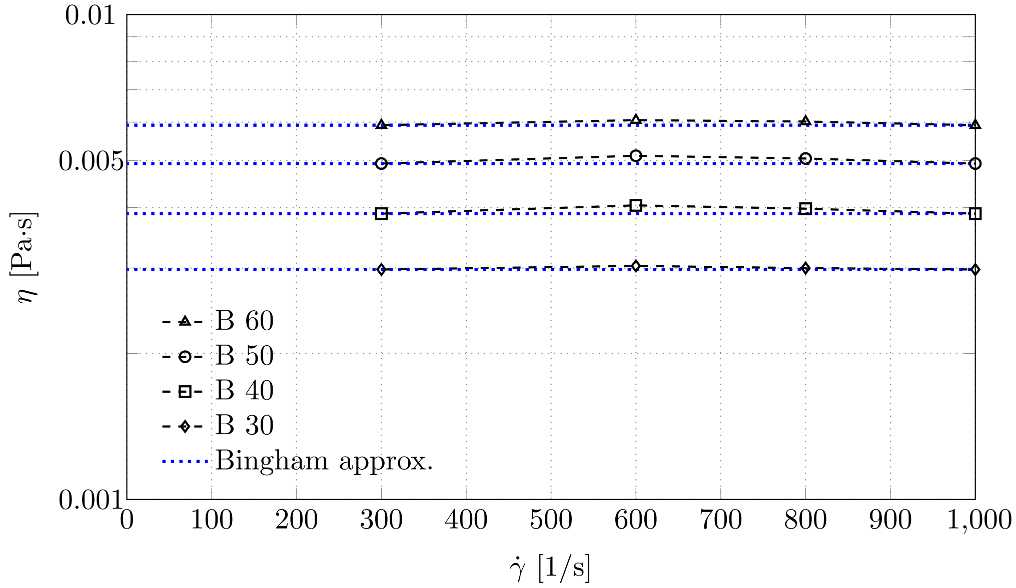

(b) Viscosity η

Figure C.10.: Bulk rheology of bentonite suspension at 20 °C

C.6. Power-law parameter determination

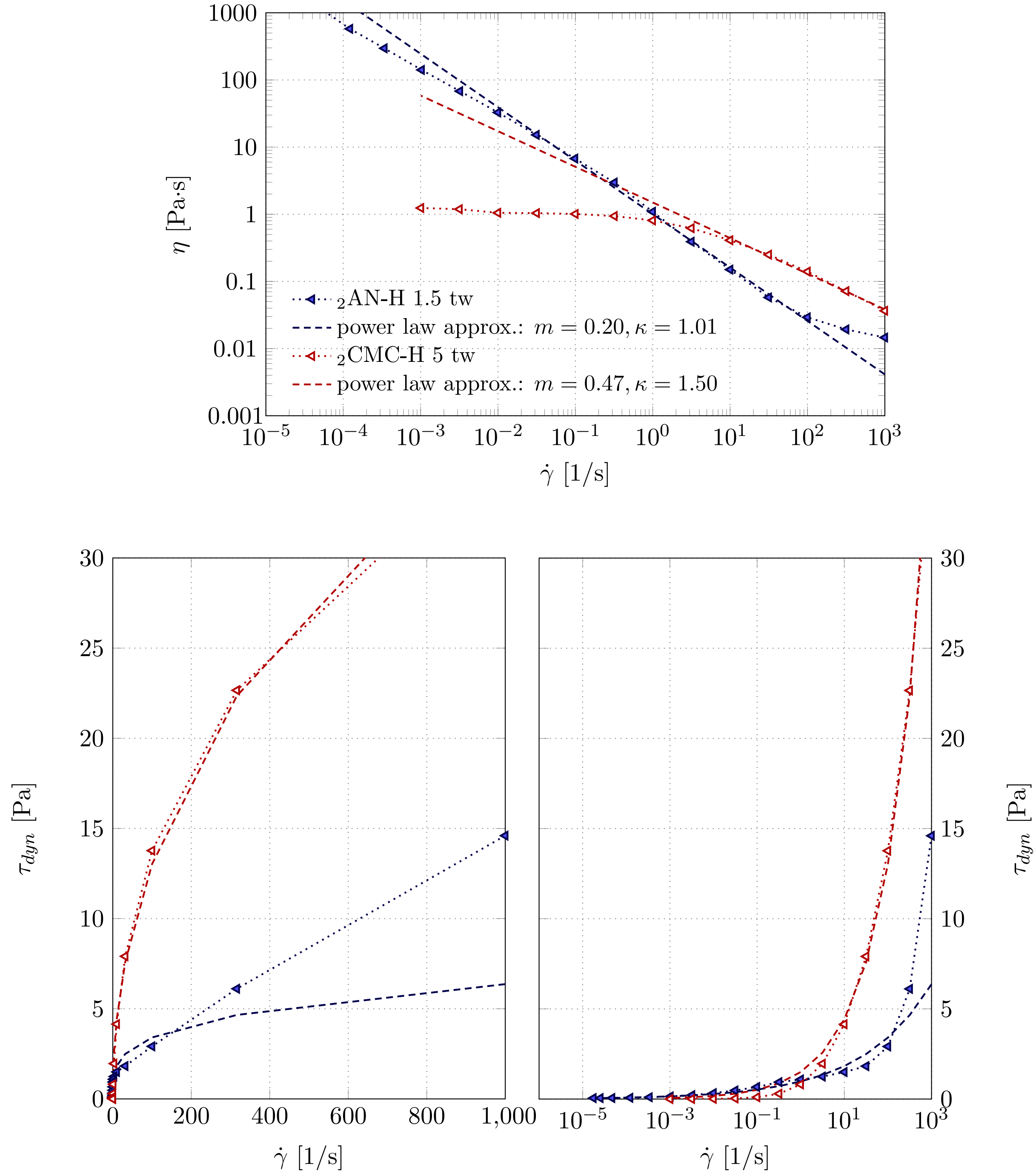

Figure C.11.: Rheometer interpretation – two exemplary power-law parameter interpretations

D. V-L

D.1. Device

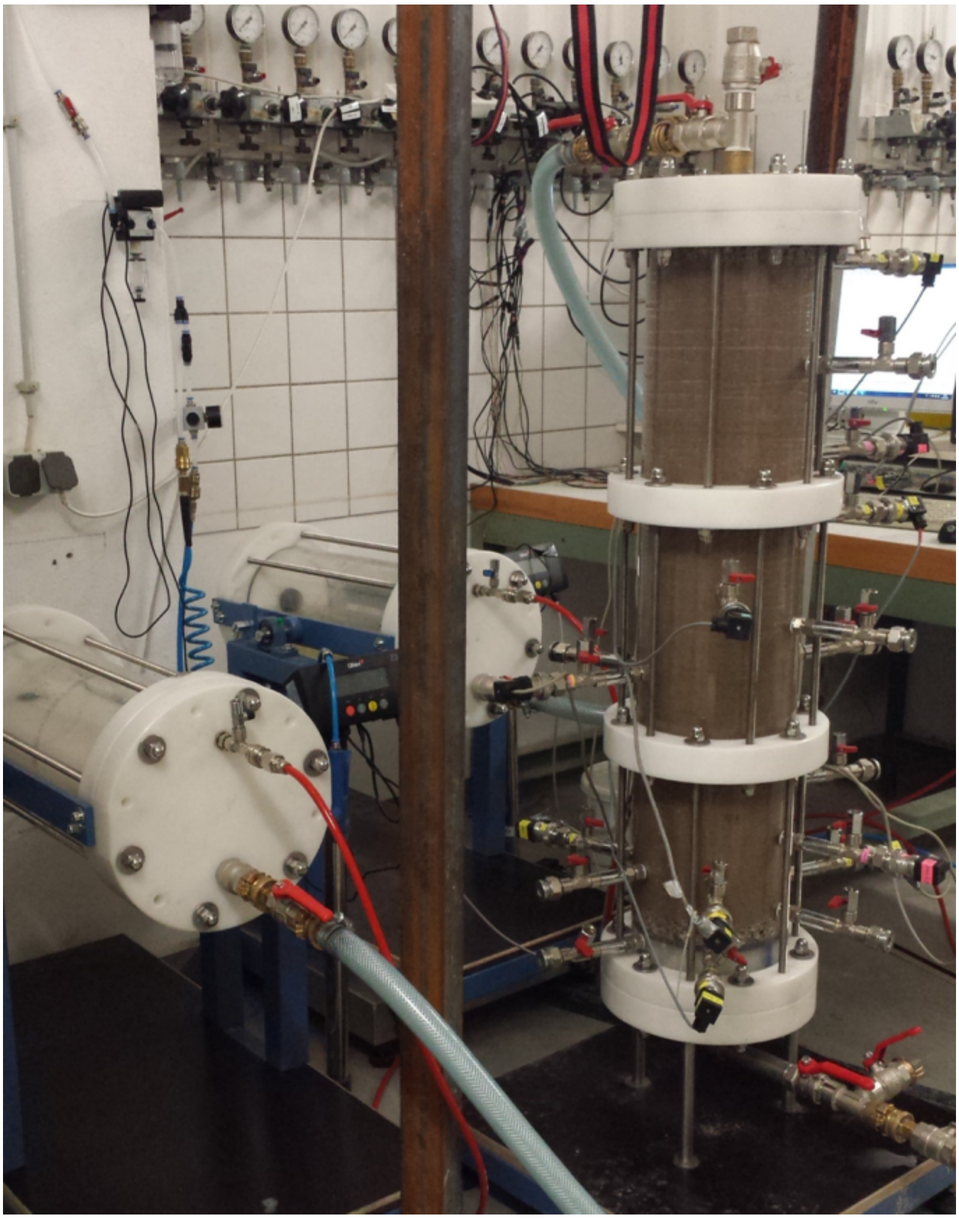

Figure D.1.: Testing device with three elements

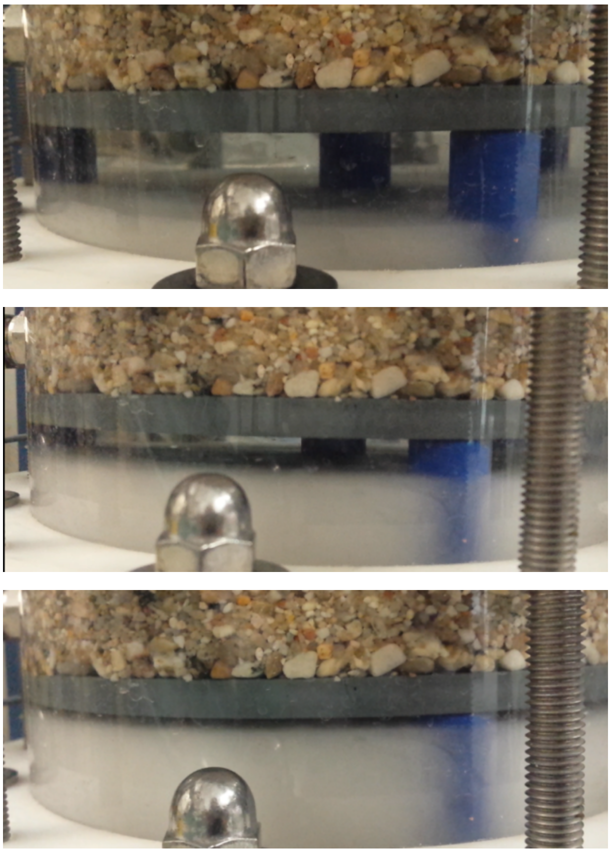

Figure D.2.: Test initiation: even inflow conditions $_1$AN-M 0.75 + S$_{XS}$ 20

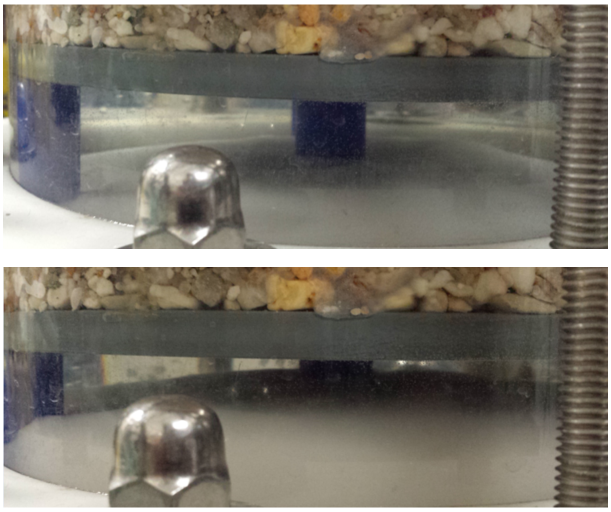

Figure D.3.: Test initiation: even inflow conditions $_1$AN-H 0.75 + S$_{XS}$ 20

(a) Soil 0.5/1.2 mm – CMC-H 5 $S_{XS/S}$ 2x10

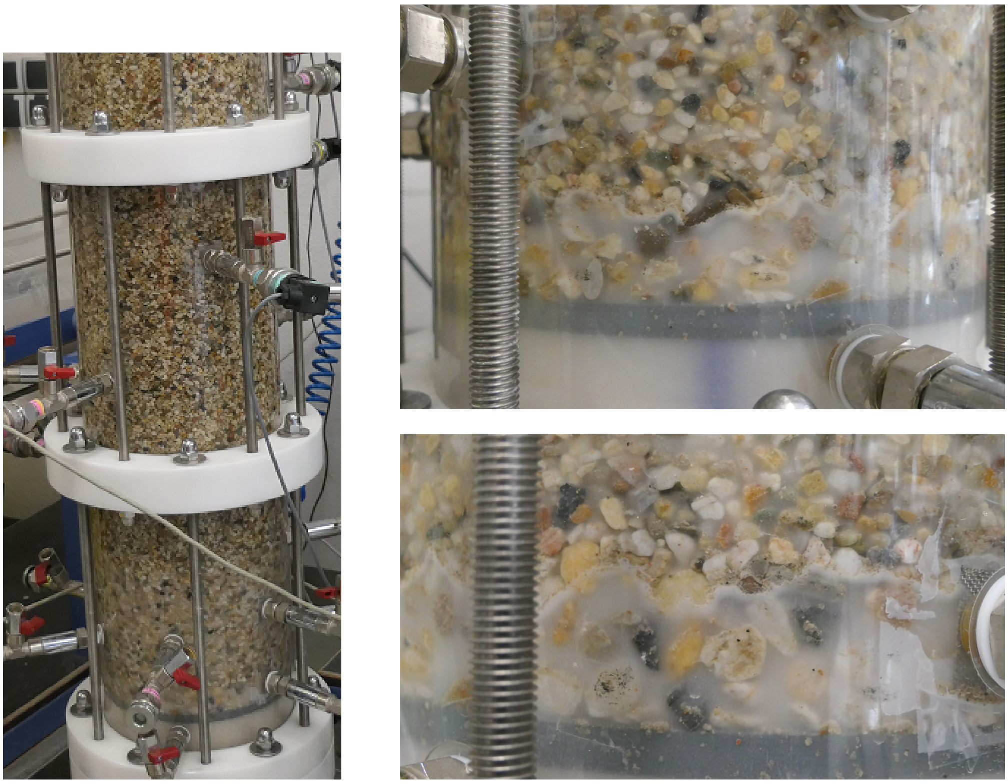

(b) Soil 3/5 mm – XAN 2.5 $S_{XS/S/M/G}$ 4x40

Figure D.4.: V-L: filter cake formation with XAN/CMC-H

D.2. Start of polymer penetration

In order to clarify the definition of the start of polymer penetration into the test soil, Fig. D.6-D.5 show the 'raw' development of the penetration depth over time for 0/2 soil for the first 30-40 cm of penetration depth. Fig. D.8 illustrates the related development of the pressure transfer shown exemplarily for the the pressure mobilized (transferred) between the first two sensors ($p_F - p_{S1} = p_{mob,wall}$) with increasing penetration depth. A full illustration of the development of all sensors is given in appendix D.3. Fig. D.7 show the same relationships for the tests in finer sand material (0.125/0.355). The different methods for the determination of the point where the polymer solution likely reaches the test material as described in section3.3.1 are marked by reference lines.

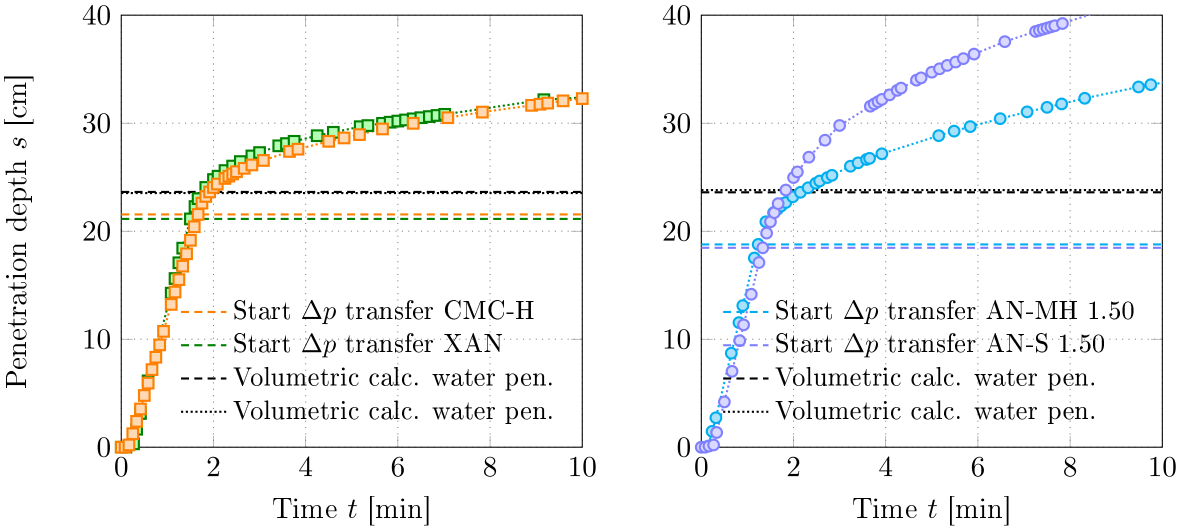

(a) $_1$CMC-H 5 / $_1$XAN 2.5 (dw)

(b) $_1$AN-S 1.5 / $_1$AN-MH 1.5 (dw)

Figure D.5.: 0/2 – no additives: 'raw' penetration depth including water penetration (CMC-H, XAN, AN-S, AN-MH)

The initial water penetration can be distinguished by an initially linear increase in penetration depth, i.e. a relatively constant penetration rate. However, a deviation from this line as well as the start of pressure transfer to the ground start before the polymer solution is calculated to reach the sand interface, which is indicated by the black lines (volumetric determination). Deviations range around

AN-S/AN-MH (ca. 5 cm) > AN-H/ANmix (ca. 3 cm) > CMC-H/XAN (ca. 1-2 cm)

The peak of the earth wall pressure transfer $p_{mob,wall}$ is reached at a higher penetration depth (after the black reference line) for the polymers of natural origin (CMC-H and XAN) than the peak of the synthetic representatives (at or slightly before the black reference line).

One possible explanation could be that polymer solution and water mix at their interface before reaching the sand bottom. Visual evaluation immediately before reaching the soil filter material found no visible mixing effect, but rather a clear front (exemplarily shown in appendix Fig. D.2-D.3). It cannot be ruled out, however, that mixing occurs to a small degree, e.g. when passing the soil filter.

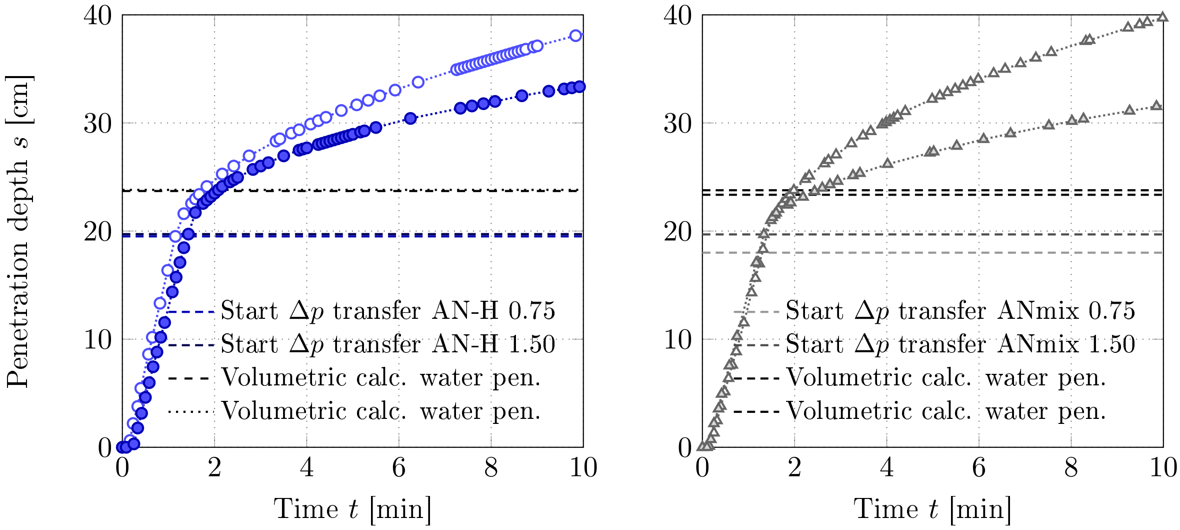

(a) $_1$AN-H 1.5 / 0.75 (dw)
(b) $_1$ANmix 1.5 / 0.75 (dw)

Figure D.6.: 0/2 – no additives: ‘raw’ penetration depth including water penetration (AN-H, ANmix)

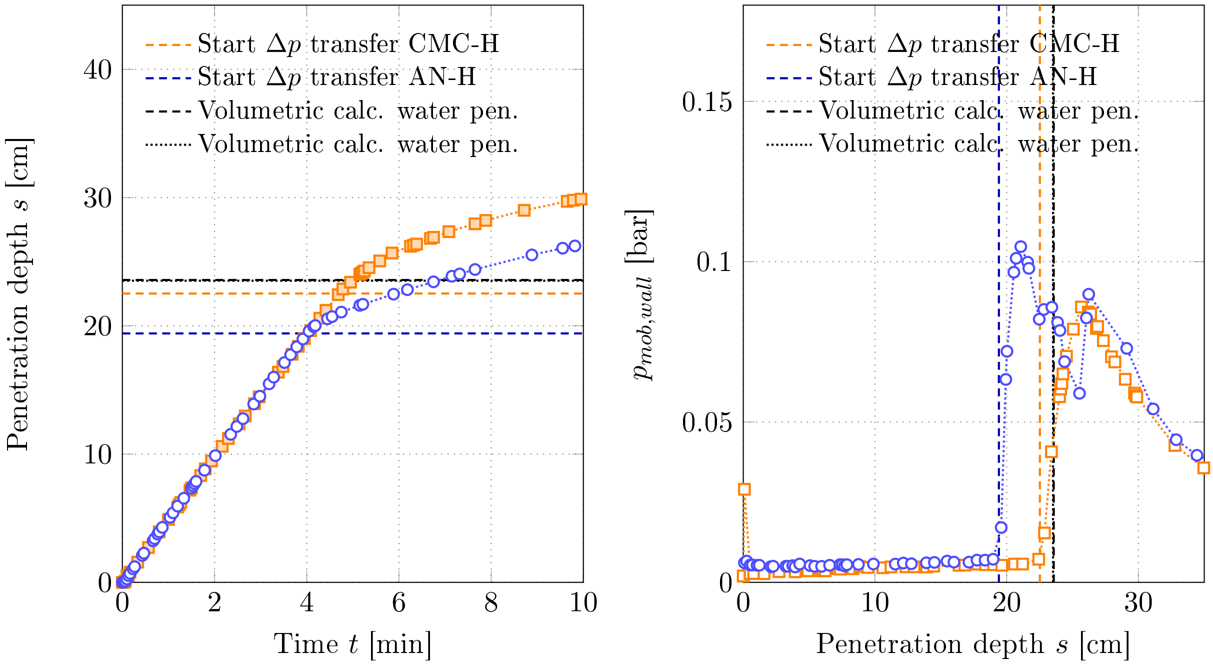

Figure D.7.: 0/2 – no additives: ‘raw’ pressure-penetration relationships including water penetration for $_2$CMC-H 2.5 / $_2$AN-H 0.75 (dw)

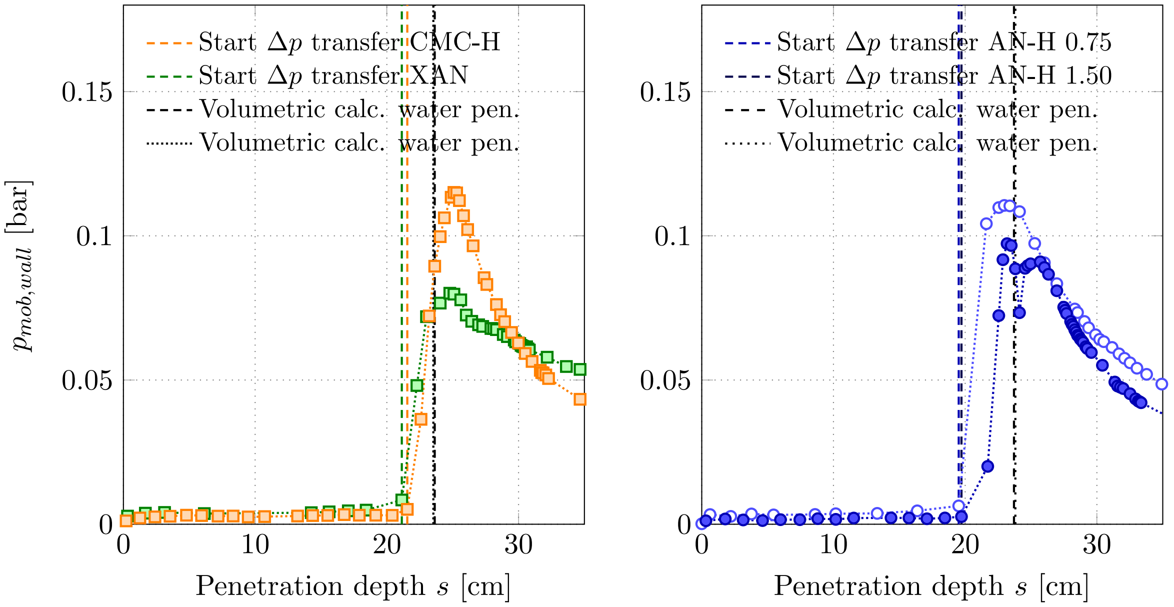

(a) $_1$CMC-H 5 / $_1$XAN 2.5 (dw)

(b) $_1$AN-H 1.5 / 0.75 (dw)

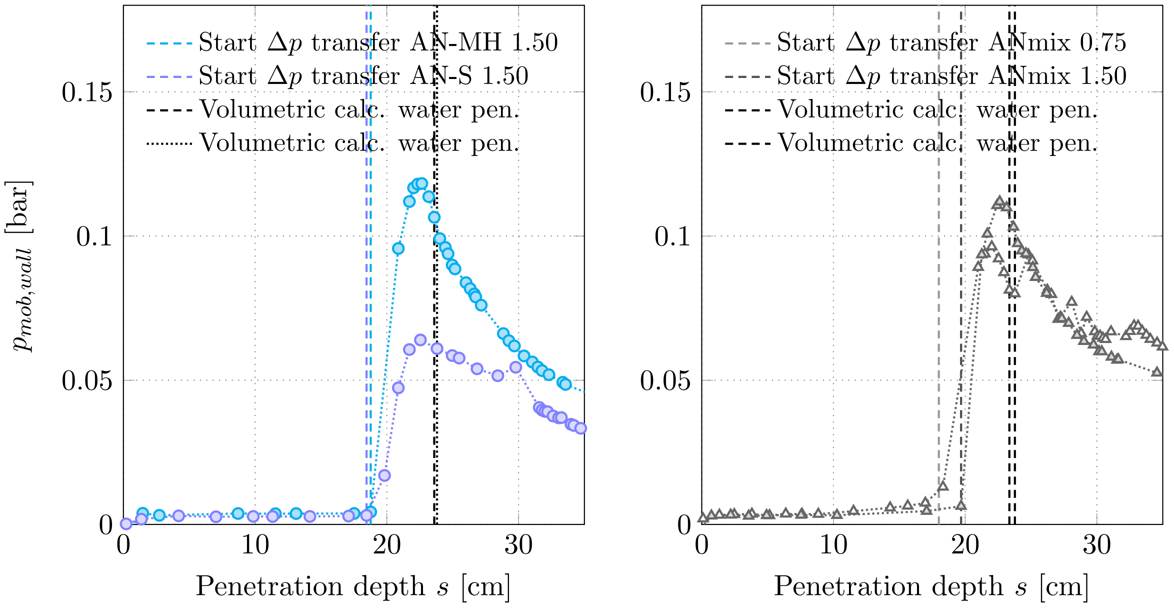

(c) $_1$AN-S 1.5 / $_1$AN-MH 1.5 (dw)

(d) $_1$ANmix 1.5 / 0.75 (dw)

Figure D.8.: 0/2 – no additives: 'raw' development of $p_{mob,wall} = p_F - p_{S1}$ including water penetration

D.3. Pressure sensor development

Vertical lines of the same colour as the pressure curve indicate where $s(t)$ reaches the level of the respective sensor:

- solid lines: as calculated from water volume in the system
- dashed lines: from start of pressure transfer / deviation in penetration rate

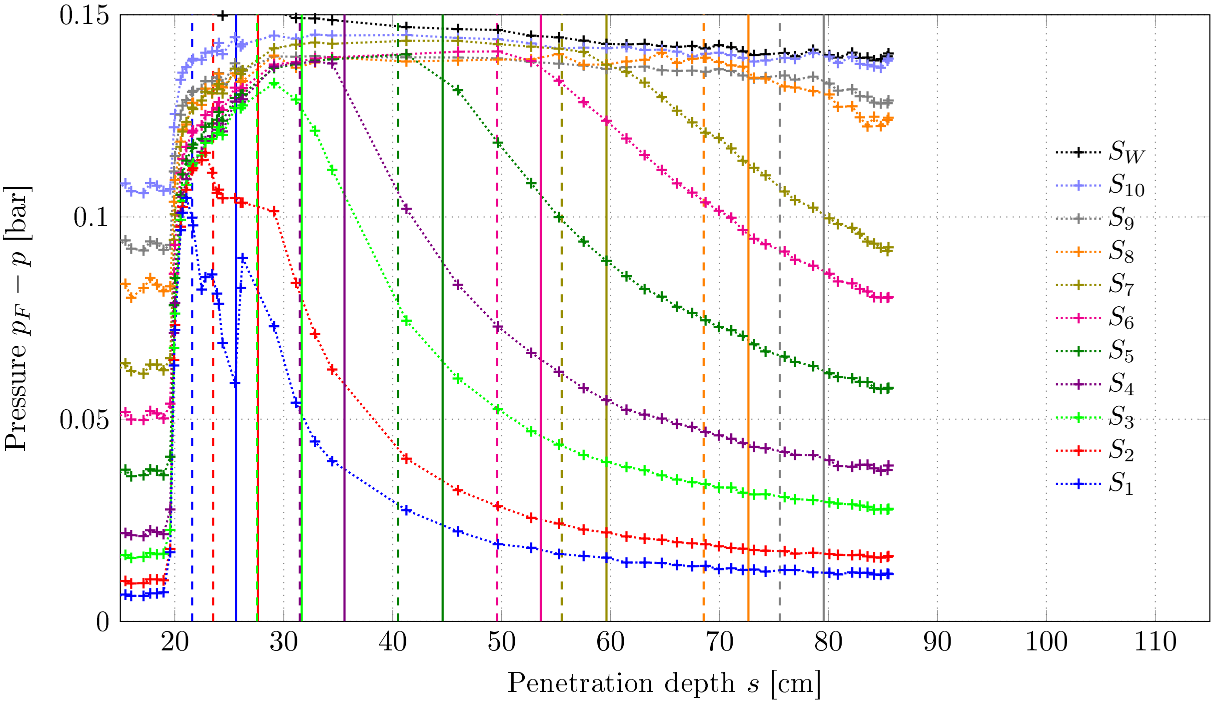

Figure D.9.: Pressure transfer $p_{mob}(s)$: 0.125/0.355 mm – $_2$AN-H

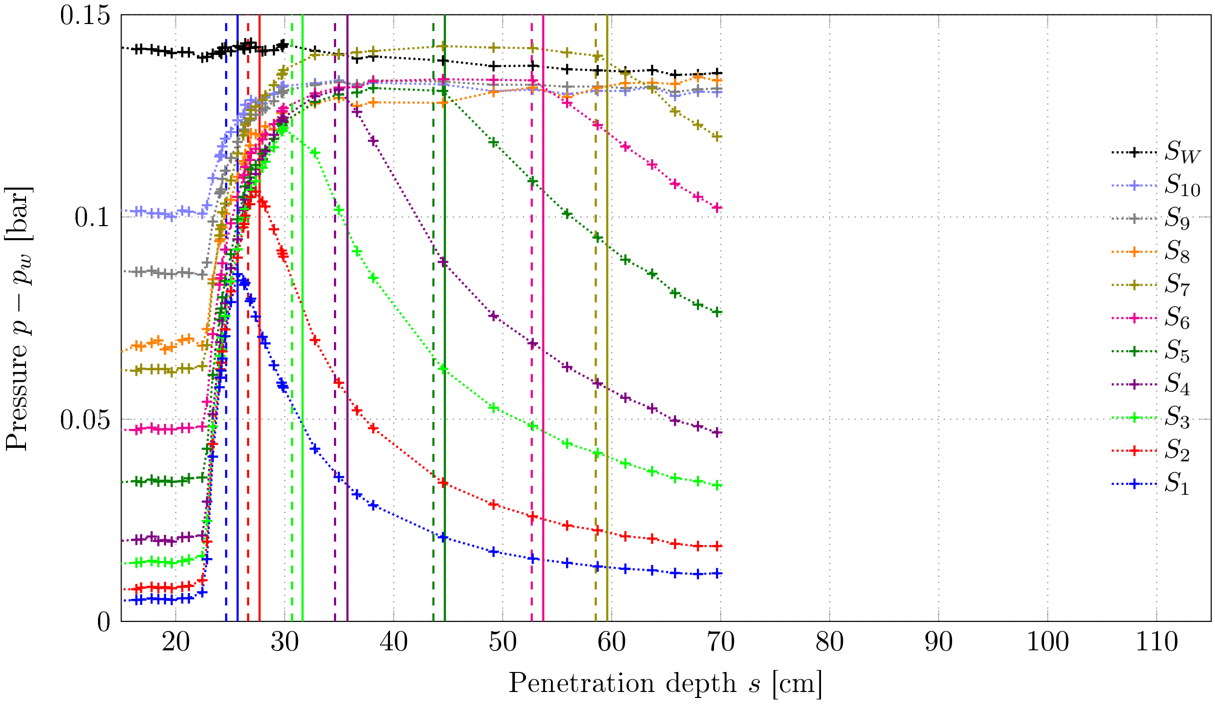

Figure D.10.: Pressure transfer $p_{mob}(s)$: 0.125/0.355 mm – $_2$CMC-H tw

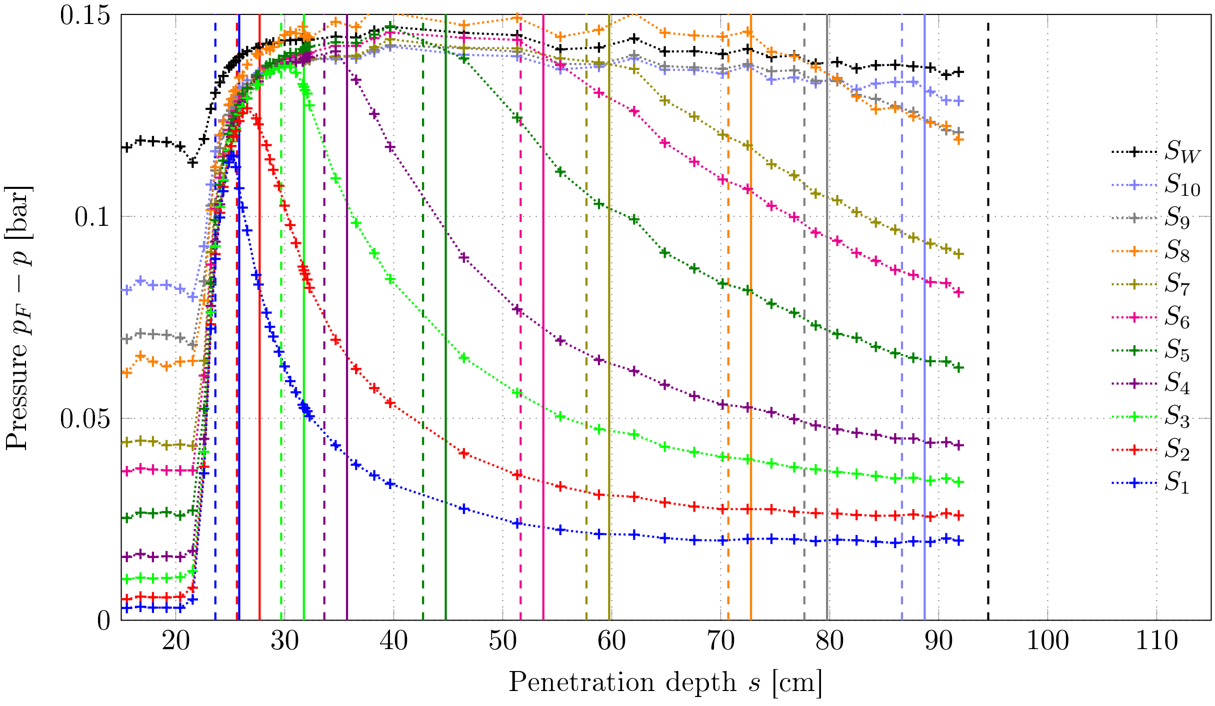

Figure D.11.: Pressure transfer $p_{mob}(s)$: 0/2 mm – $_1$CMC-H 5.00

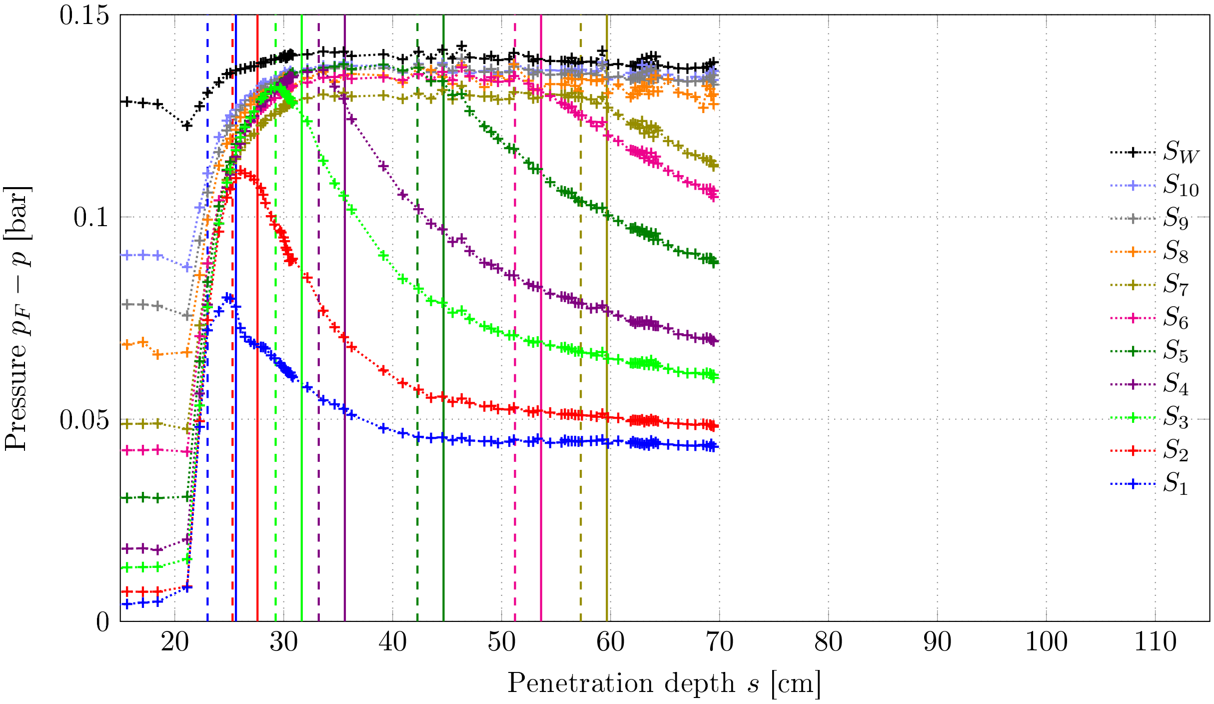

Figure D.12.: Pressure transfer $p_{mob}(s)$: 0/2 mm – ${}_1$XAN 2.50

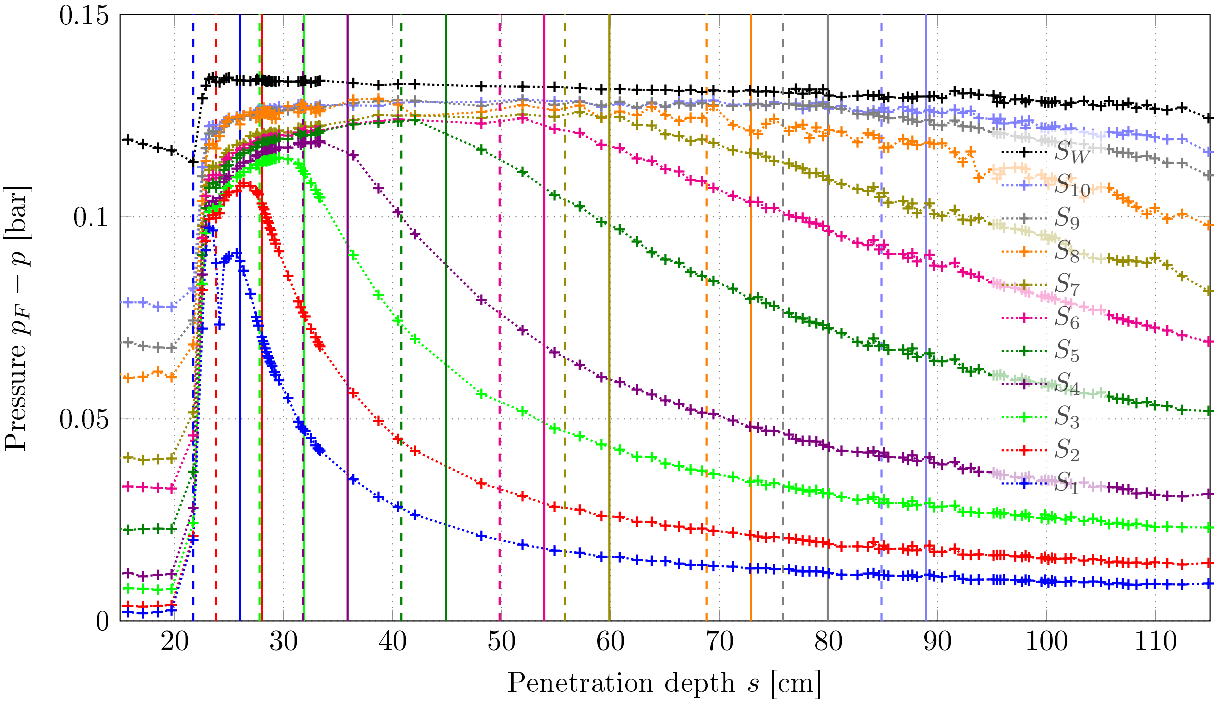

Figure D.13.: Pressure transfer $p_{mob}(s)$: 0/2 mm – ${}_1$AN-H 1.50

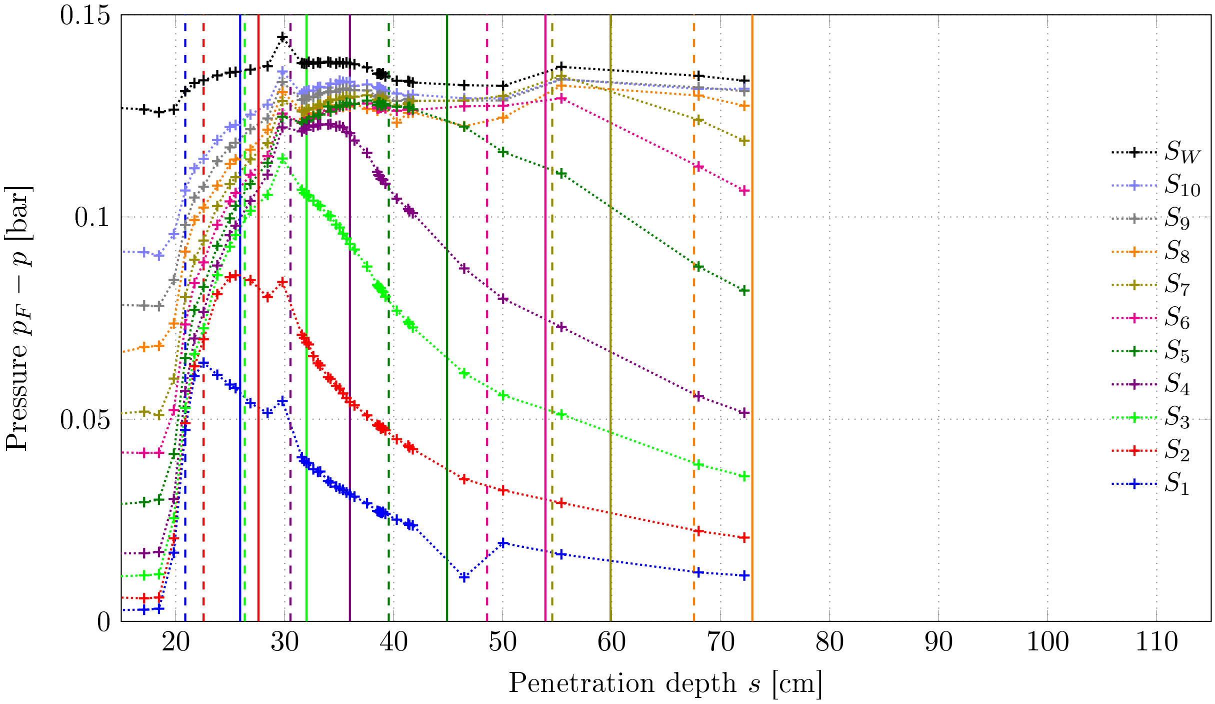

Figure D.14.: Pressure transfer $p_{mob}(s)$: 0/2 mm – $_1$AN-S 1.50

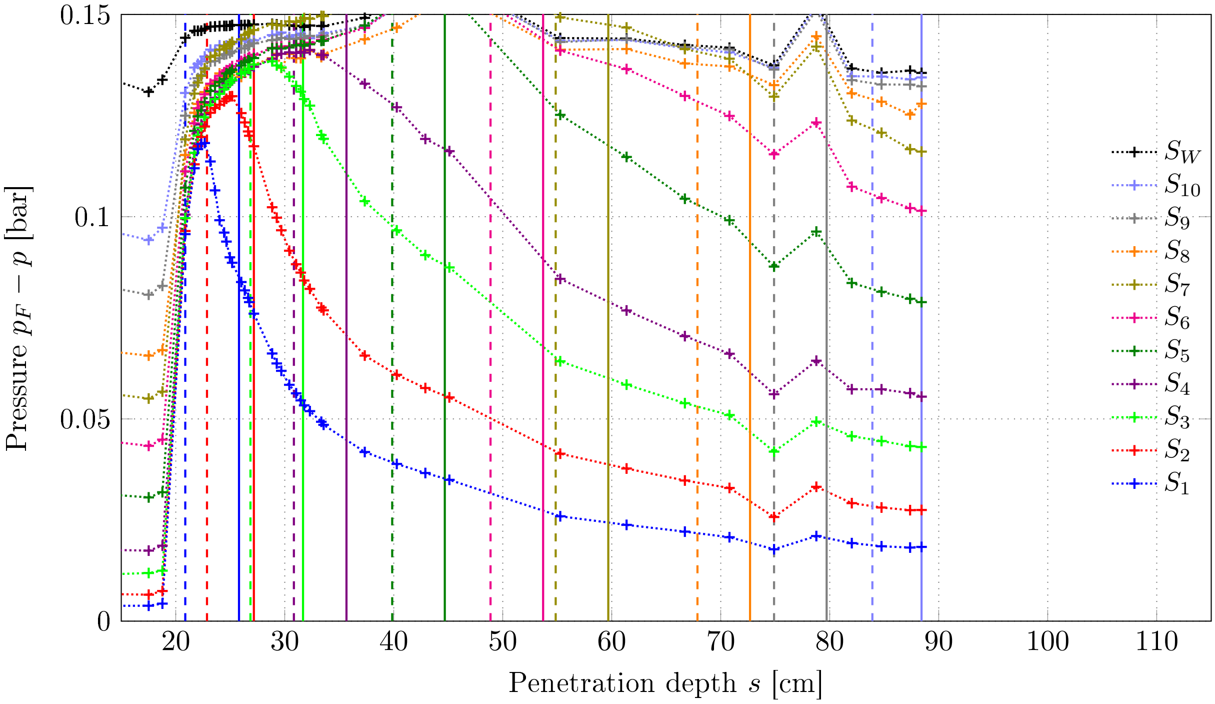

Figure D.15.: Pressure transfer $p_{mob}(s)$: 0/2 mm – $_1$AN-MH 1.50

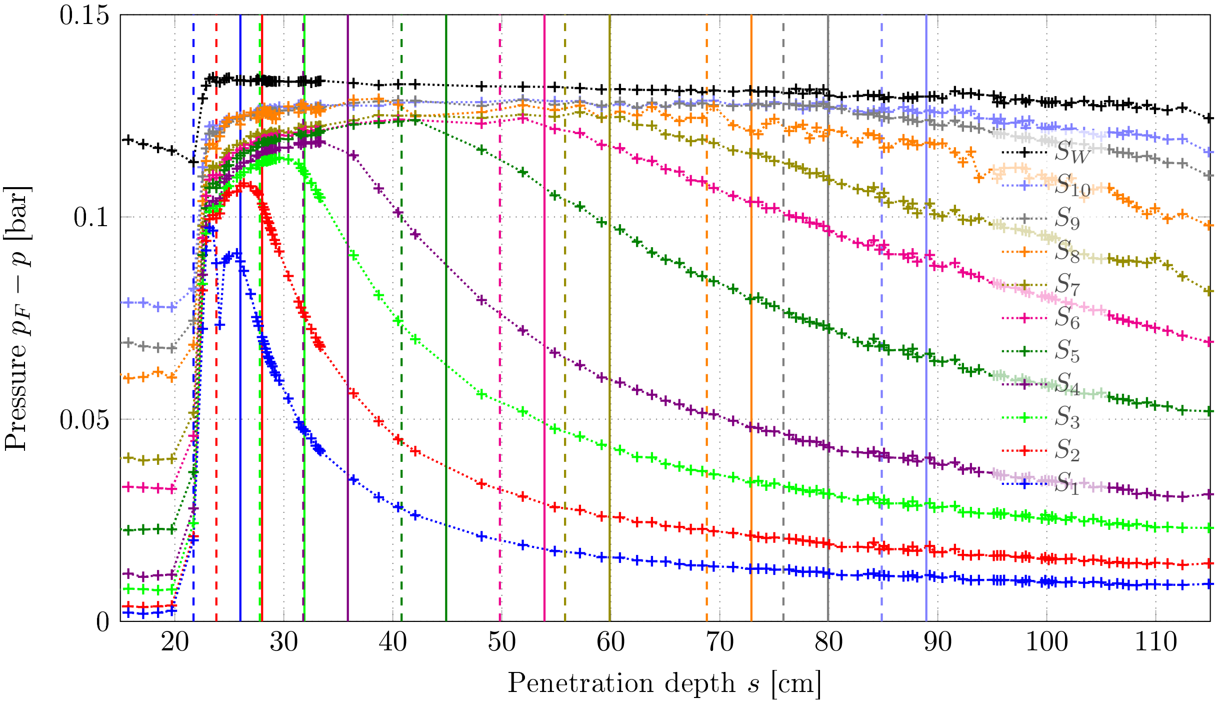

Figure D.16.: Pressure transfer $p_{mob}(s)$: 0/2 mm – $_1$AN-H 1.50

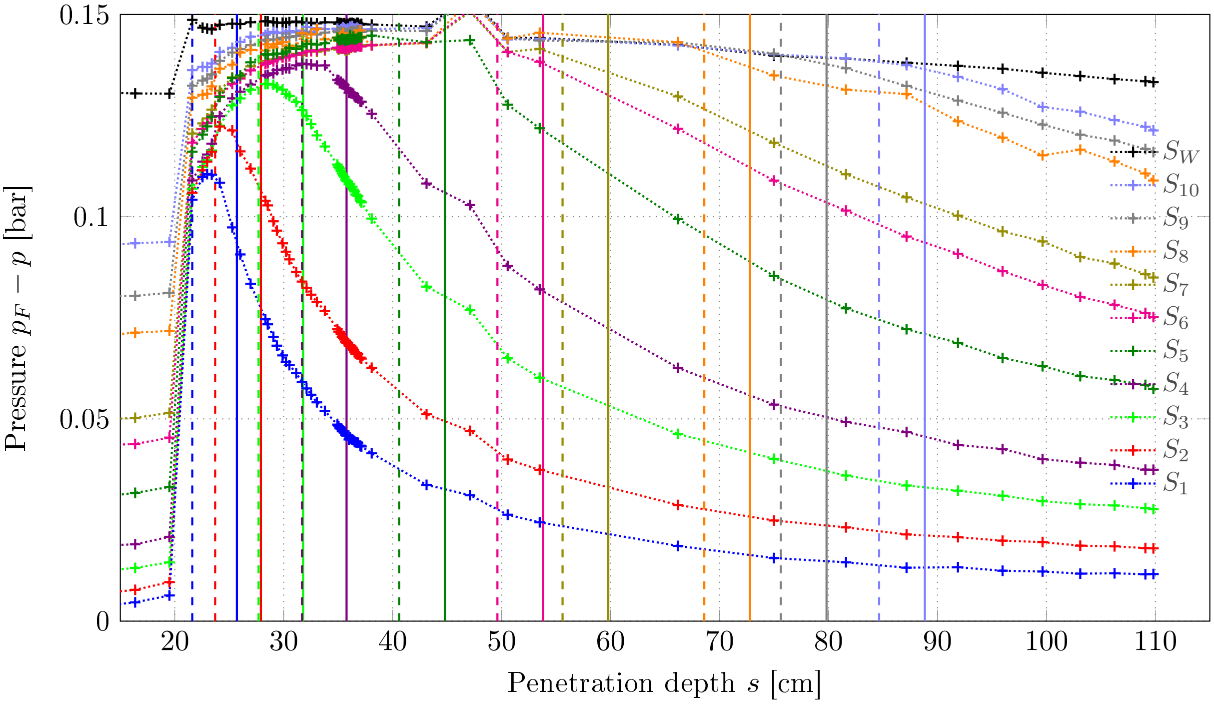

Figure D.17.: Pressure transfer $p_{mob}(s)$: 0/2 mm – $_1$AN-H 0.75

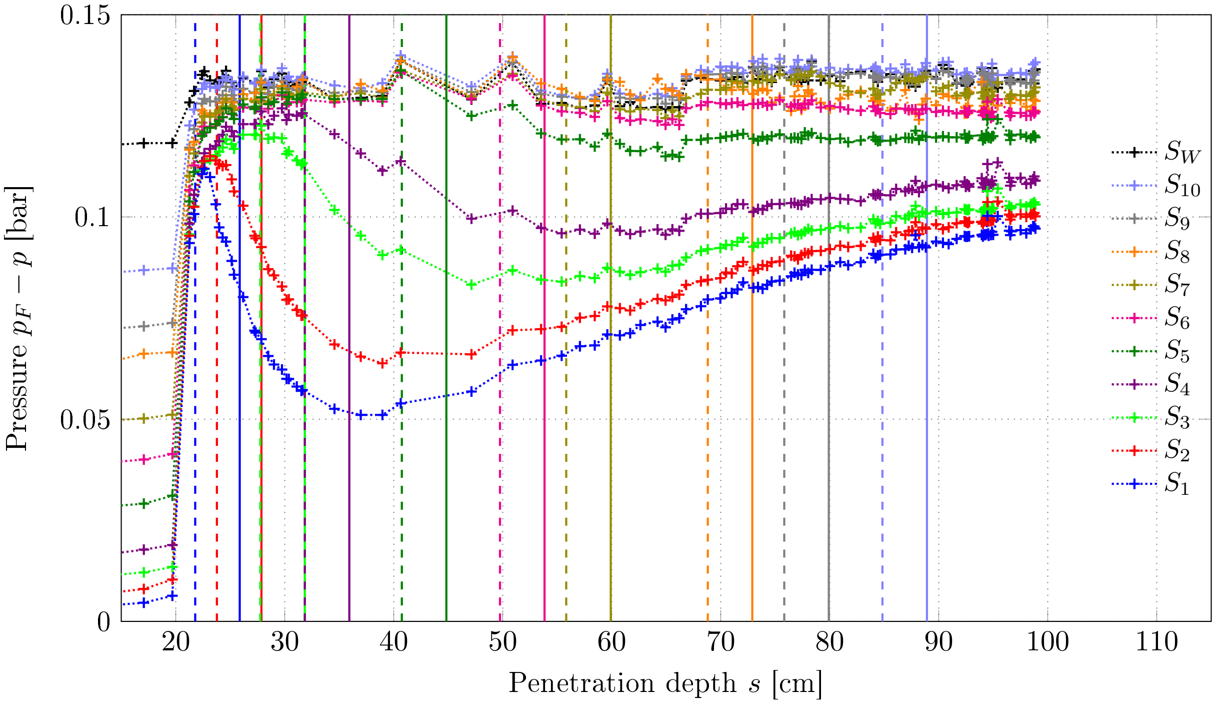

Figure D.18.: Pressure transfer $p_{mob}(s)$: 0/2 mm – $_1$ANmix 1.50

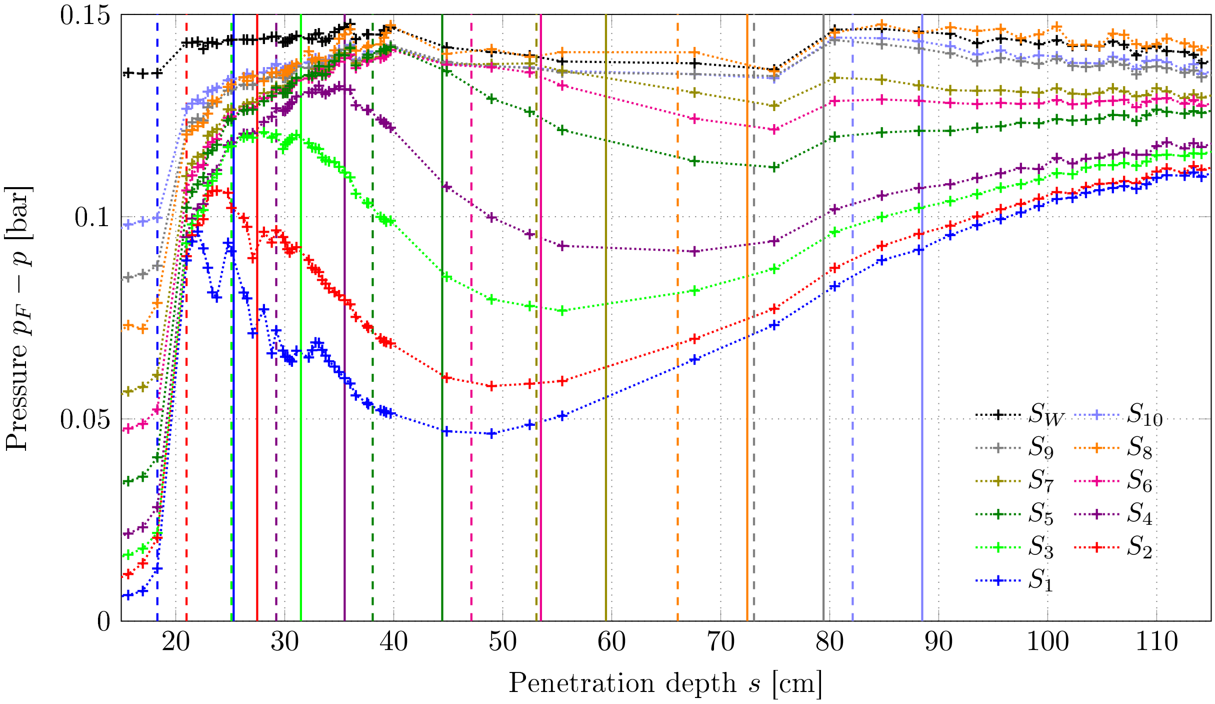

Figure D.19.: Pressure transfer $p_{mob}(s)$: 0/2 mm – $_1$ANmix 0.75

D.4. Pressure drop curvatures normalized along s – no additives

(based on s instead of s_P)

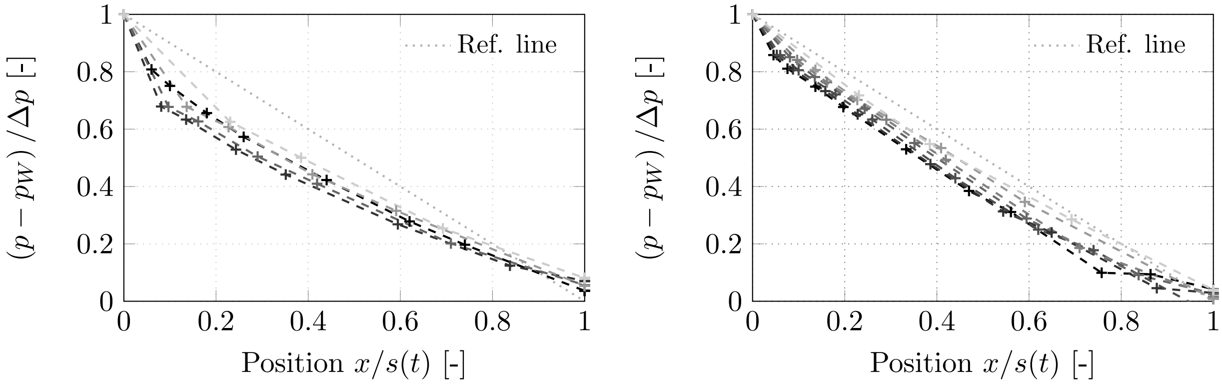

(a) $_1$XAN 2.5 dw
$s(t) = h_{s4}$ (light gray) → $s(t) = h_{s8}$ (black)

(b) $_1$CMC-H 5.00 dw
$s(t) = h_{s4}$ (light gray) → $s(t) = h_{s10}$ (black)

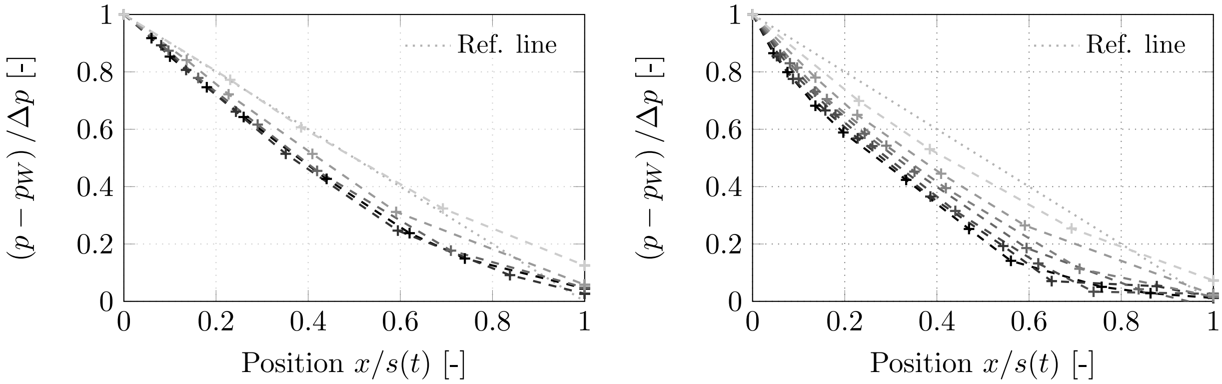

(c) $_1$AN-S 1.5 dw
$s(t) = h_{s4}$ (light gray) → h_{s8} (black)

(d) $_1$AN-MH 1.5 dw
$s(t) = h_{s4}$ (light gray) → h_{s10} (black)

Figure D.20.: V-L: normalized pressure drop curvature along the penetration depth: 0/2 – CMC-H, XAN, AN-S, AN-MH

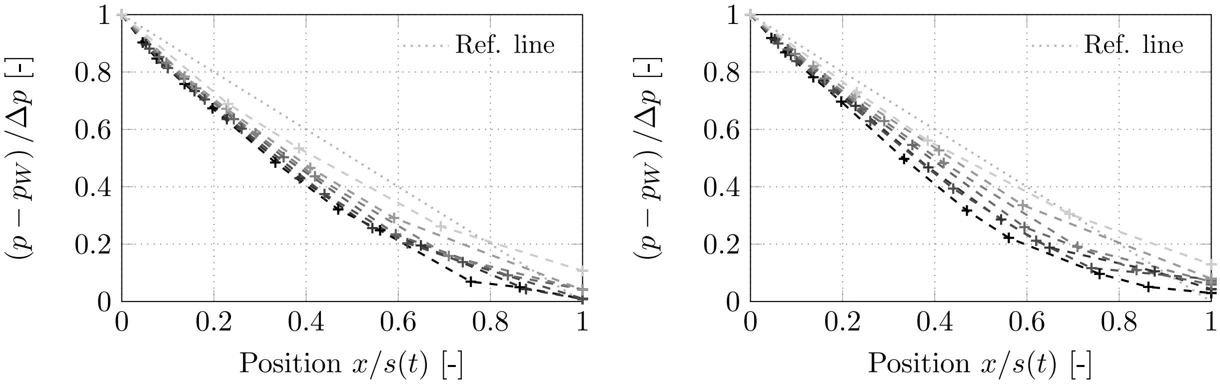

(a) ${}_1$AN-H 0.75 dw
$s(t) = h_{s4}$ (light gray) $\rightarrow h_{s10}$ (black)

(b) ${}_1$AN-H 1.5 dw
$s(t) = h_{s4}$ (light gray) $\rightarrow h_{s10}$ (black)

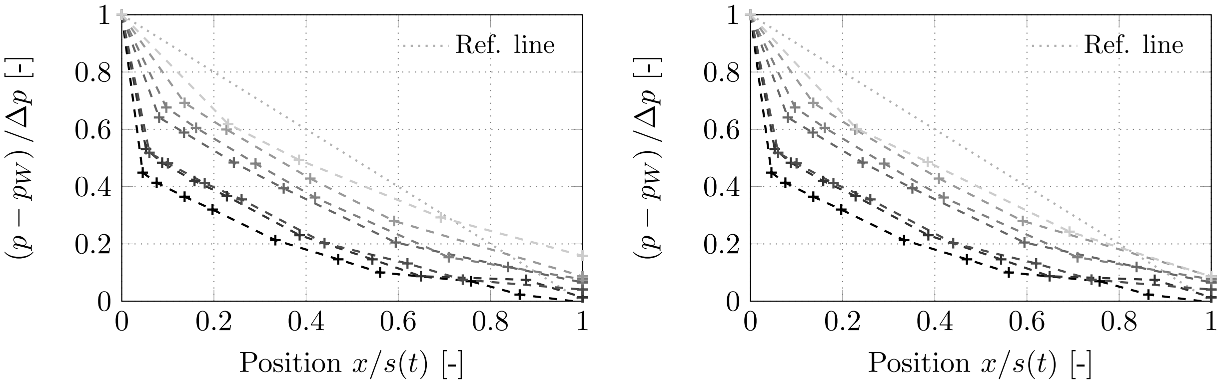

(c) ${}_1$ANmix 0.75 dw
$s(t) = h_{s4}$ (light gray) $\rightarrow h_{s10}$ (black)

(d) ${}_1$ANmix 1.5 dw
$s(t) = h_{s4}$ (light gray) $\rightarrow h_{s10}$ (black)

Figure D.21.: Normalized pressure drop curvature along the penetration depth: 0/2 – AN-H vs. ANmix

D.5. Capillary bundle approximation

D.5.1. Determination of Newtonian plateaus

The points of intersection between Newtonian plateau and power-law viscous flow behaviour are determined based on equal gradients (v) at equal penetration depth s_i (related to i)

(1) Determine point of intersection i_1 ($= \Delta p/s_1$) between lower Newtonian plateau behaviour (top red) and viscous behaviour (blue) (Fig. D.22) based on:

- $v = ds_{Newton,\eta min}/dt$ (Eq. 2.23)
- $v = ds_{visk}/dt$ (Eq. 2.22)

(2) $s(T) = s_{Newton,\eta min}(t)$ until s_1
(3) $s(T) = s_{visk}(t)$ after s_1
(4) Determine point of intersection s_2 between viscous behaviour (blue) and upper Newtonian plateau behaviour (bottom red) (Fig. D.22) based on:

- $v = ds_{Newton,\eta max}/dt$ (Eq. 2.23)
- $v = ds_{visk}/dt$ (Eq. 2.22)

(5) Determine time frames for the respective stages via superposition (Fig.D.23) for a given time frame T until $T = T_{max}$

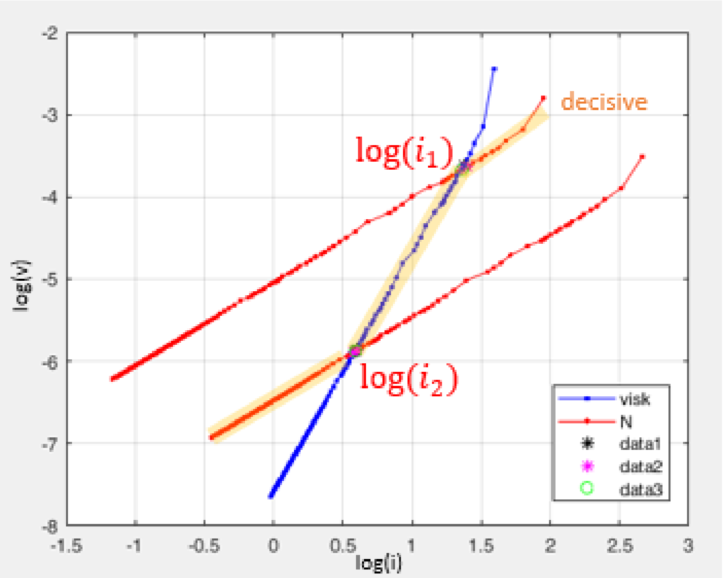

Figure D.22.: Determination of points of intersection at $v - i$ (blue: power law, red: Newtonian plateaus)

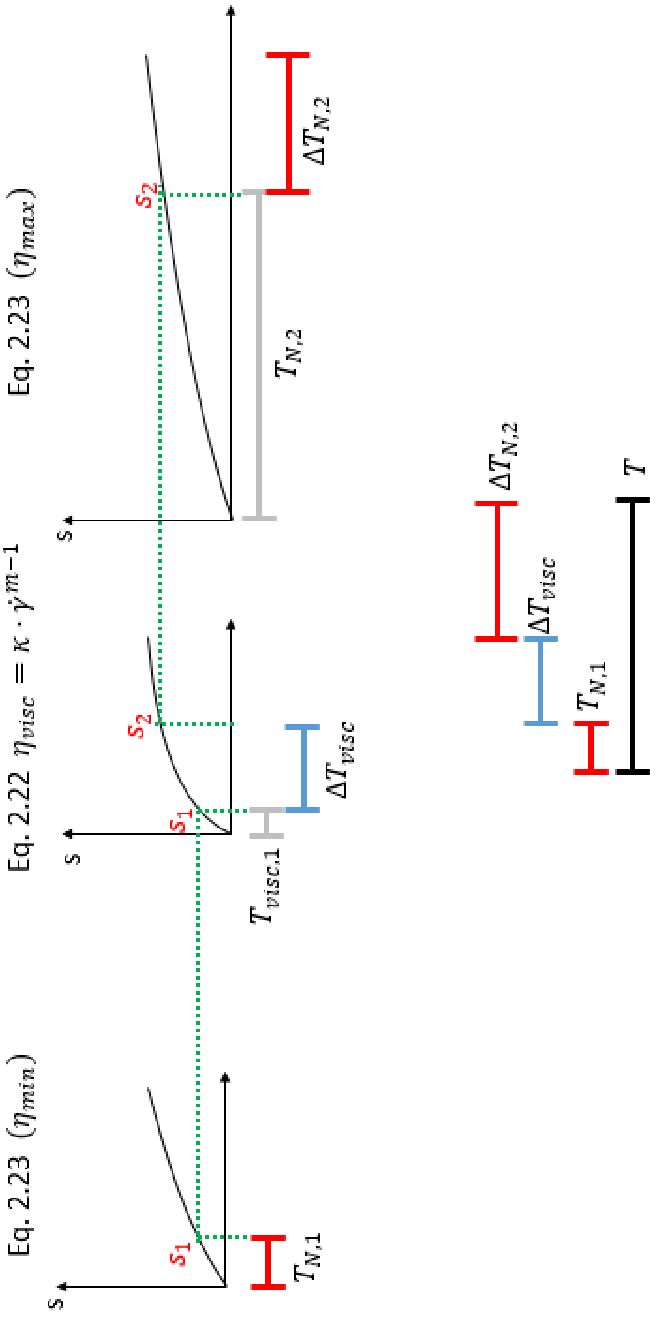

Figure D.23.: Composition of s(T): superposition

D.5.2. Examplary display of the influence of individual approximation parameters

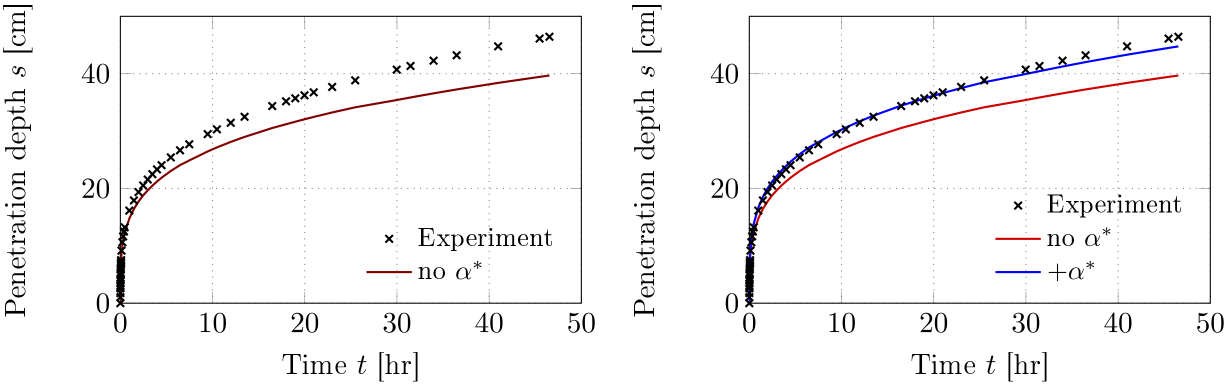

(a) no α^*

(b) $+\alpha^*$

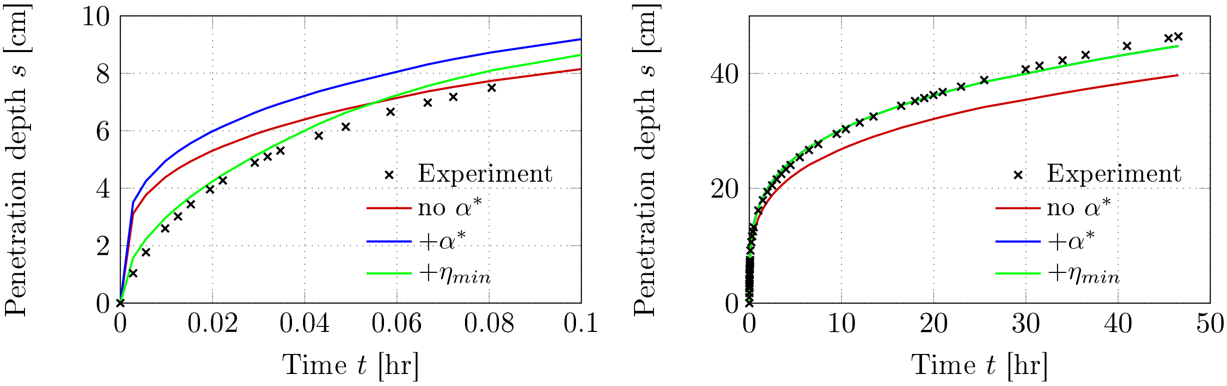

(c) $+\alpha^* + \eta_{min}$

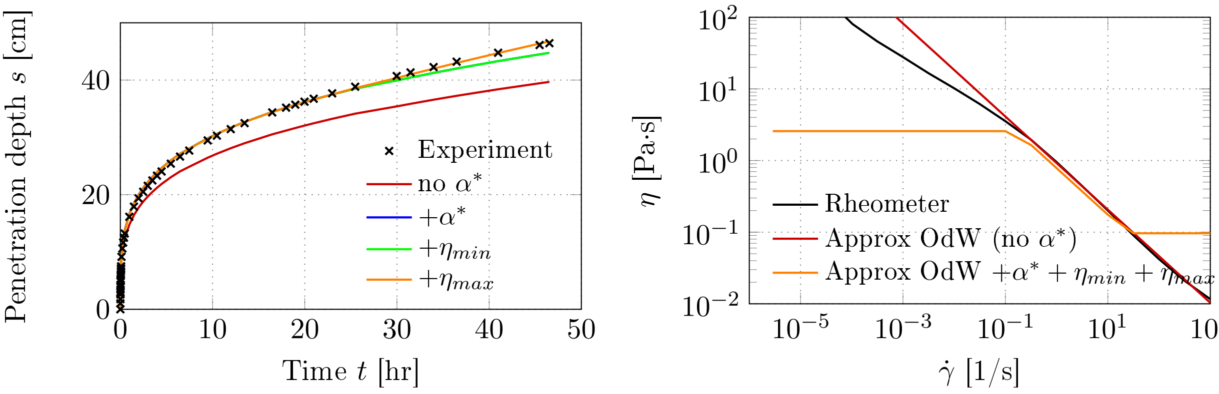

(d) $+\alpha^* + \eta_{min} + \eta_{max}$

(e) Related fluid rheology

Figure D.24.: Examplary display of the influence of individual approximation parameters for ${}_1$XAN 2.50 dw in 0/2 mm

D.5.3. Results

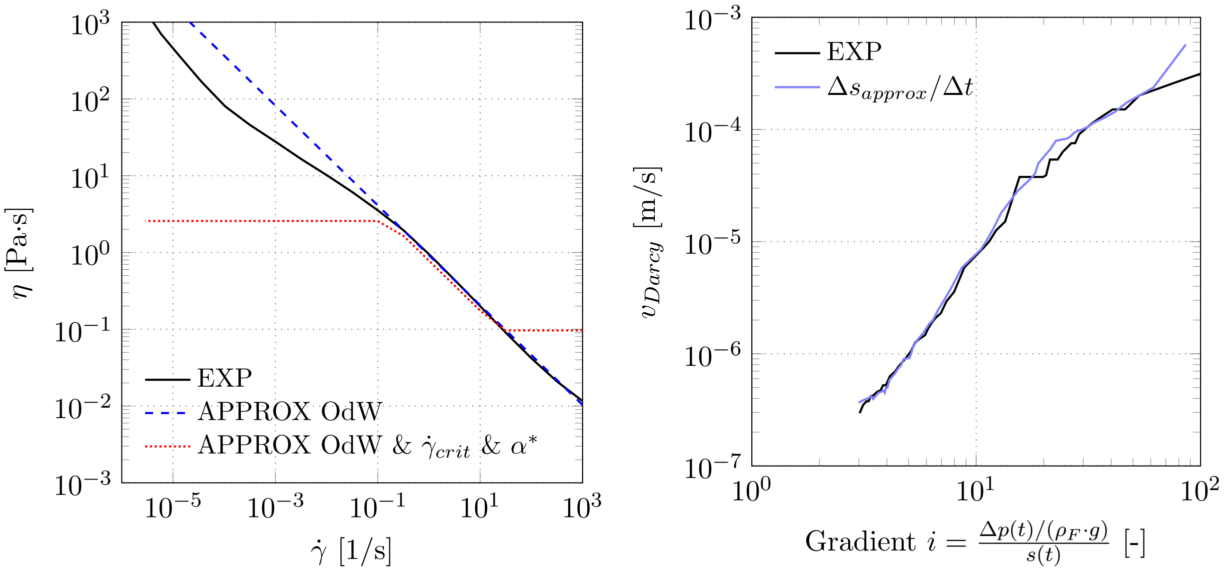

(a) Fluid rheology

(b) Filter velocity

Figure D.25.: Rheology and filter velocity approximation: 0/2 mm – $_1$XAN 2.50 dw

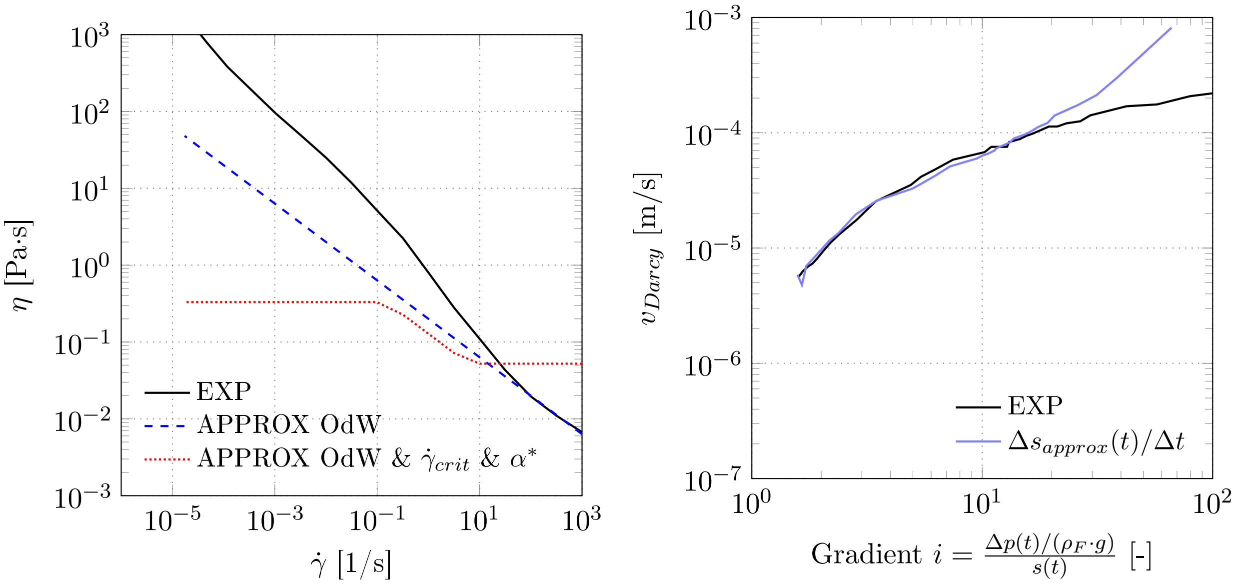

(a) Fluid rheology

(b) Filter velocity

Figure D.26.: Bulk rheology and filter velocity approximation: 0/2 mm – $_1$AN-H 0.75 dw

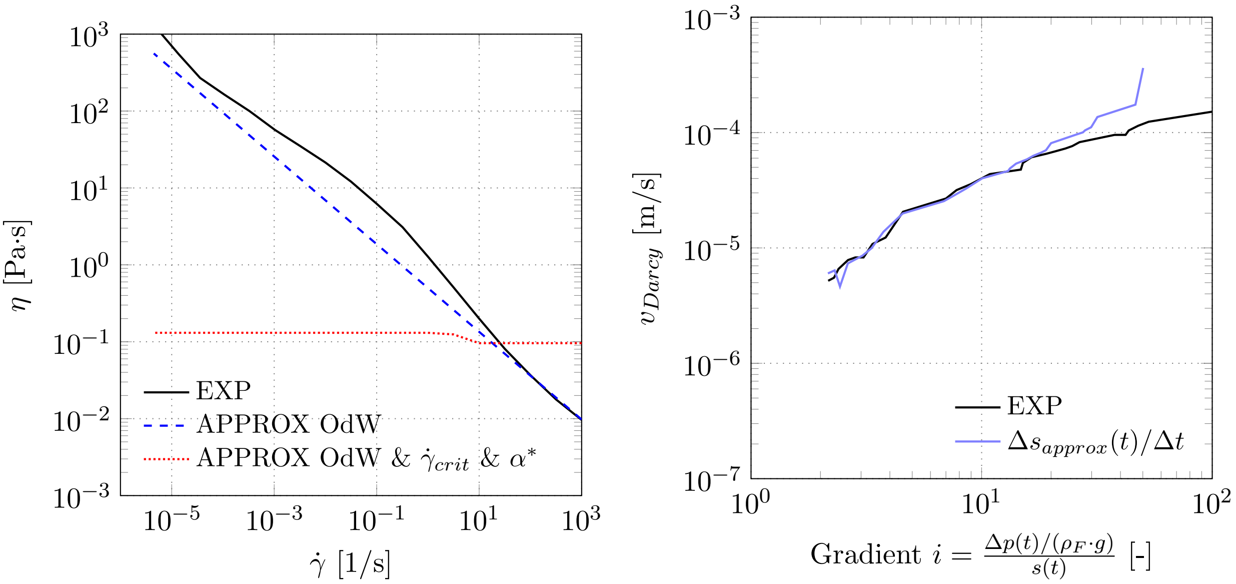

(a) Fluid rheology

(b) Filter velocity

Figure D.27.: Bulk rheology and filter velocity approximation: 0/2 mm – $_1$AN-MH 1.50 dw

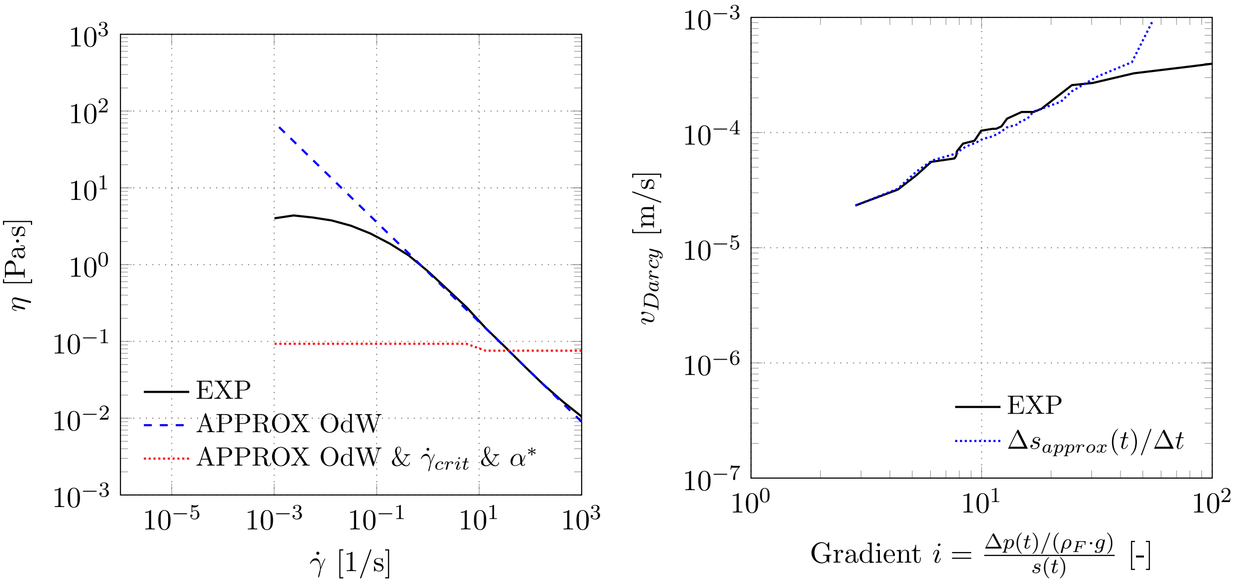

(a) Fluid rheology

(b) Filter velocity

Figure D.28.: Bulk rheology and filter velocity approximation: 0/2 mm – $_1$AN-S 1.50 dw

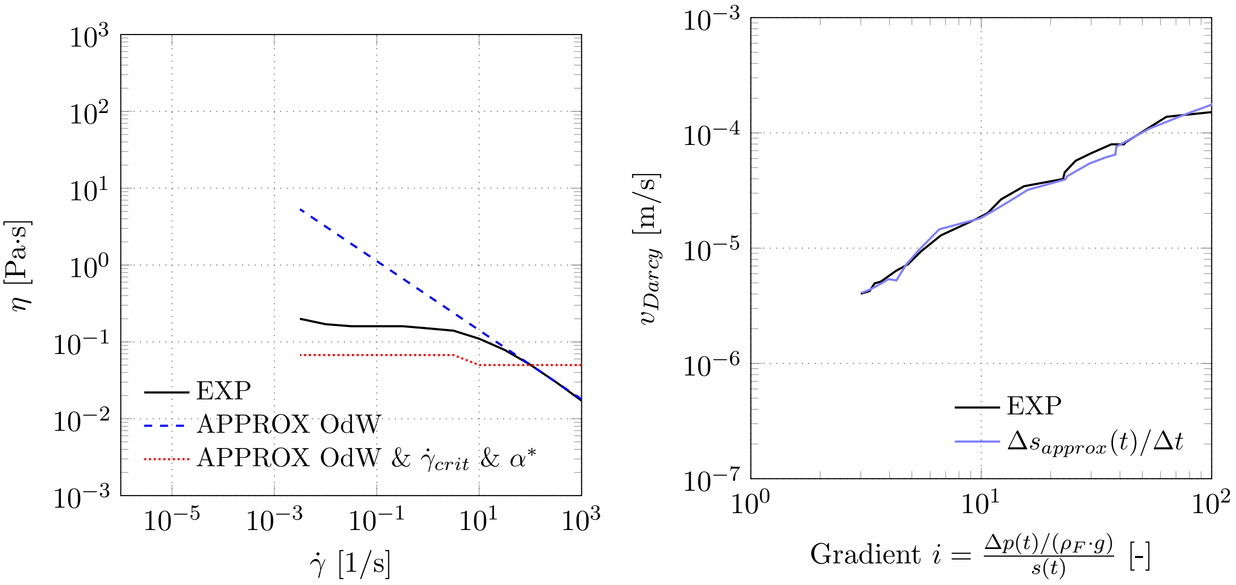

(a) Fluid rheology

(b) Filter velocity

Figure D.29.: Bulk rheology and filter velocity approximation: 0.1/0.4 mm – $_{2}$CMC-H 2.50 tw

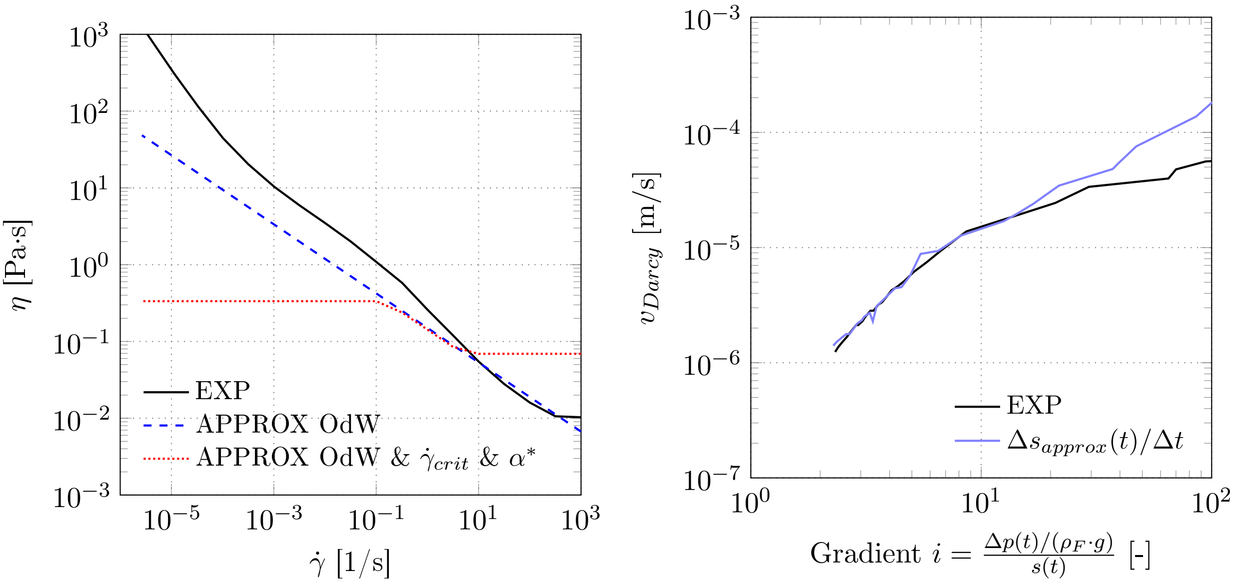

(a) Fluid rheology

(b) Filter velocity

Figure D.30.: Bulk rheology and filter velocity approximation: 0.1/0.4 mm – $_{2}$AN-H 0.75 tw

E. V-S/H-P/H-R

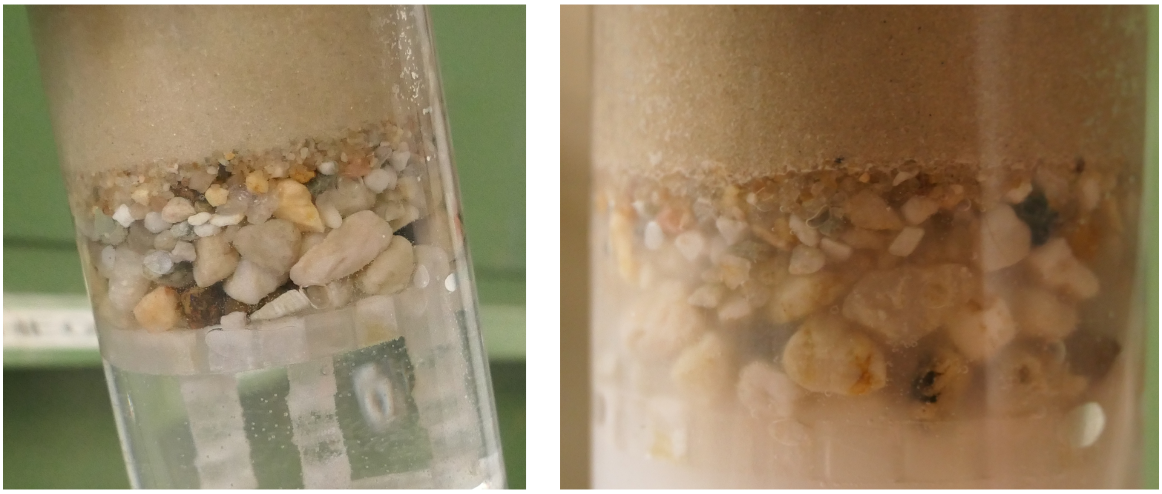

(a) Soil 0.125/0.25 mm – XAN 1.5 + S_{XS} 20

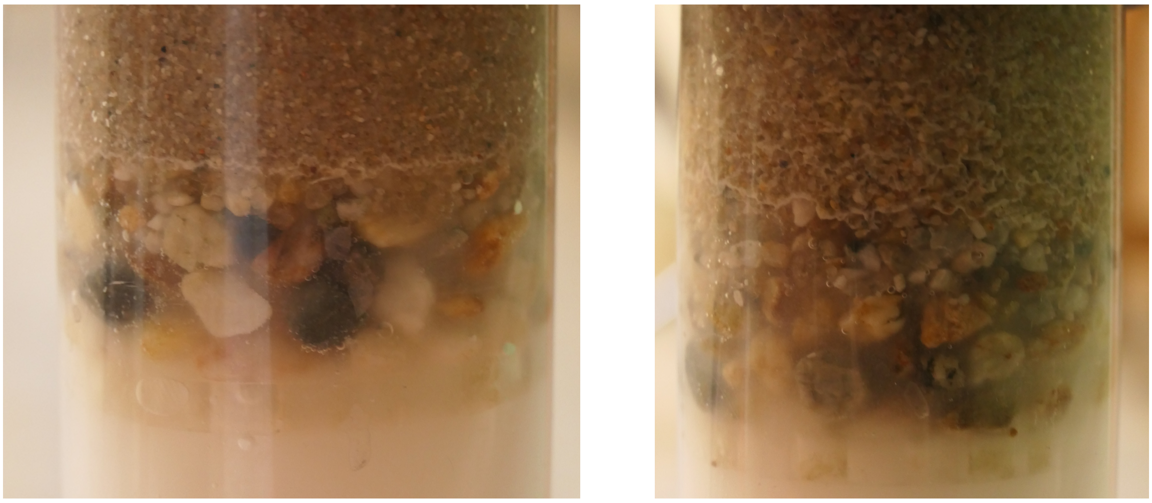

(b) Soil 0.4/0.5 mm – XAN 1.5 + S_{XS} 20

(c) Soil 0.71/1 mm – XAN 2.5 + S_{XS} 20

Figure E.1.: V-S: filter cake formation with XAN in sand

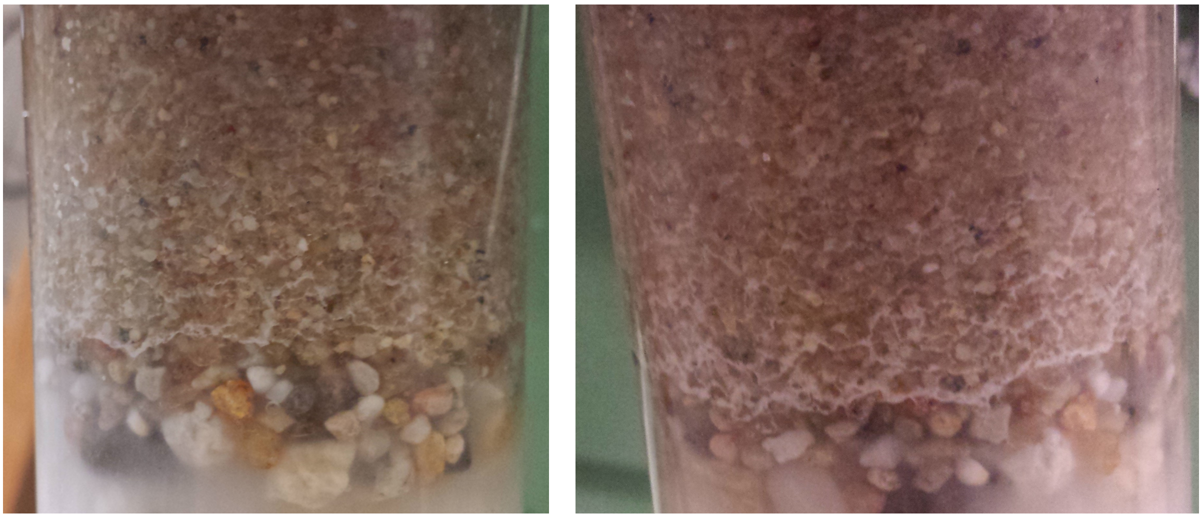

(a) Soil 0.71/1 mm – CMC-H 5 + S_{XS} 20 (effective, but slightly slower filter-cake formation with visible colmation zone)

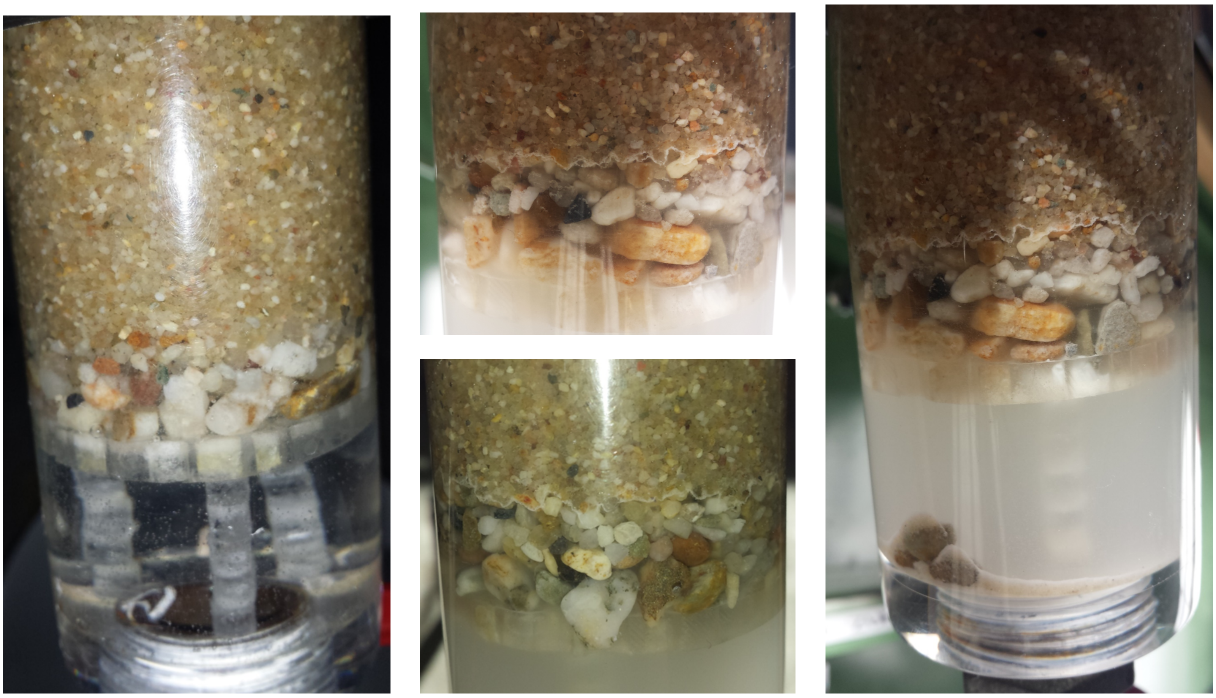

(b) Soil 0.71/1 mm – CMC-H 5 + $\mathrm{S}_{XS/S}$ 2x10 (immediate clear-cut filter cake from effective colmation with addition of a larger fines fraction)

Figure E.2.: V-S: filter cake formation with CMC-H in sand

(a) Soil 5/8 mm – CMC-H 5 + $S_{XS/S/M/G}$ 4x80 (effective colmation, but no clear outer filter cake line due to surface effects)

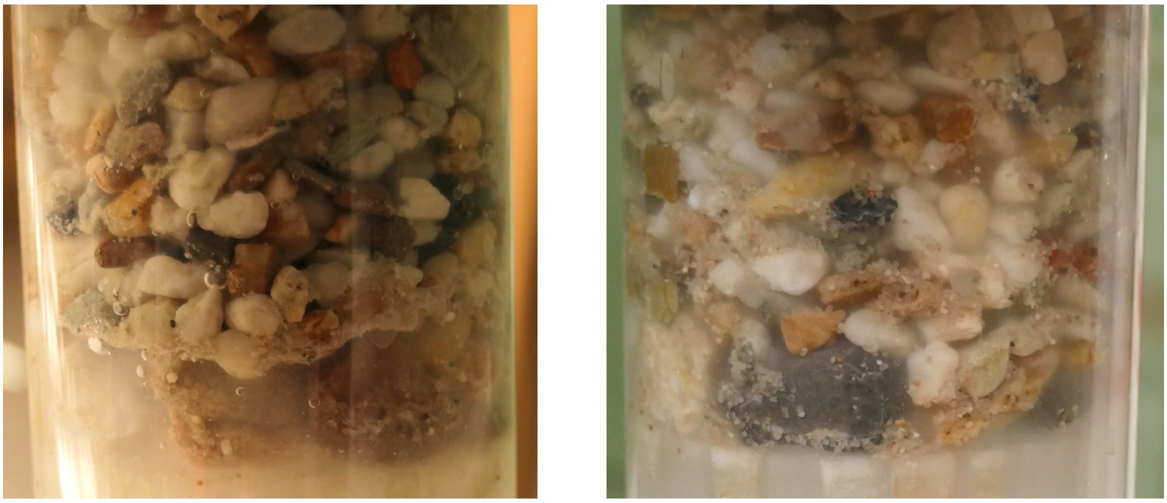

(b) Soil 2.8/4 mm – XAN 2.5 + $S_{XS/S/M/G}$ 4x10 (effective immediate colmation with adapted grain size distribution of fines)

(c) Soil 2.8/4 mm – XAN 2.5 + S_S 20 (no colmation due to missing fine fraction)

Figure E.3.: V-S: filter cake formation with CMC-H/XAN in gravel

(a) Soil 0.125/0.25 mm –AN-H 1.5 + S_{XS} 20

(b) Soil 1.6/2 mm – AN-H 0.75 + $\mathrm{S}_{XS/S}$ 2x10 (no colmation, visible flow paths through filtered fines)

(c) Soil 0.71/1 mm – AN-M 0.75 + S_{XS} 20 (colmation)

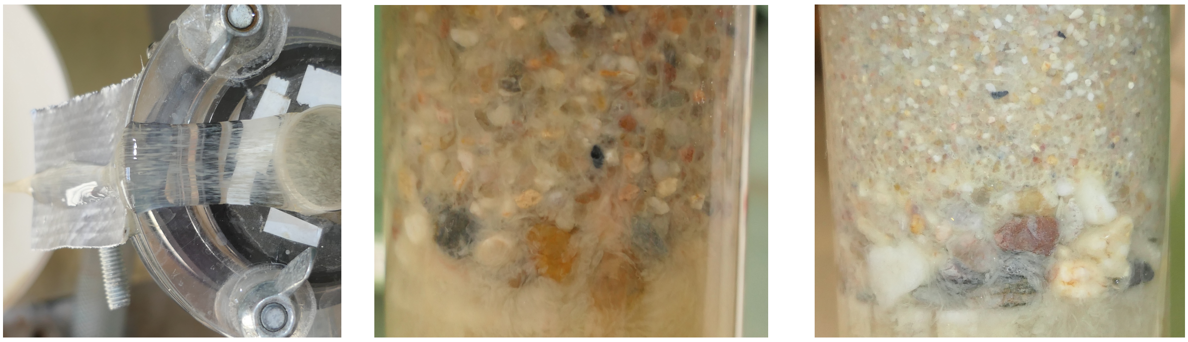

(d) Soil 1.6/2 mm – AN-H 0.75 + B 5 (no colmation, visible flow paths with oriented bentonite flocks)

(e) Soil 0.71/1 mm – AN-H 0.75 + B 5 (colmation)

Figure E.4.: V-S: filter cake formation with AN-M/AN-H in sand

Figure E.5.: V-S: testing device

Figure E.6.: H-R: testing device

Figure E.7.: H-R: testing device at penetration stage

Figure E.8.: H-R: testing device at concreting stage

Mitteilungshefte

Grundbau, Bodenmechanik und Unterirdisches Bauen

Herausgegeben von Prof. Dr.-Ing. B. Walz

Bericht – Nr. 1, 1982
H. Grasshoff:
Optimierung der Baugrunderkundungen bei der Planung von Bauobjekten einfacher Art
B.Walz:
Bodenmechanische Modelltechnik als Mittel zur Bemessung von Grundbauwerken

Bericht – Nr. 2, 1983
M. Pulsfort, C. Drenkelfuß:
Elastische Einspannung von Pfählen im Boden
J. Gerlach, B. Walz:
Die Berechnung des Erddruckes bei räumlichen Problemen mit einem geotechnischen Bruchmechanismus

Bericht – Nr. 3, 1985
D. Genske:
Ingenieurgeologische Erkundung und Beurteilung von Felsböschungen im Rheinischen Schiefergebirge
M. Pulsfort, J. Gerlach, B. Walz, H. Meckenstock:
Einsatz der Nahbereichs-Photogrammetrie zur Messung von Bodendeformationen bei kleinmaßstäblichen Modellversuchen in der Bodenmechanik

Bericht – Nr. 4, 1986
M. Pulsfort:
Untersuchungen zum Tragverhalten von Einzelfundamenten neben suspensionsgestützten Erdwänden begrenzter Länge

Bericht – Nr. 5, 1986
J. Gerlach:
Experimentelle Ermittlung der Bruchkörperform und Entwicklung eines daraus abgeleiteten Berechnungsverfahrens zur Bestimmung des aktiven räumlichen Erddrucks

Bericht – Nr. 6, 1987
H. Graßhoff:
Systemsteifigkeit und Flächengründung
B. Walz, K. Hock:
Berechnung des räumlich aktiven Erddrucks mit der modifizierten Elementscheibentheorie

Bericht – Nr. 7, 1988
G. Leonhardt:
Gebirgsumlagerungen und Geländesenkungen bei Tunneln – das technische Modell des schubsteifen Balkens in seiner Anwendung auf Fragen des Tunnelbaus

Bericht – Nr. 8, 1988
D. Genske:
Ansatz für ein probabilistisches Sicherheitskonzept ungesicherter Felsböschungen im Rheinischen Schiefergebirge

Bericht – Nr. 9, 1991
Vorträge und Einzelveröffentlichungen 1989 bis 1991

Bericht – Nr. 10, 1991
P. Waldhoff:
Untersuchungen zum Setzungsverhalten von Einzelfundamenten neben flüssigkeitsgestützten Erdwänden begrenzter Länge

Bericht – Nr. 11, 1991
R. Rauh:
Beitrag zum Tragverhalten horizontal belasteter, im nichtbindigen Boden eingespannter Wandsysteme unter besonderer Berücksichtigung einer Böschungsgeometrie

Bericht – Nr. 12, 1992
K. Hock-Berghaus:
Berechnung aktiver Erddruckkräfte nach der Variationsrechnung

Bericht – Nr. 13, 1993
J. Steinhoff:
Standsicherheitsbetrachtungen für polymergestützte Erdwände

Bericht – Nr. 14, 1995
M.-Th. Steinhoff:
Die Belastung von Schächten in Deponien

Bericht – Nr. 15, 1995
O. Emde:
Der unterspannte schubsteife Balken – ein mechanisches Modell für geotextilbewehrte Tragschichten

Bericht – Nr. 16, 1996
T. Happe:
Entwicklung eines empirisch-mathematischen Verfahrens zur Abschätzung der Setzungen von Einzelfundamenten neben suspensionsgestützten Schlitzen begrenzter Länge

Bericht – Nr. 17, 1997
K. Hock-Berghaus:
Unterfangungen, Konstruktion, Statik und Innovation

Bericht – Nr. 18, 1998
A. Kremer:
Das Tragverhalten von eingespannten biegsamen Stützwänden im bodenmechanischen 1g-Modellversuch

Bericht – Nr. 19, 1998
B. Schaupp:
Grundlagen der Bewertung von Deponien unter Anwendung der Fuzzy-Logik

Bodenmechanik und Grundbau

Herausgegeben von Prof. Dr.-Ing. B. Walz und Prof. Dr.-Ing. M. Pulsfort

Bericht – Nr. 20, 1999
A. Kaddis:
Untersuchungen zum Ankerquerdruck an vorspringenden Baugrubenecken

Bericht – Nr. 21, 1999
M. Thewes:
Adhäsion von Tonböden beim Tunnelvortrieb mit Flüssigkeitsschilden

Bericht – Nr. 22, 1999
M. Herten:
Räumlicher Erddruck auf Schachtbauwerke in Abhängigkeit von der Wandverformung

Bericht – Nr. 23, 2000
J. Quarg-Vonscheid:
Berechnungsmodell für die Tragfähigkeit und das Gruppenverhalten von Zugpfählen

Bericht – Nr. 24, 2002
B. Bergschneider:
Zur Reichweite beim Düsenstrahlverfahren im Sand

Bericht – Nr. 25, 2003
Fach-Kolloquium Geotechnik, 26. September 2003

Bericht – Nr. 26, 2003
N. Mörchen:
Zur Grenzlast eines Druckpfahls – Untersuchungen für den Einzel- und den Gruppenpfahl

Bericht – Nr. 27, 2004
K. Dörendahl:
Das Tragverhalten von Einphasen-Dichtwandmassen als Ausfachung von Baugrubenwänden

Berichte des Lehr- und Forschungsgebietes Geotechnik

Herausgegeben von Prof. Dr.-Ing. M. Pulsfort und Prof. em. Dr.-Ing. B.Walz

Nr. 28, 2005
M. Pohl:
Modellierung von granularen Böden und biegsamen Bauwerken mit Hilfe der DEM am Beispiel einer eingebetteten Spundwand

Nr. 29, 2005
C. Hauser:
Boden-Bauwerk-Interaktion bei parallelwandigen Verbundsystemen – Bodenmechanische Modellversuche unter Anwendung innovativer Auswerteverfahren

Berichte des Lehr- und Forschungsgebietes Geotechnik

Herausgegeben von Prof. Dr.-Ing. M. Pulsfort

Nr. 30, 2010
A. Stolz:
Untersuchungen zur Beanspruchung von Vortriebsrohren beim Rohrvortrieb mit gekrümmter Linienführung in nicht bindigen Böden

Nr. 31, 2011
Ch. Thienert:
Zementfreie Mörtel für die Ringspaltverpressung beim Schildvortrieb mit flüssigkeitsgestützter Ortsbrust

Nr. 32, 2011
M. Pulsfort (Hrsg.):
Beiträge zum 3. RuhrGeo Tag 2011 - Innerstädtischer Tunnelbau und Spezialtiefbau

Nr. 33, 2011
T. Welskopf:
Untersuchungen zum Tragverhalten von Pfählen unter aktiver Horizontalbelastung

Nr. 34, 2015
M. Pulsfort (Hrsg.):
Festschrift anlässlich des 60. Geburtstages von Matthias Pulsfort

Nr. 35, 2016
M. Pulsfort (Hrsg.):
Beiträge zum 7. RuhrGeo Tag 2016 – Qualitätssicherung und Schadensprävention im Grund- und Tunnelbau

Nr. 36, 2019
M. Pulsfort (Hrsg.):
Beiträge zum 10. RuhrGeo Tag 2019 – Neue Erkenntnisse und Bauverfahren in der Geotechnik

Nr. 37, 2019
B. Böhle:
Untersuchungen im Großmaßstab zum Fließ- und Ansteifverhalten von Beton bei der Herstellung von Bohrpfählen

Nr. 38, 2019
C. Fierenkothen genannt Kaiser:
Numerische Simulationen und Laborversuche zur Ausbreitung von Frischbeton in Bohrpfählen

Nr. 39, 2021
R. Verst:
Stabilisation mechanisms of polymer solutions in the context of temporary earth-wall support – Stabilisierungswirkung von Polymerlösungen bei der Stützung von Erdwänden

Print: ISBN 978-3-00-071148-0
eBook: ISBN 978-3-00-071149-7